

Effects of mutual diffusion on morphology development in polymer blends

Citation for published version (APA):

Tufano, C. (2008). *Effects of mutual diffusion on morphology development in polymer blends*. [Phd Thesis 1 (Research TU/e / Graduation TU/e), Mechanical Engineering]. Technische Universiteit Eindhoven.
<https://doi.org/10.6100/IR634831>

DOI:

[10.6100/IR634831](https://doi.org/10.6100/IR634831)

Document status and date:

Published: 01/01/2008

Document Version:

Publisher's PDF, also known as Version of Record (includes final page, issue and volume numbers)

Please check the document version of this publication:

- A submitted manuscript is the version of the article upon submission and before peer-review. There can be important differences between the submitted version and the official published version of record. People interested in the research are advised to contact the author for the final version of the publication, or visit the DOI to the publisher's website.
- The final author version and the galley proof are versions of the publication after peer review.
- The final published version features the final layout of the paper including the volume, issue and page numbers.

[Link to publication](#)

General rights

Copyright and moral rights for the publications made accessible in the public portal are retained by the authors and/or other copyright owners and it is a condition of accessing publications that users recognise and abide by the legal requirements associated with these rights.

- Users may download and print one copy of any publication from the public portal for the purpose of private study or research.
- You may not further distribute the material or use it for any profit-making activity or commercial gain
- You may freely distribute the URL identifying the publication in the public portal.

If the publication is distributed under the terms of Article 25fa of the Dutch Copyright Act, indicated by the "Taverne" license above, please follow below link for the End User Agreement:

www.tue.nl/taverne

Take down policy

If you believe that this document breaches copyright please contact us at:

openaccess@tue.nl

providing details and we will investigate your claim.

Effects of mutual diffusion on morphology development in polymer blends

CIP-DATA LIBRARY TECHNISCHE UNIVERSITEIT EINDHOVEN

Tufano, C.

Effects of mutual diffusion on morphology development in polymer blends /
by C. Tufano. - Eindhoven: Technische Universiteit Eindhoven, 2008.

A catalogue record is available from the Eindhoven University of Technology Library.

Proefschrift. - ISBN 978-90-386-1269-0

Reproduction: University Press Facilities, Eindhoven, The Netherlands.

Cover design: C. Tufano and Oranje.

Cover illustration: blend morphologies obtained by shear flow in a confined parallel plate geometry.

Effects of mutual diffusion on morphology development in polymer blends

PROEFSCHRIFT

ter verkrijging van de graad van doctor aan de Technische Universiteit Eindhoven, op gezag van de Rector Magnificus, prof.dr.ir. C.J. van Duijn, voor een commissie aangewezen door het College voor Promoties in het openbaar te verdedigen op woensdag 4 juni 2008 om 16.00 uur

door

Carmela Tufano

geboren te Napels, Italië

Dit proefschrift is goedgekeurd door de promotor:

prof.dr.ir. H.E.H. Meijer

Copromotoren:

dr.ir. G.W.M. Peters

en

dr.ir. P.D. Anderson

Contents

Summary	ix
1 Introduction	1
1.1 State of the art	1
1.2 Morphology development of immiscible polymer blends	1
1.3 Partial miscibility	3
1.4 ...going small	3
1.5 Objectives of the thesis	5
1.6 Survey of the thesis	6
References	7
2 Transient interfacial tension of partially-miscible polymers	11
2.1 Introduction	12
2.2 Modeling	13
2.2.1 A continuous kinetic model	13
Constant interphase thickness	16
Time dependent interphase thickness	17
2.2.2 A discrete kinetic model	19
2.3 Relation with molecular parameters	23
2.4 Experimental	27
Materials	27
Methods	28
2.5 Results of transient measurements	29
2.5.1 Experimental results at different temperatures	29
The standard blend systems	29
The inverse blend systems	32
2.5.2 Discrete model results	32
2.5.3 Shi model results	32
2.6 Results of steady-state measurements	35
2.7 Conclusions	36

References	37
3 Transient interfacial tension and morphology evolution in partially-miscible polymers	41
3.1 Introduction	42
3.2 Materials and methods	43
3.3 Transient interfacial tension experiments	45
$M_n(\text{dispersed phase}) < M_n(\text{continuous phase})$	45
$M_n(\text{dispersed phase}) > M_n(\text{continuous phase})$	47
3.4 Model predictions	48
Discrete model results	48
Kinetic model results	50
3.5 Influence of a transient interfacial tension on morphology development in flow	52
$M_n(\text{dispersed phase}) < M_n(\text{continuous phase})$	52
$M_n(\text{dispersed phase}) > M_n(\text{continuous phase})$	53
3.6 Comparing experimental results with sharp-interface drainage models	55
3.7 Conclusions	58
References	59
4 Effects of partial miscibility on drop-wall and drop-drop interactions	63
4.1 Introduction	64
4.2 Materials and methods	66
Materials	66
Experimental methods	66
4.3 Diffuse-interface model	67
Governing equations	67
Final governing equations	70
Ginzburg-Landau approximation	71
The gradient energy parameter	73
Numerical method	74
Validation of the model	74
Influence of the mobility parameters	75
Influence of concentration of LMW species on the computed interfacial tension	79
4.4 Interfacial tension results	79
4.5 Experimental results	80
Drop-drop interaction: PB/PDMS system	80
Drop-drop interaction: PBD/PDMS system	82
Drop-wall interaction: PB/PDMS system	82

	Drop-wall interaction: PBD/PDMS system	83
4.6	Numerical results	85
	Drop-drop interaction	86
	Drop-wall interaction	94
4.7	Conclusions	98
	References	98
5	Study of morphological hysteresis in <i>partially-miscible</i> polymers	101
5.1	Introduction	102
5.2	Materials and methods	103
	Materials	103
	Experimental methods	104
	Morphology probing using dynamic measurements	104
5.3	Hysteresis zone	106
	Theories to probe the morphological hysteresis	106
	Hysteresis results	108
	PB in PDMS	108
	PBD in PDMS	113
5.4	Coalescence after a step-down in shear rate	115
	Modeling coalescence	115
	Coalescence results	117
	PB in PDMS	118
	PBD in PDMS	119
5.5	Conclusions	121
	References	123
6	Confined flow of polymer blends	127
6.1	Introduction	128
	Blends in unconfined flow	128
	Blends in confined flow	129
6.2	Materials and methods	131
	Materials	131
	Experimental methods	131
6.3	Modeling	133
	Maffettone-Minale model	133
	Minale model	134
	Minale model with effective viscosity	135
6.4	Results	136
	6.4.1 PBD/PDMS system.	136
	6.4.2 PB/PDMS system	139
	6.4.3 Conditions to identify strings	143

20 wt% PBD	145
20 wt% PB	146
Dependence of L and B on the dimensionless shear rate	146
6.4.4 Steady-state morphology and layering effects	147
Average droplet size	147
Layering effect	148
6.5 Conclusions	149
References	150
7 Conclusions and recommendations	153
7.1 Conclusions	153
7.2 Recommendations	156
Samenvatting	157
Acknowledgements	161
Curriculum Vitae	163

Summary

Effects of mutual diffusion on morphology development in polymer blends

Compared to designing and synthesizing new polymers, mixing of two or more polymers is a relatively fast, flexible and cost-efficient way to create tailor-made materials. The final properties of the materials obtained by physical blending are determined by the morphology, which is the result of a dynamic equilibrium between coalescence and break-up processes occurring simultaneously during the compounding step. The interfacial tension is a key parameter since it affects both processes. The goal of this work is to investigate the effects of partial miscibility of the composing polymers on the interfacial tension and thus, on the morphology development of the polymeric suspensions.

Three grades of polybutene (PB), differing in average molecular weight, and a single grade of polybutadiene (PBD) with polydispersity index close to 1, are used as the dispersed phase; polydimethylsiloxane (PDMS), with a molecular weight much higher than the drop phases, is used as the continuous phase.

Transient and steady interfacial tension measurements are carried out. For the PB/PDMS systems, a peculiar transient interfacial tension behavior, different from the PBD/PDMS system, is found. When contact between a PB-drop and the matrix is established, the interfacial tension starts to decrease in time. This effect is attributed to the diffusion of low molecular weight (LMW) species from the drop into the matrix which increases the interfacial thickness. While time proceeds, molecules accumulated at the interface migrate into the matrix and, consequently the transient interfacial tension increases. When the diffusion process is exhausted, since the drop is a finite source, a final plateau value is reached and sustained. Drop volume

reduction confirms the diffusion from the drop into the matrix. It is shown that the PB/PDMS systems are highly diffusive, while the PBD/PDMS is “non diffusive” (i.e. low diffusion compared to the PB/PDMS systems). The time scale to complete the diffusion process is found to increase with the molecular weight of the PB drop phase, while increasing the temperature yields to longer times to complete the diffusion process.

A continuous model, based on the diffusion equation, was developed and used to qualitatively predict the trends in transient interfacial tension. A discrete version of this model allows us to calculate the time scales for the diffusion process, it is able to describe the experimental results quite well.

Diffusive interfaces cause some special effects. For quiescent drop-drop interaction experiments with the lowest molecular weight PB drops in PDMS, with the drops separated over distance smaller than the equivalent radius but much larger than the critical film thickness, mutual attraction and coalescence are observed. For the PBD/PDMS systems, drops do not coalesce even when they are brought in close contact. On the contrary, repulsion between them occurs. These two phenomena are explained in terms of a gradient in the interfacial tension along the drop surfaces due to a inhomogeneous thickness of the diffuse interface, which induces Marangoni convection, which is an interfacial flow.

In order to show that interfacial tension gradients can induce drop displacement, single drops of both materials are put close to walls of different materials. For the PB drop, displacement towards the wall is observed (attraction); glass and Teflon walls are used to exclude wetting effects. These phenomena are supported by numerical results based on the diffuse interface method.

In diluted systems the effect of the transient interfacial tension on shear-induced coalescence is investigated by means of two in-situ techniques, small angle light scattering and optical microscopy. Dilute PB/PDMS and PBD/PDMS systems and the reversed blends are studied, all showing a strong influence of the transient interfacial tension on the final morphology.

For semi-diluted and concentrated PB/PDMS and PBD/PDMS systems the morphology evolution is studied with optical microscopy and rheological measurements using a cone-plate geometry. For these concentrations droplets larger than expected from theory are found. These large droplets become of a size comparable to the (varying) gap in cone-plate geometry and they start to interact with the walls,

leading to confinement effects. Due to the presence of these confined drops, the walls influence the morphology development process. A relatively high degree of confinement is generated by enhanced coalescence in the partially miscible systems investigated.

The effects of a confinement on the morphology evolution in time are therefore investigated more systematically for three concentrations (10, 20, and 30 wt %) of both systems, PB/PDMS and PBD/PDMS. The results are compared to (i) the Maffettone-Minale model (MM model), derived for bulk behavior, (ii) to the Minale model (M model), which includes the degree of confinement in the MM model, and (iii) to a modification of the M model (mM model), in which the viscosity of the matrix is substituted with the effective viscosity of the blend to account for the concentration of dispersed phase. A transition from "bulk-like" behavior towards "confined" behavior is found for all systems at degrees of confinement lower than expected. Critical degrees of confinement are found above which the experimental data do not follow the model predictions, and it is shown that this critical value increases with decreasing shear rate. Different degrees of confinement induce different final structures.

Based on the results presented, it is concluded that partial miscibility between polymer pairs can strongly affect the morphology of the final emulsion and, once this phenomenon is understood well, it can be used in order to control the final properties of a product.

CHAPTER ONE

Introduction

1.1 State of the art

Demanding applications of polymeric materials require improved, or new (combinations of) properties, which are difficult to obtain by commodity polymers that dominate the polymer market. The synthesis of special polymer is troublesome and expensive. Therefore, a considerable scientific and industrial interest exists in modifying and combining state-of-the-art polymers with the goal to achieve properties that are comparable to engineering polymers and high-tech non-polymeric materials. The design of thermodynamically stable polymer blends offers great potential as an alternative for the synthesis of new polymers. Control over blending operations also still poses significant scientific and industrial challenges.

Properties of a polymeric product resulting from a process of mixing two or more polymers are determined by the mechanical and the interfacial properties of the components and the blend morphology. This morphology is the result of the thermo-mechanical history experienced by material elements during preparation and processing of the blend in relation to its phase behavior, and in special cases (e.g. micro-processing) by the presence of geometrical confinements.

1.2 Morphology development of immiscible polymer blends

Mixing of polymers is thermodynamically unfavorable [1] and, given the high viscosity of the polymers used for industrial applications, most of the blends can be considered immiscible. Many studies focuss on understanding the relations between the flow history and the final structure of a two-phase mixture on a

macroscale, assuming that mutual diffusion is negligible in the time scale of the experiments [2–7]. Using optical, rheological and rheo-optical techniques, the influence on the morphology is examined of component properties, volume fraction of the dispersed phase, flow field and flow history. Two examples, a drop-matrix structure and a co-continuous morphology are shown in Figure 1.1. Small-scale micron-size arrangements control the morphology and result from the competition of two processes simultaneously occurring during multi-phase flow: drop deformation and break-up, and drop coalescence.

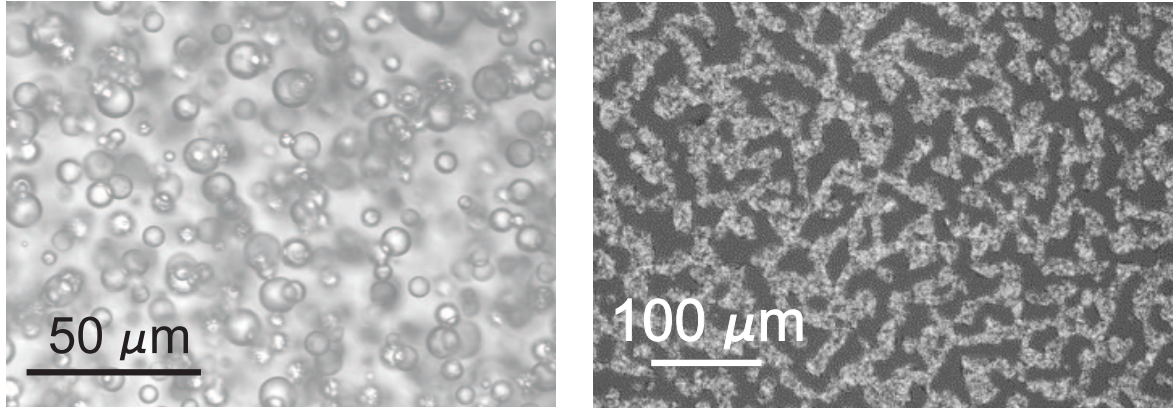


Figure 1.1: Different morphologies of polymer blends.

For unconfined flows, i.e. cases in which the characteristic size of the generated morphology is much smaller than the size of the geometrical device, several models have been developed to describe deformation, breakup and coalescence in different flow conditions, based on two dimensionless numbers, the viscosity ratio, p , and the capillary number, Ca , defined as:

$$p = \frac{\eta_d}{\eta_m}, \quad Ca = \frac{\eta_m \dot{\gamma} R}{\sigma}, \quad (1.1)$$

these η_d and η_m are the viscosities of the dispersed and continuous phase, respectively, $\dot{\gamma}$ is the shear rate applied, R is the average droplet size, and σ the interfacial tension. Ca can also be considered as the ratio between a surface-tension relaxation time, $\eta_m R / \sigma$, and a time for flow-induced deformation, $\dot{\gamma}^{-1}$. Several theories describe the morphology evolution of polymer blends based on these quantities, excellent reviews exist: Tucker et al. [8], Stone et al. [9].

Usually blends are assumed to be fully immiscible and the characteristic size of the morphology generated is assumed to be much smaller than the size of the geometrical device. However, these two assumptions have to be reconsidered.

1.3 Partial miscibility

When polymers with a relative low molecular weight and high degree of polydispersity are considered or when a large asymmetry in molecular weight across an interface is present, the smaller - and therefore faster - molecules can diffuse from one phase into the other, giving rise to mass transport. This interdiffusion process of the low molecular weight species, LMW, can occur in time scales comparable with the experimental ones and, therefore, in those cases mutual diffusion has to be taken into account [10]. The blends are “partially miscible” and the diffusion of LMW species across the interface can have a decisive influence on interfacial properties and therefore on the morphology evolution during mixing. Interfaces are usually rather thin, and therefore it is difficult to directly measure interface properties such as interdiffusion, concentrations, local flow fields and changes in local thicknesses. The most easily accessible thermodynamic parameter related to the interfacial zone, that also controls morphology and adhesion properties in polymer blends, is the interfacial tension and the focus is to study its evolution in time (Peters et al. [10], Kamal et al. [11], Nam et al [12], Shi et al. [13], and Anastasiadis et al. [14]). In case of partial miscibility, the interface between the two material components can not be considered sharp, diffusive layers are formed and transient interfacial tension results [15]. It could be expected that partial miscible blends behave similar to immiscible blends with added soluble surfactants. Studies on the interfacial tension gradients of low viscous systems deal with adsorbed species (surfactants) on drop interfaces [16, 17], preventing coalescence. Film drainage between two approaching droplets cause an inhomogeneous distribution of surfactants by convection along the drop surfaces to result in accumulation at the drop equator and interfacial concentration gradients. Tangential (Marangoni) stresses result inducing interfacial flow in the direction opposite to the drainage flow, eventually causing interface immobilization [16]. While for soluble and insoluble surfactants these phenomena have been demonstrated, there is lack of data on this topic for *partially miscible* polymer blends.

1.4 ...going small

Liquid-liquid dispersions are widely processed in *macroscopic* devices, i.e. flow geometries having a characteristic size much larger than the typical size of the morphology generated. However, new applications and technologies use flow devices with length scales in the order of microns or even smaller [18]. This opens the way to an area called *droplet-based microfluidics*, an emerging field, less than a decade old. Many, diverse applications for these devices can be listed, based on the opportunity to perform chemical or biochemical analysis and kinetics or crystallization studies or to produce customized microemulsions, by manipulating tiny volumes of samples or reagents. The challenge is to explore how droplets having individual volumes of micro- to picoliter size can be generated, transported, mixed, split, and analyzed meanwhile being inside closed thin channels or sandwiched between two plates.

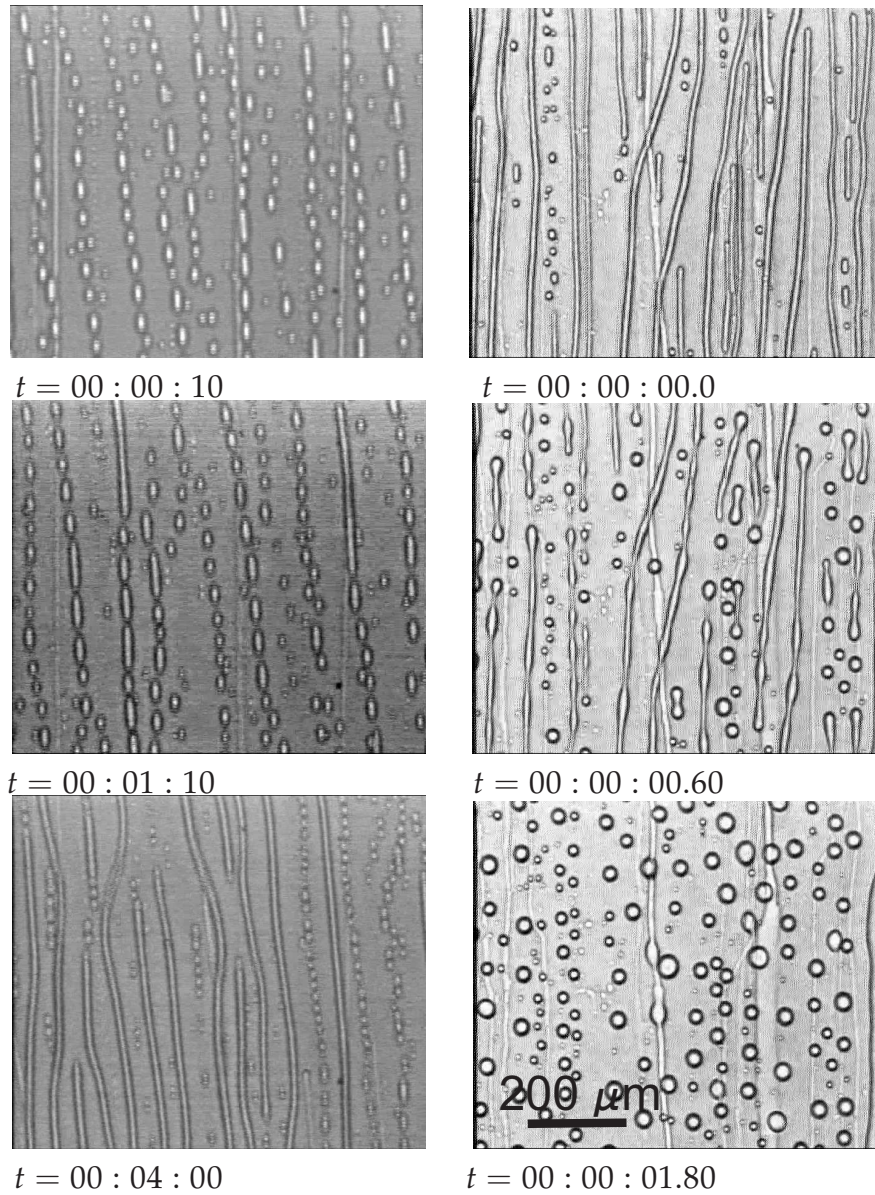


Figure 1.2: Left: string formation for a 10% PBD/PDMS blend upon shearing at constant shear rate of 10s^{-1} in a confined parallel-plate geometry with $40\mu\text{m}$ gap. Right: break-up upon cessation of flow for the same blend.

Several studies focus on isolated drop deformation and breakup inside a cylindrical tube [19–23], and between parallel plates [24–28]. The degree of confinement, defined as the ratio between drop diameter and the characteristic size of the flow device, is introduced as a new basic quantity. For degrees of confinement above 0.4, studies on single droplets show remarkable deviations of drop deformation and break-up compared to the unconfined situations.

A phenomenological model for single droplet deformation in a shear flow, proposed by Maffettone and Minale [29], is shown to work reasonably well for degrees of con-

finement lower than 0.3. Recently, Minale (Rheol. Acta, in press) modified this model to account for confinement effects and we will use this model for larger confinement ratios.

A further step towards real-life applications is made when studying the morphology development of concentrated systems in confined geometries. In that case, coalescence has to be taken into account and only a few studies are available in literature [30–33]. The main conclusion is the existence of a transition from bulk behavior, as observed in unconfined flows, to the confined behavior, yielding special stable morphologies, not observed in unconfined geometries. Figure 1.2 left shows an example of string formation in flow, while Figure 1.2 right reveals that by stopping the flow, the drop-matrix morphology is easily recovered.

1.5 Objectives of the thesis

We study the effects of the transient interfacial tension on morphology development of polymeric blends during *macroscale* and *microscale* processing.

The first part of the thesis deals with the transient interfacial properties of a series of polymer blends, with its effect on drop-drop interactions, and on the morphology evolution of diluted and concentrated polymer blend systems on the *macroscale*. The transient and the steady interfacial tension of polymers with different molecular weights and polydispersities are measured for a range of temperatures. Models are proposed to interpret the transient interfacial tension measured in terms of mutual diffusion. Drop-drop interaction is affected by gradients in interfacial tension along the drop surface, related to interdiffusion between the two polymeric phases. The experimental data on drop-drop interaction are compared to the numerical results obtained with a diffuse interface model. To investigate the effects of a transient interfacial tension on the morphology evolution, diluted blends (mostly with concentration of 1%) are studied with two in-situ techniques: small angle light scattering and optical microscopy. The morphology evolution is compared to predictions using coalescence models for sharp interphases and the differences between “immiscible” and “partially miscible” blends on the final structure of the mixture are highlighted. The second part of the thesis is based on rheological measurements (cone and plate), and optical microscopy (parallel plates) for semi-diluted and concentrated blends that show morphology to evolve towards a bimodal distribution. At some stages, the droplets reach average diameters that are too large to exclude confinement effects. Therefore, we systematically study how geometrical confinement affects the morphology evolution of two polymer blends, differing in component properties, such as molecular weight, polydispersity and viscosity of the phases. Different concentrations ranging from 10% till 30% of the dispersed phase are used. We investigate the steady-state morphology generated on the *microscale* applying different shear rates. Phenomenological models derived to describe the deformation of drops in unconfined as well as in confined flows, are used to interpret the experimental

results.

1.6 Survey of the thesis

This work is organized as follows:

In Chapter 2 three blends, based on three different grades of polybutene (PB) as the phase dispersed in a continuous phase of PDMS are used to study the transient and steady interfacial tension for a wide range of temperatures. The resulting transient interfacial tension behavior is explained in terms of mutual diffusivity and variable interface thicknesses. A diffusion model is used to allow us to analytically predict the transient interfacial tension and, by fitting the experimental data, to obtain the typical time scale for diffusion in the blends. Two different model formulations, one with a constant, the other with a time dependent interphase thickness, are proposed, and in the end also a kinetic model, basically a special case of the more general thermodynamic model, is used.

Chapter 3 compares the transient interfacial tension, measured at different temperatures, of the most diffusive blend of Chapter 2, with that of a "immiscible" blend. Application of the models developed in Chapter 2 results in different diffusion time scales for the two blends. The influence of a transient interfacial tension on morphology development is studied for low-concentrated mixtures by means of rheo-optical methods and small angle light scattering. The evolution of the average-drop radii for both blends is compared to the results based on a coalescence model for sharp interfaces. Also phase inversion is studied.

Chapter 4 deals with the influence of the mutual diffusion, and, therefore, of interfacial tension gradient along the drop surface, using drops of the highly-diffusive material (thick interface) and of the slightly-diffusive material (thin interface) presented in Chapter 3. Gradients in interfacial tension along the drop surface, which induce tangential (Marangoni) stresses, can cause drop lateral motions. The kinetics of drop-drop interactions, eventually leading to coalescence, are investigated. The diffuse interface model is extended to include three phases (source phase, migrating molecules and receiving phase). Simulations supports the experimental results.

Chapter 5 studies morphology development at different flow histories by means of rheological measurements and optical microscopy. Concentrations of 10 wt% and 20 wt% of the blends presented in Chapter 3 are used. The experimental results are compared to coalescence and break-up theories for droplets, and the occurrence of geometrical confinement during the flow experiments is also investigated. The presence of a hysteresis zone is studied and flow induced coalescence experiments, performed with step-downs of 1/4, 1/10, and 1/40 in shear rate, are carried out. From dynamic measurements the relaxation spectra are derived and used to

calculated the average radii in the blend, optical microscopy is also performed with the same histories of flow. The formation of large droplets in these experiments, suggest that confinement effects can not be neglected. Therefore Chapter 6 is dedicated to the morphology development of blends during *confined* flow. With a systematic analysis it is shown how all the possible different morphological structures can form. The results are compared to the Maffettone and Minale model (MM), a phenomenological model for drop deformation in unconfined flow, and to the Minale model (M model), which is the MM model modified to account for geometrical confinement. We extended the last model to a modified M model (mM model), in which the matrix viscosity is substituted by the effective viscosity of the continuous phase, as defined by Choi and Schowalter [34].

Finally, in Chapter 7, the conclusions of this thesis are drawn, and suggestions for future work are made.

References

- [1] Olabisi, O., Robeson, L.M., Shaw, M.T. (1979). *Polymer-polymer miscibility*. Academic London.
- [2] Fortelny, I. and Kovar, J. (1988). Theory of coalescence in immiscible polymer blends. *Polym. Compos.*, **9**, 119–124.
- [3] Elmendorp, J.J. and van der Vegt, A. (1986). A study on polymer blending micro-rheology: Part iv. the influence of coalescence on blend morphology origination. *Polym. Eng. Sci.*, **26**, 1332–1338.
- [4] Rusu, D. and Peuvrel-Disdier, E. (1999). In-situ characterization by small angle light scattering of the shear-induced coalescence mechanisms in immiscible polymer blends. *J. Rheol.*, **43**, 1391–1409.
- [5] Verdier, C. and Brizard, M. (2002). Understanding droplet coalescence and its use to estimate interfacial tension. *Rheol. Acta*, **43**, 514–523.
- [6] Vinckier, I., Moldenaers, P., Mewis, J. (1996). Relationship between rheology and morphology of model blends in steady shear flow. *J. Rheol.*, **40**, 613–631.
- [7] Lyu, S.P., Bates, F.S., Macosko, C.W. (2000). Modeling of coalescence in polymer blends. *AIChE J.*, **48**, 7–14.
- [8] Tucker, C.L. and Moldenaers, P. (2002). Microstructural evolution in polymer blends. *Annu. Rev. Fluid Mech.*, **34**, 177–210.
- [9] Stone, H.A., Stroock, A.D., Ajdari, A. (2004). Engineering flows in small devices: Microfluidics toward a lab-on-a-chip. *Annu. Rev. Fluid Mech.*, **36**, 381–411.
- [10] Peters, G.W.M., Zdravkov, A., Meijer, H.E.H. (2005). Transient interfacial tension and dilatational rheology of diffuse polymer-polymer interfaces. *J. Chem. Phys.*, **122**, 104901–1–10.
- [11] Kamal, M.R., Lai-Fook, R., Demarquette, N.R. (1994). Interfacial tension in polymer melts. part ii: Effects of temperature and molecular weight on interfacial tension. *Polym. Eng. Sci.*, **34**, 1834–1839.

- [12] Nam, K.H. and Ho Jo, W. (1995). The effect of molecular weight and polydispersity of polystyrene on the interfacial tension between polystyrene and polybutadiene. *Polymer*, **36**, 3727–3731.
- [13] Shi, T., Ziegler, V.E., Welge, I.C., An, L., Wolf, B.A. (2004). Evolution of the interfacial tension between polydisperse “immiscible” polymers in the absence and in the presence of a compatibilizer. *Macromolecules*, **37**, 1591–1599.
- [14] Anastasiadis, S.H., Gancarz, I., Koberstain, J.T. (1988). Interfacial tension of immiscible polymer blends: Temperature and molecular weight dependence. *Macromolecules*, **21**, 2980–2987.
- [15] Anderson, D.M., McFadden, G.B., Wheeler, A.A. (1998). Diffuse-interface methods in fluid mechanics. *Annu. Rev. Fluid Mech.*, **30**, 139–165.
- [16] Ivanov, I.B. (1980). Effect of surface mobility on the dynamic behavior of thin liquid films. *Pure Appl. Chem.*, **52**, 1241–1262.
- [17] Lin, C.Y. and Slattery, J.C. (1982). Thinning of a liquid film as a small drop or bubble approaches a solid plane. *AIChE J.*, **28**, 147–156.
- [18] Stone, H.A. and Kim, S. (2001). Microfluidics: Basic issues, applications, and challenges. *AIChE J.*, **47**, 1250–1254.
- [19] Ho, B.P. and Leal, L.G. (1975). The creeping motion of liquid drops through a circular tube of comparable diameter. *J. Fluid Mech.*, **71**, 361–383.
- [20] Coutanceau, M. and Thizon, P. (1981). Wall effect on the bubble behavior in highly viscous liquids. *J. Fluid Mech.*, **107**, 339–373.
- [21] Olbricht, W.L. and Kung, D.M. (1992). The deformation and breakup of liquid drops in low Reynolds number flow through a capillary. *Phys. Fluids A*, **4**, 1347–1354.
- [22] Graham, D.R. and Higdon, J.J. (2000). Oscillatory flow of droplets in capillary tubes. part 1. straight tubes. *J. Fluid Mech.*, **425**, 31–53.
- [23] Graham, D.R. and Higdon, J.J. (2000). Oscillatory flow of droplets in capillary tubes. part 2. constricted tubes. *J. Fluid Mech.*, **425**, 55–77.
- [24] Mietus, W.G., Matar, O.K., Lawrence, C.J., Briscoe, B.J. (2002). Droplet deformation in confined shear and extensional flow. *Chem. Eng. Sci.*, **57**, 1217–1230.
- [25] Son, J., Martys, N.S., Hagedorn, J.G., Migler, K.B. (2003). Suppression of capillary instability of a polymeric thread via parallel plate confinement. *Macromolecules*, **36**, 5825–5833.
- [26] Vananroye, A., Van Puyvelde, P., Moldenaers, P. (2006). Effect of confinement on droplet breakup in sheared emulsions. *Langmuir*, **22**, 3972–3974.
- [27] Sibillo, V., Pasquariello, G., Simeone, M., Cristini, V., Guido, S. (2006). Drop deformation in microconfined shear flow. *Phys. Rev. Lett.*, **97**, 0545021–0545024.
- [28] Vananroye, A., Van Puyvelde, P., Moldenaers, P. (2007). Effect of confinement on the steady-state behavior of single droplets during shear flow. *J. Rheol.*, **51**, 139–153.
- [29] Maffettone, P.L. and Minale, M. (1998). Equation of change for ellipsoidal drops in viscous flow. *J. Non-Newton. Fluid Mech.*, **78**, 227–241.
- [30] Migler, K.B. (2001). String formation in sheared polymer blends: coalescence, breakup, and finite size effect. *Phys. Rev. Lett.*, **86**, 1023–1026.

-
- [31] Pathak, J.A., Davis, M.C., Hudson, S.D., Migler, K.B. (2002). Layered droplet microstructures in sheared emulsions: finite-size effects. *J. Coll. Int. Sci.*, **255**, 391–402.
- [32] Pathak, J.A. and Migler, K.B. (2003). Droplet-string deformation and stability during microconfined shear flow. *Langmuir*, **19**, 8667–8674.
- [33] Vananroye, A., Van Puyvelde, P., Moldenaers, P. (2006). Structure development in confined polymer blends: steady-state shear flow and relaxation. *Langmuir*, **22**, 2273–2280.
- [34] Choi, S.J. and Showalter, W.R. (1975). Rheological properties of nondilute suspensions of deformable particles. *Phys. Fluids*, **18**, 420–427.

CHAPTER TWO

Transient interfacial tension of partially-miscible polymers¹

The interfacial tension of three different binary polymer blends has been measured as function of time by means of a pendant drop apparatus, at temperatures ranging from 24°C to 80°C. Three grades of polybutene (PB), differing in average molecular weight and polydispersity, are used as dispersed phase, the continuous phase is kept polydimethylsiloxane (PDMS), ensuring different asymmetry in molecular weight across the interface. The interfacial tension changes with time and, therefore, this polymer blends can not be considered fully immiscible.

Changes in interfacial tension are attributed to the migration of low-molecular weight components from the source phase into the interphase and, from there, into the receiving phase. In the early stages of the experiments, just after the contact between the two phases has been established, the formation of an interphase occurs and the interfacial tension decreases with time. As time proceeds, the migration process slows down given the decrease in driving force which is the concentration gradient and, at the same time, molecules accumulated in the interphase start to migrate into the “infinite” matrix phase. A quasi-stationary state is found before depletion of the low-molecular weight fraction in the drop occurs and causes the interfacial tension $\sigma(t)$ to increase. The time required to reach the final stationary value, σ_{stat} , increases with molecular weight and is a function of temperature. Higher polydispersity leads to lower σ_{stat} and a weaker dependence of σ_{stat} on temperature is found. A model coupling the diffusion equation in the different regimes is applied to interpret the experimental results. Numerical solutions of the diffusion equation are proposed in the cases of a constant and a changing interphase thickness. In the latter case, the interphase is defined by tracking with time a fixed limiting concentration in the

¹Reproduced from: Tufano, C., Peters, G.W.M., Anderson, P.D., Meijer, H.E.H., Transient interfacial tension of partially-miscible polymers. *J. Coll. Int. Sci.*, submitted.

transient concentration profiles and the variations found in $\sigma(t)$ are attributed to the changes in the interphase thickness. A discrete version of this continuous model is proposed and scaling arguments are reported to compare the results obtained with the predictions of the continuous model. The kinetic model as proposed by Shi et al. [1] appears as a special case of the discrete model, when depletion is not taken into account. Using the models, time scales for the diffusion process can be derived, which fit the experimental results quite well.

2.1 Introduction

Properties of polymer blends and mixtures depend on the morphology and, therefore, phenomena involved in morphology evolution during mixing are studied. Since polymers consist of long molecules, mixing them is thermodynamically unfavorable [2] and their viscosity is high while diffusion is slow compared to the experimentally available time-scales [3]. In addition, partial miscibility between polymers is usually considered negligible and blends are assumed to consist of immiscible mixtures [4–9]. This immiscibility assumption is, however, not valid when low-molecular weight polymers, e.g. in case of high polydispersity, and pronounced asymmetries in average molecular weights across interfaces are present [10]. In polydisperse polymers, smaller molecules have a higher mobility and, for entropic reasons, they diffuse from one phase into the other causing the concentration of small molecules in the interfacial zone to increase. Mutual diffusion is important and affects the interfacial properties in polydisperse, thus partially-miscible polymer blends. Since interphases are usually rather narrow, it is difficult to directly measure phenomena occurring, like interdiffusion, local flow fields and changes in local thicknesses. The most easily accessible thermodynamic parameter related to the interfacial zone, that also controls morphology and adhesion properties in polymer blends, is interfacial tension and therefore, the focus is to study its evolution in time. In Peters et al. [10] it is concluded that increasing the molecular weight of either phase, matrix or drop, leads to higher values of the interfacial tension, in accordance with the results shown in [1, 11–13], and it is reported that, above a critical molecular weight value, a plateau value in interfacial tension is approached. The influence of temperature is studied in [1, 11, 13–15], and both an increase and a decrease in interfacial tension with temperature are reported. Wagner et al. [14] even found a maximum in $\sigma(T)$ for some combinations of chain lengths, attributed to close miscibility gaps. For immiscible polymer pairs with infinite molecular weights, interfacial tension can be related to the Flory-Huggins interaction parameter [16]. Broseta et al. [17] studied interfacial tension in immiscible polymer blends with finite molecular weight, dropping the assumption of complete immiscibility and showed that, in polydisperse systems, small chains accumulate to the interface, lowering the interfacial tension and the Gibbs free energy of the system. In literature usually only steady state values of interfacial tension are reported and transient data are scarce. However, when preparing a blend, time scales of mixing are limited and a transient

interfacial tension, which plays a crucial role in the morphology evolution, can indeed be important.

We study the transient interfacial tension at different temperatures for three dispersed phases, different in molecular weight, attributing the non-constant interfacial tension measured to mutual miscibility in the time scale of the experiments. Increasing the average molecular weight of the drop component leads to longer time scales to complete the diffusion process and thus the time needed to reach a steady interfacial tension, increases. Increase in temperature yields higher mobility of the shorter chains and, therefore, enhances diffusion resulting in stronger and faster changes in $\sigma(t)$ values. In addition, the steady-state values decrease with increasing polydispersity at all temperatures investigated. To support the interpretation of the experimental results, we apply diffusion models. To analyse the total transient behavior of $\sigma(t)$, the diffusion equation is numerically solved for a three-zone system using two approaches. First, the interphase thickness is considered an input parameter in the model and effects of different thicknesses on time scales of diffusion are investigated. In the second approach only two zones are considered, the source and the receiving phases, separated by an interphase. The thickness of this interphase is defined by choosing a limit concentration, c_{lim} , and tracking in time its position relative to the interface position at $t = 0$, allowing to predict both thickening and thinning of the interphase in time. Now the concentration c_{lim} is the input parameter and its influence on diffusion and on time evolution of the interphase thickness is investigated. Other model parameters are the ratio of the diffusion coefficients between the three/two zones and also their influence is studied. Next, a three-zone discrete approximation is derived, preserving the features of the continuous model and using the time scales for diffusion of the blend systems investigated, and a fitting of experimental data to this discrete model is performed. Finally the kinetic model reported in [1] has been derived as a special case of this discrete model, imposing an infinite drop radius, thus effectively neglecting depletion of small molecules in the course of time.

2.2 Modeling

First we discuss the diffusion equations for a single drop in a matrix in the presence of an interphase. Next, two discrete approximations of the continuous diffusion problem are presented, one of which reduces to the kinetic model reported by Shi et al. [1].

2.2.1 A continuous kinetic model

The interfacial tension between two liquid pairs depends on the chain lengths of the components. Changing the average molecular weight in one phase, M_n , while keeping constant the molecular weight of the second component, a simple relation was found [18]:

$$\sigma = \sigma_{\infty} - \frac{C}{M_n^z}, \quad (2.1)$$

where σ_{∞} is the limiting value of the interfacial tension for infinite molecular weight, M_n the number averaged molecular weight and C and z are constants. Due to migration of short chains into the interface, the interfacial tension and, therefore, the Gibbs free energy of the system, is lowered. It is assumed that the systems investigated are sufficiently ideal to obey Fick's law with constant diffusion coefficients. Furthermore, the chemical potential is continuous throughout the system, except at boundaries. A source and a receiving phase, separated by an interface, are considered. Two approaches to model the diffusion process in these phases are investigated. In the more general case, the system can be considered a three zone system, schematically depicted in Fig. 2.1 left. The interface zone is assumed to have a thickness δ , thus it is an interphase in which the concentration as a function of time is calculated. M_A is the molecular weight of the source material, M_{A_1} is the lower molecular weight fraction of the source material, and M_B is the molecular weight of the receiving material.

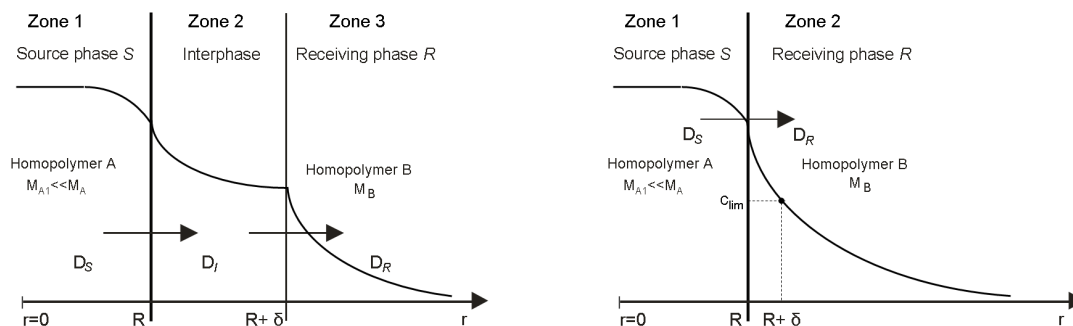


Figure 2.1: Schematic representation of the three-region system (left) and the two-region system (right). The lower molecular weight fraction of material A, M_{A_1} , is the phase that migrates into the interphase and, from that, into the matrix material B.

The second possibility is to consider only two zones, the source and the receiving phases, and to assume that the thickness of the interphase is defined by a critical, limiting concentration (see Fig. 2.1 right). Choosing a specific concentration and tracking in time the spacial positions at which this concentration is reached, yields the transient interphase thickness and the average concentration in the interphase can be determined. In both cases, it is possible to assume a continuous or a discontinuous concentration profile across the boundaries. Here we will not consider discontinuous profiles since equilibrium distribution coefficients between bulk and interphase

are unknown. For each zone, we assume Fick's law to apply [19]. In spherical coordinates (a drop in a matrix is considered) this reads:

$$\dot{c}_i = \frac{1}{r^2} \frac{\partial}{\partial r} \left[r^2 \left(D_i \frac{\partial c_i}{\partial r} \right) \right] \quad i = \{S, I, R\}, \quad (2.2)$$

where $\dot{c} = \partial c / \partial t$ since convection in the system is assumed to be absent, r is the radius direction, c_i is the concentration of the diffusing molecules, D_S is the diffusion coefficient of the source phase, D_I of the interphase (when present), and D_R of the receiving phase, see Fig. 2.1. For the three-zone model, given a continuous chemical potential through the three zones, the Nernst's distributive relation applies to the boundaries between source phase and interphase and between interphase and receiving phase [19]. Moreover, mass fluxes across boundaries are equal:

$$\left. \begin{array}{l} c_S = c_I \\ D_S \frac{\partial c_S}{\partial r} = D_I \frac{\partial c_I}{\partial r} \end{array} \right\} \quad \text{at } r = R, \quad (2.3)$$

$$\left. \begin{array}{l} c_R = c_I \\ D_R \frac{\partial c_R}{\partial r} = D_I \frac{\partial c_I}{\partial r} \end{array} \right\} \quad \text{at } r = R + \delta. \quad (2.4)$$

The initial conditions are:

$$c(r, t = 0) = c_0 \quad r \leq R, \quad (2.5)$$

$$c(r, t = 0) = 0 \quad r > R. \quad (2.6)$$

When only two zones are considered, i.e. S and R , as shown in Fig.2.1 right, the boundary conditions reduce to:

$$\left. \begin{array}{l} c_S = c_R \\ D_S \frac{\partial c_S}{\partial r} = D_R \frac{\partial c_R}{\partial r} \end{array} \right\} \quad r = R. \quad (2.7)$$

Notice that we have assumed that the drop radius is constant, i.e. the change of the drop volume due to mass transport of the low-molecular weight part is negligible. In both formulations of the diffusion process, diffusion coefficients need to

be known. While this is not a problem for the two bulk phases, the coefficient D_I as well as the thickness of the interface, δ , can not be measured. However the ratio D_I/δ is a permeability parameter which can be used to characterize the magnitude of the interfacial resistance to diffusive mass transport. Under the assumption of a continuous concentration profile, the number of unknown parameters reduces to the diffusion constants, the thickness of the interphase in the three-zone model and the critical concentration in the two-zone model. Numerically, the diffusion equation is solved in radial coordinates by using a three-point central difference scheme while a two-point forward and backward scheme is used at the boundaries, the number of nodes is in the order of 700 (with a slightly higher density in the interphase). Time integration is performed using an implicit Euler scheme, and time steps are in the order of 10^{-5} .

Constant interphase thickness

The three-zone model is used to describe the influence of the interphase thickness on the diffusion process between two partially miscible polymers. The continuous modeling allows us to calculate transient concentration profiles and to explain the depletion of the interphase. Dimensionless variables used are:

$$t^* = \frac{tD_R}{R^2}, \quad c^* = \frac{c}{c_0}, \quad r^* = \frac{r}{R}, \quad \delta^* = \frac{\delta}{R}, \quad D_1^* = \frac{D_S}{D_I}, \quad D_2^* = \frac{D_R}{D_I}.$$

In Fig. 2.2 (a) the evolution of the concentration profile with time is given for a fixed value of the interphase thickness. Using three different values for interphase thickness, we can calculate the average concentration in the interphase, \bar{c}^* , see Fig. 2.2 (b). The concentration goes through a maximum before reducing to zero. The thinner the interphase, the faster is the filling process, therefore the average concentrations in the interphase will be higher and its maximum is reached faster.

Fig. 2.2 (c) shows the average concentration evolution for four different combinations of D_1^* and D_2^* , referred to as case 1, 2, 3, and 4. An interphase of constant thickness, $\delta^* = 0.04$, is considered. In cases 1 and 2, diffusion from source phase to interphase is larger than, or equal to, that from interphase to matrix. In case 1 more accumulation in the interphase is found compared to case 2, since the interphase fills up faster than it is emptied. A higher maximum in concentration, and longer time scales to complete diffusion, are found. For cases 3 and 4, diffusion from source phase to interphase is equal or lower than diffusion from interphase to matrix. Therefore, filling of the interphase occurs at equal speed, but emptying is faster in case 4 than in case 3. This explains the higher maximum and longer time scale in case 3. Comparing cases 1 and 3, we see emptying at the same rate, and faster filling in case 1, thus more accumulation. The total time scale for diffusion is determined by the slowest diffusion from interphase to matrix and is therefore the same in both cases. Comparing

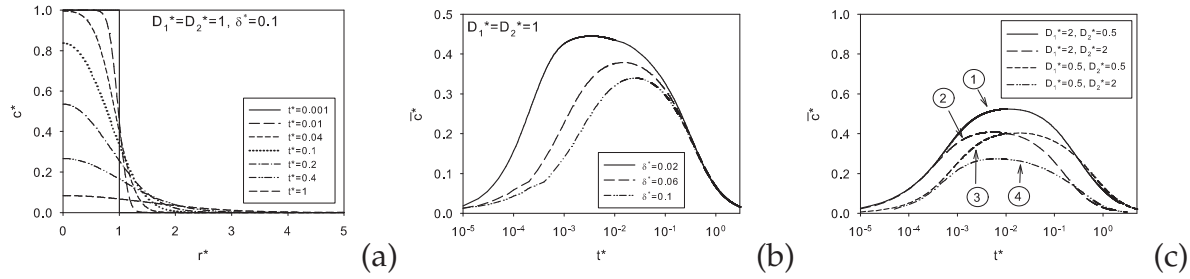


Figure 2.2: Transient concentration profiles for a fixed interphase thickness (left), time evolution of the average concentration of molecules in the interphase for three different interphase thicknesses, with the dimensionless parameters D_1^* and D_2^* set equal to one (middle), and for four different combinations of the dimensionless parameters D_1^* and D_2^* (right).

cases 2 and 4 gives similar observations. In conclusion D_1^* affects the time scale for the accumulation of molecules in the interphase, while D_2^* controls the depletion of the interphase.

Transient interphase thickness

Now we remove the assumption of constant interphase thickness, to be able to describe, at least qualitatively, the transient interfacial tension observed in the experiments reported in Section 2.5.1. Eq. 2.2 is solved considering two zones only (the source and the receiving phases), assuming a continuous concentration profile across the boundary, for three different ratios of the diffusion coefficient. The interphase thickness is defined by choosing three different specific concentrations and tracking in time the location at which this concentration is reached. Solutions are obtained in terms of the dimensionless variables:

$$t^* = \frac{tD_R}{R^2}, \quad c^* = \frac{c}{c_0}, \quad r^* = \frac{r}{R}, \quad D^* = \frac{D_R}{D_S},$$

for $D^* = 0.5, 1$ and 2 . Fig. 2.3 top shows how the interphase thickness evolves for three different limiting concentrations and for three different ratios of the diffusion coefficients. We observe an increase and collapse of the interphase in time. Increasing the limiting concentration, leads to a smaller interphase thickness and reduces the time scale of the total process. Increasing the ratio of the diffusion coefficients limits the accumulation of interfacially active molecules in the interphase and shortens the time scale of the thickening and thinning process.

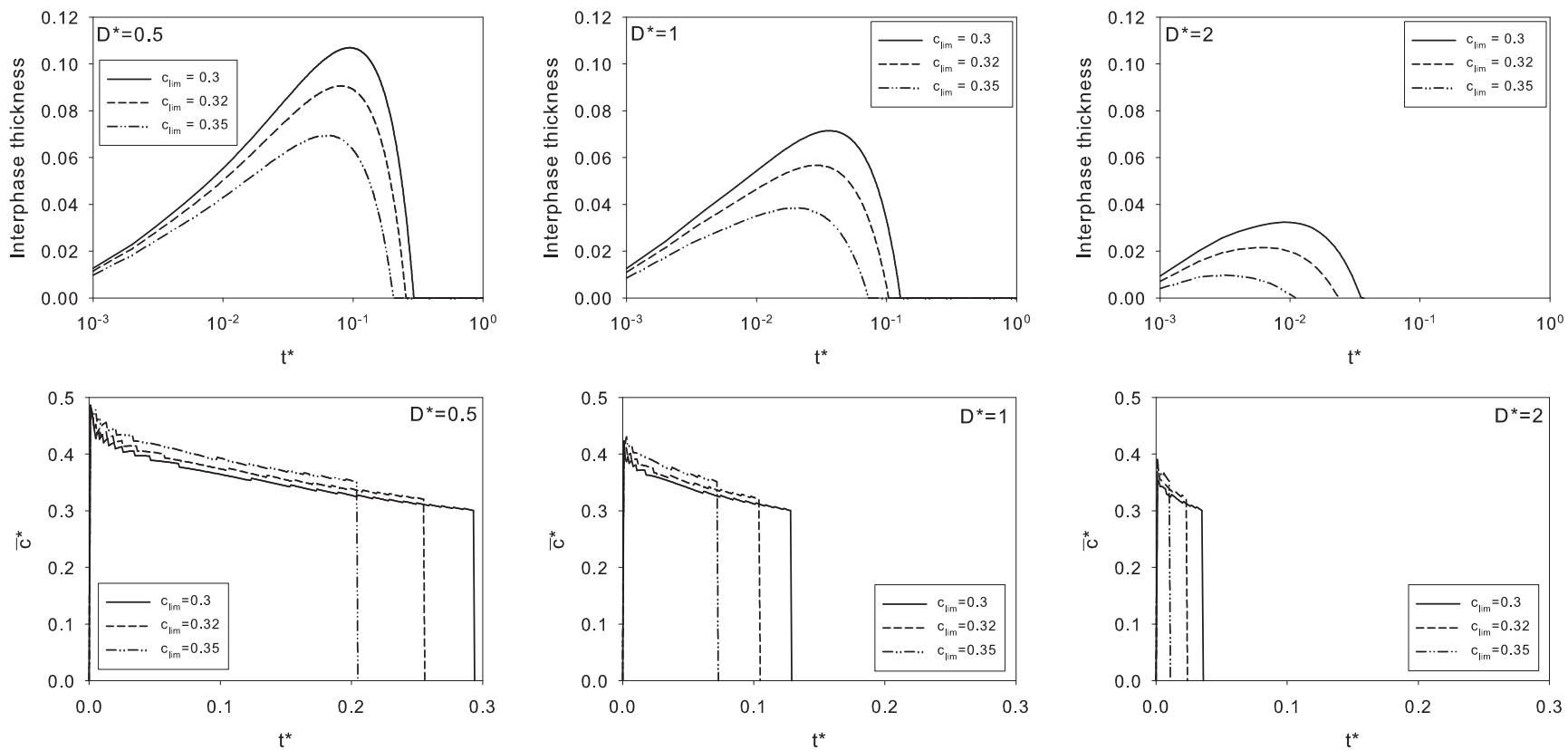


Figure 2.3: Dimensionless transient interphase thickness (top row) and average concentration in the time dependent thickness interphase (bottom row), both for three diffusion coefficients ratios.

Fig. 2.3 bottom shows the average concentration \bar{c}^* of molecules inside the transient interphase thickness. Similar trends as with the interphase thickness are observed. The steep drop in concentration found in all results after reaching the maximum interphase thickness is just a characteristic feature of this model, it is not observed experimentally and, therefore, we will not discuss this approach any further.

2.2.2 A discrete kinetic model

The discrete kinetic model for binary systems by Shi et al. [1] describes diffusion of low-molecular weight components of both phases into an interphase. Starting from the continuous diffusion equation we will derive a three-zone discrete approximation which has, in a qualitative sense, the same features as the continuous model. The model reported in Shi et al. [1] is a special case of this discrete approximation. Eq. 2.2 is approximated by considering average concentrations in the three zones only, $\bar{c}_S, \bar{c}_I, \bar{c}_R$, see Fig. 2.4. The average concentration \bar{c}_R in the matrix is taken zero ($\bar{c}_R = 0$).

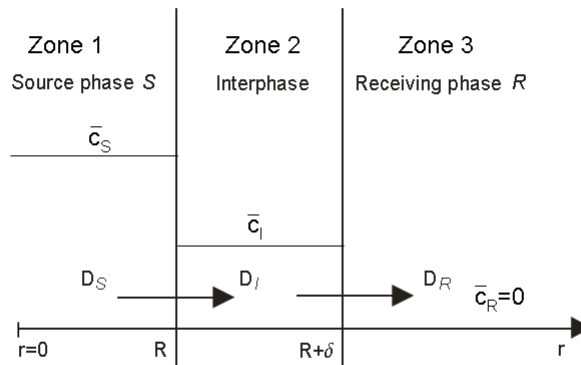


Figure 2.4: Schematic representation of the three-zone system. The concentration in each zone is assumed to be constant and, in the receiving phase, set equal to zero.

To get expressions in terms of the average concentrations Eq. 2.2 is integrated over the domain $[0, R + \delta]$:

$$\int_0^{R+\delta} \dot{c} r^2 dr = \int_0^{R+\delta} \frac{\partial}{\partial r} \left[r^2 D_i \frac{\partial c}{\partial r} \right] dr, \quad (2.8)$$

where D_i is the diffusion coefficient in the zone $i = \{S, I, R\}$. The rate of change of concentrations is replaced by the rate of change of average concentrations in each region: $\dot{\bar{c}}_S, \dot{\bar{c}}_I, \dot{\bar{c}}_R = 0$. Separating the drop region $[0, R]$ and the interphase region $[R, R + \delta]$, this leads to:

$$\frac{R^3}{3} \dot{\bar{c}}_S = \left[r^2 D_{SI} \frac{\partial c}{\partial r} \right] \Bigg|_0^R, \quad (2.9)$$

$$R^2 \delta \dot{\bar{c}}_I = \left[r^2 D_{IR} \frac{\partial c}{\partial r} \right] \Bigg|_R^{R+\delta}, \quad (2.10)$$

where D_{SI} and D_{IR} are yet to be chosen diffusion coefficients that are functions of the source, interphase and receiving phase diffusion coefficients, D_S, D_I and D_R . In deriving Eq. 2.10 higher-order terms in the left hand term have been neglected. The right hand terms are fluxes into (Eq. 2.9) and out of (Eq. 2.10) the interphase region. Next, concentration gradients are approximated by expressing them in terms of the average concentrations and a characteristic length scale. For the interphase the length scale is δ and, since the flux out of the droplet should be the same as the flux into the interphase, the same length scale should be used in the approximation of the right hand term of Eq. 2.9. Again, neglecting higher order terms, this leads to:

$$\dot{\bar{c}}_S = \frac{3K_1\delta}{R} (\bar{c}_S - \bar{c}_I), \quad K_1 = \frac{D_{SI}}{\delta^2}. \quad (2.11)$$

For the interphase, for which $\delta \ll R$, we take $r \sim \text{constant}$ and this leads to:

$$\dot{\bar{c}}_I = K_1(\bar{c}_S - \bar{c}_I) - K_2\bar{c}_I, \quad K_2 = \frac{D_{IR}}{\delta^2}, \quad (2.12)$$

after applying initial conditions:

$$\bar{c}_S(t=0) = c_0, \quad (2.13)$$

$$\bar{c}_I(t=0) = 0. \quad (2.14)$$

For the diffusion coefficients D_{SI} and D_{IR} we chose the average values of the diffusion coefficients of the corresponding regions:

$$D_{SI} = \frac{D_S + D_I}{2}, \quad (2.15)$$

$$D_{IR} = \frac{D_I + D_R}{2}. \quad (2.16)$$

In the limit of a very large drops, $R \rightarrow \infty$, the source of migrating molecules can be considered infinite and the model reduces to the one of Shi et al. [1], i.e. only Eq. 2.12 applies and the initial concentration (Eq. 2.14) is replaced by a boundary condition $\bar{c}_I(r=R) = \bar{c}_0$.

From the set of linear differential equations, Eqs. 2.11-2.12, we obtain the two characteristic time scales of the diffusion process by solving a standard eigen value problem. The time-dependent concentration of molecules accumulating in the interphase can then be expressed as follows:

$$\bar{c}_I = Ae^{(-t/\tau_1)} - Be^{(-t/\tau_2)}, \quad (2.17)$$

and the transient interfacial tension as:

$$\sigma(t) = \sigma_{\text{stat}} - ae^{(-t/\tau_1)} - be^{(-t/\tau_2)}. \quad (2.18)$$

The complete transient behavior, obtained experimentally, can be fitted by using Eq. 2.18. The coefficients A , B and a , b and the time constants τ_1 and τ_2 depend, in a complex way, on the material properties D_S , D_I , D_M , and on the geometrical properties R and δ . Using Eqs. 2.11 and 2.12 we can solve the diffusion problem using the same parameter values as for the continuous case and compare the results, in terms of the average interphase concentration, of the two approaches, see Fig. 2.5 (a).

It is observed that the time scales of the early diffusion process are different, shifting the maximum to the right (longer time scale), for the discrete approach. The time scale of the final diffusion process is the same for both approaches. This mismatch in the early time scales can be solved by considering simple scaling arguments based

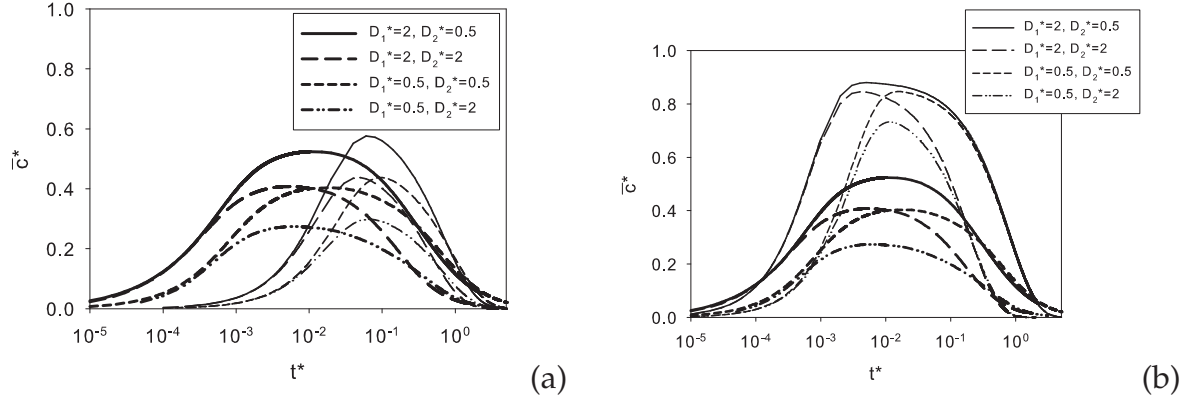


Figure 2.5: Average concentration in the interphase from the continuous model (thick lines) and from the discrete approximation (thin lines), see Eq. 2.2 and Eqs. 2.11 and 2.12 (left) and with K_2 defined as in Eq. 2.23 (right).

on analytical solutions of the dimension full problem for special cases. In the early stages the interphase is filled only by the low-molecular weight species from the droplet, the droplet concentration can be assumed constant and the concentration profile in the interphase is given by:

$$\bar{c}_I = \bar{c}_S \left[1 - \operatorname{erf} \left(\frac{r - R}{\sqrt{D_I t}} \right) \right] \quad R \leq r \leq R + \delta, \quad (2.19)$$

in which erf is the error function. The characteristic time scale for diffusion into the interphase is:

$$\tau_{\text{early}} = \frac{\delta^2}{D_I}. \quad (2.20)$$

At later stages of the diffusion process the concentration in the interphase becomes similar to the droplet concentration and is given by:

$$\bar{c}_I \simeq \bar{c}_S = \exp \left(-\frac{Rt}{D_I} \right), \quad (2.21)$$

so the characteristic time scale for diffusion from the interphase becomes:

$$\tau_{\text{final}} = \frac{R\delta}{D_I}. \quad (2.22)$$

According to this scaling the characteristic time scale in the discrete model of the second term of the righthand side of Eq. 2.12 should change as:

$$K_2 = \left(\frac{D_{IR}}{\delta^2} \right)_{t \sim 0} \rightarrow K_2 = \left(\frac{D_{IR}}{R\delta} \right)_{t \sim \infty} .$$

A simple approximation that gives the right limiting behavior is given by:

$$K_2 = \left(\frac{D_{IR}}{f\delta} \right), \quad (2.23)$$

$$f = -(R - \delta) \cdot (\bar{c}_S - \bar{c}_I) + R, \quad \bar{c}_S(0) = 1, \quad \bar{c}_I(0) = 0. \quad (2.24)$$

If this approximation is included in Eqs. 2.11 and 2.12, the resulting average concentration profiles, in terms of dimensionless variables \bar{c}^* and t^* , and using the same parameters as for the continuous case (see Fig. 2.2 (c)), are given in Fig. 2.5 (b).

Notice that indeed the time scales do agree quite well but the maximum average concentration is overestimated. However, since the interfacial tension is proportional to the average concentration in an unknown way, we do not consider this as a problem. Scaling the results in Fig. 2.5 (b) with a constant, the maximum can be made of the same level as for the continuous case and the curves for the discrete and continuous case do agree quite well. In the experimental section we will use the discrete cases to obtain characteristic time scales by fitting the experimental results to compare the different material combinations. Transforming these experimental time scales to diffusion coefficients, that could be used in the diffusion equation, is outside the scope of this chapter.

2.3 Relation with molecular parameters

In Shi et al. [1] the parameters in the model (K_1 and K_2 , see Eq. 2.12) are related to molecular characteristics. We will summarize these relations here in order to interpret our experimental results in terms of the known molecular parameters of our materials. In Shi et al. [1] an interface with a certain unknown thickness is proposed, thus an interphase, as schematically represented in Fig. 2.1 (left). The model relates the transient behavior of the interfacial tension to the diffusion of species through the interphase. For a blend composed of polydisperse components, short molecules of both phases can migrate into and out of the interphase until a steady-state concentration c_{stat} is reached. Assuming that the concentration c_S of low-molecular weight chains M_{A_1} (see Fig. 2.1 (left)) remains constant in the source phase and is negligible

in the receiving phase during the time window of interest, the time dependence of the concentration of the low-molecular weight chains, \bar{c}_I , in the interphase is modeled as reported in Eq. 2.12. From this model, the stationary value for the concentration in the interphase, c_{stat} , can be obtained:

$$c_{\text{stat}} = \frac{K_1 \bar{c}_S}{K_1 + K_2}. \quad (2.25)$$

Redefining the independent variable as $(c_{\text{stat}} - c)$, the following expression can be derived:

$$\frac{d(c_{\text{stat}} - \bar{c}_I)}{dt} = (K_1 + K_2)(c_{\text{stat}} - \bar{c}_I). \quad (2.26)$$

Integrating Eq. 2.26, the time dependence of c can be expressed as:

$$\bar{c}_I = c_{\text{stat}} + (\bar{c}_0 - c_{\text{stat}})e^{-(K_1+K_2)t}, \quad (2.27)$$

where \bar{c}_0 is the value of \bar{c}_I at $t = 0$. Note that for sufficient long time, \bar{c}_I approaches the steady-state value, c_{stat} . The kinetic constants depend on the thermodynamic driving forces for the diffusion of short molecules into and out of the interphase, the chain length of the diffusing species and the viscosities of the two bulk phases. Since the details of the thermodynamic parameters, see [1], are not available, these contributions are incorporated into the factors K_1^* and K_2^* :

$$K_1 = \frac{K_1^*}{M_{A_1}^d \eta_S}, \quad K_2 = \frac{K_2^*}{M_{A_1}^d \eta_R}, \quad (2.28)$$

where the unknown exponent d expresses the mobility of the migrating species and η_S and η_R are the viscosities of the source and receiving phase respectively. Under the assumption that the interfacial tension decreases with accumulation of component A_1 in the interphase, i.e. postulating a proportionality between c_I and σ , Eq. 2.27 can be rewritten as:

$$\sigma = \sigma_{\text{stat}} + \Delta\sigma e^{-t/\tau}, \quad \Delta\sigma = \sigma_0 - \sigma_{\text{stat}}, \quad (2.29)$$

where σ_0 is the interfacial tension measured at $t = 0$, σ_{stat} is the steady-state interfacial tension value and τ is defined as:

$$\tau = M_{A_1}^d \left(\frac{K_1^*}{\eta_S} + \frac{K_2^*}{\eta_R} \right)^{-1}. \quad (2.30)$$

In terms of material properties introduced in Eq. 2.1, Eq. 2.29 reads:

$$\sigma = \sigma_{\text{stat}} + \frac{K}{M_n} \exp\left(-\frac{t}{\tau}\right), \quad M_n = M_{A_1}^d. \quad (2.31)$$

In addition, we assume that $M_n \simeq M_{A_1}^d$, which implies that a lower-molecular weight leads to larger changes in interfacial tension. Clearly, the time needed to reach steady state decreases when reducing the average length of the chains and the viscosity of the two phases. Polymer blends, however, are made by mixing two different polymers, and both of them exhibit a molecular weight distribution. Consequently, from each of the two phases, migration of molecules can occur. Assuming that both diffusion processes contribute individually to the changes in interfacial tension, Eq. 2.29 can be generalized:

$$\sigma = \sigma_{\text{stat}} + \Delta\sigma_S e^{-t/\tau_S} + \Delta\sigma_R e^{-t/\tau_R}. \quad (2.32)$$

The model is not able to predict depletion, and thus, for the cases where it occurs, only the data relative to the filling of the interphase should be used. By fitting the data with Eq. 2.32, the characteristic diffusion time of the short molecules that migrate from the source phase into the receiving phase and vice versa, can be obtained at each temperature. The characteristic time according to Eq. 2.30 increases with the viscosity η and the temperature dependence of τ and η is expressed through the activation energies:

$$E_X = R \frac{d \ln X}{d(1/T)}, \quad (2.33)$$

where X can be τ or η . If temperature effects are assumed to be included in the characteristic times and viscosities only, and not in K_1^* and K_2^* , differentiation of Eq. 2.30 using Eq. 2.33 gives (see [1]):

$$E_\tau = \omega_S E_{\eta_S} + (1 - \omega_S) E_{\eta_R}, \quad (2.34)$$

in which:

$$\omega_s = \frac{K_1^* \eta_r}{K_2^* \eta_s + K_1^* \eta_r}. \quad (2.35)$$

ω_s expresses to which extent the process is dominated by the viscosities of the dispersed ($\omega_s = 1$) or the continuous phase ($\omega_s = 0$).

To investigate how the mobility of the chains, d , changes with temperature according to this model, indices 1 and 2 are introduced in Eq. 2.30 for two species differing in molar mass. The reference system, with index 1, is chosen to be the most diffusive blend (PB 635/PDMS). Once the characteristic times are obtained for the two systems, the following expression to calculate d can be derived:

$$\frac{\tau_1}{\tau_2} = \left(\frac{M_1}{M_2} \right)^d \frac{E_2}{E_1}, \quad (2.36)$$

where

$$E_i = \left(\frac{K_1^*}{\eta_s} + \frac{K_2^*}{\eta_r} \right)_i \quad i = \{1, 2\}. \quad (2.37)$$

Since K_1^* and K_2^* are unknown, we will assume them to be identical. In case the two polymers have similar molecular weight distributions, the ratio M_1/M_2 equals the ratio of their average molar mass. In case of dissimilar molecular weight distributions, a minimum *disproportionation*² factor is introduced:

$$f_{min} = \left[2D - 1 + 2\sqrt{D(D - 1)} \right]^{0.5}, \quad (2.38)$$

where $D = \frac{M_w}{M_n} = \sum w_i M_i \sum \frac{w_i}{M_i}$ is the polydispersity index, w_i is the weight fraction and M_i the molar mass of the component i . The following relation holds:

$$\frac{M_1}{M_2} = \frac{f_{min2}}{f_{min1}}. \quad (2.39)$$

The minimum *disproportionation* factor can be calculated starting from a molecularly uniform polymer species. We can disproportionate them into two components: M/f and $M \cdot f$, with $f > 1$. Denoting with w the weight fraction of the shorter chains:

²nomenclature used by Shi et al. [1]

$$D = \frac{[f^2 - w(f^2 - 1)][w(f^2 - 1) + 1]}{f^2}. \quad (2.40)$$

Solving this equation with respect to w , the amount of each component needed for a given certain polydispersity, yields:

$$w = \frac{1}{2} \pm \frac{\sqrt{f^4 + f^2(2 - 4D) + 1}}{2(f^2 - 1)}. \quad (2.41)$$

Clearly, many combinations of molar masses and mixing ratios exist to model a certain polydispersity. For each mixture the smallest factor f is required and, under this condition, the square root of Eq. 2.41 becomes zero and we obtain Eq. 2.39. From Eq. 2.36 it is now possible to derive d . Results are reported in Table 2.6, below, see Section 2.5.3.

2.4 Experimental

Materials

Three different grades of polybutene (PB, Indopol H-25, H300, H1200, BP Chemicals, UK) for the dispersed phase, and one grade of polydimethylsiloxane (PDMS, UCT) for the continuous phase, are selected. The materials are liquid and transparent over the whole range of temperatures relevant to this work. They are chosen given their differences in asymmetry in average molecular weight across the interface. Zero shear viscosities, η , are measured using a rotational rheometer (Rheometrics, ARES) equipped with a parallel-plate geometry, and applying steady shear. The polymers exhibit Newtonian behavior in the range of shear rates applied ($0.01 - 10 \text{ s}^{-1}$) and at all temperatures investigated ($0^\circ\text{C} - 80^\circ\text{C}$). A digital density meter (DMA 5000, Anton Paar) is used to measure the temperature dependence of the density, ρ , in the range $24^\circ\text{C} - 80^\circ\text{C}$, yielding an approximately linear relation with constants a and b . The number average molecular weight M_n , the molecular weight polydispersity M_w/M_n , the viscosity values at 23°C , and the coefficients a and b are given in Table 2.1.

Table 2.1: Selected model components. $\rho[\text{g}/\text{cm}^3] = a - b * 10^{-4} * T[^\circ\text{C}]$.

Sample	M_n^3	$\frac{M_w^1}{M_n}$	η	a	b
	[g/mol]	[-]	[Pa · s]	[g/cm ³]	[g/(cm ³ · °C)]
PB (H25)	635	2.1	3.7	0.8874	5.778
PB (H300)	1300	1.65	80	0.9087	5.377
PB (H1200)	2100	1.8	307.6	0.9152	5.291
PDMS	62700	1.8	10.9	0.9931	8.823

Methods

Various techniques exist to measure interfacial tension and we distinguish: equilibrium, transient and rheological methods. From these methods we chose the pendent/sessile drop method (PAT-1, Profile Analysis Tensiometer, Sinterface, Germany) (equilibrium category) since it provides more accurate measurements than the dynamic and rheological methods available nowadays, although several conditions need to be fulfilled for a proper use [13]. First, transparent components are required with densities that differ more than 4 - 5% at the experimental temperatures. In order to create a pendent configuration, the matrix should be less dense than the drop. Our matrix, PDMS, possess the highest density in the whole range of temperatures investigated and therefore, a tailor made u-shaped capillary is designed and used. Experiments are carried out in the range 24°C - 80°C, with an accuracy of ±0.5°C, while for the lowest molecular weight dispersed phase, also lower temperatures are used. Attention is paid to create drops in their equilibrium shape and to avoid influences of dilatation or shrinkage of drops due to thermal effects. The glass cell is filled with the matrix material and the u-shaped metal capillary with the dispersed phase. To guarantee uniform temperatures they are left at the experimental temperature for a sufficient long time (at least 1 night) without contact between the polymeric phases, to avoid mutual diffusion to begin. Next, the drop is created by means of a home-made dosing system that allows a good control of the drop volume. Real time images are available during drop creation and during the transient interfacial tension measurements. Dependent on the viscosity of the dispersed phase (given the same viscosity of the matrix phase in all experiments), different times, typically in the order of 1-2 minutes for the lowest molecular weight PB and 5-10 for the other PB grades, are needed to obtain a symmetrical drop, necessary for the further analysis. Once the drop approaches its equilibrium shape, measurements are started and images are systematically acquired and digitized by a frame grabber for a certain time window. The images recorded during the measurements are analyzed using the Gauss-Laplace equation, that relates the curvature of a liquid meniscus with the

³Provided by supplier.

surface tension σ . All measurements are repeated at least three times with varying drop sizes (0.9-1.5 mm) and good reproducibility (see next Section) is obtained for all combinations and at all temperatures. The fitting procedure gives σ values with standard deviations that are always below 10^{-3} mN/m.

2.5 Results of transient measurements

2.5.1 Experimental results at different temperatures

The standard blend systems

Fig. 2.6 top row left shows the transient interfacial tension of PB 635 in PDMS at different constant temperatures (lines connect the data points). Although the sample is polydisperse, at 0°C diffusion is slow. Increasing the temperature, up to 80°C, reduces the interfacial tension in the earlier stages, due to fast accumulation of low-molecular weight species that migrate from the drop to the interphase. After a short pseudo-steady state, i.e. plateau value in σ , an increase in interfacial tension is found caused by depletion of short molecules in the interphase, until finally an equilibrium state is reached. Raising the temperature gives a stronger reduction in $\sigma(t)$ with lower minimum values reached at longer times, and with shorter pseudo-steady states. An increase in temperature yields, on one hand, a higher fraction of molecules with sufficient mobility to cross the interphase and results, on the other hand, in a faster interdiffusion process. The larger fraction of diffusing molecules gives higher concentrations in the interphase, thereby lowering the minimum in the transient interfacial tension, and requires a longer time to complete the diffusion process. For the system PB 635/PDMS, both these effects are observed (see Fig. 2.6 top row left), thus the larger number of molecules involved in the interdiffusion process at higher temperatures dominates over the effect of the diffusion rate. Increasing the average molecular weight of the dispersed phase, higher interfacial tension values are expected (Eq. 2.1). Fig. 2.6 bottom row shows the transient interfacial tension for the PB 1300/PDMS (left) and PB 2100/PDMS (right) systems and confirms this expectation.

For experimental convenience, the experiments for the higher molecular weight systems were performed at different temperatures compared to the lowest molecular weight system. Increasing the temperature in PB 1300/PDMS system, we first recognize a reduction in $\sigma(t)$, corresponding to an increasing concentration in the interphase, followed by an increase in $\sigma(t)$, corresponding to a decreasing concentration in the interphase (Fig. 2.6 bottom row left). For the highest molecular weight system, PB 2100/PDMS, Fig. 2.6 (bottom row right), in the same time scale only a concentration increase is observed in the interphase, except for the data at 80°C. For these two higher molecular weight systems, clearly longer time scales are needed to reach equilibrium and results of extended experiments are given in Fig. 2.6 (bottom row left) for the PB 1300/PDMS system. To reach steady state times are needed two orders

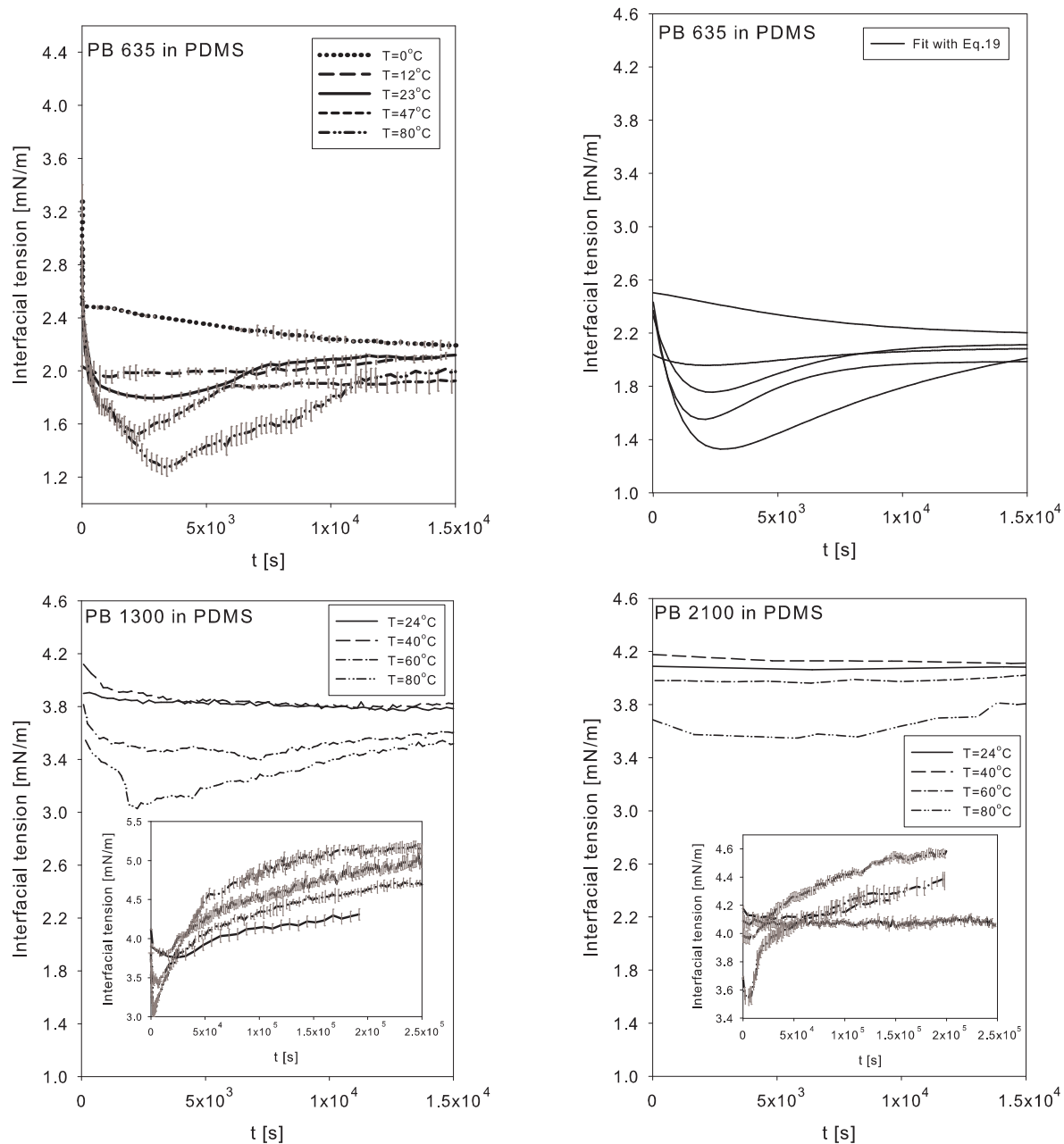


Figure 2.6: Transient interfacial tensions $\sigma(T)$ for the PB 635/PDMS system (top row) and for the PB 1300/PDMS and PB 2100/PDMS (bottom row). On the right of the top row the fit using Eq. 2.18 and values for τ in Table 2.3 is shown for the PB 635/PDMS. The insets show the same results over the full experimental time scale and with error bars.

of magnitude longer compared to the lowest molecular weight drop phase PB 635. Despite the longer time required to complete the diffusion process, a similar tran-

sient behavior, $\sigma(t)$, is recorded and now we recognize, at all temperatures, that the minimum in interfacial tension value occurs in the early stages of the measurements. Lower minima are found with increasing temperature while the pseudo-stationary state, if present at all, decreases with increasing temperature. After sufficient long times, a plateau in interfacial tension is approached and sustained. In contrast to the PB 635/PDMS system, for the PB 1300 drop, we find the minimum in $\sigma(t)$ to shift towards shorter times with increasing temperature. This could however, also be related to an artifact. Due to the high viscosity of the drop phase, longer times are needed to form a drop in its equilibrium shape. During this equilibration time, contact is present between the two phases and, therefore, diffusion starts. Since diffusion is already in progress, this results in uncertainty at $t = 0s$, the time at which the measurements starts. Fig. 2.6 (bottom row right) shows the results for the highest molecular weight system. Due to the high viscosity, at 24°C transport of matter from one phase into the other is limited and, therefore, no appreciable changes in interfacial tension are recorded. Increasing the temperature enhances diffusion due to the higher mobility of the short molecules and due to a reduced viscosity of the drop phase; again all four stages in the development of the transient interfacial tension are recognized with the same conclusions as in the PB 1300/PDMS system. To confirm that diffusion occurs from the dispersed phase into the continuous phase, the volume of the drop is recorded during the interfacial tension measurements. Since care is taken that no leaking occurs in the system, any measured change in volume can be attributed to diffusion. Table 2.2 shows the initial radii of the droplets, R_0 , and their decrease after four hours, ΔR_{4h} , for the three drop phases at room temperature. All the radii decrease in time, confirming that the transient character of the interfacial tension is due to migration of molecules from the drop phase into the matrix phase (and not vice versa). As expected, ΔR_{4h} is higher for the lowest molecular weight drop phase, and it is zero for the highest molecular weight PB. Measurements of the drop volumes during the total time window of the interfacial tension experiments, confirm that all the three grades, at each temperature, show a reduction in drop radius, corroborating the interpretation of the interfacial tension results given above. Since the thickness of the interphase layers around drops were estimated to be at least of the order of magnitude of ΔR , we can conclude that by increasing the average molecular weight of the drop phase, while keeping constant the matrix grade, the interface becomes thinner.

Table 2.2: Characteristic length scale of drop size reduction in PB/PDMS 62700 systems at $T = 24^\circ\text{C}$.

Drop	R_0 [mm]	ΔR_{4h} [μm]
PB635	1.13	209
PB1300	1.25	13
PB2100	1.44	0

The inverse blend systems

In all cases presented, diffusion holds from the drop phase into the matrix. The effects of the direction in which diffusion occurs are investigated for the inverse system having the highest asymmetry in molecular weight across the interface, i.e. PDMS/PB 635, at two temperatures, 12°C and 24°C. In this case, the low-molecular weight component is in the matrix, which now is the source phase, while the drop is the receiving phase. The transient interfacial tension and the drop volumes measured for this system, are given in Fig. 2.7. At both temperatures, the volume of the drop increases, confirming that molecules are migrating from matrix into the drop. The initial drop radius is $R_0 = 733 \mu\text{m}$ at 12°C, and $R_0 = 788 \mu\text{m}$ at 24°C, while the increase of the drop radius, after four hours, is $\Delta R_{4h} = 18 \mu\text{m}$ and $\Delta R_{4h} = 46 \mu\text{m}$, respectively. At both temperatures investigated, the interfacial tension reduces and, after a certain time, it approaches a plateau value. These results can be interpreted with help of the modeling. The receiving phase, the drop, is much smaller compared to the infinite matrix phase and, therefore, the assumption that the average concentration of migrating molecules in the receiving phase can be considered equal to zero does not apply. When contact between the two phases is established, diffusion starts and migrating molecules accumulate in the interphase, causing the interfacial tension to decrease; only a limited fraction will be able to migrate into the drop before saturation of the drop phase occurs, where the interfacial tension approaches and sustains a steady-state value. Compared to the situation at 24°C, at 12°C the diffusion process is slower while a smaller fraction of molecules migrates and steady-state is reached after longer times, yielding a higher value in interfacial tension at 12°C than at 24°C (compare the temperature dependent behavior for the PB 635 drop in PDMS as reported in Section 2.5.1).

2.5.2 Discrete model results

The transient interfacial tension measurements for the standard blend system can be fitted using Eq. 2.18. The resulting characteristic diffusion times are listed in Table 2.3 for the three grades of PB, respectively. The quality of the fit is rather good, see Fig. 2.6 (b) as an example. In all cases, $\tau_1 < \tau_2$, meaning that accumulation of migrating molecules in the interphase occurs at all temperatures and for all systems investigated.

For the lowest molecular weight PB drop, the time scales τ_1 and τ_2 are comparable. In the other two cases, with a minor asymmetry in molecular weight across the interphase, the time scales differ one order of magnitude.

2.5.3 Shi model results

The characteristic time for diffusion can also be obtained by fitting the experimental data with Eq. 2.32 in an attempt to relate the characteristic diffusion times to molec-

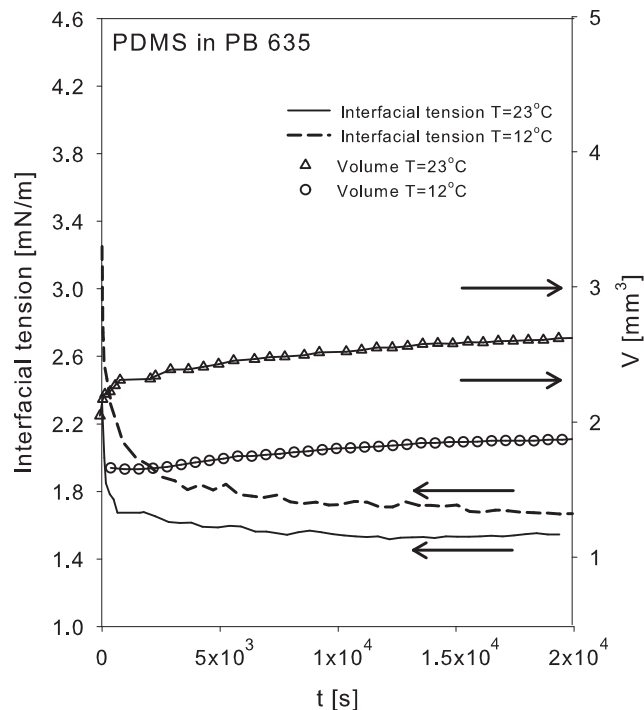


Figure 2.7: Interfacial tension and volume for the PDMS/PB 635 system at two different temperatures.

Table 2.3: Temperature dependence of the characteristic diffusion times calculated with Eq. 2.18, for the three PB/PDMS systems.

PB635			PB1300			PB2100		
$T[^\circ\text{C}]$	$\tau_1[\text{s}]$	$\tau_2[\text{s}]$	$T[^\circ\text{C}]$	$\tau_1[\text{s}]$	$\tau_2[\text{s}]$	$T[^\circ\text{C}]$	$\tau_1[\text{s}]$	$\tau_2[\text{s}]$
0	3314	3894	24	10720	84150	24	-	-
24	1970	2010	40	2417	11150	40	-	-
47	1320	1989	60	828	80320	60	2481	83230
80	1100	10000	80	1069	46470	80	444	54420

ular parameters. The kinetic model reported by Shi et al. [1] refers to the initial time scales of diffusion of short molecules from source and matrix into the interphase and no depletion is incorporated in the model. Correct application should, therefore, only use data of the initial stage of diffusion, the filling of the interphase. Since we do not know a priori the time when depletion starts, the data are omitted when they give just an indication that the time scales of migration from interphase into matrix are influencing the interfacial tension measured. Similar as in the case of analyzing the data with the discrete model (with depletion, see Section 2.5.2) a reduction in diffusion time is found with increasing temperature for all three systems investigated, see

Table 2.4. At a fixed temperature, the characteristic times increase with the molecular weight of the drop phase, i.e. when the asymmetry in molecular weight across the interface reduces and a lower polydispersity index is present (PB1300 and PB2100 compared to PB 635).

Table 2.4: Analyzing data by determining characteristic diffusion times calculated with Eq. 2.32, for the three PBs grades, at different temperatures.

$T [^{\circ}\text{C}]$	$\tau_{PB635} [s]$	$\tau_{PB1300} [s]$	$\tau_{PB2100} [s]$
0	8500	-	-
24	670	2103	-
40	-	1145	3129
47	570	-	-
60	-	330	1141
80	85	100	360

The same result was obtained with the discrete model, in Section 2.5.2. Once the viscosities and the characteristic diffusion times are known, it is possible to calculate the activation energies, using Eq. 2.33. The results are used to determine ω_s (Eq. 2.34), the factor that expresses to which extent the diffusion process is dominated by the viscosity of the drop phase ($\omega_s = 1$) or matrix phase ($\omega_s = 0$). We find $\omega_s = 0.7$ for the system PB635/PDMS, $\omega_s = 0.74$ for the system PB1300/PDMS, and $\omega_s = 0.56$ for the system PB2100/PDMS. These values of ω_s confirm that the diffusion process is mainly controlled by the drop phase. However, although the experimental observations show that increasing the molecular weight asymmetry across the interface plays a strong role, given the values found for ω_s ($\omega_s \neq 1$) it seems that diffusion is never fully dominated by the source material. A possible explanation is that the rate constants have been assumed to be temperature independent. To check this assumption, the dependence of the ratio K_2^*/K_1^* on the temperature is investigated by using Eq. 2.35, see Table 2.5.

Table 2.5: Characteristic ratio (K_2^*/K_1^*) for the three PB grades at different temperatures.

$T [^{\circ}\text{C}]$	$(K_2^*/K_1^*)_{PB635}$	$(K_2^*/K_1^*)_{PB1300}$	$(K_2^*/K_1^*)_{PB2100}$
24	1.25	0.05	0.03
40	3.81	0.14	0.07
60	14.27	0.35	0.2
80	14.7	0.71	0.48

A clear influence of temperature on the ratio (K_2^*/K_1^*) is found for all three PB grades,

most pronounced for the lowest molecular weight grade and apparently the assumption made in [1] to derive Eq. 2.34, i.e. with (K_2^*/K_1^*) temperature independent, does not fully apply to our blends. Next we determine the value of the exponent in Eq. 2.36 to determine the relative mobility of the low-molecular weight component. PB 635/PDMS blend is taken as the reference system (i.e. system 2 in Eq. 2.36). Large values of d imply a pronounced influence of chain length relative to the influence of viscosity, on the diffusion times. The calculated d values are given in Table 2.6, and we can conclude that despite the number of approximations necessary to reach this point of analysis, the effect of chain lengths on the mutual diffusion process indeed overrules viscosity influences.

Table 2.6: Temperature dependence of the d exponent in Eq. 2.36, calculated using PB635/PDMS blend as the reference system.

$T[^\circ\text{C}]$	d_{PB1300}	d_{PB2100}
24	3.35	7.2
40	4.82	10.36
60	3.19	9.98
80	1.79	8.34

2.6 Results of steady-state measurements

Finally, the steady-state values of the interfacial tension, obtained after prolonged experimental times, are analyzed. Results are summarized in Fig. 2.8 (a). An increase in the values of σ_{stat} with an increase in M_n is found, approaching a plateau value when the molecular weight exceeds 1000.

In [11] and [12], the molecular weight dependence of the interfacial tension is reported to be well approximated by Eq. 2.1 where z is assumed 1/2 and 2/3 respectively. Fitting the data gives $\sigma_\infty = 8$ and $C = 146$ for $z = 1/2$ and $\sigma_\infty = 7$ and $C = 353$ for $z = 2/3$, respectively, and the resulting curves are plotted in Fig. 2.8 (a).

Fig. 2.8 (b), shows the dependence of the steady interfacial tension on temperature, now with an indication of the different polydispersities of the drop phase. Increasing polydispersity, decreases σ_{stat} , at all temperatures investigated, and its influence is more pronounced at higher temperatures. Approximating the dependence of σ_{stat} on the temperature with a linear relation, we obtain the temperature coefficient, $\Delta S = -d\sigma_{\text{stat}}/dT$ which is the entropy change of interface formation per unit area. The PB 635/PDMS system has a small positive ΔS , indicating that a higher polydispersity results in enhanced aggregation of low-molecular weight components at the interface [12], while an increase of the steady interfacial tension with temperature for PB 1300/PDMS and PB 2100/PDMS indicates the possible existence of close

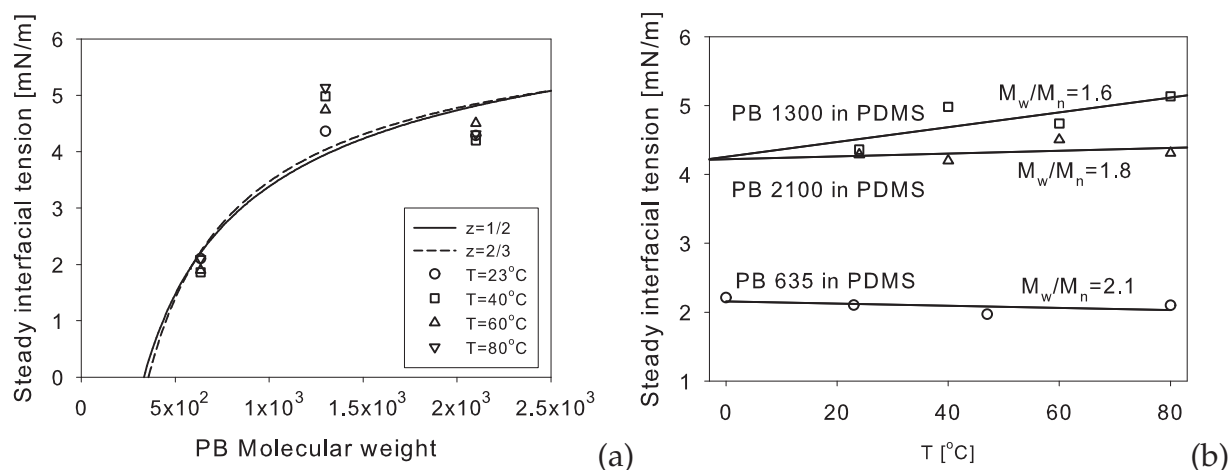


Figure 2.8: Dependence of the steady state values of the interfacial tension, at different temperatures, on the molecular weight of the drop phase. Lines in the left figure are according to Eq. 2.1.

miscibility gaps [14].

2.7 Conclusions

Binary blends PB/PDMS with a range of molecular weight, as investigated here, can not be considered fully immiscible. For the lowest molecular weight system (PB 635/PDMS), which also has the highest polydispersity index, the transient interfacial tension starts to decrease immediately after the formation of a fresh interface. This reduction is attributed to mutual diffusion: the fraction of shorter molecules present in the drop phase starts to migrate and accumulates in the interphase. As time proceeds, the active molecules start to diffuse out of the interphase in the receiving matrix phase, which can be considered much larger than the drop. Continued diffusion from drop to matrix, via the interphase, finally causes depletion in the drop phase and, therefore, an increase in interfacial tension is found. Increasing the temperature values, a larger number of molecules are involved in this diffusion and mutual dissolution process, influencing the time scales in a unexpected way. Total mass transport increases and time scales become *longer* at higher temperatures, with concomitant temporarily higher concentrations in the interphases and thus lower values of $\sigma_{min}(t)$. When reversing the blend, the behavior observed is consistent with the ideas explained above; the drop is a finite receiving phase and the depletion does not occur. In addition, the temperature effects are the same compared to the inverse blend. Back to the standard system we found that increasing the molecular weight of the drop phase does not affect the transient behavior of the interfacial tension other than extending the time scales of the total process. This slower diffusion is due to longer molecules and higher viscosity of the drop phases. Steady and transient inter-

facial tension values increase with molecular weight and a clear separation between values measured for PB 635/PDMS system, on one hand, and PB 1300/PDMS and PB 2100/PDMS systems, on the other hand, are shown.

For a qualitative interpretation of the experimental findings the diffusion equation is used assuming that Fick's law applies and using constant diffusion coefficients and a continuous chemical potential. Two possible choices for concentration profiles are continuity or discontinuity at the phase boundaries. When discontinuous profiles are hypothesized, an assumption on the equilibrium distribution coefficient is needed. Therefore, in order to limit the number of assumptions made, only the case of continuous concentration profiles is treated. A first version of the model assumes a constant interphase thickness, while in a second case the thickness of the interphase, δ , is changing. The ratios of the diffusion coefficients of the source phase and interphase, D_1^* , and interphase and receiving phase, D_2^* , are varied keeping the value of the thickness δ^* constant. The choice of the parameter D_1^* affects the time scale of the accumulation of molecules into the interphase, while D_2^* controls the time scale of depletion. When considering the two-zone model, without a fixed thickness of the interphase, and defining it by choosing a limiting concentration and tracking its position in time, it is found that, due to diffusion, thickening of the interphase occurs, followed by a pseudo-stationary value that disappears and the interfacial tension increases to reach, after sufficient long time, a plateau value. A discrete model was then derived from the continuous model. It guarantees the same features of the continuous formulation but, at the same time, allows us to derive an expression to fit the experimental data. A scaling analysis has been performed in order to link the parameters in the continuous and in the discrete forms of the model.

The characteristic times of diffusion of low-molecular weight components from the source (drop) phase into the interphase are always shorter than the characteristic times of migration of molecules from the matrix phase into the interphase in the blend systems used. A special case of the discrete model, that assumes the source of the migrating molecules to be constant (no depletion), can be compared to the kinetic model proposed in Shi et al. [1]. Since no depletion is present, the model is not suited to corroborate our experimental results, but it is used to attempt to link the early time of diffusion time scales found to know molecular parameters. Using this model, the characteristic times of migration of molecules from drop into interphase are found to be shorter than those from matrix into interphase and that chain lengths of the migrating molecules play a dominant role compared to the bulk viscosities of the polymers. Future work should focus on monodisperse, bimodal systems that are better defined and, therefore, are more accessible for comparison with modeling results.

References

- [1] Shi, T., Ziegler, V.E., Welge, I.C., An, L., Wolf, B.A. (2004). Evolution of the interfacial tension between polydisperse "immiscible" polymers in the absence

- and in the presence of a compatibilizer. *Macromolecules*, **37**, 1591–1599.
- [2] Olabisi, O., Robeson, L.M., Shaw, M.T. (1979). *Polymer-polymer miscibility*. Academic London.
- [3] Jones, R.A.L. and Richards, R.W. (1999). *Polymer at Surfaces and Interfaces*. Cambridge University Press.
- [4] Fortelny, I. and Kovar, J. (1988). Theory of coalescence in immiscible polymer blends. *Polym. Compos.*, **9**, 119–124.
- [5] Elmendorp, J.J. and van der Vegt, A. (1986). A study on polymer blending micro-rheology: Part iv. the influence of coalescence on blend morphology origination. *Polym. Eng. Sci.*, **26**, 1332–1338.
- [6] Rusu, D. and Peuvrel-Disdier, E. (1999). In-situ characterization by small angle light scattering of the shear-induced coalescence mechanisms in immiscible polymer blends. *J. Rheol.*, **43**, 1391–1409.
- [7] Verdier, C. and Brizard, M. (2002). Understanding droplet coalescence and its use to estimate interfacial tension. *Rheol. Acta*, **43**, 514–523.
- [8] Vinckier, I., Moldenaers, P., Mewis, J. (1996). Relationship between rheology and morphology of model blends in steady shear flow. *J. Rheol.*, **40**, 613–631.
- [9] Lyu, S.P., Bates, F.S., Macosko, C.W. (2000). Modeling of coalescence in polymer blends. *AIChE J.*, **48**, 7–14.
- [10] Peters, G.W.M., Zdravkov, A., Meijer, H.E.H. (2005). Transient interfacial tension and dilatational rheology of diffuse polymer-polymer interfaces. *J. Chem. Phys.*, **122**, 104901–1–10.
- [11] Kamal, M.R., Lai-Fook, R., Demarquette, N.R. (1994). Interfacial tension in polymer melts. part ii: Effects of temperature and molecular weight on interfacial tension. *Polym. Eng. Sci.*, **34**, 1834–1839.
- [12] Nam, K.H. and Ho Jo, W. (1995). The effect of molecular weight and polydispersity of polystyrene on the interfacial tension between polystyrene and polybutadiene. *Polymer*, **36**, 3727–3731.
- [13] Anastasiadis, S.H., Gancarz, I., Koberstain, J.T. (1988). Interfacial tension of immiscible polymer blends: Temperature and molecular weight dependence. *Macromolecules*, **21**, 2980–2987.
- [14] Wagner, M. and Wolf, B.A. (1993). Interfacial tension between poly(isobutylene) and poly(dimethylsiloxane): Influence of chain length, temperature, and solvents. *Macromolecules*, **26**, 6498–6502.
- [15] Stammer, E. and Wolf, B.A. (1998). Effect of random copolymer additives on the interfacial tension between incompatible polymers. *Macromol. Rapid Commun.*, **19**, 123–126.
- [16] Helfand, A. and Tegami, Y. (1972). Theory of the interface between immiscible polymers. ii. *J. Chem. Phys.*, **56**, 3592–3601.
- [17] Broseta, D., Fredrickson, G.H., Helfand, E., Leibler, L. (1990). Molecular weight and polydispersity effects at polymer-polymer interfaces. *Macromolecules*, **23**, 132–139.

-
- [18] LeGrand, D.G. and Gains, G.L. (1975). Immiscibility and interfacial tension between polymer liquids: Dependence on molecular weight. *J. Coll. Int. Sci.*, **50**, 272–279.
- [19] Auer, P.L. and Murbach, E.W. (1954). Diffusion across an interface. *J. Chem. Phys.*, **22**, 1054–1059.

CHAPTER THREE

Transient interfacial tension and morphology evolution in partially-miscible polymers¹

The influence of molecular weight asymmetry across an interface on the transient behavior of the interfacial tension is investigated for two different polymer combinations, polybutadiene (PBD)/polydimethylsiloxane (PDMS) and polybutene (PB)/PDMS. This choice ensures a minor diffuse interface using the first combination and a very diffuse interface in the latter case. Measurements of the interfacial tension as a function of time are carried out using a pendent/sessile drop apparatus at different temperatures ranging from 0°C to 80°C. Variations in the transient interfacial tension are attributed to diffusion of the lower molecular weight components from one phase into the other and the most pronounced changes are measured for the most diffusive systems (low molecular weight and high polydispersity) when diffusion goes from the drop into the matrix. By reversing the phases, only minor changes in the transient interfacial tension are measured. This is due to a fast saturation of the drop phase since the drop volume is much smaller than that of the continuous phase. In all cases investigated, after a sufficient time a steady value of the interfacial tension is reached. To estimate the characteristic diffusion times of the migrating species, a discrete solution of the diffusion equation proposed by Tufano et al. [1] and a kinetic model from literature are applied. Results obtained are in line with the experimental observations. The importance of a changing interfacial tension on morphology development is studied on dilute (1%) blends, using two in-situ techniques: small angle light scattering (SALS) and optical microscopy (OM). The SALS patterns yield the time evolution of the drop size, which is subsequently compared

¹Reproduced from: Tufano, C., Peters, G.W.M., Van Puyvelde, P., Meijer, H.E.H., Transient interfacial tension and morphology evolution in partially-miscible polymers. *J. Coll. Int. Sci.*, submitted.

with the morphology following from OM. Depending on the diffusivity of the system, the morphology development is dominated by either diffusion or coalescence. Existing sharp-interface drainage models indeed do not apply for the diffuse blends and an improved quantitative estimation of the value of the critical film thickness is needed.

3.1 Introduction

Mixing of polymers is a common industrial route to produce materials with tailor-made properties as increased stiffness, impact strength, permeability, and/or electrical and optical properties. The final properties of a material made by dispersive mixing are, to a great extent, determined by the morphology. Depending on the parent components, the flow history applied during preparing and processing of the blend, and taking into account that most of the polymers are thermodynamically immiscible or partially-miscible, different morphologies can be obtained. Two competitive phenomena occur during dispersive mixing: break-up and coalescence. The final morphology is a result of a dynamic equilibrium, while the interfacial tension is a key parameter since it affects both processes. It is common to assume that the interfacial tension is constant since mutual solubility between polymers is negligible during the morphology evolution (see e.g. [2–7]), and that mixing of different polymers is thermodynamically unfavorable (see e.g. [8]) because they consist of long molecules that also give their high viscosity and low diffusivity. For these reasons the kinetics of polymer-polymer interdiffusion (with typical diffusion coefficients in the order of $10^{-17} \text{m}^2/\text{s}$ and smaller, [9]) is expected to be slow compared to the processing or experimental time-scale, but this assumption is not correct when a large asymmetry in molecular weight across an interface is present. Indeed, small, and therefore fast, molecules can diffuse from one phase into the other for entropic reasons, resulting in some mass transport. The concentration of short molecules in the interfacial zone increases affecting the interfacial properties of the now partially-miscible polymer blend. Although many studies have been performed on break-up of a single drop and coalescence for two or more drops (see e.g. [10–14]), there is only a limited number of studies that takes into account mutual diffusion during morphology evolution [15–20]. Although several experimental techniques exist to measure interfacial tension as a function of time (and at different temperatures), an accurate model to predict the time scale of mutual diffusion between partially-miscible polymers and to relate diffusion to thinning or thickening of interfaces is still lacking. Some attempts exist. The time dependent interfacial tension of a blend of polystyrene/poly(propylene) has been modeled, using a single exponential equation [21], while a double exponential model was applied for the systems poly(dimethylphenylsiloxane) and poly(dimethylsiloxane) blended with random copolymer additives, [22]. The time dependence of the interfacial tension was mainly attributed to two phenomena: diffusion of components in the vicinity of the phase boundary and hydrodynamic relaxation of the drop. Recently, a model was

proposed by Shi et al. [20], who attributed changes in interfacial tension to transport of low molecular weight fractions across the interface. They applied a double exponential kinetic model to describe the time dependency of the interfacial tension.

We study the evolution of interfacial tension in time at different temperatures, ranging from 0°C to 80°C , for two blends with different diffusivity. Molecular weights of the drop and matrix phases differ up to two orders of magnitude for the two polymer combinations. Volume changes in time of a single drop in a matrix are recorded to investigate mutual solubility. The experimental results are interpreted using two models, the first based on a discrete solution of the complete diffusion equation, the second on a simpler kinetic model, the Shi model, [20], derived as a special case of the discrete model (see Chapter 2). Next we investigate the evolution of blend morphology under the influence of a *measured* transient interfacial tension. Two in-situ techniques, small angle light scattering (SALS) and optical microscopy (OM), are used to map the morphology evolution at a constant temperature (23°C) and at a viscosity ratio $p = 1$. The influence of reversing the two phases is investigated and a sharp-interface drainage model [23, 24] is applied (for immobile, partially-mobile, and fully mobile interfaces) to compare the measured results with model predictions.

3.2 Materials and methods

Materials used are polybutene (PB, Indopol H-25, BP Chemicals, UK), polybutadiene (PBD, Ricon 134, Sartomer) and polydimethylsiloxane (PDMS, UCT); they are liquid and transparent over the whole range of temperatures used in this work. Density is measured with a digital density meter (DMA 5000, Anton Paar) in the range 0°C - 80°C yielding a linear relation with constants a and b . The number average molecular weight M_n , the polydispersity M_w/M_n and the coefficients a and b to calculate density are given in Table 3.1. Zero shear viscosities are measured using a rotational rheometer (Rheometrics, ARES) equipped with a parallel-plate geometry and applying steady shear. All polymers exhibit Newtonian behavior in the range of shear rates applied ($0.01 - 10 \text{ s}^{-1}$) and at all temperatures; results are shown in Table 3.5. Blend systems investigated are PB/PDMS and PBD/PDMS, guaranteeing different asymmetries in molecular weight across the interface (two orders of magnitude in the first case and one order in the second case). The first system has a very diffuse interface while the second shows a minor diffusion (see Section 3.3). Given the considerable differences in activation energy, the viscosity ratio of the systems can easily be altered by changing the temperature in the flow experiments performed to investigate morphology evolution.

To measure interfacial tension, the pendent/sessile apparatus (PAT-1, Profile Analysis Tensiometer, Sinterface, Germany) is chosen since these measurements are based on an equilibrium method that provides more accurate data compared to dynamic

²Provided by supplier.

Table 3.1: Selected model components. $\rho [g/cm^3] = a + b * 10^{-4} * T [^{\circ}C]$.

Sample	M_n^2	$\frac{M_w^2}{M_n^2}$	a	b
	[g/mol]		[g/cm ³]	[g/(cm ³ . ^o C)]
PB	635	2.1	0.8874	-5.778
PBD	8000	1.1	0.9051	-6.042
PDMS	62700	1.8	0.9931	-8.823

and rheological methods [19]. The polymer pairs have to be transparent and the density difference should be larger than 4 - 5%. All systems investigated satisfy these requirements. To have a pendent configuration the matrix should possess the lowest density. By means of a u-shaped capillary, also in cases where the dispersed phase has the lowest density, measurements in a pendent mode could be performed. A summary of the experiments performed is given in Table 3.2.

Table 3.2: Summary of the systems and conditions investigated in the morphology probing part (Section 3.5).

Sample	Polymer combination	T [°C]
PB 635 in PDMS 62700	ED	12; 23;
PBD 8000 in PDMS 62700	SD	23; 28;
PDMS 62700 in PB 635	rED	12; 23;
PDMS 62700 in PBD 8000	rSD	23; 28;

In the following, we will refer to the polymer combination with PB as dispersed phase as the extremely diffusive blend, ED, and with PBD as dispersed phase as a slightly-diffusive blend, SD. The reversed blends will be indicated as reversed extremely diffusive, rED, and reversed slightly-diffusive blends, rSD, respectively. Flow experiments are performed on freshly made mixtures of these polymer systems using a shear cell (CSS 450 from Linkam Scientific Instruments) consisting of two parallel quartz plates. Two in-situ techniques, SALS and OM, are applied. All blends are prepared following the proven protocol of [4] and [25]. The correct amount (leading to 1% concentration) of the two phases are weighted and mixed by hand with a spatula. A white, cream like blend is obtained and put in a vacuum oven at room temperature to make it air-free. Sample thickness is kept 200 μm to limit multiple scattering during the SALS measurements. The same flow history is applied to all samples. To erase the influence of loading and stirring, preshear at a high shear rate of $40s^{-1}$ is applied for 4000 strain units followed by a low constant shear rate of $0.2s^{-1}$. No break-up and only coalescence occurs under these second, mild shear conditions. From time to time, the flow is stopped to acquire images with OM and patterns with SALS. It was checked that during stopping of the flow no morphological changes occur. Images from OM were analyzed manually and the SALS patterns

were analyzed applying the Debye-Bueche theory, a model for randomly arranged polymer blends. In both cases, an average radius of the dispersed drops in the blend is derived.

3.3 Transient interfacial tension experiments

M_n (dispersed phase) < M_n (continuous phase)

First, we investigate the case where the molecular weight of the dispersed phases (PB or PBD) is lower than that of the continuous phase (PDMS). Using a capillary, a drop is introduced in the matrix and its volume is subsequently recorded to find a characteristic diameter change and time scale caused by mutual diffusion [26]. Table 3.3 shows the initial radius of the drops at room temperature and the change in the radius after 4 hours, ΔR_{4h} . Since no external factors (like leaking in the system) influence the drop volume, any variation in volume is due to mutual diffusion. For the lowest molecular weight PB drop phase (the ED system), the reduction in the drop volume is pronounced, and no stationary value is found, even after four hours. For PBD, the higher molecular weight drop phase and the SD system, the volume reduces only in the early stages and reaches a plateau value within 1000s. Apparently a larger asymmetry in molecular weight across the interface, and a higher polydispersity, enhance mutual diffusion. Assuming that the thickness of the diffusion layer around a drop scales with the magnitude of ΔR (see Table 3.3), it follows that the system PB/PDMS has a much thicker interface compared to the system PBD/PDMS, rationalizing the ED and SD notation, respectively. Next the transient interfacial tension is determined from the drop radius as a function of time and the influence of the temperature is investigated, see Figure 3.1.

Table 3.3: Characteristic length scale of drop size reduction.

Drop	Matrix	R_0	ΔR_{4h}
		[μm]	[μm]
PB635	PDMS62700	1130	209
PBD8000	PDMS62700	1220	6

Trying to interpret the results from these experiments, it is useful to glance at a schematic picture like that in Figure 3.2. The source and the receiving phase can be seen as separated by an interphase, which is a transition phase. Short molecules move from the source phase into the interphase and, from there, into the receiving phase. Just after contact between the two polymeric phases is established, the interfacially active molecules start to accumulate into the interphase, reducing the interfacial tension. When time proceeds, a condition of pseudo-stationary state is reached in

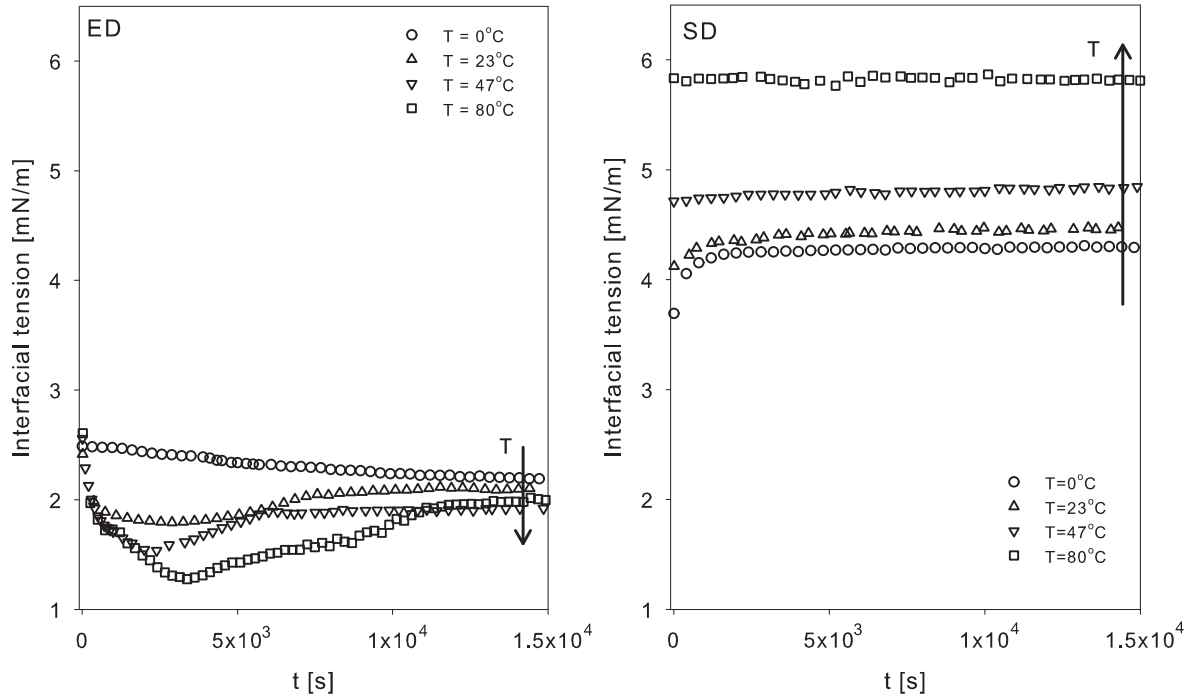


Figure 3.1: Transient interfacial tension at different temperatures for the ED system (left) and for the SD system (right).

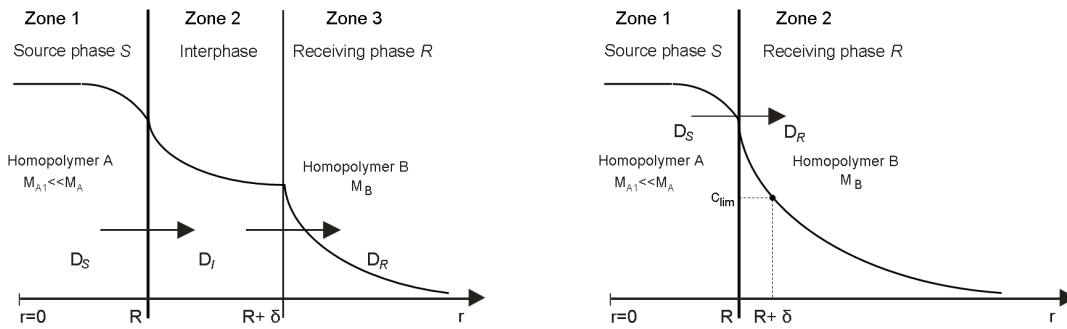


Figure 3.2: Left: Schematic representation of the three-region system. The lower molecular weight fraction of material A, M_{A_1} , is the phase that migrates into the interphase and, from that, into the matrix material B. Right: A simplification by using averaged concentrations.

which the interfacial tension becomes constant. Due to depletion of molecules with sufficient mobility to cross the interphase, the interfacial tension increases again. For

sufficiently long times, a steady state is eventually reached and the interfacial tension levels off.

For the ED system, all these steps are recognizable, especially at the higher temperatures, see Figure 3.1 (left). Increasing the temperature, increases the number of molecules with sufficient mobility to play this game. A larger number of molecules first accumulates (lower value of the minimum in the interfacial tension) and then crosses the interphase, yielding longer times to complete the process. Apparently for the ED system the larger number of molecules involved at higher temperatures wins from their higher individual velocities and diffusion rates at these higher temperatures. Different is the case of the SD system, Figure 3.1 (right), where the higher molecular weight drop phase leads to higher values of the interfacial tension. In this case the amount of interfacially active molecules is small compared to that in the ED system, (the molecular weight is higher and polydispersity smaller than that of the ED system). This all apparently leads to an overruling effect of temperature on the rate of the diffusion process involved, such that thickening (decrease in the interfacial tension) and eventually even thinning (increase in the interfacial tension) are no longer recorded at higher temperatures.

M_n (**dispersed phase**) > M_n (**continuous phase**)

Reversing the phases, the shorter molecules (that migrate from one phase into the other by crossing the interface) are present in the matrix fluid and not in the drop as before. In Figure 3.3 (left), the time evolution of the volume of the PDMS drop and the transient interfacial tension are shown at room temperature and at 12°C (i.e. the temperature where the viscosity ratio p equals one) for the rED system. The volume of the drop increases in the early stages of the measurements due to the mass transport and, while time proceeds, it levels off due to saturation of the drop confirming diffusion from matrix into the drop. At 12°C the process is slower than at 23°C due to the higher viscosity of the phases and, therefore, lower mobility also of the shorter chains. For the ED system we found in Section 3.3 diffusion yielding, in the early stages, an accumulation of short molecules in the interphase, followed by depletion of those molecules in the drop, making the interphase shrink to finally reach a plateau in interfacial tension. In the case of rED system the same asymmetry in molecular weight is present, and diffusion is as important. The difference now is that the diffusion takes place from the matrix into a drop, which is much smaller in size compared to the matrix. Consequently, as soon as diffusion starts, a thick interphase, thus a diffuse layer, is formed, reducing the interfacial tension, until saturation of the receiving phase occurs and diffusion stops; a constant value of the interfacial tension is reached. Figure 3.3 (right) shows drop volume and transient interfacial tension for the rSD system at room temperature and at 28°C (temperature of equal viscosities). As in the SD system, the number of molecules available for transport is small and an equilibrium in interfacial tension is again reached within 1000s.

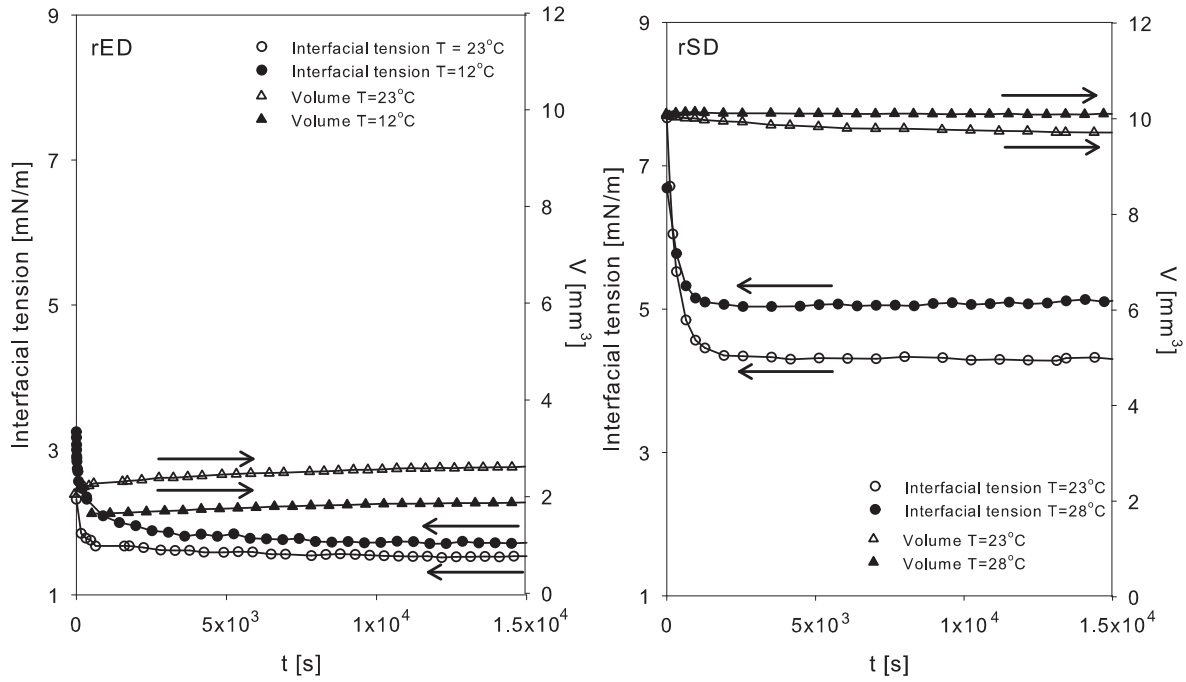


Figure 3.3: Transient interfacial tension (circle) and drop size evolution (triangle) for the rED system (left) and for the rSD system (right). Open symbols (\circ , Δ) for experiments at 23°C. Filled symbols (\bullet , \blacktriangle) for experiments at 12°C for the rED and 28°C for the rSD ($p = 1$).

3.4 Model predictions

Discrete model results

The transient interfacial tension, Figure 3.1, of both blends, where M_n of the dispersed phase is smaller than that of the continuous phase, and at all temperatures, can be fitted using the model proposed by Tufano et al. [1]:

$$\sigma(t) = \sigma_{\text{stat}} - ae^{(-t/\tau_1)} - be^{(-t/\tau_2)}. \quad (3.1)$$

The fits obtained are shown in Figure 3.4 and the resulting characteristic diffusion times, τ_1 and τ_2 for the inflow and outflow of the interphase, respectively, are listed in Table 3.4.

For the SD system, the data at 47°C and 80°C are not fitted because at these temperatures only the steady-state values of the interfacial tension could be measured. For both systems, the characteristic time of migration of molecules from the source phase into the interface, τ_1 , is shorter compared to the characteristic time of migration from

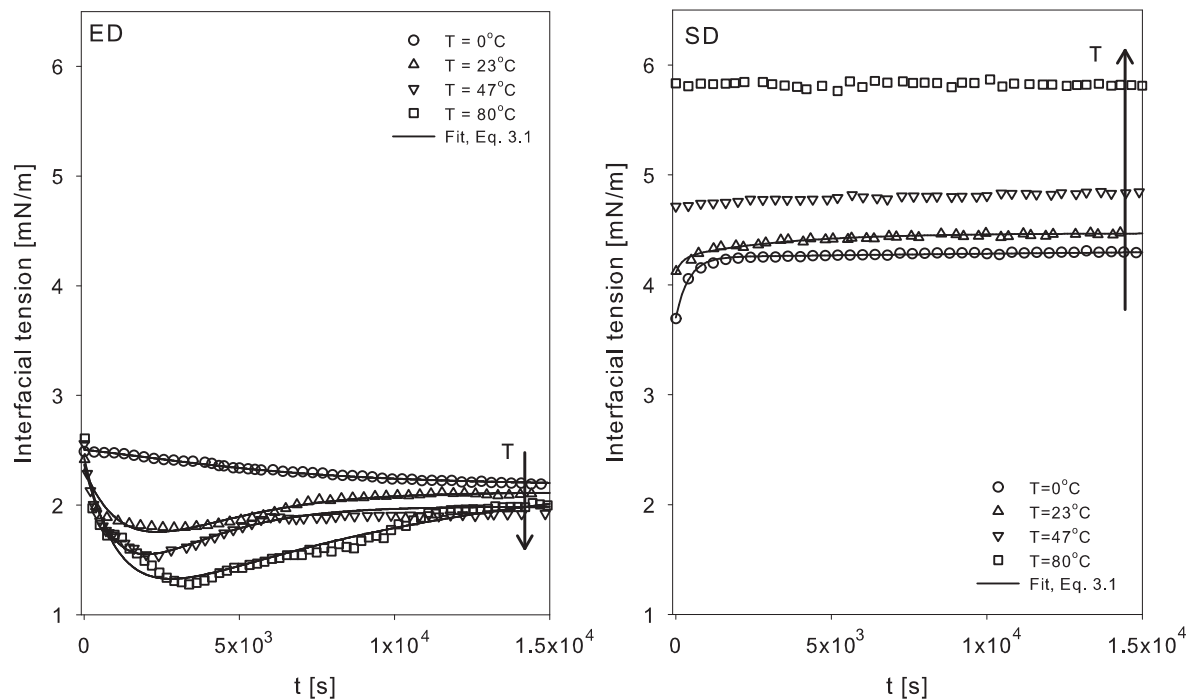


Figure 3.4: Experimental and fitted (Eq. 3.1) transient interfacial tension for the ED system (left) and for the SD system (right).

the interphase into the receiving phase, τ_2 , meaning that filling of the interphase occurs in the early stages of the process and only at longer times depletion starts. The characteristic times of filling of the interphase (τ_1) for the ED system are higher than those of the SD system, rationalized by the lower molecular weight and higher polydispersity of PB compared to PBD. Therefore a larger amount of molecules can migrate in the ED system compared to the SD system, and longer times are required to complete the diffusion process.

Table 3.4: Temperature dependence of the characteristic diffusion times calculated with the discrete model, for the ED (PB/PDMS) and SD (PBD/PDMS) systems.

T [°C]	PB635		PBD8000	
	τ_1 [s]	τ_2 [s]	τ_1 [s]	τ_2 [s]
0	3314	3894	415	33000
24	1970	2010	200	3254
47	1320	1989	-	-
80	1100	10000	-	-

Since saturation is not implemented in the model, a similar analysis of the reversed systems rED and rSD is not possible.

Kinetic model results

Shi et al. developed a kinetic model for the transient interfacial tension in polymer blends, [20], but since this model does not account for depletion, only data concerning the filling of the interphase can be considered, i.e. data from $t = 0$ s till the time at which the minimum in interfacial tension is reached in case of PB/PDMS, while only the emptying of the interphase is fitted in case of PBD/PDMS system. The results of the fit with Eq. 2.32 (Chapter 2) are shown in Figure 3.5 and the characteristic diffusion times found are listed in Table 3.5.

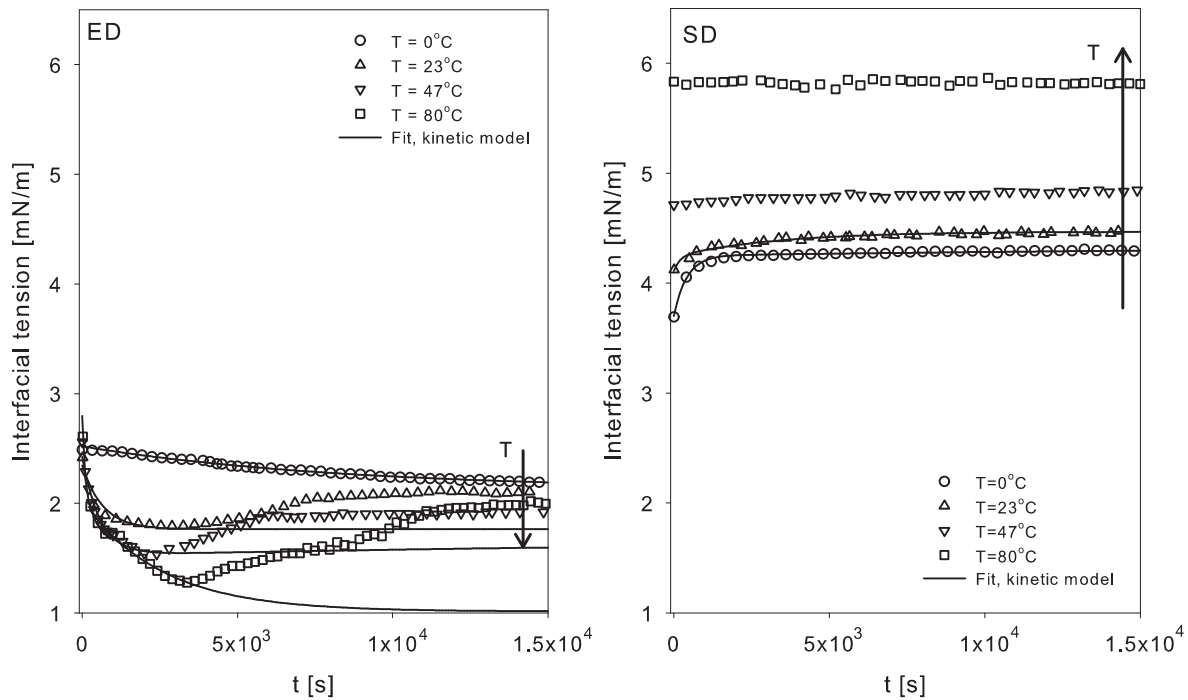


Figure 3.5: Experimental and fitted transient interfacial tension for the ED system (left) and for the SD system (right).

Given the characteristic diffusion times and viscosities at different temperatures (Table 3.5), the Shi model gives an expression to calculate activation energies for diffusion and for viscous flow, and a parameter, ω_s , which expresses to which extent the activation energies of the two phases (drop and matrix) contribute to that of diffusion, provided that the kinetic constants are temperature independent (see Eqs. 2.33 and 2.34 in Chapter 2). Calculations with our systems yield $E_\tau^{ED} = 42.7$, $E_\tau^{SD} = 21.3$, $E_\eta^{PB} = 54.3$, $E_\eta^{PBD} = 37.5$ and $E_\eta^{PDMS} = 14.9$, all in $[KJ/mol]$, from which we can then

derive $\omega_S^{ED} = 0.7$ and $\omega_S^{SD} = 0.28$ [-]. If $\omega_S = 1$, the diffusion process is dominated by the viscosity of the dispersed phase, while if $\omega_S = 0$ the viscosity of the matrix phase is dominating the diffusion process. Apparently the viscosity of the drop is dominating the diffusion process for the ED system, while the viscosity of the matrix becomes important for the SD system. It is important to notice that, in the case of the SD system, calculations of E_τ are based on two points only. Furthermore, ω_S is calculated assuming that the temperature does not affect the diffusion constants, K_1 and K_2 . To check this last assumption, with the values of ω_S obtained and knowing the viscosities of the phases, we calculated, at each temperature, the ratio K_1/K_2 , see Table 3.6. Clearly this assumption is incorrect. Finally, at the temperatures of 0°C and 23°C , where we have the fitted characteristic diffusion times for both blends, it is possible to calculate the value for the parameter d , that according to Shi et al. (see Eq. 24 in [20]), gives an indication of the mobility of the molecules at each temperature. The results obtained, shown in Table 3.6, are in the same order as those reported by Shi et al., who gave an average $d = 3.5$, and indicate a pronounced influence of chain length relative to the influence of viscosity on the diffusion times. We can, with some care, conclude that despite the number of approximations necessary to reach this point of analysis, the effect of chain lengths on the mutual diffusion process indeed overrules viscosity influences.

Table 3.5: Temperature dependence of the characteristic diffusion times, calculated with the kinetic model of Shi et al. [20], and measured viscosities of the phases.

T [$^\circ\text{C}$]	S=PB 635		S=PBD 8000		R=PDMS 60K
	τ_S [s]	η_S [Pa · s]	τ_S [s]	η_S [Pa · s]	η_R [Pa · s]
0	8500	26.8	415	59.6	18.3
23	661	3.7	200	13.6	10.9
47	570	0.7	-	4.5	6.7
80	85	0.13	-	1.5	4.2

Table 3.6: Temperature dependence of the ratio of the rate constants for diffusion and values of the d parameter calculated with the kinetic model of Shi et al. [20].

T [$^\circ\text{C}$]	ED	SD	d
	K_2/K_1	K_2/K_1	
0	0.39	0.75	4.85
23	1.25	1.95	2.66
47	4.18	3.72	-
80	14.7	7.19	-

Here the rED and rSD systems will not be analyzed because it was already reported in [26] that the correlation used in [20] to calculate the value of d fails when the matrix material is changed.

3.5 Influence of a transient interfacial tension on morphology development in flow

M_n (dispersed phase) < M_n (continuous phase)

SALS experiments and OM measurements are carried out for 1% weight concentrated blends at temperatures of 23°C (where the viscosity ratio $p = \eta_{drop}/\eta_{matrix}$ is 0.34 for the ED blend and 1.24 for the SD blend), and 12°C for the ED system and 28°C for the SD system (both $p = 1$). The evolution of the average drop radii obtained from SALS are in good agreement with the values measured by optical microscopy. Figure 3.6 (left) shows the transient interfacial tension and the average drop radii for the freshly made ED system. The morphology follows the same trend as the interfacial tension. In the first 2000s, the average drop radii decrease, and, as time proceeds, they increase again leveling off in the late stage of the measurement. These results are explained taking into account two parallel phenomena: diffusion, which in these systems goes from drop into the continuous phase and reduces the drop radii due to mass transport, and coalescence, which leads to increasing radii. In the first 2000s of the experiment, the diffusion is pronounced and therefore, despite coalescence, a reduction in the drop size is observed. As time proceeds, diffusion slows down and coalescence takes over, resulting in increasing radii till a plateau value is reached. To support this explanation, the experiments were repeated with an old blend, prepared 48h before, where diffusion is exhausted. The results are plotted in Figure 3.6 (right) and now the morphology development is clearly governed by coalescence only in all stages of the experiment.

The influence of concentration is investigated by performing experiments, using the same operating conditions, for a fresh 5 wt% concentrated ED blend (also in Figure 3.6 right). The average radii only increase in time and the explanation is that the coalescence rate increases with increasing drop concentration due to the higher number of collisions between drops. The experiments for $T=12^\circ\text{C}$ ($p = 1$) also show the same trend as those at room temperature, but the minimum in drop size is reached faster, see Figure 3.7, due to the lower fraction of short molecules that, at lower temperature, are able to cross the interface, causing the diffusion process to be exhausted faster.

Figure 3.8 shows the same data for the SD blend at room temperature and at $T=28^\circ\text{C}$ ($p = 1$). The interfacial tension reaches its plateau fast, and, therefore, as expected, no influence of mass transport is detected in the radius development.

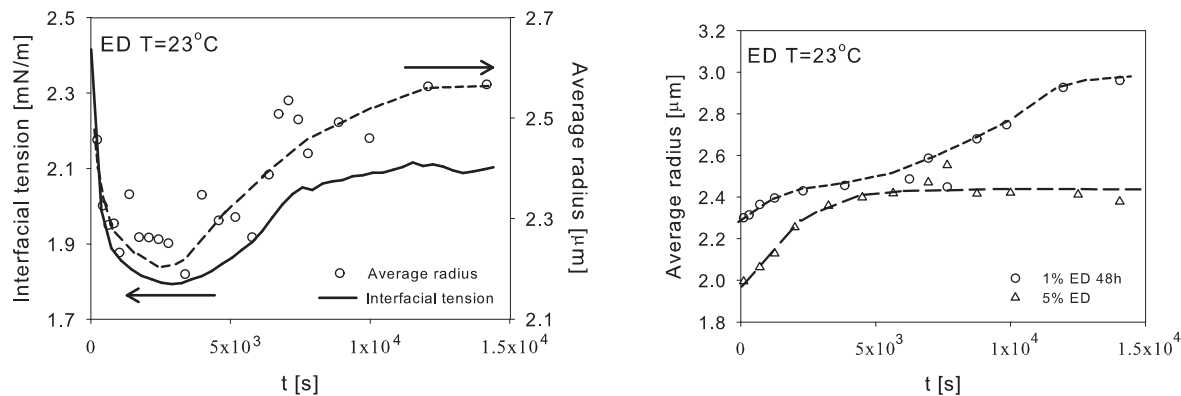


Figure 3.6: Transient interfacial tension (line) and drop size evolution (○) obtained via SALS and OM in-situ techniques for the ED system, for a 1% fresh blend (left) where the interfacial tension is transient. Drop size evolution for a 1% old ED blend (○) and for a higher concentrated (5%) fresh ED system (△) (right). Dashed lines to guide the eye.

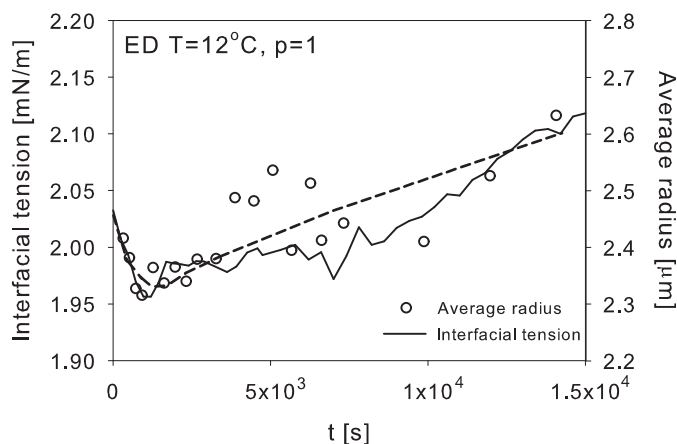


Figure 3.7: As Figure 3.6 (left), for T=12°C.

M_n (dispersed phase) > M_n (continuous phase)

To investigate the effect of phases inversion on flow-induced coalescence, 1 wt% rED and rSD blends are investigated applying the same flow conditions. Figure 3.9 shows the results at room temperature for both blends, T=12°C for the rED, and T=28°C for the rSD ($p = 1$). Although the same differences in molecular weight across the interface exist as in Section 3.3 and 3.5, and in accordance with the conclusion presented in Section 3.3, no influence of a transient interfacial tension on structure development is detected, most probably due to the limited size of the drops that limits the total mass transport from matrix into the dispersed phase causing diffusion to be

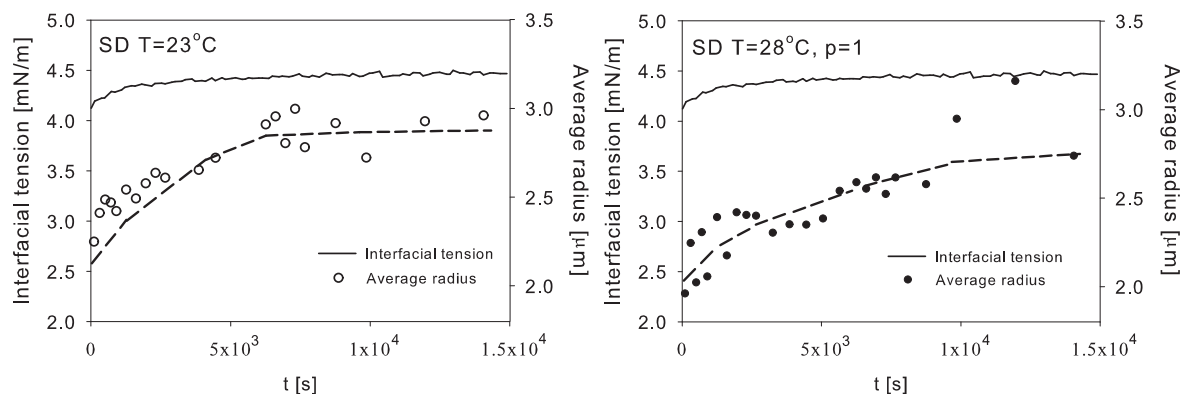


Figure 3.8: Transient interfacial tension (line) and drop size evolution (circle) obtained via SALS and OM in-situ techniques for the SD system, at room temperature (○) (left) and at $T=28^{\circ}\text{C}$ (●) (right). Dashed lines to guide the eye.

exhausted faster.

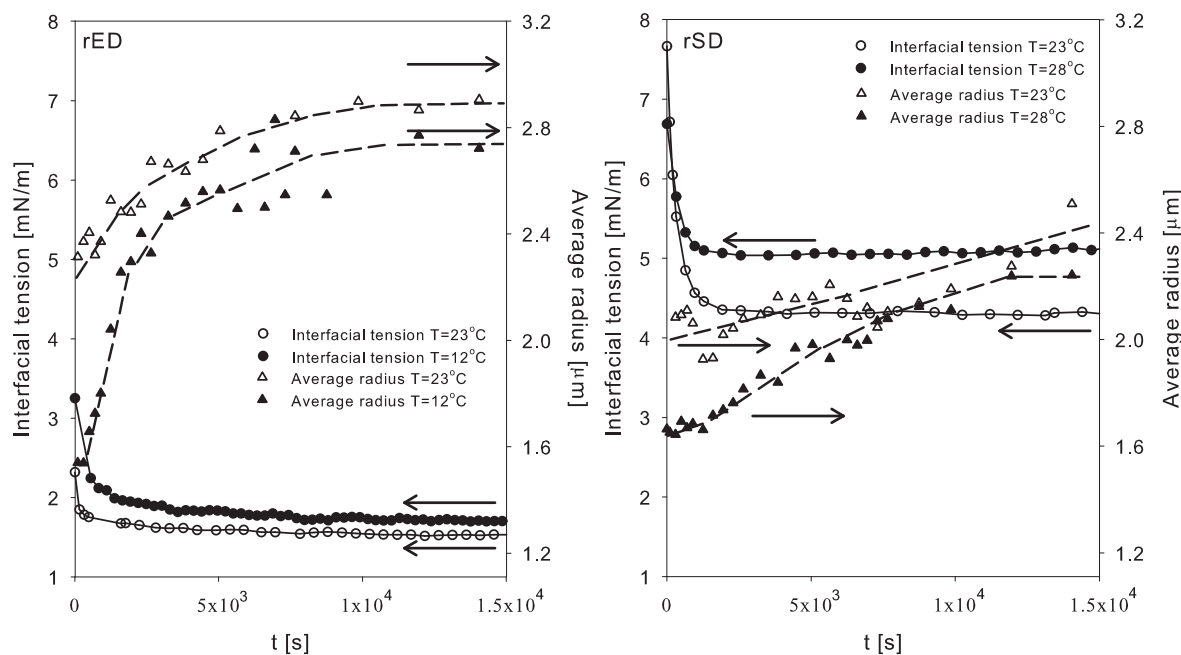


Figure 3.9: Transient interfacial tension (circle) and drop size evolution (triangle) obtained via SALS and OM in-situ techniques for the rED system (left) and for the rSD system (right). Open symbols (○, Δ) for experiments at 23°C . Filled symbols (●, ▲) for experiments at $T=12^{\circ}\text{C}$ for the rED, and $T=28^{\circ}\text{C}$ for the rSD ($p = 1$). Dashed lines to guide the eye.

3.6 Comparing experimental results with sharp-interface drainage models

Coalescence under transient interfacial tension was the topic of Section 3.5 and in the process a number of sequences can be distinguished: (1) collision of drops; (2) drainage of the film trapped between the drops; (3) rupture of the film and finally (4) drop coalescence. The drainage rate dh/dt is determined by the (Stokes drag dependent) contact force that acts during the interaction time of the drops and the mobility of the interfaces. At a (local) critical value of the film thickness, h_{cr} , Van der Waals forces cause the film to rupture. Coalescence occurs if the contact time between drops, that is of the order of $1/\dot{\gamma}$ in a shear flow at shear rate $\dot{\gamma}$, is longer than the drainage time required to reach this critical film thickness h_{cr} , else the drops tumble and separate. The mobility of the interface greatly determines the thinning rate dh/dt , changing from immobile interfaces with pure pressure flow, via partially mobile interfaces, to fully mobile interfaces (usually only found in gas bubbles dispersed in a liquid) where drainage is caused by drag flow. By equating contact time to drainage time, expressions for the critical drop size above which no coalescence takes place, can be obtained for the three distinguished situations of immobile, partially mobile and fully mobile interfaces [23,24]:

Immobile interfaces ²

$$R_{IM} = \left(\frac{32}{9}\right)^{1/4} \left(\frac{h_{cr}\sigma}{\eta_m\dot{\gamma}}\right)^{1/2}, \quad (3.2)$$

Partially mobile interfaces

$$R_{PM} = \left(\frac{4}{\sqrt{3}} \frac{h_{cr}}{p}\right)^{2/5} \cdot \left(\frac{\sigma}{\eta_m\dot{\gamma}}\right)^{3/5}, \quad (3.3)$$

Fully mobile interfaces

$$R_{FM} \ln\left(\frac{R_{FM}}{h_{cr}}\right) = \frac{2}{3} \cdot \frac{\sigma}{\eta_m\dot{\gamma}}, \quad (3.4)$$

where η_m is the viscosity of the continuous phase, p is the viscosity ratio ($p=\eta_d/\eta_m$, with η_d the viscosity of the dispersed phase) and $\dot{\gamma}$ is the shear rate. The main difficulty at this point is to evaluate h_{cr} , and Chesters [23] proposed:

²Originally, an expression for the drainage time was proposed when considering a single drop of radius R coalescing on a flat layer [23]. When considering two drops, a factor 4 is needed to have the correct expression for the contact time and this explains the discrepancy between the factor 32 reported in Eq. 3.2 and the factor 8, Eq. 23a, reported in [24].

$$h_{cr} \approx \left(\frac{AR}{8\pi\sigma} \right)^{1/3}, \quad (3.5)$$

with A the Hamaker constant [$O(10^{-20})J$], σ the interfacial tension and R the drop radius. In [27] a different expression for the h_{cr} is used, valid when diffusion is from the matrix into the drop:

$$h_{cr} \approx \left(\frac{K_1 AR_{eq}}{8\pi\sigma \left(1 + \frac{R_{eq}\Delta\sigma}{2K_2\sigma\sqrt{DT}} \right)} \right)^{1/3}, \quad (3.6)$$

where K_1 and K_2 are constants of order unity and $\Delta\sigma$ is the interfacial tension difference between film and outer region. However, $\Delta\sigma$ and a value for the molecular diffusivity are unknown, therefore we will limit the discussion to the ED and SD blends, leaving out the reversed systems, rED and rSD. Two different approaches to calculate h_{cr} are followed. In the first case the radius R is chosen to be equal to the initial experimental radius while σ is assumed to be equal to the steady-state value of the interfacial tension. In the second case, for each blend, the minimum and the maximum of the experimental radii and interfacial tensions are used to calculate a minimum and a maximum critical film thickness according to Eq. 3.5. With these two values of h_{cr} , the transient radius predicted by the immobile interface theory is calculated in time using the transient interfacial tension in Eq. 3.2. The critical film thickness and the radii calculated with Eqs. 3.2- 3.5 respectively for the direct systems are shown in Table 3.7.

Table 3.7: Critical film thickness and radii calculated with the immobile, partially mobile, and fully mobile interface models.

	ED		SD	
	12°C	23°C	23°C	28°C
h_{cr} [nm]	3.56	3.62	2.77	2.65
R_{IM} [μm]	2.34	2.63	3.18	3.62
R_{PM} [μm]	8.18	14.42	11.32	14.66
R_{FM} [μm]	56	68	120	159

The radii calculated with the fully-mobile interface model are, in all cases, at least one order of magnitude larger than the experimental values and it is therefore not suited to describe such systems as already reported by Minale et al. [28]. The partially-mobile interface model also gives radii larger than the experimental values, therefore,

we will not consider these two cases any further. In [29] it was reported that, for the ED system, film drainage is approximately two orders of magnitude faster compared to the partially mobile model predictions. This high drainage rate was attributed to a Marangoni flow acting in the same direction as film drainage. Reported time scales are in the order of 100s. It is now worthwhile to consider the effect of a transient interfacial tension $\sigma(t)$, since it apparently acts instantaneously given the substantial differences in time scales of drainage and morphology evolution, on the critical film thickness and on the evolution of drop radii. To do that, the immobile-interface assumption is applied using the measured transient interfacial tension values, calculating drop radii using a minimum and maximum value of the critical film thickness h_{cr} (Eq. 3.2 now contains $\sigma(t)$). Results using the steady-state σ (full lines) and the transient $\sigma(t)$ (dashed lines) are shown in Fig. 3.10 for the ED system and in Fig. 3.11 for the SD system.

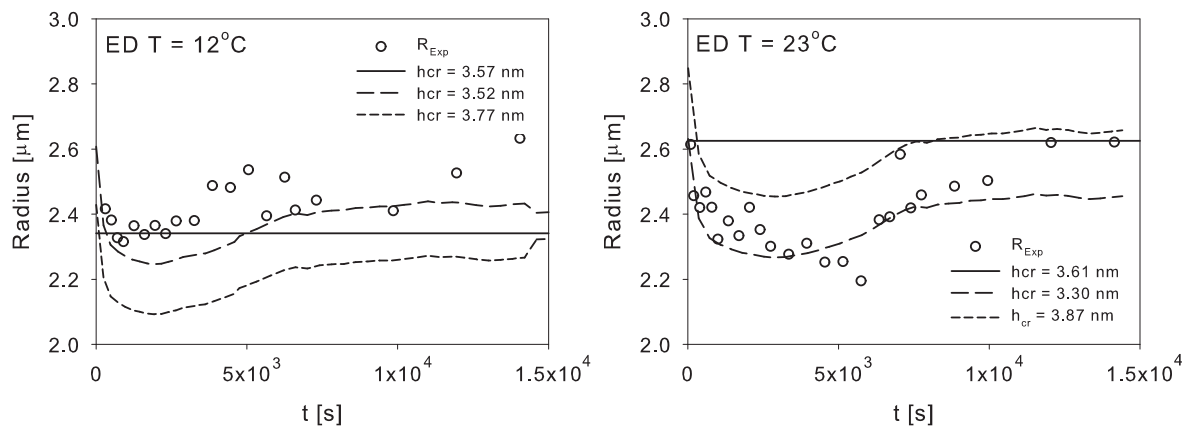


Figure 3.10: Experimental and calculated morphology evolution for the ED system.

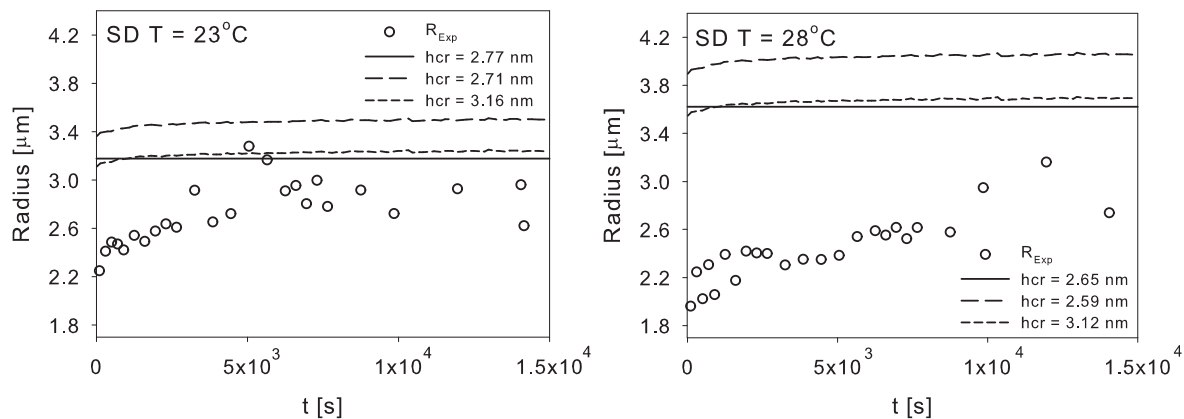


Figure 3.11: Experimental and calculated morphology evolution for the SD system.

The critical film thicknesses are in good agreement with the typical value of h_{cr} for micron-sized polymer droplets reported by Chesters [23], and Janssen and Meijer [24]. Other values on the critical film thicknesses found in literature range between $1 - 10^3 \text{ nm}$ [10, 14, 28, 30], but most of the values are not calculated from a theoretical model, like in this work, but considered as an adjustable parameter, used to fit results. In this way, h_{cr} loses its physical meaning and it becomes a concentration dependent parameter. In our case, blends are very diluted and the low concentration does not substantially change the value of h_{cr} when used as a fitting parameter. Therefore, we refrain from using a fitting procedure here.

For the ED system, the immobile-interface theory gives a good prediction of morphology development when the transient interfacial tension is used. For both temperatures, the experimental radii reach their maximum value predicted by the theory above which coalescence does not occur anymore. The transient interfacial tension $\sigma(t)$ seemingly acts instantaneous on the average radii of the blends. When the SD system is considered, at both temperatures the model predictions are above the experimental radii, implying that coalescence still can occur. The ED system is very diffusive and coalesces faster than the SD system. Finally, all coalescence models are based on sharp interfaces, while we are dealing with diffuse interfaces. An analysis of model predictions using DIM, diffuse interface modeling [31–33], is outside the scope of this chapter and will be dealt, for two-drop systems, in Chapter 4.

3.7 Conclusions

The binary blends investigated can not be considered fully immiscible. For the ED, extreme diffusive, blend system, the transient interfacial tension starts to decrease immediately after the formation of a new interface. This reduction is attributed to diffusion of the fraction of shorter molecules present in the drop phase that migrates and accumulates into the interphase that thickens. Simultaneously, the active molecules start to diffuse from the interphase into the receiving phase, which has relative to the drop an infinite volume. As time proceeds, depletion occurs (the amount of molecules that can diffuse from the drop is finite) and the interfacial tension increases again. Increasing the temperature causes a larger number of molecules to cross the interphase, thus interestingly increasing the time scale of mass transport and increasing the concentration of short molecules into the interphase. The case of the SD, slightly-diffusive, blend system, with lower polydispersity, mixed into the same matrix, shows a time window for the filling of the interphase which is in the order of magnitude of the time required to reach a Laplacian shaped drop. Therefore we can not capture the initial effect of diffusion on the interfacial tension, corresponding to the filling of the interphase. By reversing the phases, changes in the interfacial tension are limited due to the fast saturation of the drops.

To interpret the results and find characteristic diffusion times for the systems investigated, a three-zone model, proposed by Tufano et al. [1] is used. The model could be accurately fitted to the experimental data and resulting time constants show that

first filling of the interphase occurs, followed by depletion. Increasing the temperature lowers the characteristic time for diffusion. The kinetic model proposed in Shi et al. [20], although limited due to some serious assumptions, helps in interpreting part of the data in a different perspective. We could conclude that the data illustrate that the effects of chain length on diffusion overrules the effects of viscosity on diffusion. Changes in the interfacial tension affect the morphology development, at least for low concentrated blend systems. A qualitative analysis using drainage models based on sharp interfaces shows that the interfaces in our systems are immobile. We demonstrated that mutual solubility in polymer blends caused by polydispersity is present and that molecular weight, difference in molecular weight across the interface, polydispersity and temperature (influencing mobility and viscosity of both phases) result in a transient interfacial tension that affects morphology evolution.

References

- [1] Tufano, C., Peters, G.W.M., Anderson, P.D., Meijer, H.E.H. (2008). Transient interfacial tension of partially-miscible polymers. *J. Coll. Int. Sci.*, **Submitted**.
- [2] Elmendorp, J.J. and van der Vegt, A. (1986). A study on polymer blending micro-rheology: Part iv. the influence of coalescence on blend morphology origination. *Polym. Eng. Sci.*, **26**, 1332–1338.
- [3] Fortelny, I. and Kovar, J. (1988). Theory of coalescence in immiscible polymer blends. *Polym. Compos.*, **9**, 119–124.
- [4] Vinckier, I., Moldenaers, P., Mewis, J. (1996). Relationship between rheology and morphology of model blends in steady shear flow. *J. Rheol.*, **40**, 613–631.
- [5] Rusu, D. and Peuvrel-Disdier, E. (1999). In-situ characterization by small angle light scattering of the shear-induced coalescence mechanisms in immiscible polymer blends. *J. Rheol.*, **43**, 1391–1409.
- [6] Lyu, S.P., Bates, F.S., Macosko, C.W. (2000). Modeling of coalescence in polymer blends. *AIChE J.*, **48**, 7–14.
- [7] Verdier, C. and Brizard, M. (2002). Understanding droplet coalescence and its use to estimate interfacial tension. *Rheol. Acta*, **43**, 514–523.
- [8] Olabisi, O., Robeson, L.M., Shaw, M.T. (1979). *Polymer-polymer miscibility*. Academic London.
- [9] Jones, R.A.L. and Richards, R.W. (1999). *Polymer at Surfaces and Interfaces*. Cambridge University Press.
- [10] Minale, M., Moldenaers, P., Mewis, J. (1997). Effect of shear history on the morphology of immiscible polymer blends. *Macromolecules*, **30**, 5470–5475.
- [11] Grizzuti, N. and Bifulco, O. (1997). Effects of coalescence and breakup on the steady-state morphology of an immiscible polymer blend in shear flow. *Rheol. Acta*, **36**, 406–415.
- [12] Yamane, H., Takahashi, M., Hayashi, R., Okamoto, K., Kashihara, H., Masuda, T. (1998). Observation of deformation and recovery of poly(isobutylene) droplet

- in a poly(isobutylene)/ poly(dimethyl siloxane) blend after application of step shear strain. *J. Rheol.*, **42**, 567–580.
- [13] Tsakalos, V.T., Navard, P., Peuvrel-Disdier, E. (1998). Deformation and breakup mechanisms of single drops during shear. *J. Rheol.*, **42**, 1403–1417.
- [14] Vinckier, I., Moldenaers, P., Terracciano, A.M., Grizzuti, N. (1998). Droplet size evolution during coalescence in semiconcentrated model blends. *AIChE J.*, **44**, 951–958.
- [15] LeGrand, D.G. and Gains, G.L. (1975). Immiscibility and interfacial tension between polymer liquids: Dependence on molecular weight. *J. Coll. Int. Sci.*, **50**, 272–279.
- [16] Grace, H.P. (1982). Dispersion phenomena in high viscosity immiscible fluid systems and application of static mixers as dispersion devices in such systems. *Chem. Eng. Commun.*, **14**, 225–277.
- [17] Varanasi, P.P., Ryan, M.E., Stroeve, P. (1994). Experimental study on the breakup of model viscoelastic drops in uniform shear flow. *Ind. Eng. Chem. Res.*, **33**, 1858–1866.
- [18] Ferrari, M., Liggieri, L., Ravera, F., Amodio, C., Miller, R. (1997). Adsorption kinetics of alkylphosphine oxides at water/hexane interface. *J. Coll. Int. Sci.*, **186**, 40–45.
- [19] Xing, P., Bousmina, M., Rodrigue, D., Kamal, M.R. (2000). Critical experimental comparison between five techniques for the determination of interfacial tension in polymer blends: Model system of polystyrene/polyamide-6. *Macromolecules*, **33**, 8020–8034.
- [20] Shi, T., Ziegler, V.E., Welge, I.C., An, L., Wolf, B.A. (2004). Evolution of the interfacial tension between polydisperse “immiscible” polymers in the absence and in the presence of a compatibilizer. *Macromolecules*, **37**, 1591–1599.
- [21] Demarquette, N.R. and Kamal, M.R. (1994). Interfacial tension in polymer melts. I: An improved pendant drop apparatus. *Polym. Eng. Sci.*, **34**, 1823–1833.
- [22] Stammer, E. and Wolf, B.A. (1998). Effect of random copolymer additives on the interfacial tension between incompatible polymers. *Macromol. Rapid Commun.*, **19**, 123–126.
- [23] Chesters, A.K. (1991). The modelling of coalescence processes in fluid-liquid dispersions. *Trans IChemE*, **69A**, 259–281.
- [24] Janssen, J.M.H. and Meijer, H.E.H. (1995). Dynamics of liquid-liquid mixing: A two zone model. *Polym. Eng. Sci.*, **35**, 1766–1780.
- [25] Takahashi, Y., Kurashima, N., Noda, I. (1994). Experimental tests of the scaling relation for textured materials in mixtures of two immiscible fluids. *J. Rheol.*, **38**, 699–712.
- [26] Peters, G.W.M., Zdravkov, A., Meijer, H.E.H. (2005). Transient interfacial tension and dilatational rheology of diffuse polymer-polymer interfaces. *J. Chem. Phys.*, **122**, 104901–1–10.
- [27] Saboni, A., Alexandrova, S., Gourdon, C., Chesters, A.K. (2002). Interdrop coalescence with mass transfer: comparison of the approximate drainage models with numerical results. *Chem. Eng. J.*, **88**, 127–139.

-
- [28] Minale, M., Mewis, J., Moldenaers, P. (1998). Study of the morphological hysteresis in immiscible polymer blends. *AIChE J.*, **44**, 943–950.
- [29] Zdravkov, A., Peters, G.W.M., Meijer, H.E.H. (2006). Film drainage and interfacial instabilities in polymeric systems with diffuse interfaces. *J. Coll. Int. Sci.*, **296**, 86–94.
- [30] Al-Mulla, A. and Gupta, R.K. (2000). Droplet coalescence in the shear flow of model emulsions. *Rheol. Acta*, **39**, 20–25.
- [31] Keestra, B.J., Van Puyvelde, P., Anderson, P.D., Meijer, H.E.H. (2003). Diffuse interface modeling of the morphology and rheology of immiscible polymer blends. *Phys. Fluids*, **15(9)**, 2567–2575.
- [32] Khatavkar, V.V., Anderson, P.D., Meijer, H.E.H. (2007). Capillary spreading of a droplet in the partially wetting regime using a diffuse-interface model. *J. Fluid Mech.*, **572**, 367–387.
- [33] Khatavkar, V.V., Anderson, P.D., Duineveld, P.C., Meijer, H.E.H. (2007). Diffuse-interface modelling of droplet impact. *J. Fluid Mech.*, **581**, 97–127.

CHAPTER FOUR

Effects of partial miscibility on drop-wall and drop-drop interactions

The effects of mutual diffusion between two polymeric phases on the transient interfacial tension, the interaction of a single drop with a nearby wall and the interaction and coalescence of two nearby drops in quiescent conditions, are investigated for two *partially-miscible* systems, differing in the miscibility of the components. Transient interfacial tension measurements show that the system polybutene (PB)/polydimethylsiloxane (PDMS) is *highly-diffusive*. For this system, a reduction in interfacial tension is followed by an increase, while in the last stage a plateau value is reached. These experimental findings are interpreted in terms of migration of low-molecular weight species from the drop into the interphase and, from there, into the matrix, influencing the interphase thickness and, consequently, the interfacial tension. For the less miscible polybutadiene (PBD)/PDMS system limited changes are found and attributed to the higher molecular weight and lower polydispersity of the drop phase.

Drop-drop interaction is studied in quiescent conditions in a Couette geometry. Drops of the *highly-diffusive* PB/PDMS system, with radii ranging from $90\ \mu\text{m}$ up to $350\ \mu\text{m}$, are placed at distances closer than their equivalent radius. They appear to attract each other and coalesce with a rate that, in the last stage of the coalescence process (order of 100s), is the same for all drop combinations. For the slightly-diffusive PBD/PDMS system no coalescence occurs and, in contrast, even repulsion between the drops is observed. These phenomena are qualitatively explained by considering that for partially-miscible polymers, overlap of diffuse layers formed at the drop surface can occur when two drops are placed close enough to each other, yielding concentration gradients of the diffusing low-molecular weight species (LMW), i.e. gradients in the interfacial tension on the drop surface. These gradients, when strong enough, yield Marangoni stresses that induce convection flows from zones with lower to zones with higher interfacial tension, which, in turn, causes attraction or repulsion.

To further check whether tangential Marangoni stresses are strong enough to displace a drop in quiescent conditions, single drops of PB and PBD are placed in a PDMS matrix in the vicinity of a wall to create concentration gradients in the diffusing LMW species along the drop surface. A lateral drop motion towards the wall is observed for the highly-diffusive PB/PDMS system only, while, due to the limited amount of LMW species, PBD drops did not move.

The diffuse-interface model is considered as a good candidate to capture these phenomena described since this model couples the mutual diffusion of LMW, drop, and matrix, with hydrodynamic forces, i.e. diffusion-induced macroscopic motion. This model provides intrinsically the interface properties like thickness and interfacial tension, while this was not the case for the models used in [1], see also Chapter 2, which did not include hydrodynamic interactions. We have used numerical simulations, based on this model to investigate if the experimental results could be qualitatively reproduced and confirm our explanations.

4.1 Introduction

Interfacial properties are important in multi-phase systems because they affect break-up and coalescence events during the processing of blends, defining the transient and steady morphologies, which are the result from the dynamic equilibrium between these phenomena. Usually polymers are considered fully immiscible (e.g. [2–8]); however, cases exist where diffusion of low-molecular weight (LMW) species across an interface occurs in the experimental time scale [1, 9–11], and the mass transfer between the two phases, although limited, creates a gradient in the concentration of migrating molecules, changing the interface properties, thus affecting drop deformation dynamics and film drainage between two approaching drops [12, 13]. Hu et al. [14] reported that a reduction of 3% in the interfacial tension, reduces the critical capillary number for coalescence by a factor 6. Mutual miscibility can cause gradients in interfacial tension, the LMW species accumulated at the interface indeed behave as surfactants. To balance this gradient, tangential stresses appear at the drop interface influencing film drainage, usually referred to as Marangoni flow [15, 16]. Depending on the direction of the mass transfer along the drop surface, gradients in the interfacial tension differ in sign and can accelerate or decelerate film drainage, promoting or suppressing coalescence, respectively.

Mackey and Mason [17] showed that the rate of thinning of the film separating two approaching drops increases when diffusion of a third component (mutual solvent) occurs from the drop phase into the matrix and decreases in the opposite case. Pu and Chen [18, 19] investigated jump-like coalescence between two captive drops of oil in water and in absence of external forces, showing that the presence of a third diffusing component enhances coalescence, while the binary coalescence time is retarded by the addition of a surfactant. They proposed an equation to express the binary coalescence time as a function of a so-called thin-film coefficient, which reflects the thin-film properties: the molecular properties of the inner phase, the

interface and the continuous phase, thus the interfacial concentration gradients of surfactant, the viscosity of continuous phase, and the influence of steric hindrance and temperature on interdiffusion. By interpreting the experimental data by using this expression, they found support that the larger the difference in drop size, the shorter the coalescence time. Velvet et al. [20] found thick and very stable aqueous films between oil phases when a surfactant is diffusing from the interface towards the film and attributed the film stability to the aggregation of surfactant micelles in the film area, generating an osmotic pressure difference between the film interior and the aqueous meniscus. Film drainage between two captive PEO-water drops in a PDMS matrix is found to be very sensitive to an increase in film radius, Zdravkov et al. [21], who attributed the effect to a depletion of PEO molecules adsorbed on the drop interfaces into the film. The same authors [22] carried out further investigations on the effects of mutual diffusion on film drainage showing that for highly-diffusive systems, the drainage rate is 100 times faster than predicted by existing theoretical models, while, when a slightly-diffusive system is considered, good agreement with the partially mobile model prediction is found. The results are explained in terms of Marangoni convection flows, which promote film drainage when overlap of the diffusion layers formed around the drop surface occurs, and slow it down in the opposite case.

Extensive numerical studies have been carried out to describe the interface between two or more liquids, defined as a space in which a rapid but smooth transition of physical quantities between the bulk fluid values occurs. Equilibrium thermodynamics of interfaces was developed by Poisson [23], Maxwell [24] and Gibbs [25]. Rayleigh [26] and Van der Waals [27] developed a model to describe a diffuse-interface, based on gradient theories that predicts the interface thickness, thus an interphase, which tends to infinite as the critical temperature is approached. A review on the diffuse-interface methods in fluid mechanics was given by Anderson et al. [28].

In this work a *highly-diffusive* system, polybutene (PB) in polydimethylsiloxane (PDMS), and a *slightly-diffusive* system, polybutadiene (PBD) in PDMS, are used to investigate the effects of partial miscibility between the two polymeric phases on the transient interfacial tension of the system, on the lateral motion of a single drop and on the coalescence of two drops in quiescent conditions. Details on the experimental approach of the transient interfacial tension are given in Tufano et al. [11].

A pendent drop apparatus is used to measure interfacial tension, and the results are compared to the prediction of the diffuse-interface model (DIM) modified to account for three components, the drop phase, the LMW migrating molecules and the matrix phase.

Drop coalescence under quiescent conditions is experimentally investigated for different drop radii and distances between them. The results are interpreted in terms of diffusivity of LMW component, drop and matrix, which induce gradients in interfacial tension on the drop surface.

In addition, we show that similar phenomena can be observed for a drop close to a wall, i.e. drop-wall interaction.

4.2 Materials and methods

Materials

The polymers used as dispersed phase are polybutene (PB, Indopol H-25, BP Chemicals, UK) and polybutadiene (PBD, Ricon 134, Sartomer). The continuous phase is polydimethylsiloxane (PDMS, UCT). The materials are liquid and transparent at room temperature. The number average molecular weights M_n and the polydispersities M_w/M_n of the materials are given in Table 4.1. Densities measured with a digital density meter (DMA 5000, Anton Paar) and steady interfacial tension measured with a pendent drop apparatus, at room temperature, are also listed in Table 4.1. Zero shear viscosities are measured using a rotational rheometer (Rheometrics, ARES) equipped with a parallel-plate geometry, applying steady shear. All polymers exhibit Newtonian behavior in the range of shear rates applied ($0.01\text{-}10\text{ s}^{-1}$) and the viscosities at room temperature are added to Table 4.1. While measuring the interfacial tension, also the changes in the droplet radii are measured. Variations of the drop radius in four hours (ΔR_{4h}) are used as a measure for the blend diffusivity, see the last column in Table 4.1. Assuming that the thickness of the diffusion layer around the drop is proportional to ΔR_{4h} , the system PB/PDMS is more diffusive compared to the system PBD/PDMS and will have a thick diffusive layer, while the PBD/PDMS system will have a thin diffuse layer.

Table 4.1: Selected model components.

Sample	M_n^1 [g/mol]	M_w/M_n^1	ρ [g/cm ³]	σ [mN/m]	η [Pa · s]	R_0 [mm]	ΔR_{4h} [μm]
PB/PDMS	635/62700	2.1/1.8	0.874/0.975	2.2	3.7/10.9	1.13	209
PBD/PDMS	8000/62700	1.1/1.8	0.891/0.975	4.2	13.6/10.9	1.22	6

Experimental methods

Coalescence experiments are performed in a home-made Couette device, ensuring simple shear flow between the concentric cylinders. The diameters of the inner and

¹Provided by supplier.

outer cylinders are $25 \cdot 10^{-3} \text{ m}$ and $75 \cdot 10^{-3} \text{ m}$, respectively. The cylinders are actuated by two DC motors (Maxon) that can rotate independently and in both directions. The motors are controlled by a TUEDAC, an in-house developed digital \rightleftharpoons analog converter, and two amplifiers are used to strengthen the signals. The real time control of the motors is guaranteed by home made software. Images are acquired via a 45° oriented polished surface placed below the cylinders. A stereo-microscope (Olympus) and a digital camera serve the acquisition of images, which are further analyzed. In all experiments, a single droplet is introduced in the stagnation plane, obtained by concentric counter-rotating conditions, using a syringe, and the critical capillary number is reached to break the droplet in two or more daughter droplets. The angular velocities of the two cylinders are controlled such that the droplet position is stationary and images can be acquired during the whole process. When droplets of the required sizes are created, the flow is reversed, bringing the droplets at the required distance. The reversed flow is chosen to be very slow to avoid any a priori drop deformation. Once the flow is stopped, quiescent coalescence is investigated.

To further investigate drop motion, induced by gradients in interfacial tension, a cubic cell with flat glass surfaces is used. Drops of PB and PBD are placed in the cell filled with the PDMS, in the proximity of the wall. Images are acquired from the bottom of the cell following the same procedure described for the Couette device. In order to exclude wetting effects on the possible lateral migration of the drops, the same experiments are carried out in a cubic cell with polytetrafluorethylene (PTFE, Teflon) side walls.

4.3 Diffuse-interface model

The diffuse-interface model allows us to account for interfaces with non-zero thickness. It is based on the van der Waals approach to the interface problem [27] and developed by Cahn and Hilliard [29]. The interface thickness is not numerically prescribed, but follows from the governing equations that describe the thermodynamic and hydrodynamic forces in the interface. The main points of this theory, and the coupling between thermodynamics and hydrodynamics are summarized by Anderson et al. [28]. Here the diffuse-interface model is applied to describe a three-phase systems, LMW, drop, and matrix.

Governing equations

For a chemical inert N -component system, the mass balance can be written as:

$$\frac{\partial \rho}{\partial t} + \nabla \cdot \rho \mathbf{v} = 0, \quad (4.1)$$

with ρ the density of the mixture, defined as the sum of the N -component densities, $\rho = \sum_{i=1}^N \rho_i$, and \mathbf{v} is the barycentric velocity:

$$\mathbf{v} = \frac{1}{\rho} \sum_{i=1}^N \rho_i \mathbf{v}_i, \quad (4.2)$$

where ρ_i , \mathbf{v}_i are the density and velocity of the i^{th} component respectively. The composition equation reads:

$$\frac{\partial \rho_i}{\partial t} + \nabla \cdot \rho_i \mathbf{v} = -\nabla \cdot \mathbf{j}_i, \quad (4.3)$$

where \mathbf{j}_i is the mass flux of the i^{th} component of the considered fluid, with i ranging between 1 and N .

The momentum balance, taking into account the mass balance (Eq. 4.1), can be written as:

$$\rho \frac{\partial \mathbf{v}}{\partial t} + \rho (\mathbf{v} \cdot \nabla) \mathbf{v} = \rho \mathbf{f}^{\text{ex}} + \nabla \cdot \boldsymbol{\sigma}, \quad (4.4)$$

where \mathbf{f}^{ex} are the external forces such as gravity, $\boldsymbol{\sigma}$ is the Cauchy stress tensor. To complete this set of equations, constitutive relations are required for the Cauchy stress tensor $\boldsymbol{\sigma}$. Different from classical thermodynamics, in which the internal energy u is a function of s , the specific entropy, and the density of the components, $u = u(s, \rho)$, in Cahn Hilliard case an extra non-local term is introduced to describe inhomogeneous fluids, and the internal energy is defined as $u = u(s, \rho, \nabla \rho)$. Applying gradient theory, the Cauchy stress tensor is given by (see Verschueren [30]):

$$\boldsymbol{\sigma} = \boldsymbol{\tau} - p \mathbf{I} - \sum_{i=1}^N \frac{\partial \rho u}{\partial \nabla \rho_i} \nabla \rho_i, \quad (4.5)$$

where p is the pressure, $\boldsymbol{\tau}$ is an extra stress tensor that, assuming isothermal conditions, for a Newtonian system is taken to be $\boldsymbol{\tau} = 2\eta \mathbf{D}$, \mathbf{D} is the deformation tensor given by $\mathbf{D} = (\nabla \mathbf{v} + (\nabla \mathbf{v})^T)/2$ and η is the viscosity of the mixture (for a more complete description of the model see Verschueren [30] and Keestra [31]). An additional gradient term, similar to the Cauchy stress tensor, is added to the chemical potential of each of the N species, and to the pressure:

$$\mu_i = \mu_{0i} - \nabla \cdot \frac{\partial \rho \mathbf{u}}{\partial \nabla \rho_i}, \quad (4.6)$$

$$p \mathbf{I} = p_0 \mathbf{I} - \sum_{i=1}^N \rho_i \nabla \cdot \frac{\partial \rho \mathbf{u}}{\partial \nabla \rho_i}, \quad (4.7)$$

in which μ_{0i} and p_0 are defined with respect to the homogeneous reference state. Substituting the expression of $\boldsymbol{\tau}$ and $\boldsymbol{\sigma}$ in the momentum balance, and writing ρ_i as $c_i \rho$, with $c_i = \rho_i / \rho$, the momentum balance reads:

$$\rho \frac{\partial \mathbf{v}}{\partial t} + \rho (\mathbf{v} \cdot \nabla) \mathbf{v} = \rho \mathbf{f}^{ex} + \nabla \cdot (2\eta \mathbf{D}) - \nabla p - \nabla \sum_{i=1}^N \frac{\partial \rho \mathbf{u}}{\partial \nabla c_i} \nabla c_i. \quad (4.8)$$

It was shown that [30]:

$$-\nabla \sum_{i=1}^N \frac{\partial \rho \mathbf{u}}{\partial \nabla c_i} \nabla c_i = -\rho \nabla f + \rho \sum_{i=1}^{N-1} (\mu_i - \mu_N) \nabla c_i, \quad (4.9)$$

where $f = u - Ts$ is the specific Helmholtz free energy of the system, T is temperature and s entropy. Substituting Eq. 4.9 and the specific Gibbs free energy, defined as $g = f + p/\rho$, in Eq. 4.8, and dividing all terms by ρ , the momentum balance reduces to:

$$\frac{\partial \mathbf{v}}{\partial t} + (\mathbf{v} \cdot \nabla) \mathbf{v} = \mathbf{f}^{ex} + \frac{1}{\rho} \nabla \cdot (2\eta \mathbf{D}) - \nabla g + \sum_{i=1}^{N-1} (\mu_i - \mu_N) \nabla c_i. \quad (4.10)$$

The ∇g term can be considered as a modified pressure and the interfacial tension is now evaluated as a body force ($\sum_{i=1}^{N-1} (\mu_i - \mu_N) \nabla c_i$), as shown in Lowengrub and Truskinovsky [32]. If we substitute the density of each component (ρ_i) with its mass fraction ($c_i = \rho_i / \rho$), and we express \mathbf{j}_i in terms of μ_i , Eq. 4.3 can be written as:

$$\frac{\partial c_i}{\partial t} + \mathbf{v} \cdot \nabla c_i = \nabla \cdot \mathbf{M} \nabla \mu_i. \quad (4.11)$$

For a three-phase system we define Eq. 4.12 where M_1 and M_2 are input parameters in the model, describing the mobility between LMW and drop, and matrix and drop,

respectively:

$$\mathbf{M} = \begin{bmatrix} M_1 & 0 \\ 0 & M_2 \end{bmatrix}. \quad (4.12)$$

Note that in general M_1 and M_2 can be a function of c_i but they are taken constant here. Writing the internal energy u in terms of the specific Helmholtz free energy of the system, f , the chemical potential can be written as (Verschueren (1999)):

$$\mu_i - \mu_N = \frac{\partial f}{\partial c_i} - \frac{1}{\rho} \nabla \cdot \left(\rho \frac{\partial f}{\partial \nabla c_i} \right). \quad (4.13)$$

The final set of equations describing the multiphase system is:

- Mass balance:

$$\frac{\partial \rho}{\partial t} + \nabla \cdot \rho \mathbf{v} = 0, \quad (4.14)$$

- Momentum balance:

$$\rho \frac{\partial \mathbf{v}}{\partial t} + \rho (\mathbf{v} \cdot \nabla) \mathbf{v} = \rho \mathbf{f}^{ex} - \nabla g + \nabla \cdot (2\eta \mathbf{D}) + \sum_{i=1}^{N-1} (\mu_i - \mu_N) \nabla c_i, \quad (4.15)$$

- Composition equation:

$$\frac{\partial c_i}{\partial t} + \mathbf{v} \cdot \nabla c_i = M_i \nabla^2 \mu_i, \quad (4.16)$$

- Chemical potential:

$$\mu_i - \mu_N = \frac{\partial f}{\partial c_i} - \frac{1}{\rho} \nabla \cdot \left(\rho \frac{\partial f}{\partial \nabla c_i} \right). \quad (4.17)$$

Governing equations for a three-phase system

When a three-phase non-homogeneous system is investigated assuming isothermal conditions, density-matched phases, incompressible fluids, constant viscosities of the

phases and neglecting inertia and external forces, and using μ_1 and μ_2 in the momentum balance to express the chemical potential differences, the system of governing equations reduces to:

- Mass balance:

$$\nabla \cdot \mathbf{v} = 0, \quad (4.18)$$

- Momentum balance:

$$0 = -\nabla g + \eta \nabla^2 \mathbf{v} + \mu_1 \nabla c_1 + \mu_2 \nabla c_2, \quad (4.19)$$

- Composition equation:

$$\frac{\partial c_i}{\partial t} + \mathbf{v} \cdot \nabla c_i = M_i \nabla^2 \mu_i \quad i = 1, 2, \quad (4.20)$$

- Chemical potential:

$$\mu_i - \mu_N = \frac{\partial f}{\partial c_i} - \nabla \cdot \left(\frac{\partial f}{\partial \nabla c_i} \right) \quad i = 1, 2. \quad (4.21)$$

In the Cahn-Hilliard theory, the specific Helmholtz free energy of the system is given by the sum of a homogeneous part and a gradient part:

$$f(\mathbf{c}, \nabla \mathbf{c}) = f_0(\mathbf{c}) + \frac{1}{2} \epsilon |\nabla \mathbf{c}|^2, \quad (4.22)$$

where f_0 is the homogeneous part, and $\frac{1}{2} \epsilon |\nabla \mathbf{c}|^2$ the non-local term of the free energy, and ϵ is the gradient energy parameter assumed to be constant.

The model requires one more equation of state to describe the free energy in order to solve the system of Eqs. 4.18-4.21.

Ginzburg-Landau approximation

Based on the classical Flory-Huggins theory, the intensive free energy f_0 (per monomer) of a three phase system, at a given temperature and pressure, can be written as:

$$\frac{f_0}{KT} = \left(\frac{\phi_1}{N_1} \ln \phi_1 + \frac{\phi_2}{N_2} \ln \phi_2 + \frac{\phi_3}{N_3} \ln \phi_3 + \chi_{12} \phi_1 \phi_2 + \chi_{13} \phi_1 \phi_3 + \chi_{23} \phi_2 \phi_3 \right), \quad (4.23)$$

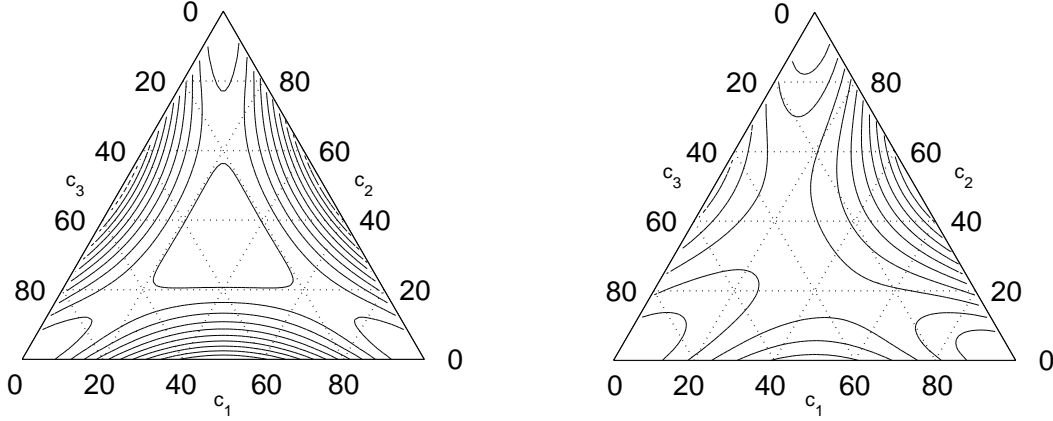


Figure 4.1: Contour plot of the free energy (Eq. 4.24) on the Gibbs triangle for $a = b = d = 1/4$ (left) and for $a = 4, b = 2, \text{ and } d = 1$ (right).

where K is the Boltzmann constant, T is the temperature, N_i and ϕ_i with $i = 1, 2, 3$ are the chain length and volume fraction of the three components respectively, and χ_{ij} the Flory-Huggins interaction parameter between the components i and j . Chosen a three-phase system, this interaction parameter defines whether mixing or demixing occurs.

For numerical purposes, we use, as an approximation, a Taylor expansion of Eq.4.23 around the critical point. In Kim et al. [33] the approximation for the free energy formulation proposed for a three phase system reads:

$$f_0(\mathbf{c}) = f_0(c_1, c_2) = \frac{1}{4} [ac_1^2c_2^2 + b(c_1^2 + c_2^2)c_3^2 - dc_1c_2c_3], \quad (4.24)$$

where $c_3 = 1 - c_1 - c_2$, and a, b and d are constants. When these three constants are assumed equal to $1/4$, as proposed in Kim et al. [33], the surface plot of the free energy for the ternary system presents free energy minima in the corners of the diagram and at the center of it, where the system is fully miscible, see Figure 4.1 left. We will use this expression to validate our numerical code by comparing with results from Kim et al. [33]. Our system consists of LMW species partially-miscible with the drop and matrix phases, and drop and matrix immiscible and this requires other values of the parameter in Eq. 4.24 or another free-energy expression. An example of changing the parameter values ($a = 4, b = 2, \text{ and } d = 1$) is given in Figure 4.1 right. It can be observed that this is not a suited parameter set, since the free-energy contour plot remains symmetrical around one of the axes.

Changing the parameter values does not solve the problem, therefore, we use the free-energy formulation for ternary partially-miscible systems proposed by Kim et al. [34]:

$$f_0(c_1, c_2) = ac_1^2(1 - c_1 - c_2)^2 + (c_1 + b)(c_2 - d)^2 + (e - c_1 - c_2)(c_2 - l)^2, \quad (4.25)$$

with $a = 2$, $b = 0.2$, $d = 0.2$, $e = 1.2$, $l = 0.4$. The surface and contour plot of this free energy formulation are shown in Figure 4.2. The contour plot corresponding to Eq. 4.25 is no longer symmetric, therefore it is suitable to describe our three-component system.

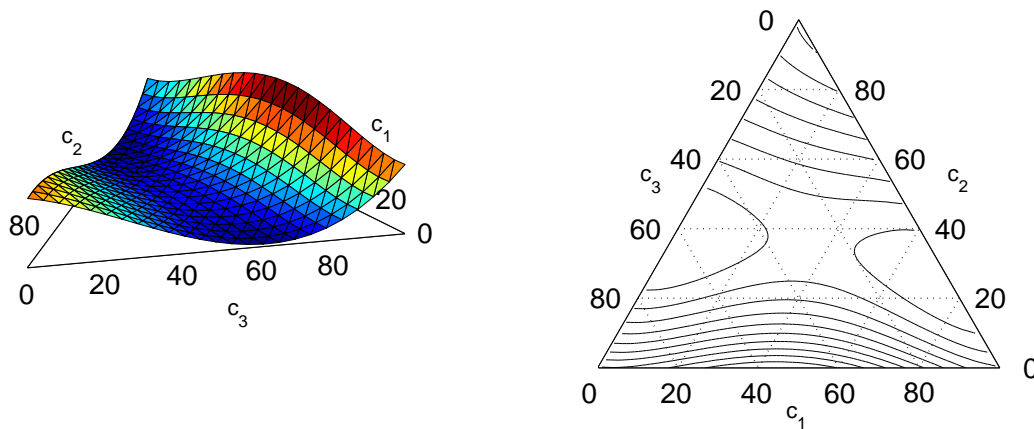


Figure 4.2: Surface plot (left) and contour plot (right) of the free energy (Eq. 4.25) on the Gibbs triangle.

At this point a choice to define the the gradient-energy parameter ϵ in the non-local term of the free energy is needed (see Eq. 4.22).

The gradient-energy parameter

Kim et al. in [33] and [34] reported different expression for the gradient-energy parameter ϵ (Eq. 4.22), according to the definition of the free energy:

$$\epsilon = \begin{bmatrix} 2\epsilon^2 & \epsilon^2 \\ \epsilon^2 & 2\epsilon^2 \end{bmatrix}, \quad (4.26)$$

while a different derivation from R. Mauri¹ yields:

¹R. Mauri, University of Pisa, Italy, personal communication.

$$\boldsymbol{\epsilon} = \begin{bmatrix} \epsilon & \frac{\epsilon}{5} \\ \frac{\epsilon}{5} & \epsilon \end{bmatrix}. \quad (4.27)$$

For simplicity, the gradient energy parameter is kept as simple as possible and we define:

$$\boldsymbol{\epsilon} = \begin{bmatrix} \epsilon & 0 \\ 0 & \epsilon \end{bmatrix} = \epsilon \mathbf{I}, \quad (4.28)$$

where we neglect the off-diagonal terms.

Numerical method

The resulting system that needs to be solved, i.e. equations Eqs. 4.18-4.21, is nonlinear and time-dependent. For the temporal discretization a first-order Euler implicit scheme is used. The nonlinear term in the chemical potential equation is linearized by a standard Picard method in each time step. Instead of substituting the chemical potential in the composition equation it is treated as a separate unknown. The main advantage of this approach is that only second-order derivatives need to be evaluated. So within each cycle of a time step, the chemical potential μ and c are solved together, using the velocity from the previous time. The velocity and pressure are determined by using the composition c and chemical potential μ from the previous time step. Roughly within five iterations a solution is found for the nonlinear problem each time step. More details about the iteration scheme can be found in [35,36]. A second-order finite element method is used for spatial discretization of the set of equations. The flow problem was solved using the velocity-pressure formulation and discretized by a standard Galerkin finite element method. The effect of the interface is included as a known volume source term. Taylor-Hood quadrilateral elements with continuous pressure that employ a biquadratic approximation for the velocity and a bilinear approximation for the pressure are used. The resulting discretized second-order linear algebraic equation is solved using a direct method based on a sparse multifrontal variant of Gaussian elimination (HSL/MA41, [37,38]).

Validation of the model

Our code is validated by repeating a test case described in Kim et al. [33]. A ternary system in a one-dimensional domain with the free energy formulation of Eq. 4.24 and the gradient-energy parameter of Eq. 4.28 is used, the uniform time step is $\Delta t = 1 \cdot 10^{-4}$ and simulations are started with the following initial conditions:

$$\begin{aligned} c_i(x) &= 0.25 + 0.01 \cos(3\pi x) + 0.04 \cos(5\pi x) & i = 1, 2, \\ c_3(x) &= 1 - c_1(x) - c_2(x), \end{aligned} \quad (4.29)$$

where $0 \leq x \leq 1$. The resulting time evolution of the three component concentrations, shown in Figure 4.3 fully agrees with those reported in Kim et al. [33]. This validated model is used hereafter to compute and interpret the experimental results.

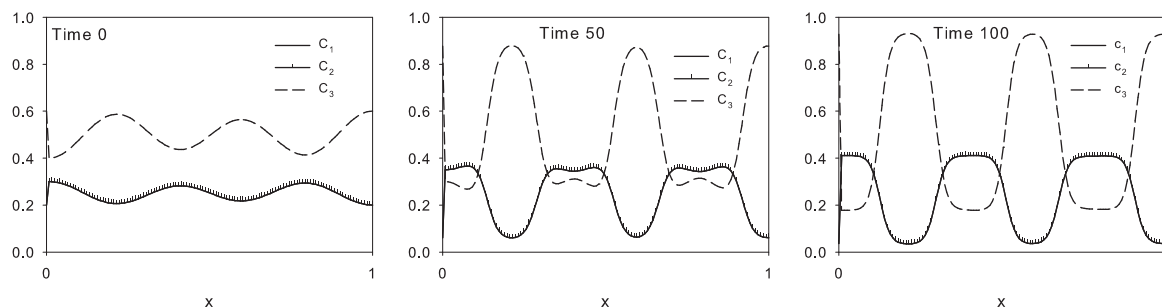


Figure 4.3: Time evolution of the concentrations c_1 , c_2 and c_3 .

Influence of the mobility parameters

The model as described in Section 4.3 needs 5 material parameters, M_1 , M_2 , ϵ , ρ , and η , once the choice for the homogeneous part of the free energy has been defined. This is one of the main drawbacks of such modeling; these parameters are in general not known for a given polymeric system. Therefore we will restrict ourselves to a qualitative analysis. Within a limited range of parameter space, the behavior of a three-phase system is investigated and compared with our experimental observations. The free energy expression adopted is given in Eq. 4.25, and the the gradient-energy parameter ϵ is set equal to $2 \cdot 10^{-4}$.

The influence of changes in the mobility parameters M_1 and M_2 is investigated. For that we use a one dimensional domain ranging from 0 to 1, with 401 nodes and a drop placed in the middle, with a constant diameter equal to the 5% of the domain. The concentration of LMW component is taken 30% and time steps of $1 \cdot 10^{-4}$ are used. A schematic picture of the domain and initial concentration is shown in Figure 4.4.

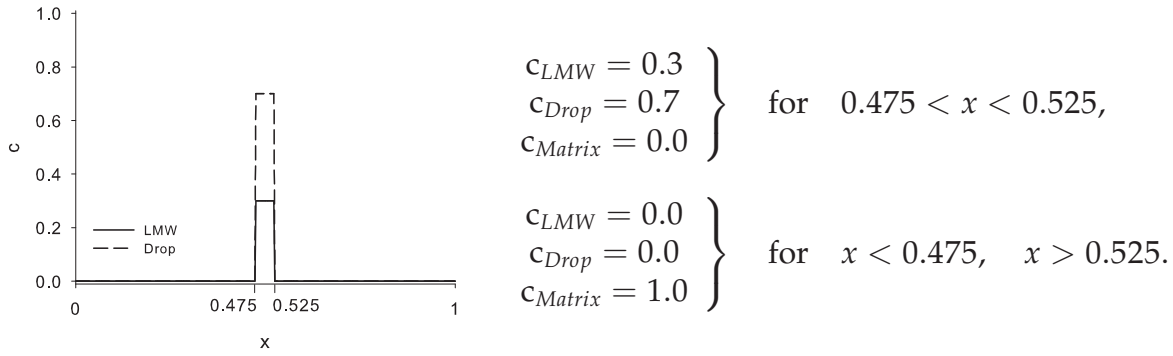


Figure 4.4: Schematic representation of the initial conditions.

The concentration profiles of the LMW species, drop and matrix, are shown in Figure 4.5 for $M_1 = 1 \cdot 10^{-2}$, and in Figure 4.6 for $M_1 = 9 \cdot 10^{-2}$, respectively. M_2 is taken equal to $4 \cdot 10^{-4}$ in both cases. It is seen that the concentration profiles do not change much but the time scale of reaching a certain profile changes drastically. For a two-component system the interfacial tension can be relate to the composition:

$$\sigma = \rho\epsilon \int (\nabla \mathbf{c} \cdot \nabla \mathbf{c}) dV. \quad (4.30)$$

Following this derivation we define

$$\bar{\sigma} = \int_0^1 \left(\frac{dc_{LMW}}{dx} \right)^2 dx. \quad (4.31)$$

The resulting interfacial tension behaviors are shown in Figure 4.7 (left) when changing M_1 gradually, in the middle when changing M_2 and on the right when lowering M_1 by orders. For these parameter sets a clear minimum in interfacial tension is observed that is reached at shorter times for a gradually increasing M_1 value, and it is not changing its value. These changes in M_1 affect the transient behavior of the system in the way it reaches the steady state. When M_2 is increased gradually, the time at which the minimum value in interfacial tension is reached stays the same but its value reduces. When M_1 is lowered by orders (Figure 4.7 right), the minimum disappears and the interfacial tension decreases only in a much slower way. The cases when a minimum appears are representative of highly-diffusive systems, when the minimum disappears the systems behaves as a slightly-diffusive one. In conclusion diffusivity can be controlled by M_1 .

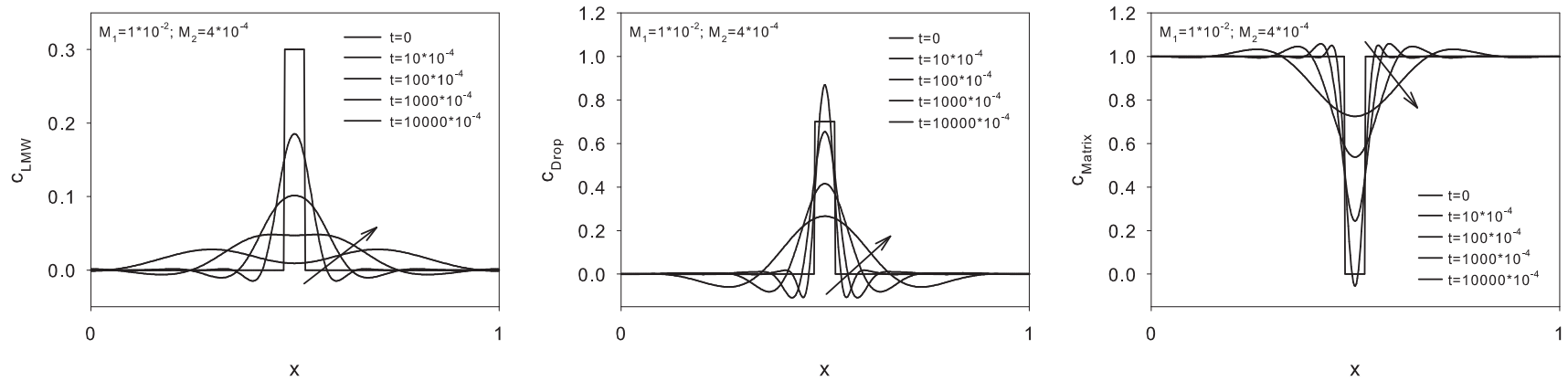


Figure 4.5: Concentration profiles in time for LMW component (left), drop (middle) and matrix (right) for a 0.3 LMW concentrated blend. Mobility parameters: $M_1 = 1 \cdot 10^{-2}$ and $M_2 = 4 \cdot 10^{-4}$.

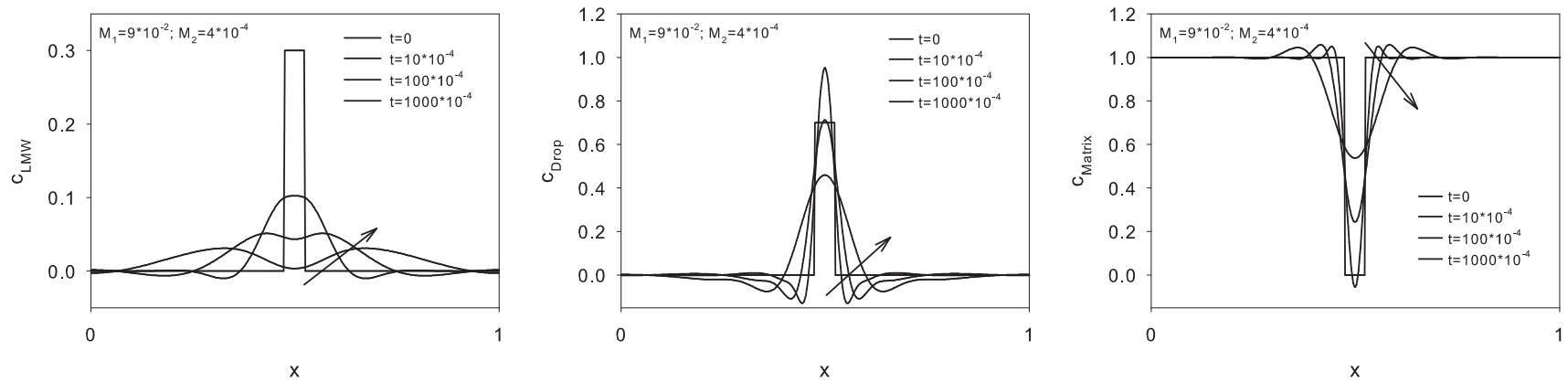


Figure 4.6: As in Figure 4.5, now with mobility parameters: $M_1 = 9 \cdot 10^{-2}$ and $M_2 = 4 \cdot 10^{-4}$ (Case A).

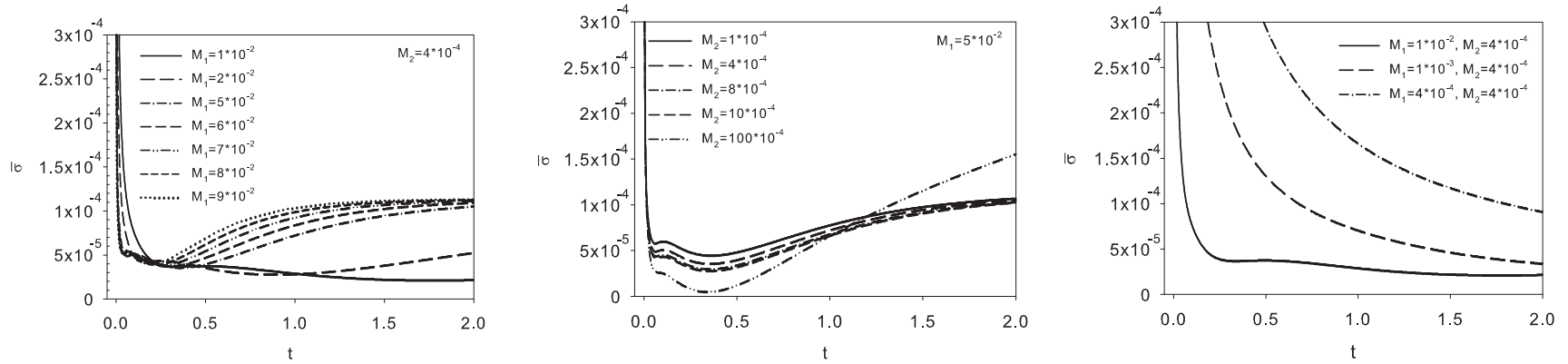


Figure 4.7: Interfacial tension computed with Eq. 4.31 for a 0.3 LMW concentrated blend. The influence of gradual changes in the mobility parameters M_1 (left) and M_2 (middle) when they differ two orders of magnitude, and when reducing this difference (right) are shown.

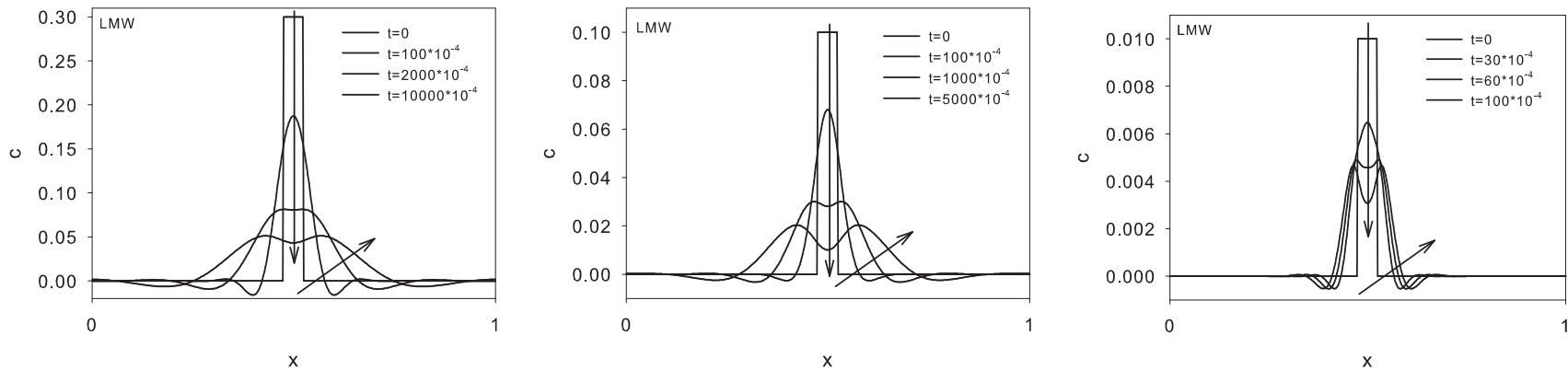


Figure 4.8: LMW concentration profiles when $M_1 = 9 \cdot 10^{-2}$ and $M_2 = 4 \cdot 10^{-4}$ (Case A) for initial concentrations of LMW species of 0.3 (left), 0.1 (middle) and 0.01 (right).

Influence of concentration of LMW species on the computed interfacial tension

To show how changes in the initial concentration of LMW species affect the interfacial tension of the system, we choose the case with a clear minimum, $M_1 = 9 \cdot 10^{-2}$ and $M_2 = 4 \cdot 10^{-4}$, which we will address as case A, and three different initial concentrations of LMW component, respectively 30%, 10% and 1% are investigated. The same drop size and time steps are used as in the previous case. The concentration profiles along the drop diameter at different time steps are shown in Figure 4.8. Reducing the initial concentration of migrating molecules reduces the typical radial length scale over which diffusion is observed and it shortens the time needed to complete the diffusion process. We have now sets of interfacial tension evolutions that can be compared with our experimental results.

4.4 Interfacial tension results

Measured transient interfacial tensions are shown for the two systems used in Figure 4.9 (left). For the *highly-diffusive* system, the interfacial tension decreases first, corresponding to thickening of the interphase, followed by an increase attributed to depletion and reaches a plateau value in the late stages. The *slightly-diffusive* system shows only thinning (i.e. an increase in the interfacial tension thickness) before the plateau value is approached [11]. In Tufano et al. [11] the differences in the interfacial behavior of these two system are partially attributed to their different polydispersities. The PB has higher polydispersity compared to the PBD, i.e. in the system PB/PDMS a larger amount of molecules will participate to the diffusion process compared to the PBD/PDMS system. Based on that, our first approach is to model the two systems by using the three-phase diffuse-interface model described in Section 4.3, with the free energy formulation reported in Eq. 4.25. The mobility parameters are chosen to be $M_1 = 9 \cdot 10^{-2}$ and $M_2 = 4 \cdot 10^{-4}$ (case A), and the parameter $\epsilon = 2 \cdot 10^{-4}$. To distinguish the two cases, the highly-diffusive system is simulated imposing 30% LMW concentration, while, for the slightly-diffusive case, this concentration is set equal to 1%. The computed behavior of interfacial tension in time in the two cases is shown in Figure 4.9 (right). Another approach is not to consider the typical time dependent interfacial tension behavior but to consider the idea of highly and slightly-diffusive only and choose to express this behavior by using different values for the M_1 parameter (relatively large for the highly-diffusive system, relatively small for the slightly-diffusive one). However, this does not reproduce the typical behavior of the interfacial tension observed experimentally (compare Figure 4.7 right with Figure 4.9 left).

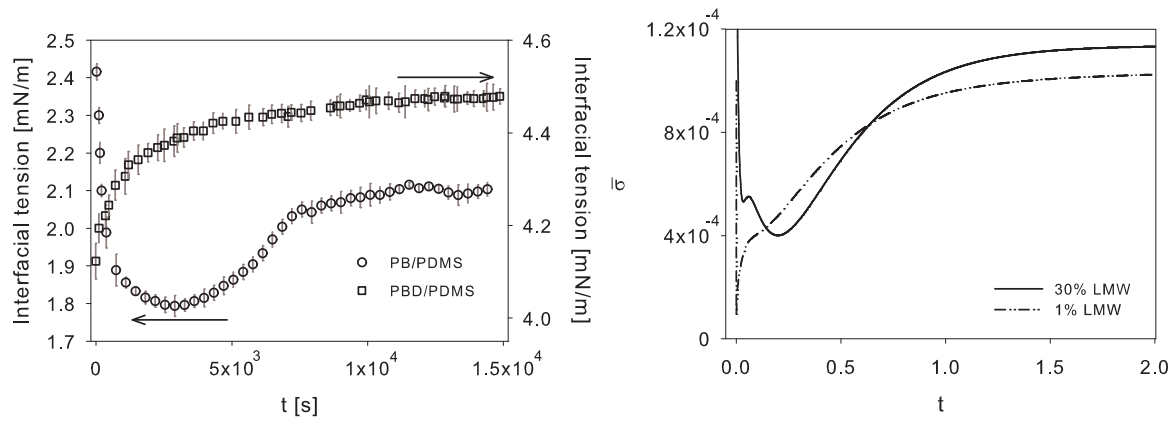


Figure 4.9: Transient interfacial tension measurement (left) and numerical predictions (right).

4.5 Experimental results

Drop-drop interaction: PB/PDMS system

Figure 4.10 shows an example of two drops of PB with nearly the same diameter and at a distance where, normally, no interaction is expected. The initial distance between the drops is created by applying a weak flow during drop approach, guaranteeing that drops keep their spherical shape and that there is no influence of flow on coalescence. Once the desired distance between the drops is reached, the flow is stopped and no other external forces are applied, time $t = 0s$ in Figure 4.10. At $t = 0s$ the residence time of the drops in the matrix is $t_r = 30$ minutes. It is clearly seen that the drops attract each other, the film is drained and when rupture occurs the drops coalesce. Figure 4.11 shows an example of mutual attraction of drops with different radii and with a shorter residence time at $t = 0s$ ($t_r = 4$ minutes). A large number of such experiments are carried out, using drops of different sizes, placed at different distances and having different residence times. Drops of PB always attract each other when they are at a distance less than order of the drop radius. In order to compare the results obtained with different drop size, the ratio distance over equivalent radius is considered. The equivalent radius is defined as:

$$\frac{2}{R_{eq}} = \frac{1}{R_1} + \frac{1}{R_2}, \quad (4.32)$$

where R_1 and R_2 are the radii of the two drops. Figure 4.12 shows the time evolution of the distance between the drops for all experiments. In the inset plot all curves are horizontally shifted to the most right curve to compensate for differences in their initial distance. In the final stages of the measurements, approximately the

last 100 seconds before coalescence occurs, the drops all attract with the same rate. Aging effects are also investigated monitoring drops with different resident times. In the first 30 minutes after the introduction of the drops in the matrix, diffusion is in progress and the interfacial tension reduces due to thickening of the interface. However, as shown in Figure 4.12, no serious variations in the rate of attraction in the late stages before coalescence occurs could be detected. Zdravkov et al. [22] reported for a similar PB/PDMS blend that film drainage is approximately 100 times faster compared to the partially-mobile model predictions. They attributed the high drainage rate to Marangoni flow, acting in the same direction as the film-drainage flow. This high drainage rate is confirmed in the experiments presented here. In conclusion, for highly-diffusive systems, mutual diffusion can not be neglected since it has an overruling effect on drop coalescence and therefore, it plays a crucial role in the morphology evolution of polymer blends, as also shown in Tufano et al. [11] for diluted blends of PB/PDMS.

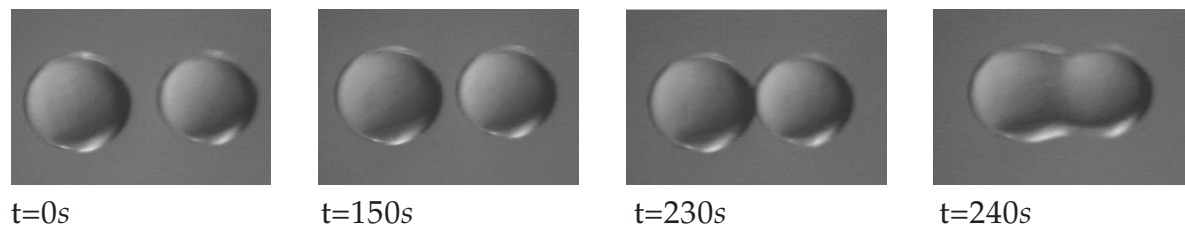


Figure 4.10: Mutual attraction and coalescence between two drops of PB in PDMS. Radii are $341 \mu\text{m}$ and $313 \mu\text{m}$, distance at the time $t=0\text{s}$ is $110 \mu\text{m}$. Residence time at $t=0\text{s}$, 1800s.

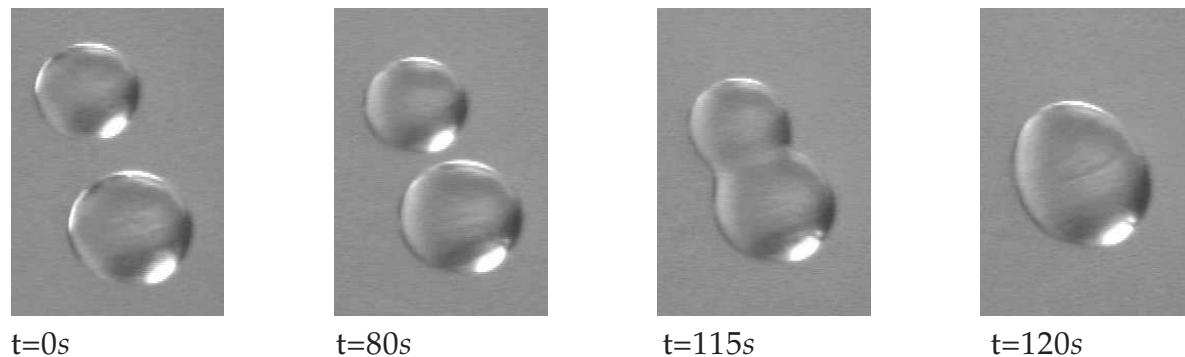


Figure 4.11: As in Figure 4.10, now radii are $220 \mu\text{m}$ and $275 \mu\text{m}$, distance at the time $t=0\text{s}$ is $95 \mu\text{m}$. Residence time at $t=0\text{s}$, 240s.

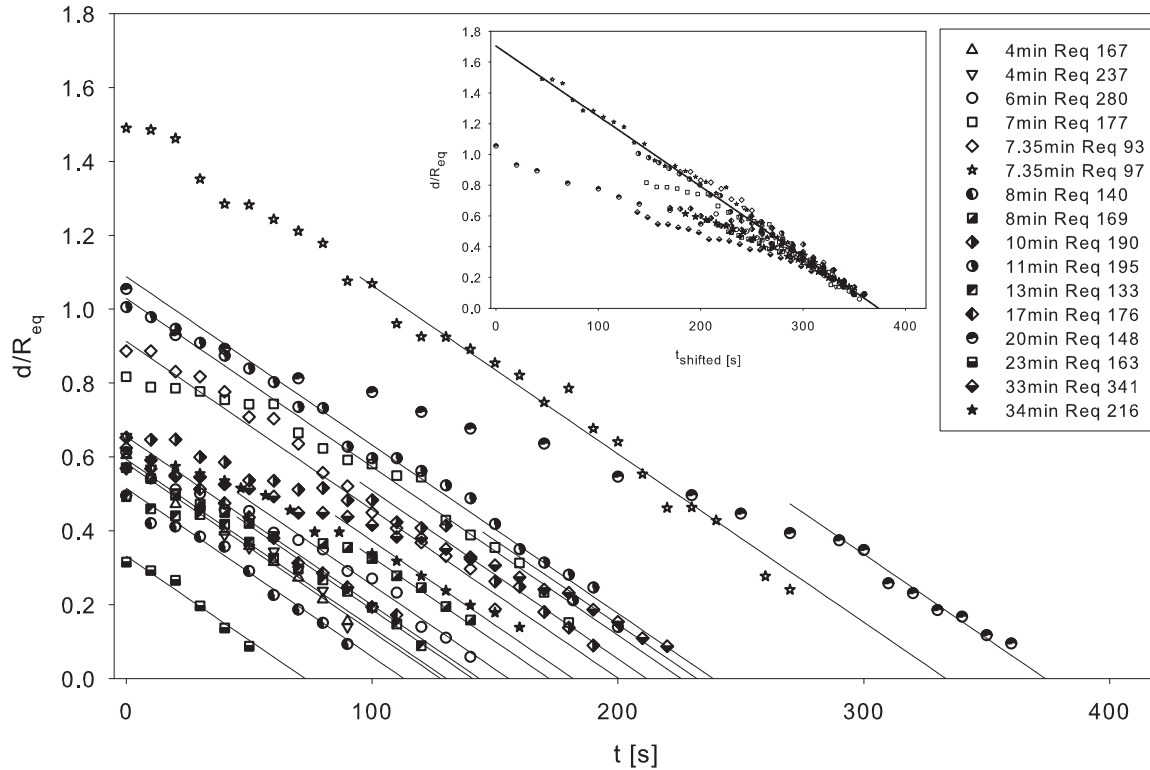


Figure 4.12: Time evolution of the scaled drop distance d/R_{eq} for the PB/PDMS system. Inset plot: curves shifted to the most right experimental curve.

Drop-drop interaction: PBD/PDMS system

The system PBD/PDMS shows a continuous increasing interfacial tension, related to a thin diffusive layer, which approach a plateau value faster than the PB/PDMS system (see Figure 4.9). When two PBD drops are brought in close contact and left in quiescent conditions, it is observed that they repel each other, see Figure 4.13. In all the cases investigated, i.e. drops with different sizes and at different distances, repulsion is observed. For a similar PBD/PDMS blend, Zdravkov et al. [22] reported that the film drainage slows down with time and eventually reverses. This was again attributed in that case to Marangoni stresses which may cause reversal of the film drainage and explain the repulsion observed for this system.

Drop-wall interaction: PB/PDMS system

When a PB drop is placed in the matrix, diffusion of short molecules from the drop into the matrix occurs. If the drop is close enough to the wall ($\leq R$), given the less space for migration of the shorter molecules on the wall side, their concentration on the drop surface, on the wall side, will be larger than on the rest of the drop surface. This induced gradient in concentration, i.e. in interfacial tension, along the drop

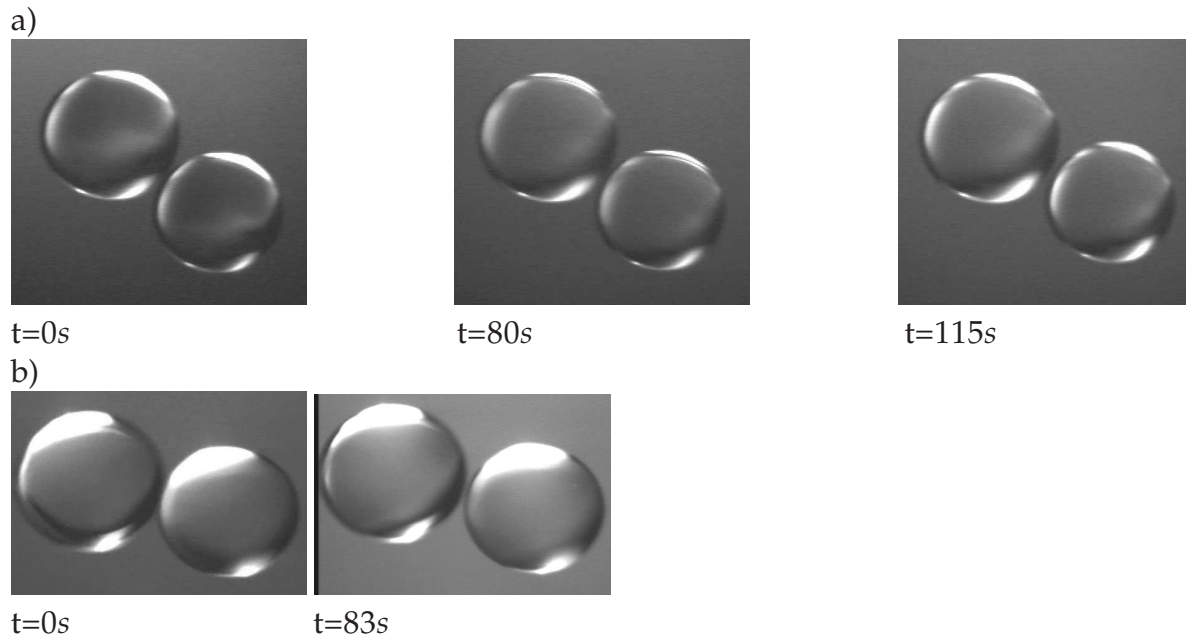


Figure 4.13: Mutual repulsion between two drops of PBD in PDMS. The radii are: a) $597\ \mu\text{m}$ and $572\ \mu\text{m}$, b) $225\ \mu\text{m}$ and $235\ \mu\text{m}$.

surface, generates Marangoni flows, which will act as to balance the concentration gradient. Movement of the migrating molecules accumulated between the drop and the wall, towards the sides of the drop, will drag also molecules of the matrix. The immediate consequence is the thinning of the matrix film between the drop and the wall. The drop then moves toward the wall, touches it and eventually wets it, see Figure 4.14 where a glass wall is used, and Figure 4.15, where a Teflon wall is used.

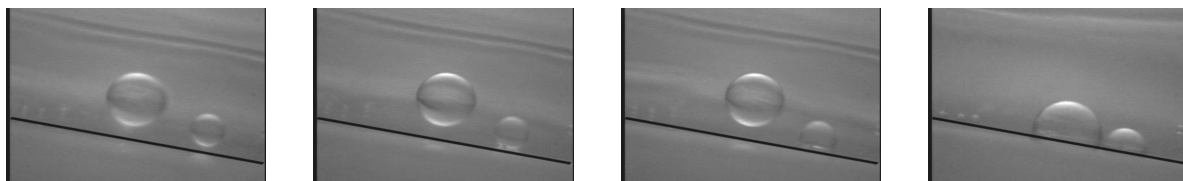


Figure 4.14: Lateral PB-drops migration toward a glass wall. The diameters are $580\ \mu\text{m}$ and $333\ \mu\text{m}$. The initial distances from the wall are $163\ \mu\text{m}$ and $59\ \mu\text{m}$ respectively. Line represents the wall.

Drop-wall interaction: PBD/PDMS system

When a drop of PBD is placed close to a wall, no lateral migration is found experimentally. The time scale of the experiment is limited by the vertical movement of

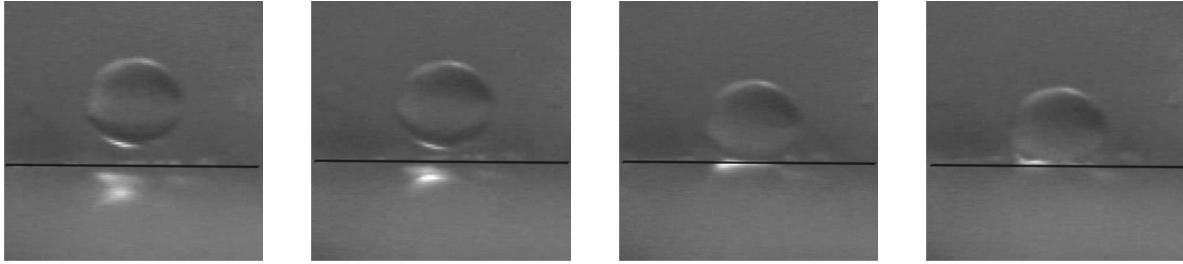


Figure 4.15: Lateral PB-drops migration toward a Teflon wall. The diameter is $247 \mu m$ and the initial distance from the wall is $45 \mu m$. Line represents the wall.

the drop, due to the difference in density. The acquisition is stopped when the drops start to move out of focus. In Figure 4.16 (a) and (b), a drop of PBD is placed close to a glass and a Teflon wall respectively. In the time scale investigated, no lateral movement is seen.

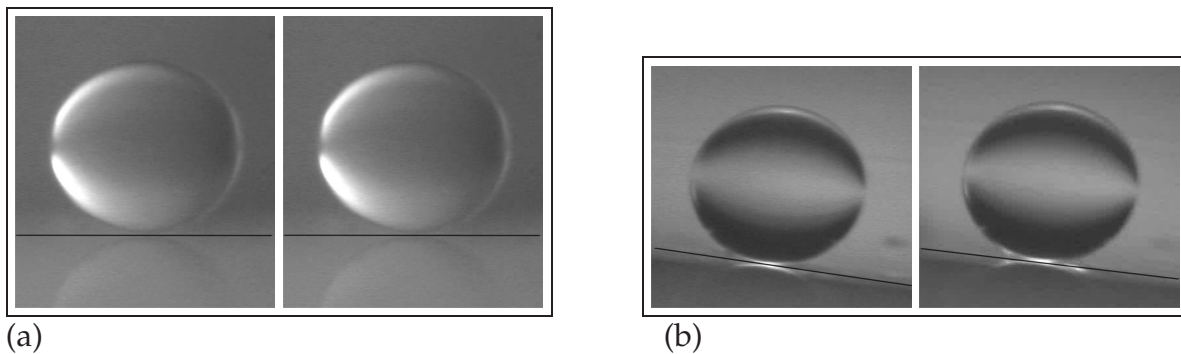


Figure 4.16: No lateral PBD-drops migration toward a wall is found. (a) glass wall, $d_{drop} = 650 \mu m$, residence time 600s. (b) Teflon wall, $d_{drop} = 900 \mu m$, residence time 720s. Line represents the wall.

4.6 Numerical results

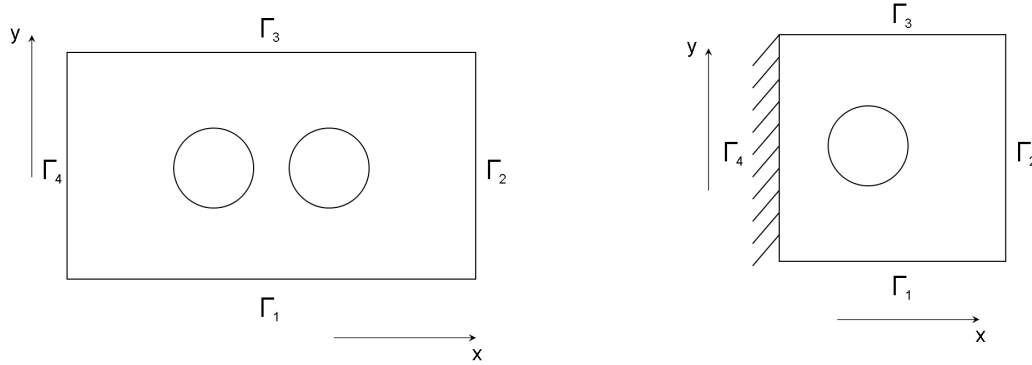


Figure 4.17: Schematic representation of the computational domain used for the drop-drop (left) and drop-wall (right) simulations.

For the drop-wall simulations, the number of elements used in the x and y direction are $N_x = N_y = 60$, while for the drop-drop simulations $N_x = 160$ and $N_y = 80$. If we indicate with $\mathbf{v} = (v_x, v_y)$, the boundary conditions can be written as:

- Drop-drop

$$\left. \begin{array}{l} \mathbf{v} = \mathbf{0} \\ \frac{\partial c_i}{\partial n} = \frac{\partial \mu_i}{\partial n} = 0 \end{array} \right\} \text{ at } \Gamma_j \quad j = 1, 2, 3, 4, \quad (4.33)$$

- Drop-wall

$$\left. \begin{array}{l} \mathbf{v} = \mathbf{0} \\ \frac{\partial c_i}{\partial n} = \frac{\partial \mu_i}{\partial n} = 0 \end{array} \right\} \text{ at } \Gamma_4, \quad (4.34)$$

$$\left. \begin{array}{l} \frac{\partial v_x}{\partial n} = \frac{\partial v_y}{\partial n} = 0 \\ \frac{\partial c_i}{\partial n} = \frac{\partial \mu_i}{\partial n} = 0 \end{array} \right\} \text{ at } \Gamma_j \quad j = 1, 2, 3. \quad (4.35)$$

Drop-drop interaction

First the numerical results for the drop-drop interaction case are presented.

In Figures 4.18 and 4.19 contour profiles of the LMW concentration for two standard cases, A and B, are presented. For case A the mobility parameters are $M_1 = 9 \cdot 10^{-2}$ and $M_2 = 4 \cdot 10^{-4}$, while, for case B, $M_1 = 4 \cdot 10^{-4}$ and $M_2 = 4 \cdot 10^{-4}$. Clearly for A30% system, the highly-diffusive example, the two drops merge after sufficient time. For the B30% system the drops remain stationary.

These contour concentration profiles do not show clearly if the drops are really moving towards each other, i.e. behave like attracting each other. Therefore, the x and y components of the velocity and the vorticity for the A30% case are shown in Figures 4.20-4.21 and Figure 4.22, respectively, from which it is observed that the drops indeed move towards each other. In Figure 4.23 the modified pressure distribution, g in Eq. 4.19, in and out of the drops is also shown.

For all the cases (A30%, A1%, B30%, B1%) the concentration profiles over the drop-drop center line are shown in Figures 4.24-4.31 where also the distance between the drops is varied. Focusing on the LMW concentration it is seen that the drop-drop attraction is present for the A30% and A1%, even for an increased drop-drop distance. The separation between the components stays clearly present in the range of time and for the two drop-drop distances investigated for the B-cases. These results indicate that sufficient LMW species that can diffuse fast enough into the matrix (A30% versus B30%) are needed to activate the drop-drop attraction. In addition, they confirm the idea that concentration-gradient induced Marangoni stresses promote the drainage of the film between two droplets in case of a highly diffusive system.

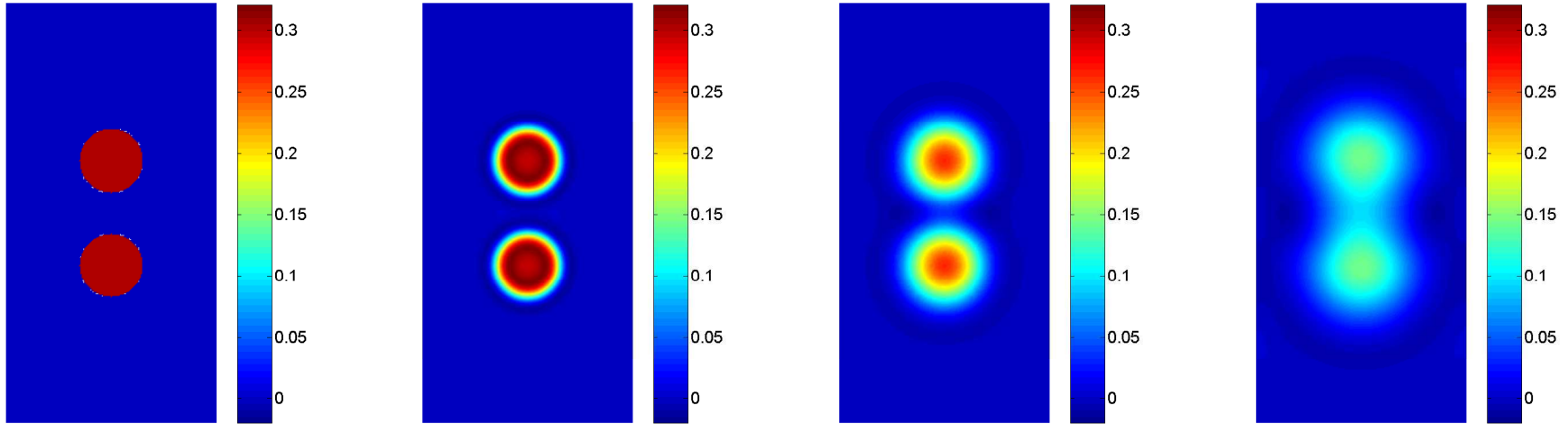


Figure 4.18: Concentration distribution of LMW component at time 0, $10 \cdot 10^{-4}$, $300 \cdot 10^{-4}$, and $1000 \cdot 10^{-4}$. The initial LMW concentration is 0.3. Mobility parameters: $M_1 = 9 \cdot 10^{-2}$ and $M_2 = 4 \cdot 10^{-4}$ (Case A).

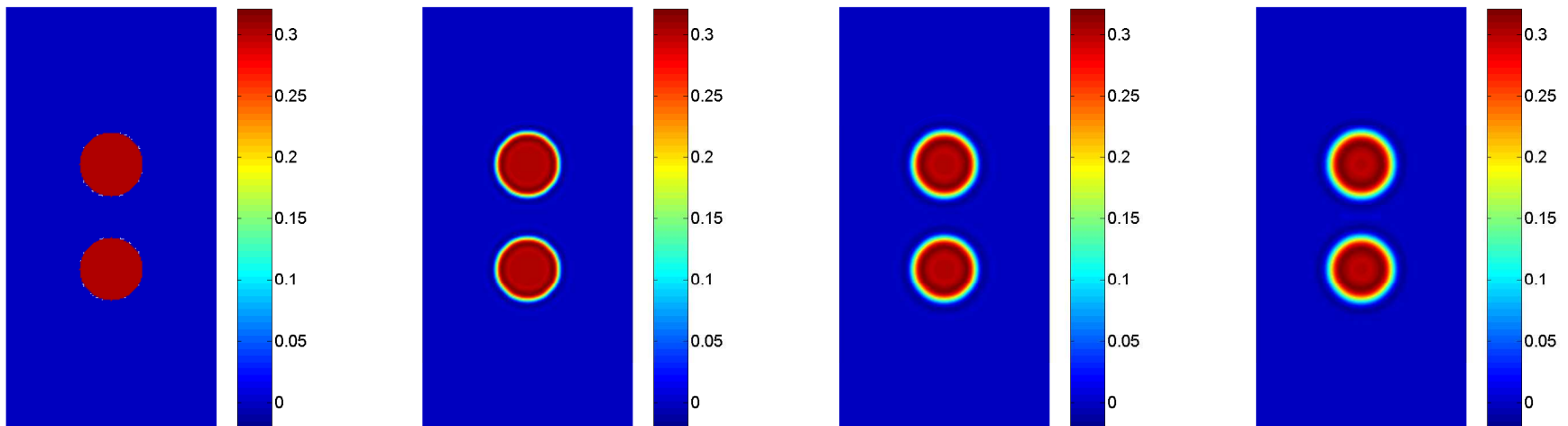


Figure 4.19: As Figure 4.18, now at time 0, $100 \cdot 10^{-4}$, $500 \cdot 10^{-4}$, and $1000 \cdot 10^{-4}$ and with mobility parameters $M_1 = 4 \cdot 10^{-4}$ and $M_2 = 4 \cdot 10^{-4}$ (Case B).

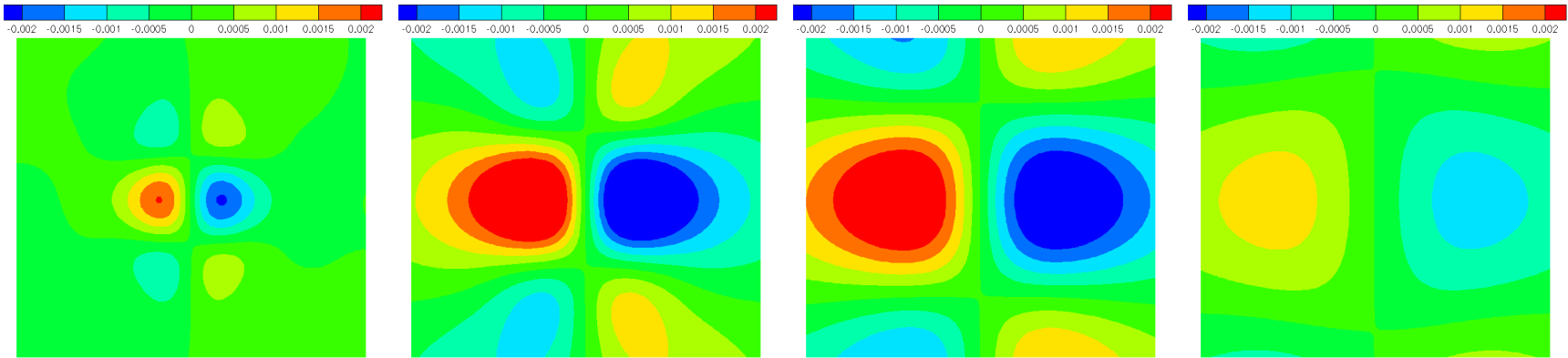


Figure 4.20: x component of velocity for A30%.

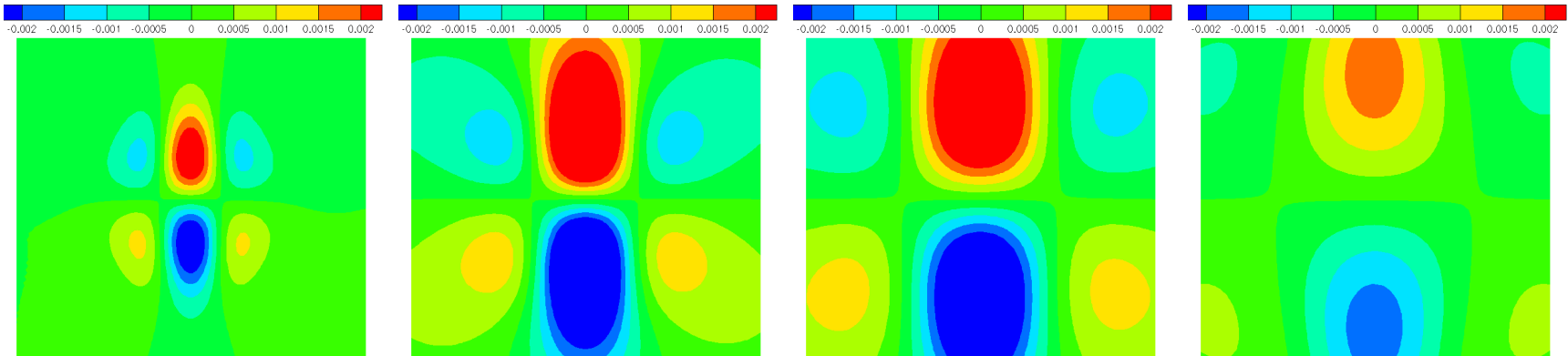


Figure 4.21: y component of velocity for A30%.

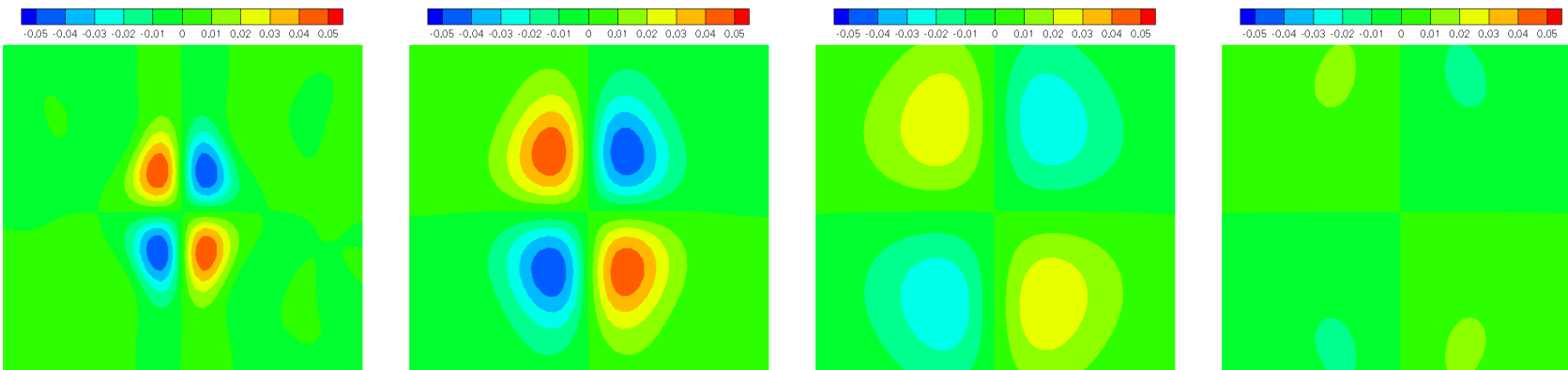


Figure 4.22: Vorticity for A30%.

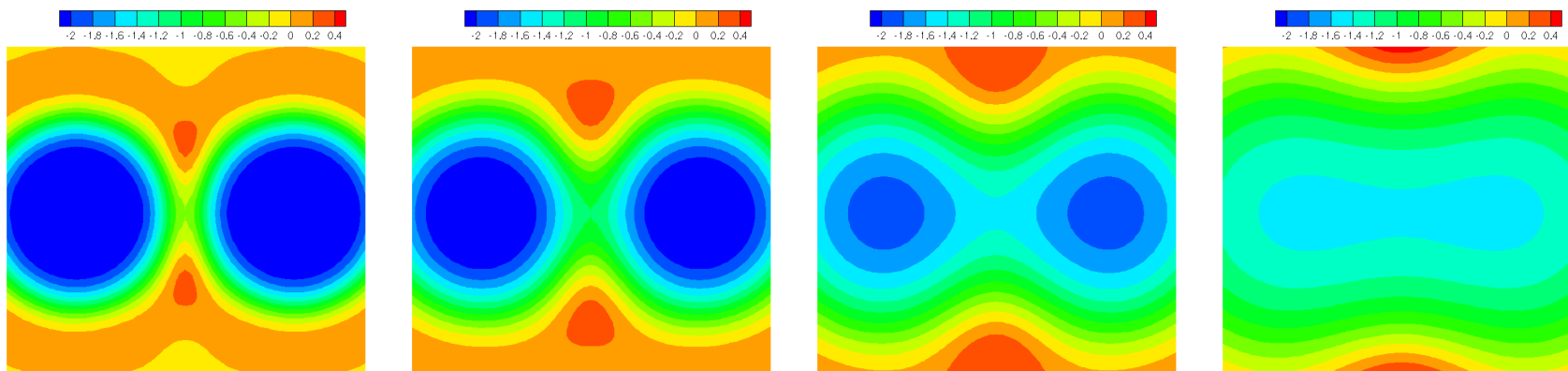


Figure 4.23: Modified pressure distribution (g in Eq. 4.19) in and out of the drops as the LMW component diffuses out for A30%.

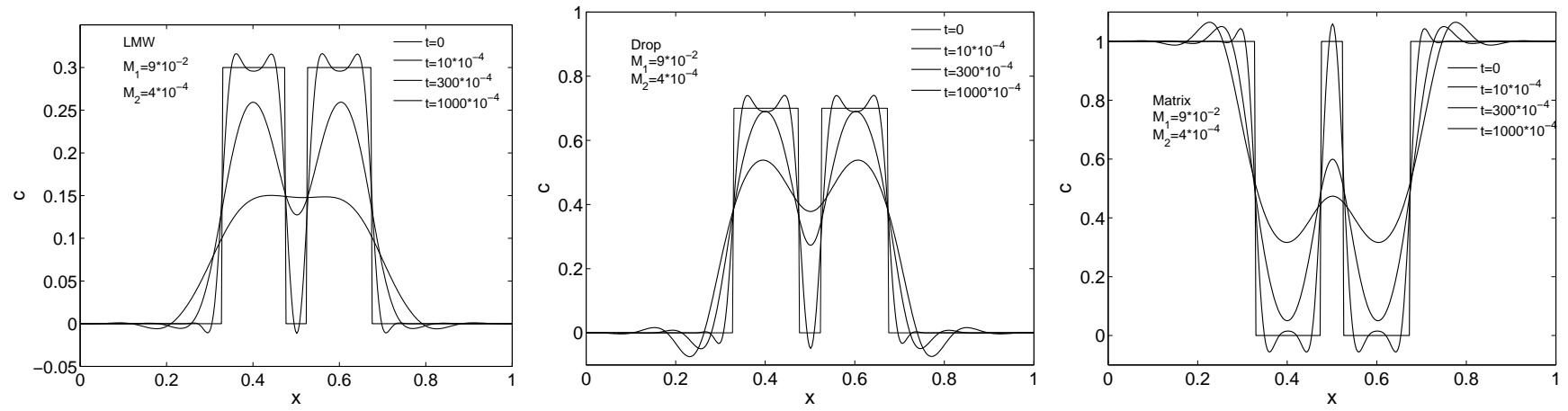


Figure 4.24: Concentration profiles in time for LMW component (left), drop (middle) and matrix (right) for a 30% LMW concentrated blend. Mobility parameters: $M_1 = 9 \cdot 10^{-2}$ and $M_2 = 4 \cdot 10^{-4}$ (Case A).

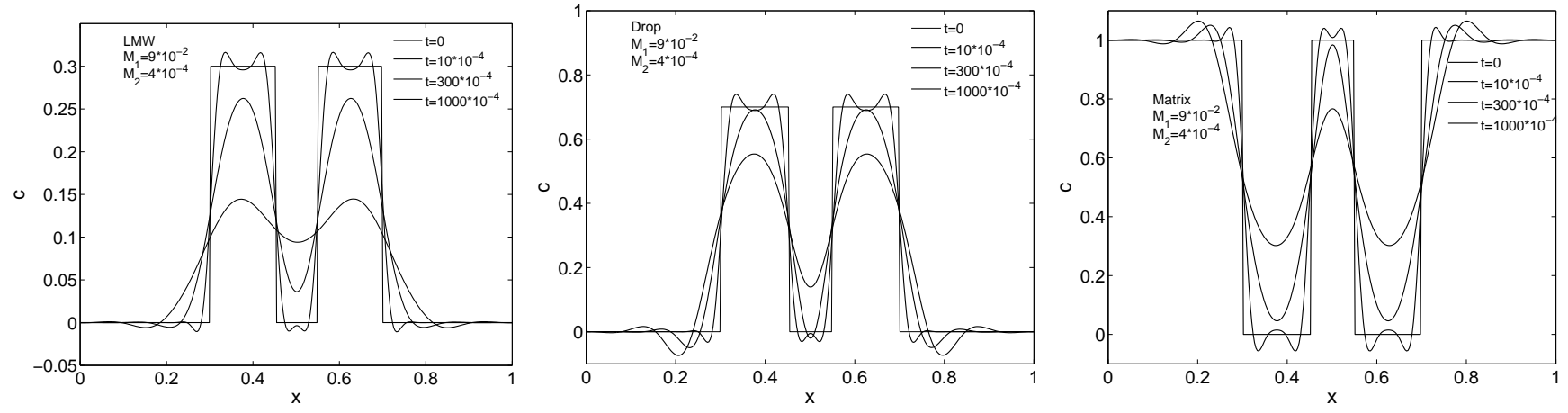


Figure 4.25: As in Figure 4.24, now with a larger distance between the drops.

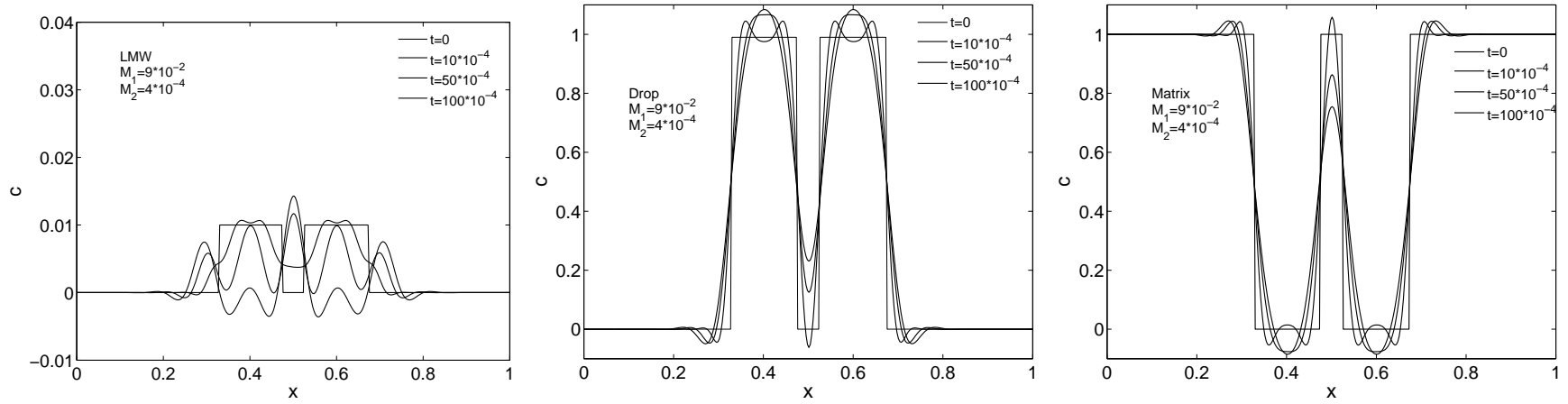


Figure 4.26: Concentration profiles in time for LMW component (left), drop (middle) and matrix (right) for a 1% in LMW concentrated blend. Mobility parameters: $M_1 = 9 \cdot 10^{-2}$ and $M_2 = 4 \cdot 10^{-4}$ (Case A).

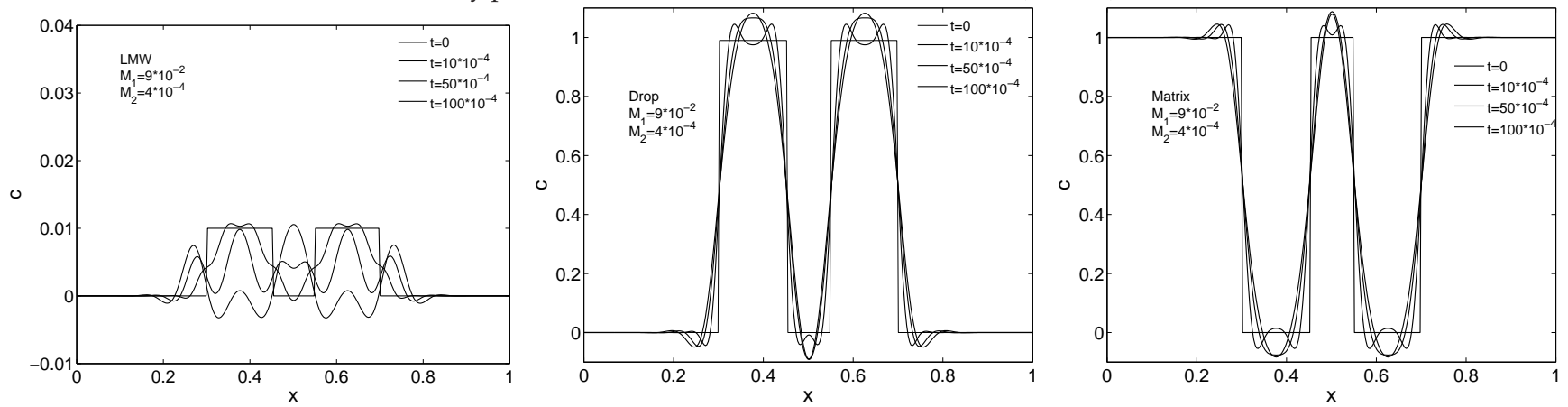


Figure 4.27: As in Figure 4.26, now with a larger distance between the drops.

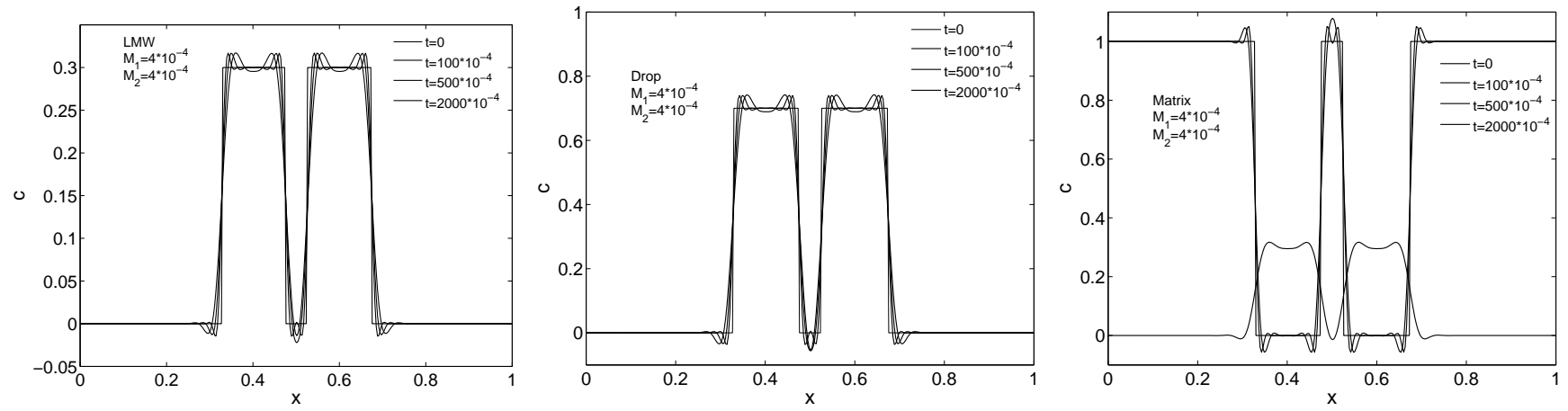


Figure 4.28: Concentration profiles in time for LMW component (left), drop (middle) and matrix (right) for a 30% in LMW concentrated blend. Mobility parameters: $M_1 = 4 \cdot 10^{-4}$ and $M_2 = 4 \cdot 10^{-4}$ (Case B).

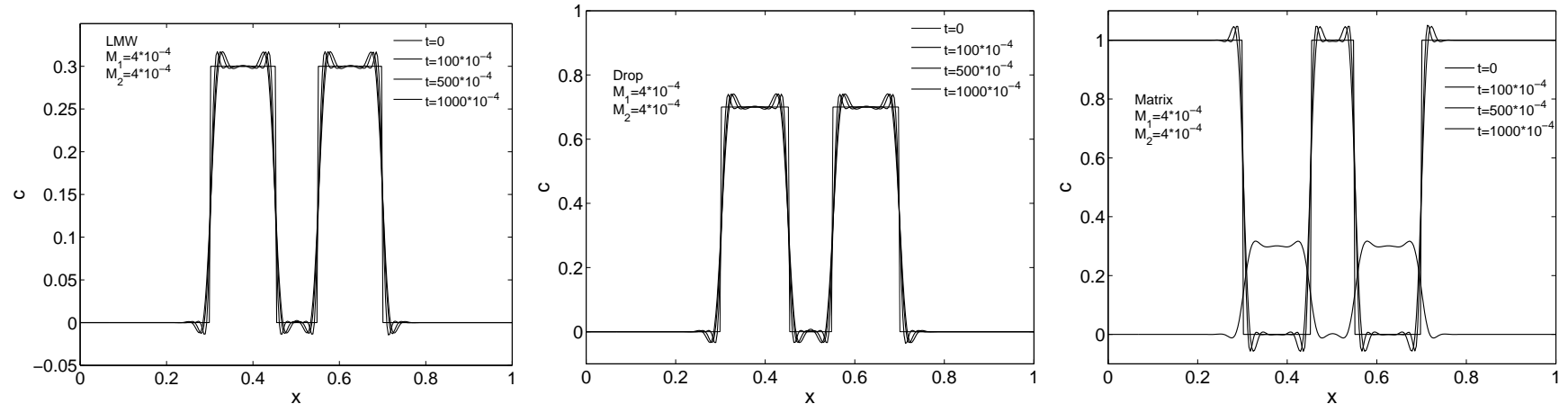


Figure 4.29: As in Figure 4.28, now with a larger distance between the drops.

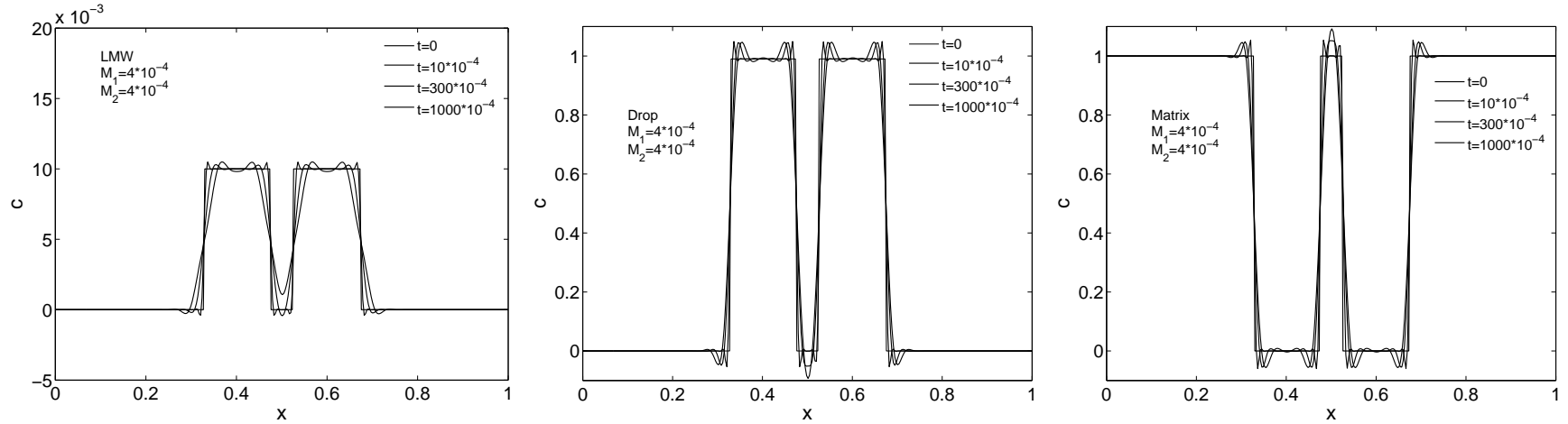


Figure 4.30: Concentration profiles in time for LMW component (left), drop (middle) and matrix (right) for a 1% in LMW concentrated blend. Mobility parameters: $M_1 = 4 \cdot 10^{-4}$ and $M_2 = 4 \cdot 10^{-4}$ are used.

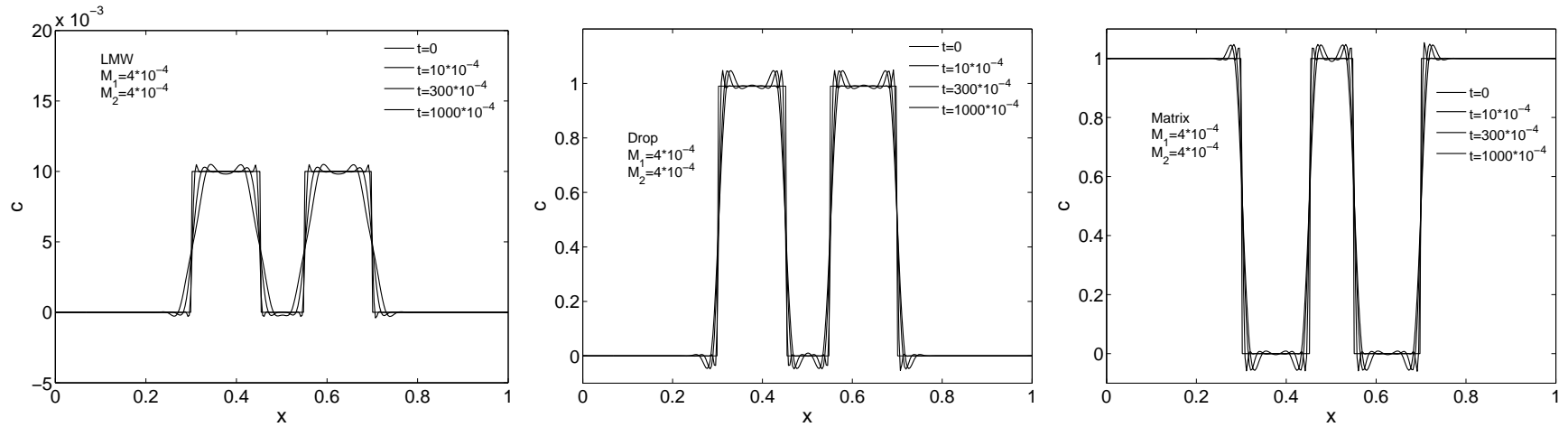


Figure 4.31: As in Figure 4.30, now with a larger distance between the drops.

Drop-wall interaction

From the drop-drop interaction results, and considering that the A30% and A1% systems have the right time-dependent behavior for the interfacial tension, these two systems seem to be preferable for investigating the drop-wall interaction of a highly-diffusive and a slightly-diffusive system, respectively. However, due to simplifications in our modeling, the A1% system shows, in the case of drop-wall interaction, results that can lead to erroneous conclusions, therefore, also the B30% is considered. The LMW-concentration contour profiles for these three cases are presented in Figures 4.32, 4.33, and 4.34, respectively. The A30% and the B30% show indeed the behavior that is anticipated from the drop-drop results: a clear interaction of the drop with the wall for the A30% case and a stationary drop for the B30% case. The A1% case also shows drop-wall interaction, although not as strong as the A30% case, see the concentration levels. This is also caused by the implicitly resulting (i.e. by not specifying it in the finite element model) 90° contact angle for the drop-wall interaction. To generate more realistic results, the modeling should be extended with an extra free-energy function at the wall that defines this contact angle [39]. For the drop-drop interaction the contact angle is not an issue. Also for these examples the concentration profiles over a line through the drop center and perpendicular to the wall are given, see Figures 4.35, 4.36, and 4.37, respectively. Since variation of the drop-wall distance did not give any new insight, no results are presented for these cases.

From these results it is concluded that the diffusive-interface model can generate, in a qualitative way, the phenomena observed in the experiments, even though a number of assumptions are used, and, therefore, is considered as good candidate to describe these phenomena also more quantitatively. For a more quantitative comparison, as discussed earlier, besides an experimentally validated free-energy formulation, also input for the mobility, viscosity and non-local interaction are needed.

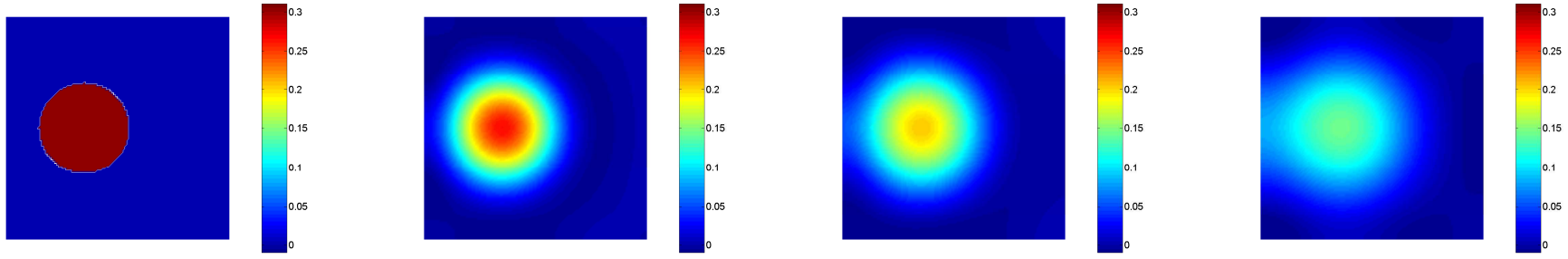


Figure 4.32: Concentration distribution of LMW component at time 0 , $100 \cdot 10^{-4}$, $200 \cdot 10^{-4}$, and $400 \cdot 10^{-4}$. The initial LMW concentration is 30%. Mobility parameters: $M_1 = 9 \cdot 10^{-2}$ and $M_2 = 4 \cdot 10^{-4}$ (Case A).

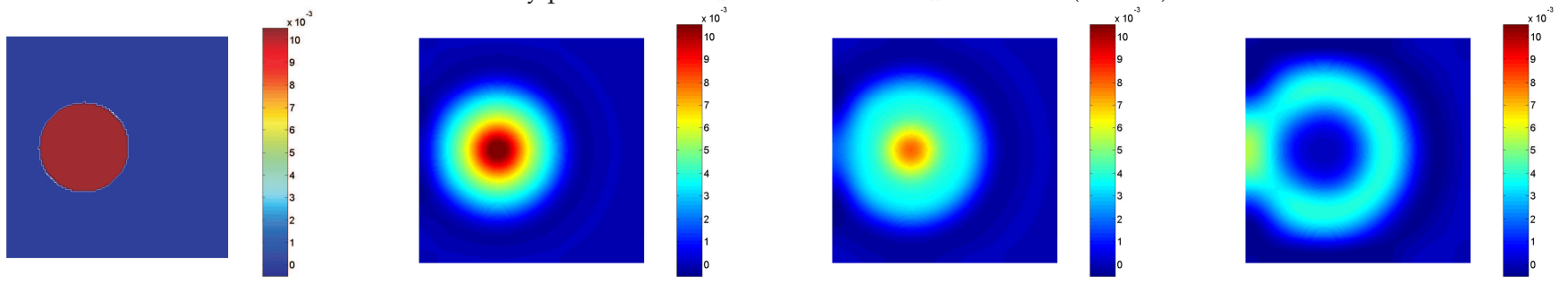


Figure 4.33: As Figure 4.18, now at time 0 , $10 \cdot 10^{-4}$, $20 \cdot 10^{-4}$, and $50 \cdot 10^{-4}$ and with 1% LMW concentration.

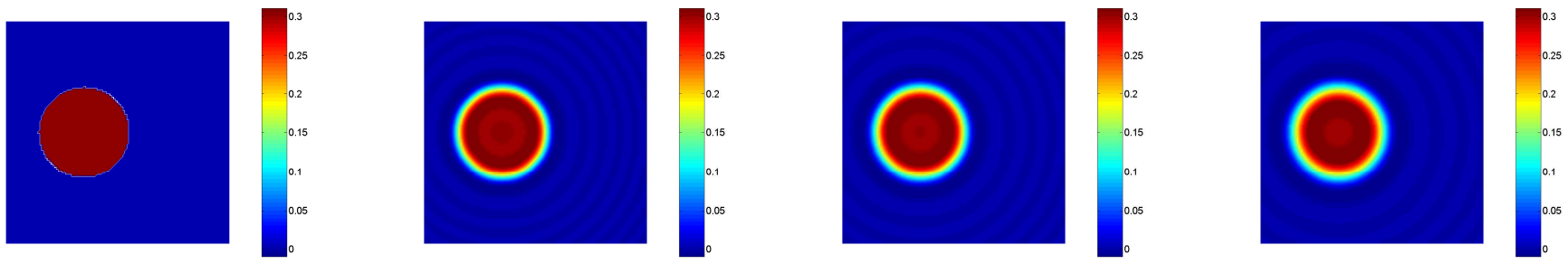


Figure 4.34: As Figure 4.18, now with mobility parameters $M_1 = 4 \cdot 10^{-4}$ and $M_2 = 4 \cdot 10^{-4}$ (Case B).

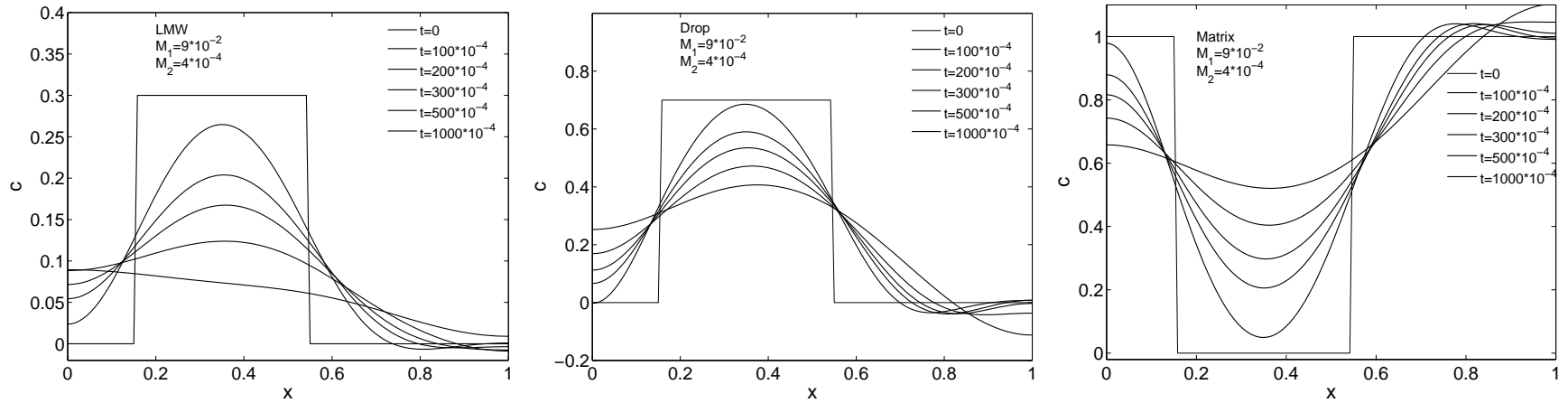


Figure 4.35: Concentration profiles in time for LMW component (left), drop (middle) and matrix (right) for a 30% LMW concentrated blend. Mobility parameters: $M_1 = 9 \cdot 10^{-2}$ and $M_2 = 4 \cdot 10^{-4}$ (Case A).

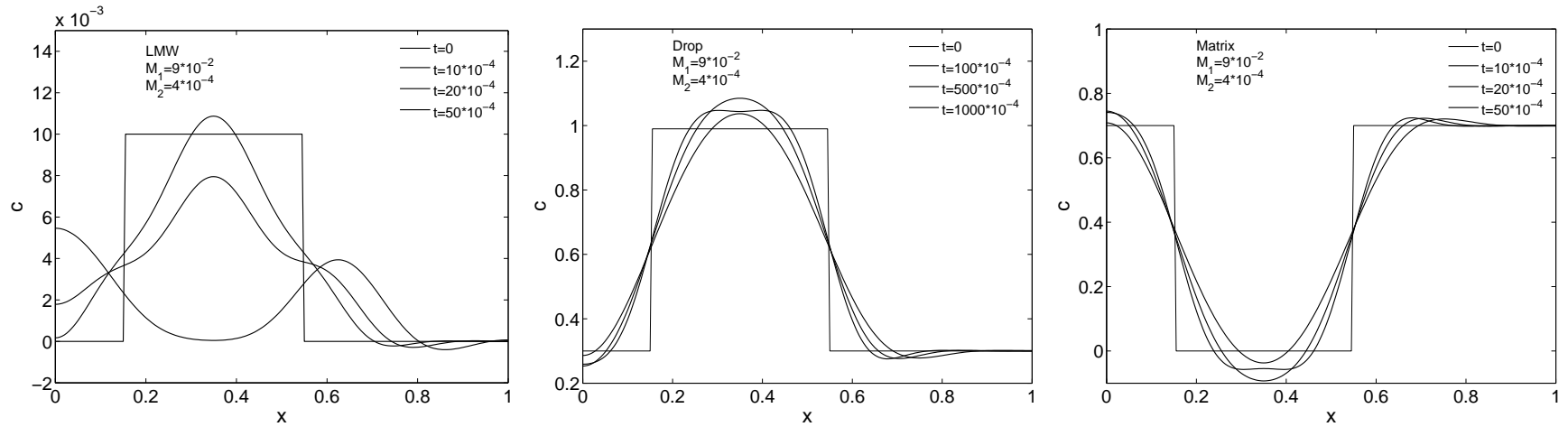


Figure 4.36: As Figure 4.35, now with 1% LMW concentration.

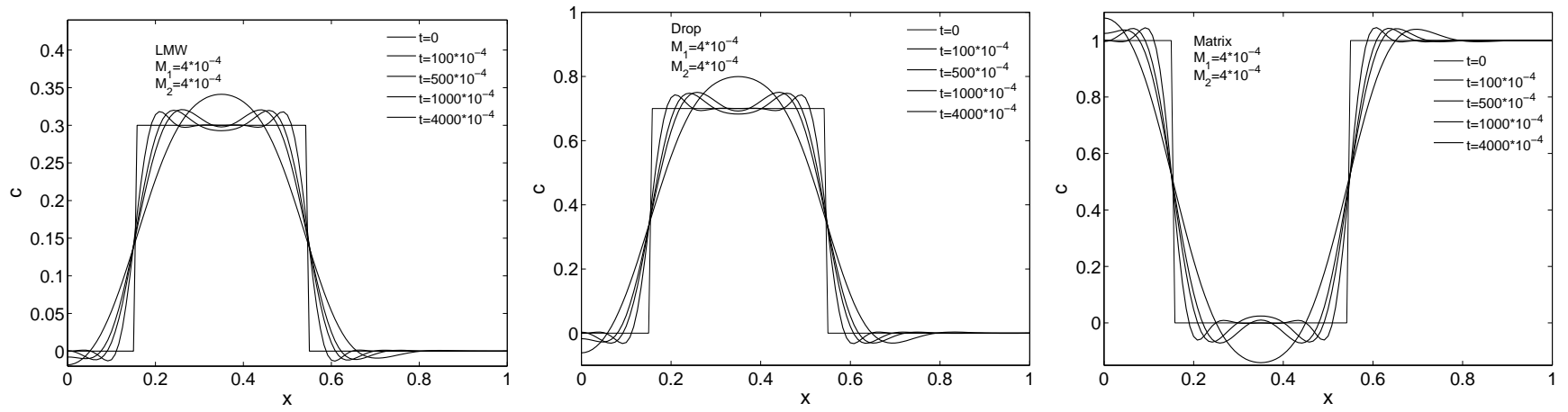


Figure 4.37: As Figure 4.35, now with mobility parameters $M_1 = 4 \cdot 10^{-4}$ and $M_2 = 4 \cdot 10^{-4}$ (Case B).

4.7 Conclusions

The effects of mutual diffusion on interfacial tension, drop-drop and drop-wall interactions in quiescent conditions are investigated experimentally and numerically. A highly-diffusive system (PB/PDMS) and a slightly-diffusive system (PBD/PDMS) are used at room temperature.

Just after contact between the phases is made, the transient interfacial tension of the highly-diffusive system reduces as a consequence of the LMW species migration from the drop into the interphase, yielding to the formation of a thick diffuse layer around the drop surface. While time proceeds, after reaching a minimum, the interfacial tension increases due to LMW species migration from the interphase into the matrix, leading to depletion of the diffusive layer. Once the diffusion process is exhausted, a plateau in interfacial tension is reached and sustained. The slightly-diffusive system, in contrast, shows only an increase in the interfacial tension, corresponding to migration of the fewer migrating molecules (polydispersity is close to one) into the matrix, followed by leveling off to a higher plateau value compared to the PB/PDMS system, which is attributed to the higher molecular weight of the drop phase.

By using a three-phase diffuse-interface model, implemented into the TFEM package, an in-house developed Finite Element code, these trends in transient interfacial tension are qualitatively predicted.

Drop-drop interaction experiments, carried out with isolated pairs of drops and in quiescent conditions, show that partial miscibility affects the final morphology of the system. Drops of the highly diffusive PB/PDMS system attract and coalesce when placed at initial distances smaller than their equivalent radius. The rate of attraction, in the last $\simeq 100$ s of the experiments, is the same for a wide range of drop sizes (radii ranging between $90 \mu m$ and $350 \mu m$) and different initial distances between them. The attraction is explained in terms of overlap of the diffusive layers around the drops, yielding gradients in interfacial tension and, thus, Marangoni flows acting in the film drainage direction, i.e. enhancing coalescence. When the slightly-diffusive system (PBD/PDMS) is considered, with a thin diffuse-interface, no attraction occurs and, when the drops are placed close together, repulsion between them is observed. Numerical simulations with a three-component diffuse interface method predict qualitatively drop-drop and drop-wall interactions, as observed in the experiments. However, for a more quantitative comparison, more studies are needed to define an experimentally validated free-energy formulation and realistic values to use as input parameters for our systems.

References

- [1] Tufano, C., Peters, G.W.M., Anderson, P.D., Meijer, H.E.H. (2008). Transient interfacial tension of partially-miscible polymers. *J. Coll. Int. Sci.*, **Submitted**.

- [2] Jones, R.A.L. and Richards, R.W. (1999). *Polymer at Surfaces and Interfaces*. Cambridge University Press.
- [3] Fortelny, I. and Kovar, J. (1988). Theory of coalescence in immiscible polymer blends. *Polym. Compos.*, **9**, 119–124.
- [4] Lyu, S.P., Bates, F.S., Macosko, C.W. (2000). Modeling of coalescence in polymer blends. *AIChE J.*, **48**, 7–14.
- [5] Elmendorp, J.J. and van der Vegt, A. (1986). A study on polymer blending micro-rheology: Part iv. the influence of coalescence on blend morphology origination. *Polym. Eng. Sci.*, **26**, 1332–1338.
- [6] Rusu, D. and Peuvrel-Disdier, E. (1999). In-situ characterization by small angle light scattering of the shear-induced coalescence mechanisms in immiscible polymer blends. *J. Rheol.*, **43**, 1391–1409.
- [7] Verdier, C. and Brizard, M. (2002). Understanding droplet coalescence and its use to estimate interfacial tension. *Rheol. Acta*, **43**, 514–523.
- [8] Vinckier, I., Moldenaers, P., Mewis, J. (1996). Relationship between rheology and morphology of model blends in steady shear flow. *J. Rheol.*, **40**, 613–631.
- [9] Shi, T., Ziegler, V.E., Welge, I.C., An, L., Wolf, B.A. (2004). Evolution of the interfacial tension between polydisperse “immiscible” polymers in the absence and in the presence of a compatibilizer. *Macromolecules*, **37**, 1591–1599.
- [10] Peters, G.W.M., Zdravkov, A., Meijer, H.E.H. (2005). Transient interfacial tension and dilatational rheology of diffuse polymer-polymer interfaces. *J. Chem. Phys.*, **122**, 104901–1–10.
- [11] Tufano, C., Peters, G.W.M., Van Puyvelde, P., Meijer, H.E.H. (2008). Transient interfacial tension and morphology evolution in partially-miscible polymers. *J. Coll. Int. Sci.*, **Submitted**.
- [12] Klaseboer, E., Chevaillier, J.P., Gourdon, C., Masbernat, O. (2000). Film drainage between colliding drops at constant approach velocity: Experiments and modeling. *J. Coll. Int. Sci.*, **229**, 274–285.
- [13] Chevaillier, J.P., Klaseboer, E., Masbernat, O., Gourdon, C. (2006). Effect of mass transfer on the film drainage between colliding drops. *J. Coll. Int. Sci.*, **299**, 472–485.
- [14] Hu, Y., Pine, D., Leal, L.G. (2000). Drop deformation, breakup, and coalescence with compatibilizer. *Phys. Fluids*, **12**, 484.
- [15] Scriven, L.E. and Sternling, C.V. (1960). The Marangoni effects. *Nature*, **187**, 186–188.
- [16] Levich, V.G. and Krylon, V.S. (1969). Surface-tension-driven phenomena. *Annu. Rev. Fluid Mech.*, **1**, 293–316.
- [17] Mackay, G.D.M. and Mason, S.G. (1963). The gravity approach and coalescence of fluid drops at liquid interfaces. *J. Chem. Eng.*, **41**, 203–212.
- [18] Pu, B. and Chen, D. (2001). Studies on the binary coalescence model i. jumping coalescence phenomenon. *J. Coll. Int. Sci.*, **235**, 1–3.
- [19] Chen, D. and Pu, B. (2001). Studies on the binary coalescence model ii. effects of drops size and interfacial tension on binary coalescence time. *J. Coll. Int. Sci.*, **243**, 433–443.

- [20] Velvet, O.D., Gurkov, T.D., Ivanov, I.B., Borwankar, R.P. (1995). Abnormal thickness and stability of nonequilibrium liquid films. *Phys. Rev. Lett.*, **75**, 264–267.
- [21] Zdravkov, A., Peters, G.W.M., Meijer, H.E.H. (2003). Film drainage between two captive drops: PeoŪwater in silicon oil. *J. Coll. Int. Sci.*, **266**, 195–201.
- [22] Zdravkov, A., Peters, G.W.M., Meijer, H.E.H. (2006). Film drainage and interfacial instabilities in polymeric systems with diffuse interfaces. *J. Coll. Int. Sci.*, **296**, 86–94.
- [23] Poisson, S.D. (1831). *Nouvelle Théorie de l'Action Capillaire*. Paris: Bachelier.
- [24] Maxwell, J.C. (1876). *Capillary action*. In *Encyclopaedia Britannica*, 9th ed. Reprinted in 1952. *The Scientific Papers of James Clerk Maxwell*. New York: Dover.
- [25] Gibbs, J.W. (1876–1878). *On the equilibrium of heterogeneous substances*. 3:108-248 and 3:343-524. Reprinted in 1906. *The Scientific Papers of J. Willard Gibbs*, pp. 55–371. London: Longmans, Green.
- [26] Rayleigh, L. (1892). *On the theory of surface forces-II. Compressible fluids*,. *Phil. Mag.*
- [27] van der Waals, J.D. (1979). The thermodynamic theory of capillarity under the hypothesis of a continuous density variation. *J. Stat. Phys.*, **20**, 197–244.
- [28] Anderson, D.M., McFadden, G.B., Wheeler, A.A. (1998). Diffuse-interface methods in fluid mechanics. *Annu. Rev. Fluid Mech.*, **30**, 139–165.
- [29] Cahn, J.W. and Hilliard, J.E. (1958). Free energy of a nonuniform system. i. interfacial free energy. *J. Chem. Phys.*, **28**, 258–267.
- [30] Verschueren, M. (1999). *A diffuse-interface model for structure development in flow*. PhD thesis, Technical Univ. of Eindhoven, Eindhoven, The Netherlands.
- [31] keestra, B.J. (2004). *Computational and experimental analysis of structure development in two-phase polymer systems*. PhD thesis, Technical Univ. of Eindhoven, Eindhoven, The Netherlands.
- [32] Lowengrub, J. and Truskinovsky, L. (1998). Quasi-incompressible Cahn-Hilliard fluids and topological transitions. *Proc. R. Soc. Lond., Ser. A*, **454**, 2617–2654.
- [33] Kim, J., Kang, K., Lowengrub, J. (2004). Conservative multigrid methods for ternary Cahn-Hilliard systems. *Comm. Math. Sci.*, **2**, 53–77.
- [34] Kim, J. and Lowengrub, J. (2005). Phase field modeling and simulation of three-phase flows. *Int. Free Bound.*, **7**, 435–466.
- [35] Keestra, B.J., Van Puyvelde, P., Anderson, P.D., Meijer, H.E.H. (2003). Diffuse interface modeling of the morphology and rheology of immiscible polymer blends. *Phys. Fluids*, **15(9)**, 2567–2575.
- [36] Khatavkar, V.V., Anderson, P.D., Meijer, H.E.H. (2006). On scaling of diffuse interface models. *Chem. Eng. Sci.*, **61**, 2364–2378.
- [37] Amestoy, P.R. and Duff, I.S. (1989). *Int. J. Supercomputer Appl.*, **7**, 64.
- [38] Amestoy, P.R. and Puglisi, C. (2002). *SIAM J. on Matrix Anal. and Appl.*, **24**, 553.
- [39] Khatavkar, V.V., Anderson, P.D., Meijer, H.E.H. (2007). Capillary spreading of a droplet in the partially wetting regime using a diffuse-interface model. *J. Fluid Mech.*, **572**, 367–387.

Study of morphological hysteresis in *partially-miscible* polymers¹

The morphology evolution of two systems of *partially-miscible* polymers is investigated by means of rheological experiments and optical microscopy. The systems differ in the miscibility of the components and two different concentrations are used for each. For *immiscible* model systems the presence of an hysteresis zone, confined between the coalescence and break-up lines, is reported, where the average drop radius is no longer an unique function of the shear rate. The goal here is to investigate whether these findings also apply to *partially-miscible* polymers. The average radii resulting from rheological experiments at different shear rates are compared to coalescence and break-up model predictions. The hysteresis zone, if present, is indeed affected by the polymer system, the concentration of the dispersed phase, and the flow history applied. Coalescence events are followed in time using a protocol with three different step-downs in shear rate. For both the 10% concentrated systems, the resulting average radii show a quite high scattering and do not match the theoretical predictions. When the concentration is increased to 20%, the average experimental drop sizes seem independent of the magnitude of the step-down in shear rate, at least during a certain period of time. Thereafter it experiences a sudden, in the time scale of the experiments unbounded, increase in size which is more pronounced for the higher step-downs in shear rate. Deviations of the experimental data from theoretical predictions are attributed to the partial miscible character of the systems, yielding enhanced coalescence which, in turn, can induce confinement effects.

¹Reproduced from: Tufano, C., Peters, G.W.M., Van Puyvelde, P., Meijer, H.E.H., Study of morphological hysteresis in *partially-miscible* polymers. *Rheol. Acta*, submitted.

5.1 Introduction

The steady-state morphology of blends obtained by mixing *immiscible polymers* has been found to be a unique function of the flow history applied, while preparing and processing the blend, and it is considered as the result of a dynamic equilibrium between two competing phenomena: break-up and coalescence [1,2]. Both processes are determined by two dimensionless numbers: the capillary number $Ca = \eta_m \dot{\gamma} R / \sigma$, with η_m the viscosity of the matrix phase, $\dot{\gamma}$ the shear rate, R the drop radius, and σ the interfacial tension of the polymer pairs, and the viscosity ratio $p = \eta_d / \eta_m$ where η_d is the viscosity of the dispersed phase. Grace [3] devoted his life to determine how the critical capillary number, defined as the capillary number at which break-up of a single drop occurs, depends on the viscosity ratio, defining in shear and extensional flows the limiting condition for break-up to occur. Concerning the flow-driven coalescence limit for two droplets, Chesters [4] proposed a probability of coalescence based on the interaction time during the collision of drops and the time needed to drain the matrix film trapped between them. Based on the mobility of the interface (*fully mobile, partially mobile and immobile*) three different expressions to calculate, for a given shear rate, the maximum radius above which coalescence does not longer occur, were proposed. Also some experimental studies on the effects of simple shear flow on the morphology evolution in immiscible polymer blends have been carried out. Elmendorp [5] showed that the equilibrium between break-up and coalescence can be reached only for shear rates higher than the critical one, which is defined as the shear rate at which the theoretical limiting curves for break-up and coalescence cross. Grizzuti and Bifulco [6], Vinckier et al. [7], and Minale et al. [8,9] showed, by means of rheological experiments and optical microscopy (OM), that the steady-state morphology is reached only after a certain critical shearing time. However, Janssen [10] reported that flow conditions might exist in which more than one morphology is possible. For shear rates below the critical one, the dynamic equilibrium between break-up and coalescence can not be reached, or, at least, not in a reasonable shearing time. In that case there exists a pseudo-equilibrium zone, in which the morphology depends on the initial conditions and neither break-up nor coalescence occurs. Minale et al. [8] demonstrated the existence of this hysteresis zone with a model blend at fixed concentration. They showed that when the average drop radius in the blend is larger than the one predicted by coalescence limits, and lower than the break-up model prediction at the same experimental shear rate, multiple steady-state morphologies, or pseudo steady-state morphologies, are possible. The final morphology was shown not only to depend on the characteristics of the blend components and history of flow, but also on the initial conditions. The effects of viscosity ratio and concentration of the blend have been studied by Minale et al. [9] for the same model system. They showed that the hysteresis region shifts to smaller shear rates and narrows with increasing the concentration of the dispersed phase. Apart from the aforementioned studies, several others can be found in

literature, all concerning the coalescence in *immiscible* polymer blends [11–14].

In this study we investigate the occurrence of a hysteresis zone and the flow-driven coalescence behavior for two *partial miscible* polymer systems, having different diffusivity. The effect of the flow history applied, initial conditions, and concentration of the blends are investigated by means of rheological measurements and optical microscopy (OM). The measured morphology evolution is compared to theories available in literature for break-up and coalescence. The use of dynamic measurements as an experimental morphology probing method is critically re-examined.

5.2 Materials and methods

Materials

The blends investigated are prepared using as disperse phase polybutene (PB, Indopol H-25, BP Chemicals, UK) and polybutadiene (PBD, Ricon 134, Sartomer) respectively, while polydimethylsiloxane (PDMS, UCT) is chosen as continuous phase. These three materials are liquid and transparent at room temperature, and they exhibit almost matched refractive indices, leading to a limited turbidity of the blends, which allows rheo-optical experiments. The densities (ρ) of the materials are measured at 23°C by means of a digital density meter (DMA 5000, Anton Paar) and, due to the small differences in the density values of the dispersed and continuous phases, buoyancy effects can be neglected given the time scale of the experiments. Zero shear viscosities (η) are measured at 23°C using a rotational rheometer (Rheometrics, ARES) equipped with a parallel-plate geometry and applying steady shear rates. The viscosity of the pure components is independent of shear rate in the whole range of shear rates applied. In addition, the first normal stress difference is too small to be measured with our equipment. The steady interfacial tensions (σ) are measured at room temperature by means of a pendant drop apparatus (PAT-1, Profile Analysis Tensiometer, Sinterface, Germany). The average molecular weight (M_n), densities and viscosities of the phases, and the interfacial tensions of the two polymer pairs at room temperature are shown in Table 5.1. Two different concentrations (10% and 20% mass fraction of PB and PBD respectively) are investigated, and mixing is performed following the protocol proposed by Takahashi et al. [1] and Vinckier et al. [2].

Table 5.1: Selected model components.

Sample	M_n	ρ	η	σ
drop/matrix	[g/mol]	[g/cm ³]	[Pa · s]	[mN/m]
PB/PDMS	635/62700	0.87/0.99	3.7/10.9	$2.2 \cdot 10^{-3}$
PBD/PDMS	8000/62700	0.89/0.99	13.6/10.9	$4.2 \cdot 10^{-3}$

Experimental methods

To erase influence of preparation and loading, all systems are preconditioned at the beginning of each experiment by shearing them for a time sufficiently long to obtain a steady state morphology. The total minimum strain required is determined in advance, using transient stress relaxation tests that are suitable for this purpose given their sensitivity to the initial morphology [1]. For our systems, the strain units required are found to be between 2500 and 3000. In all experiments we used a stress controlled rheometer (Rheometrics DSR) equipped with a cone and plate geometry (cone diameter 40 mm and cone angle 0.04 rad) and a Peltier element to control the temperature, set to 23°C, within an accuracy of $\pm 0.1^\circ\text{C}$.

After pre-shearing, the flow is stopped and oscillatory tests are performed to obtain the elastic modulus at frequencies varying from 0.1 till 100 rad/s. Subsequently a new steady shear, at a different shear rate, is applied. Experiments are carried out with both increasing and decreasing shear rates. In the case shear rates are decreased, drops coalesce and, therefore, the average radii measured in this way, are expected to follow the predictions from coalescence theory. In the opposite case, break-up dominates and results are compared to the break-up predictions.

When investigating the effect on coalescence of different step-downs in shear rate, the sample is first preconditioned at an initial shear rate of 8s^{-1} during 1250s (≈ 10000 strain units). Next the desired step-down in the shear rate is applied whereafter the flow is stopped at different time intervals from the step-down to perform the dynamic tests that ultimately yield the average drop radii. Indeed a small strain oscillatory flow does not affect the morphology [2, 15–17]. Optical microscopy (OM) is performed to interpret some of the results and to check the actual drop size.

Morphology probing using dynamic measurements

For the pure components the value of storage modulus G' is zero. The blends show a typical linear viscoelastic behavior, with a non-zero G' , even at the smallest concentrations investigated. Figure 5.1 left shows the elastic moduli of the blend measured upon cessation of the flow, after pre-shearing at a shear rate of 2s^{-1} and 0.1s^{-1} for 3000 strain units, respectively, showing a shoulder at low frequencies, that accounts for a relaxation process caused by a perturbation of the shape of the dispersed droplets during the oscillatory flow. Different pre-shear rates result in different morphologies yielding different elastic moduli. Lowering the pre-shear rate makes the shoulder to move to lower frequencies indicating that larger droplets form at these lower shear rates.

To find the average drop diameter in the blend from dynamic measurements, the continuous relaxation spectrum is calculated from the dynamic moduli using a non linear regression program (NLREG) [18], see Figure 5.1 (right). The initial part of the spectra is identical and it reflects the contribution of the pure components. We are interested in the relaxation time τ corresponding to the peak which is characteristic

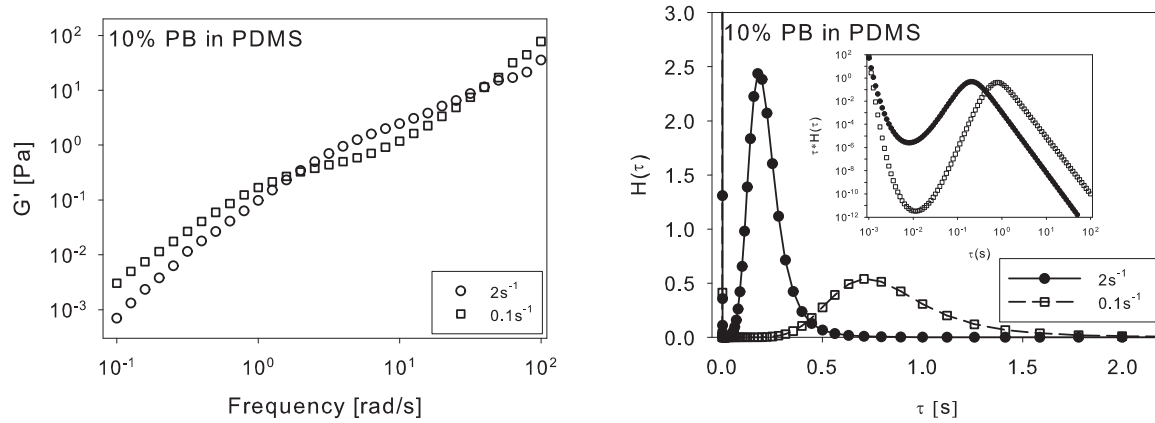


Figure 5.1: Storage moduli (left), relaxation spectra and weighted relaxation spectra (inset plot) (right) upon cessation of flow after shearing at $\dot{\gamma} = 2\text{s}^{-1}$ and $\dot{\gamma} = 0.1\text{s}^{-1}$ for 3000 strain units for a 10 wt % PB in PDMS blend.

for drop relaxation. The average droplet size R can be calculated from this relaxation τ using an approximate equation proposed by Graebling et al. [16], as derived from the emulsion model of Palierne [19]:

$$\tau = \frac{\eta_m R (19p + 16)(2p + 3 - 2\phi(p + 1))}{4\sigma (10(p + 1) - 2\phi(5p + 2))}, \quad (5.1)$$

where p is the viscosity ratio ($p = \eta_d / \eta_m$, with η_d the viscosity of the dispersed phase, and η_m the viscosity of the continuous phase), ϕ the volume fraction and σ is the interfacial tension. Although the value of τ can be directly obtained from the relaxation spectrum, as the time at which $H(\tau)$ is maximum, a different approach was proposed by Gramespacher and Meissner [15]. They suggested to plot the weighted time relaxation spectrum, $\tau \cdot H(\tau)$ vs τ , and to use the time at which this curve reaches the maximum as the relaxation time of the drops. The use of the first moment of the relaxation spectrum amplifies the contribution of slower processes, thus enhancing effects of the interfacial relaxation process. The inset plot in Figure 5.1 right shows the weighted relaxation spectra at the two shear rates considered. In both procedures a longer relaxation time and a lower maximum is found for the lower shear rate. While the relaxation time is linked to the average size of the inclusions, the magnitude of the maximum in the relaxation spectrum, as well as in the weighted relaxation spectrum, contains information on the amount of interfacial area. Decreasing the shear rate, coalescence is promoted, and, due to the constant fraction of dispersed phase, the morphology evolution will lead to less and larger drops which require longer times to relax, see Eq. 5.1. Fewer large drops imply, on the other hand, less interfacial area, which reduces the magnitude of the maximum, see Figure 5.1 right. Figure 5.2 shows the average droplet radii for the 10% PB/PDMS blend calculated using

Eq. 5.1 with the relaxation time retrieved from the time relaxation spectra and from the weighted time relaxation spectra, respectively. Experiments are performed while decreasing the pre-shear rate. Clearly, both procedures give similar results (within experimental error), indicating that the average radii obtained are a good indication of the blend morphology. However, we experienced that for the weighted relaxation spectra the amplification of the slow relaxation phenomena was often more clearly present, which makes the analysis more precise. Therefore, this procedure is used. Vinckier et al. [2] proposed a further improved approach, based on the assumption that the contribution of the different relaxation processes involved are additive. The time relaxation spectra of the pure components, weighted by their volume fraction, were subtracted from the blend time relaxation spectrum, influencing the position of the maximum in $H(\tau)$, and, therefore, the predicted average radius. However, since in our cases the relaxation of the pure components is much faster than that of the interface, these corrections is not needed here.

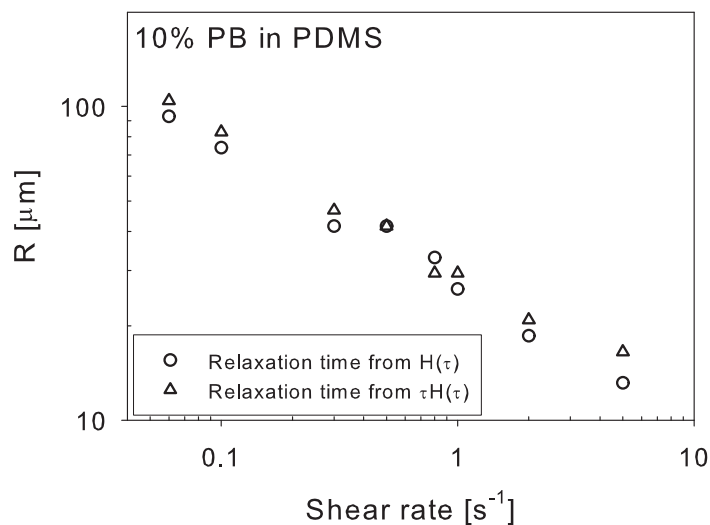


Figure 5.2: Calculated average radii (Eq. 5.1), 10 wt% PB in PDMS blend, for decreasing shear rate. Radii from relaxation time spectra (circles) and weighted relaxation time spectra (triangles).

5.3 Hysteresis zone

Theories to probe morphological hysteresis

The morphology resulting from dynamic experiments is compared to break-up and coalescence theories. At a fixed shear rate, the flow is able to break-up drops with

sizes above a critical value, whereas, drops with smaller radii, will collide and eventually coalesce. Grace [3] experimentally found the critical size of a droplet, for a fixed shear rate, above which break-up occurs and below which coalescence dominates. Based on Grace's experimental results, De Bruijn [20] suggested a fitted curve:

$$\log\left(\frac{\eta_m \dot{\gamma} R}{\sigma}\right) = -0.506 - 0.0994 \log(p) + 0.124 \log^2(p) - \frac{0.115}{\log(p) - \log(p_{cr})}, \quad (5.2)$$

where $p_{cr} = 4.08$ is the viscosity ratio above which break-up is no longer possible, at least in a start-up shear flow, $\dot{\gamma}$ is the shear rate, and R is the average drop radius in the blend. Theories and numerical models support the experimental data [21–24]. Also the coalescence process has been modeled and different mobilities of the sharp interfaces (from mobile to partially mobile and fully immobile) are distinct, greatly influencing the drainage rate. Also the more physical diffuse interfaces have obtained a lot of attention (via DIM, diffuse interface modeling) and while for break-up excellent results are obtained the spatial resolution of the mesh makes coalescence events occurring too fast [25–27]. The drainage model for sharp interfaces is chosen here. The maximum radius below which coalescence occurs is estimated for the case of a immobile interface (IM) and partially mobile interface (PM) [4]:

$$IM \quad R = \left(\frac{32}{9}\right)^{1/4} \cdot \left(\frac{h_{cr}^{1/2} p}{\eta_m \cdot \dot{\gamma}}\right)^{-1/2}, \quad (5.3)$$

$$PM \quad R = \left(\frac{4}{\sqrt{3}} \frac{h_{cr}}{p}\right)^{2/5} \cdot \left(\frac{\sigma}{\eta_m \cdot \dot{\gamma}}\right)^{3/5}, \quad (5.4)$$

where h_{cr} is the critical film thickness. The maximum drop radius above which coalescence does not occur is a function of the coalescence conditions, the viscosity ratio p and the interfacial tension. In the original paper of Mackay and Mason [28] the drainage time refers to a droplet coalescing on a flat surface while, in our experiments, coalescence occurs between two droplets. To account for that, Eq. 5.3 is corrected by a factor 4. The main difficulty is to find an adequate value for the critical film thickness of the matrix trapped between two coalescing drops, h_{cr} . A possibility is to calculate this parameter, e.g. using the formulation proposed by Chesters [4]:

$$h_{cr} \approx \left(\frac{AR}{8\pi\sigma}\right)^{1/3}, \quad (5.5)$$

where A is the Hamaker constant. Since theories are derived for isolated pairs of

droplets, when dealing with concentrated blends, some authors choose to use the h_{cr} as an adjustable parameter. It then contains all the uncertainties and approximations of the model and, to a certain extent, it is a function of the concentration [8,9]. We will use a fixed value for each system based on Eq. 5.5 and use only the predictions of the PM model.

Hysteresis results

To draw the coalescence line to theoretically bound the hysteresis zone, a value for the critical film thickness, h_{cr} , which changes with the radius (see Eq. 5.5), is required. To choose, sensitivity analysis is performed. The average radii observed in our hysteresis experiments mostly range between $5 \cdot 10^{-6} m$ and $150 \cdot 10^{-6} m$ for both blends, which, according to Eq. 5.5, lead to the h_{cr} values shown in Table 5.2. The variations of the average drop radius, predicted by the PM model (Eq. 5.4) using these h_{cr} values are small only, see Figure 5.3, which basically allows us to use a constant, concentration-independent, value of h_{cr} for each of the two systems. We choose to use the values corresponding to the average radius of $50 \cdot 10^{-6} m$ to investigate the existence and size of the hysteresis zone.

Table 5.2: Critical film thickness h_{cr} calculated with Eq. 5.5 for the PB/PDMS and PBD/PDMS systems, for three different average drop radii R .

$R [m]$	$h_{cr}^{PB} [m]$	$h_{cr}^{PBD} [m]$
$5 \cdot 10^{-6}$	$1 \cdot 10^{-8}$	$0.8 \cdot 10^{-8}$
$50 \cdot 10^{-6}$	$2 \cdot 10^{-8}$	$1.7 \cdot 10^{-8}$
$150 \cdot 10^{-6}$	$3 \cdot 10^{-8}$	$2.5 \cdot 10^{-8}$

PB in PDMS

The average radii measured for the 10 wt % PB in PDMS system, at increasing and decreasing shear rates, are shown in Figure 5.4 (top) and compared to the model predictions for break-up (solid line) and coalescence (dashed line). At the lowest shear rate, the morphology is independent of the flow history applied; the same pseudo steady-state value is found for decreasing and increasing shear rates. We use $h_{cr} = 2 \cdot 10^{-8} m$ (Eq. 5.5) which is larger than the one reported by Tufano et al. [29] for the same blend but in that work with a concentration of 1%, $h_{cr} = 0.36 \cdot 10^{-8} m$. Increasing h_{cr} values with increasing concentration were also reported in [8,9] and two possible explanations were given: a) the influence of dust particles present in the blend, or b) the theory behind Eq. 5.4 is derived for a single pair of drops and not for more concentrated systems, where a coalescence event between two drops influences those in neighboring drops [30], and collision between drops are more frequent and

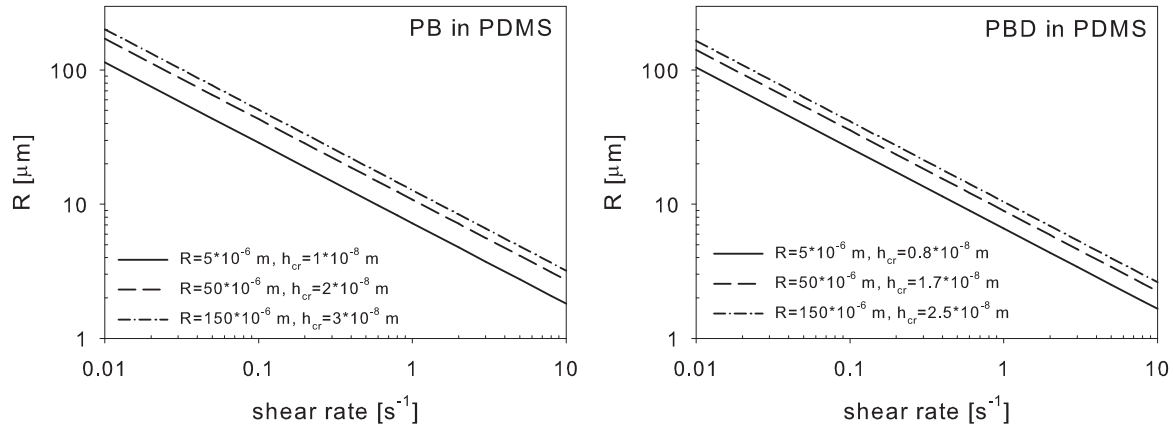


Figure 5.3: Influence of different radii, and the corresponding h_{cr} values (Eq. 5.5), on the average radii calculated with the PM model (Eq. 5.4) for the PB/PDMS system (left) and PBD/PDMS system (right).

last longer than for two isolated drops meeting in a shear flow. However, according to the model behind Eq. 5.5, the time available for the drainage is proportional to $\dot{\gamma}^{-1}$ which is fixed for a given flow. By accounting for concentration effects through larger h_{cr} values, the critical film thickness h_{cr} loses its physical meaning. It becomes a fitting parameter only and contains all the uncertainty in the model and the effects of the concentration.

Results in Figure 5.4 (top) show that, at shear rates lower than the critical one (the shear rate at which the break-up and coalescence curves cross), the hysteresis zone observed is not according to the theoretical expectations. For a decreasing shear rate, the experimental coalescence results run parallel to the theoretical curve but the radii are larger. With increasing shear rate, instead of just crossing the hysteresis zone and following the break-up line, the drop radius is decreasing with a seemingly constant slope and the results extend beyond the break-up line. For the PB-PDMS system it is, unfortunately, not possible to shear the sample at shear rates higher than the critical one due to the occurrence of shear fracture. To check whether the morphology evolution depends on the strain units of shear, the same experiments are repeated, shearing the blend for 10000 strain units. The results are in good agreement with the data for 3000 strain units, indicating that, in this case, there is no influence of the shearing time on the average radii. As a second check on the question whether the deviation from theory is real, the same flow history is applied in optical microscopy (OM) experiments. While the rheological measurements are conducted with a cone and plate geometry, the OM measurements are performed with a plate-plate configuration. The gap between the plates is set to $400 \mu\text{m}$ to limit the occurrence of confinement effects [31]. OM pictures acquired at three different shear rates are shown in Figure 5.5. The average radii (triangles) and the largest drop radius (signed triangles) resulting from the OM experiments are also plotted in Figure 5.4.

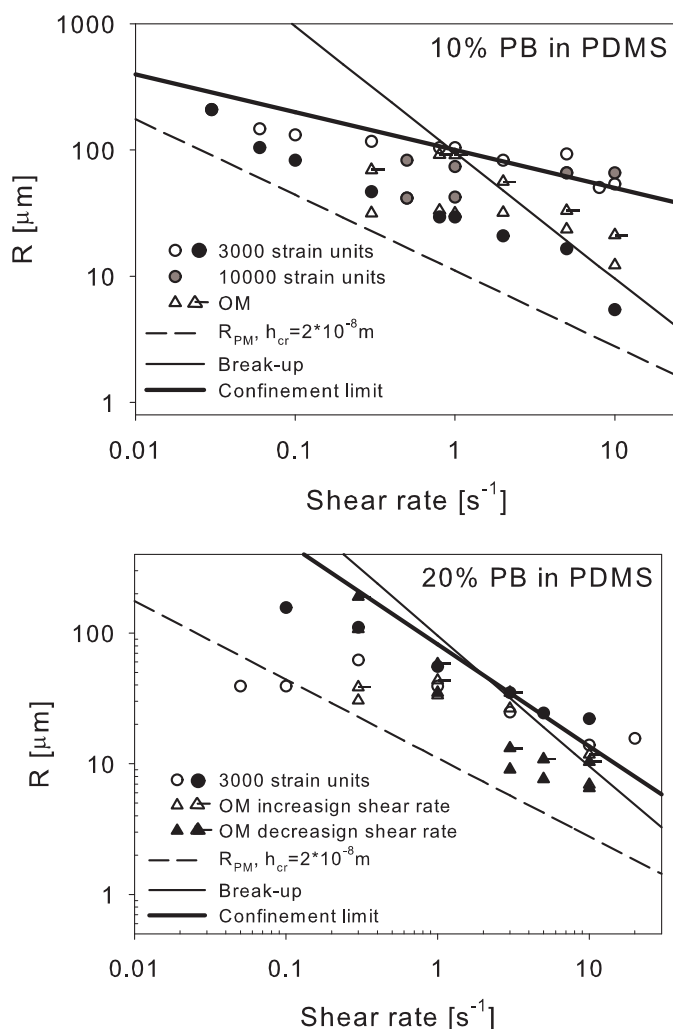


Figure 5.4: Average radii obtained by using Eq. 5.1 and relaxation times from weighted relaxation spectra, after shearing for 3000 (circle) and 10000 (gray filled circle) strain units for the 10% PB/PDMS system (top) and after shearing for 3000 (circle) strain units for the 20% PB/PDMS system (bottom). Results obtained while increasing (open symbols) and decreasing (filled symbols) pre-shear are shown. Triangles are the average radii, signed triangle the largest radii from OM results. The theoretical limiting curves for break-up (solid line, Eq. 5.2), coalescence using the PM model (dashed line, Eqs. 5.4 and 5.5) and confinement effects (thick solid line) are shown.

The morphology depicted in Figure 5.5 shows large droplets among much smaller ones, especially at the lower shear rates; the droplet distribution seems to be bimodal. At higher shear rates the drop radius distribution becomes more uniform. Since in Figure 5.4 the largest drop radii show the same trend as those obtained from rheology (although they are smaller), it follows that the rheological data mostly account

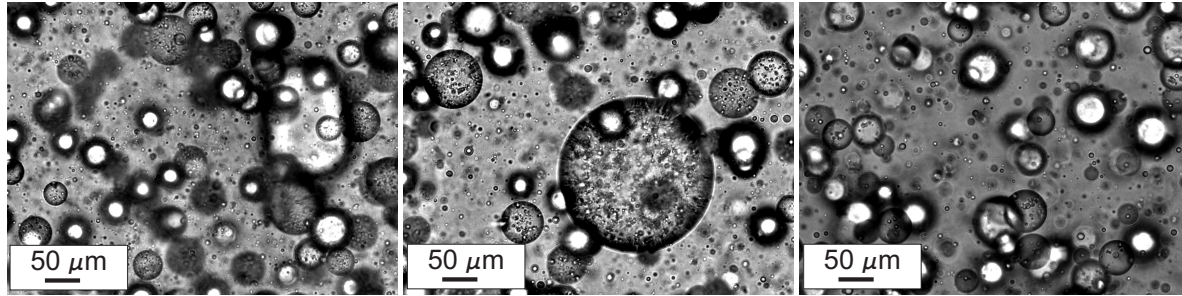


Figure 5.5: Morphology of the 10 wt % PB in PDMS blend at increasing shear rates of 0.3, 0.8, and 5 s^{-1} (left to right).

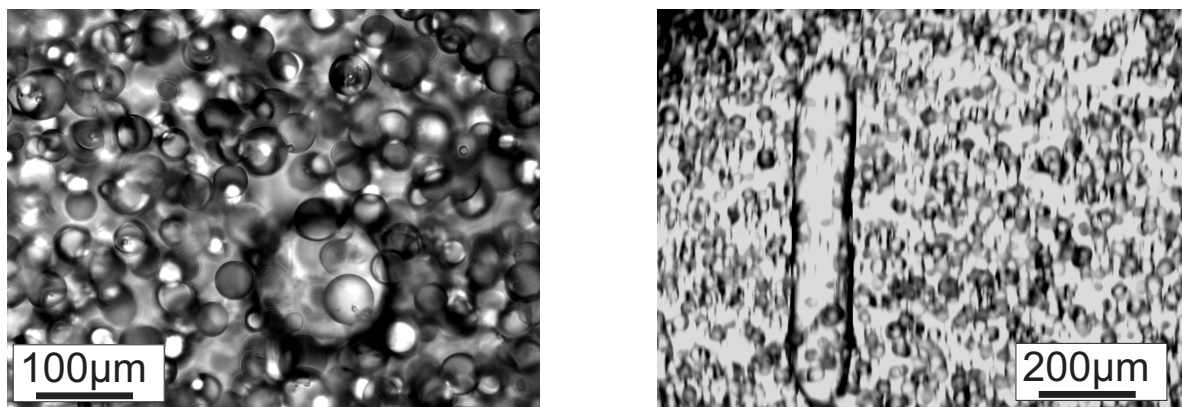


Figure 5.6: Morphology of the 20 wt % PB in PDMS blend at decreasing shear rates of 1 and 0.3 s^{-1} (left to right).

for the relaxation times of the largest droplets, giving an estimated average radius in the blend larger than the effective one.

The data for the 20% PB/PDMS blend are rather scattered (see Figure 5.4 (bottom)) and the results become even more complicated for this higher concentration. A narrowing of the hysteresis zone is observed, in accordance with [9]. The data for increasing and decreasing shear rates almost coincide (within experimental error), i.e. the morphology seems to become independent of the flow history. However, similar phenomena as for the 10% PB/PDMS blend are observed; drop radii are found that are above the break-up line and large droplets which will excessively contribute to the rheology (yielding an overestimation of the average radius) are also found with OM. In contrast to a number of published results we do not find a good agreement between theory and average radius from dynamic measurements. Although our results are somewhat scattered, trends are clear. In an attempt to interpret them, two effects are considered that might help their explanation: (i) for partial miscible blends coalescence is drastically increased [32] which leads to large drops after a step-down in shear rate, (ii) on the other hand, confinement of flows can cause phenomena like droplet ordering, string formation, etc. [31, 33–36]. Large drops, as observed with

OM, easier feel the presence of walls. This influences, in a yet unpredictable manner, the rheological results. For a cone-plate geometry, where the gap varies from zero to maximum at the edge, part of the flow can be confined, e.g. in the area of flow where drops have the same characteristic size as the gap. The size of this confined region depends on both the blend system and the flow conditions. For a given shear rate, for the four blends studied, the degree of confinement $C_d = 2R/H$, with R , the drop radius, and H , the gap spacing between the parallel plates, at which wall effects are present was measured by Tufano et al. [31] for different shear rate applied. A power law relation follows:

$$C_d = C_{d0} \dot{\gamma}^{-a}. \quad (5.6)$$

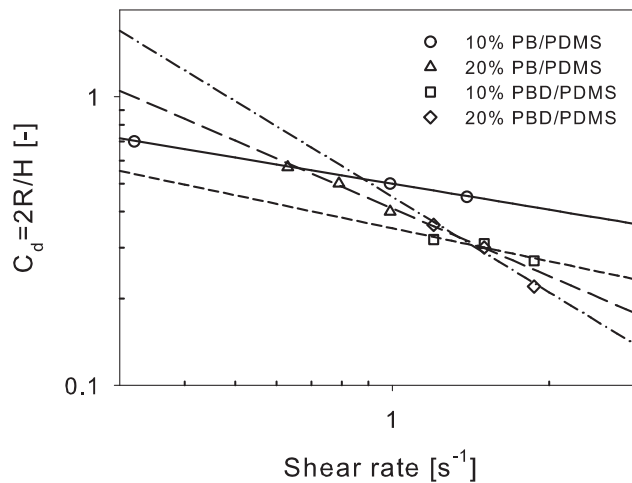


Figure 5.7: Critical degree of confinement vs shear rate. Experimental results from [31] (symbols) and fits using Eq. 5.6 (lines). The values for C_{d0} and a are given in Table 5.3.

Table 5.3: C_{d0} and a values from Eq. 5.6 for the four blends investigated.

Blend	C_{d0}	a
10% PB/PDMS	0.50	0.30
20% PB/PDMS	0.41	0.78
10% PBD/PDMS	0.50	0.38
20% PBD/PDMS	0.45	1.10

Figure 5.7 shows the measured values of C_d for all four blend systems combined with the corresponding fits, using Eq. 5.6, and the fit parameters C_{d0} and a in Table 5.3. The values of the pre-factor C_{d0} are rather close while the values of the exponent increase with viscosity ratio p and with concentration. It is tempting to (try to) create a master curve, but this is outside the scope of this work and more data are needed. For a given drop size we can deduce the sample volume that is prone to confined flow. For a drop size of $100 \mu m$, as found for the 10% PB/PDMS blend, confinement is expected up to half way the maximum cone radius (i.e. 25% of the sample area is confined or 10% of the torque is affected). Using the half way gap height and the parameter sets of Table 5.3 and Eq. 5.6 we can draw confinement lines $R(\dot{\gamma})$ in Figures 5.4 (and 5.8 in the next section for the PBD/PDMS blends). From these considerations it seems reasonable to expect confinement effects during the dynamic measurements on partially-miscible polymers. Despite that, it is yet impossible to predict what effects will occur since confinement leads to complex, transient phenomena. While the build-up time for confinement dominated morphologies typically takes in the order of minutes, the stationary state of morphology is often obtained only after hours [31, 33–36]. Therefore the transient coalescence process is coupled to effects of transient confinement. When confinement occurs, typically a mixture of standard and extended drops, or the opposite small drops, is formed, which causes an increased relaxation time (apparently larger drops) for the first case and a decreased relaxation time (apparently smaller drops) for the second case. During dynamic measurements part of the structures extend to threads that subsequently break-up leading to a bimodal distribution of drop size; the standard drops and the new drops from thread break-up. But also the thread-like structures can survive for long periods of time, depending on the local degree of confinement [37]. As an example: for the 10% PB/PDMS blend it is known that partial miscibility is present between the phases that enhances the coalescence process dramatically [32], larger droplets are formed quicker, strengthening the confinement. For the 20% PB/PDMS blend (see Figure 5.4 bottom) we expect confinement effects over the whole range of shear rate applied and indeed we have to question the reliability of the rheological results in this case. These considerations lead to the conclusions that especially for the 10% PB/PDMS system the OM results are in reasonable agreement with theory, following the break-up line, while the dynamic results are not. Only when rheology and OM results match, confinement effects can apparently be neglected and rheometry could be a useful method to investigate blend morphology.

PBD in PDMS

Similar to the 10 wt % PB in PDMS system, also for the PBD in PDMS blends it is not possible to start experiments at shear rates higher than a critical one, due to the occurrence of shear fracture. The range of shear rates investigated is $0.05s^{-1} - 10s^{-1}$, see Figure 5.8 (top), where the coalescence line is calculated with $h_{cr} = 1.7 \cdot 10^{-8} m$ (the value corresponding to the same average value of $R = 50 \cdot 10^{-6} m$ as used for the PB/PDMS system). Also for this blend the drops seem to coalesce much easier than

predicted by the theory and the average radii are always far above the coalescence model predictions. This again leads to a hysteresis zone narrower than expected from modeling. Both flow histories are repeated with OM. The results quantitatively confirm the data obtained with rheological experiments. Compared to the PB/PDMS results, the confinement line is mostly above the experimental results for the 10% blend, therefore less influence of confinement is expected, while for the 20% blend, see Figure 5.8 bottom, confinement plays a more pronounced role.

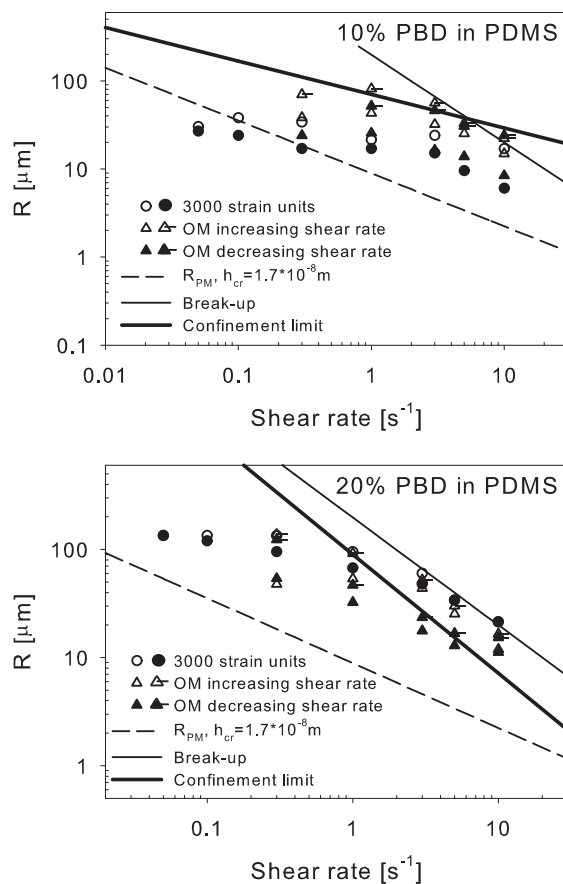


Figure 5.8: As Figure 5.4, now for 10% (top) and 20% (bottom) PBD in PDMS systems.

In line with the results for PB/PDMS, where an increase in the dispersed phase concentration narrows the hysteresis region, see also [8, 9], for the 20% PBD/PDMS system a narrow hysteresis zone is also found. For an increasing shear rate, the average radii from OM are lower than the average radii obtained by rheological measurements. However, comparing the radii of the large drops from OM at each shear rate, with the data from rheology, it is concluded that rheology accounts mainly for larger drop radii, again overestimating the average drop radius. When decreasing the shear rate, the average radii measured with OM are found on a line parallel to the coalescence line, and are smaller than the ones obtained with rheology.

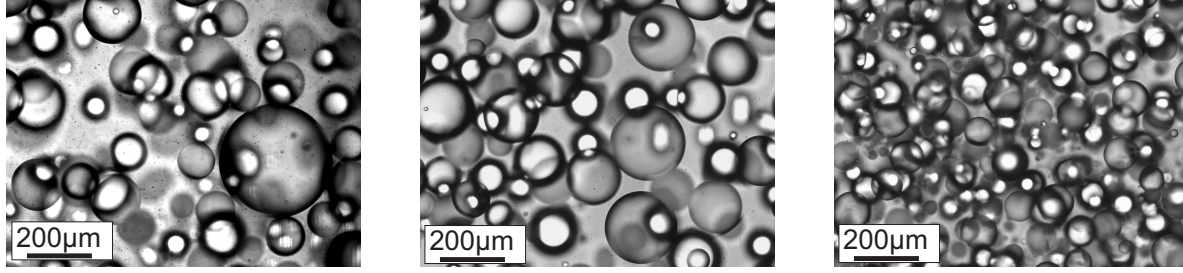


Figure 5.9: Morphology for the 20 wt % PBD in PDMS blend at increasing shear rates of 0.3, 1, and 3 s^{-1} (from left to right).

5.4 Coalescence after a step-down in shear rate

Next we investigate the morphology evolution after a step-down in shear rate, to find out whether deviations from theory observed in the hysteresis zone are also reflected in the transient coalescence process. The experimental results are compared to theories for sharp interfaces. Experiments start from the same initial shear rate of $8s^{-1}$, shearing for 10000 strain units, followed by step downs of 1/40, 1/10 and 1/4, reducing the shear rates to $0.2s^{-1}$, $0.8s^{-1}$, and $2s^{-1}$ respectively.

Modeling coalescence

The theory behind coalescence is summarized by Chesters [4]. Two characteristic times control the coalescence process; the interaction time between colliding drops, t_{int} , and the time needed to drain the matrix film trapped between the colliding drops, t_{drain} . Coalescence does not occur when the t_{drain} is longer than t_{int} . The rate of change of the interfacial area, Q , in the case of monodisperse blends, is given by:

$$\frac{dQ(t)}{dt} = C(t)P(t)\Delta S(t), \quad (5.7)$$

where $C(t)$ is the collision frequency per unit volume, $P(t)$ is the fraction of collisions that leads to coalescence, i.e. the coalescence probability, and $\Delta S(t)$ is the variation in the interfacial area associate to a single coalescence event. To find expressions for these terms, we follow Chesters [4]. First, it is assumed that droplets move affine with the macroscopic flow, yielding a collision frequency per unit volume expressed as [38]:

$$C(t) = \frac{2}{3}\dot{\gamma}D(t)^3n(t)^2, \quad (5.8)$$

where $\dot{\gamma}$ is the shear rate, $D(t)$ is the drop diameter, and $n(t)$ is the number of drops per unit volume. In Eq. 5.8 hydrodynamic interactions have been neglected, hence it applies only to relatively dilute blends. The coalescence probability is given by:

$$P(t) = \exp\left(-\frac{t_{drain}}{t_{int}}\right), \quad (5.9)$$

where t_{int} is assumed proportional to $\dot{\gamma}^{-1}$. Using an approximation for t_{drain} in the case of a partially mobile interface leads to:

$$P(t) \simeq \exp\left[-0.0765\frac{p}{h_{cr}}\left(\frac{\eta_m\dot{\gamma}}{\alpha}\right)^{3/2}D(t)^{5/2}\right]. \quad (5.10)$$

Substituting Eq. 5.8 and Eq. 5.10 in Eq. 5.7, and expressing $Q(t)$, $\Delta S(t)$, and $n(t)$ as functions of the volume fraction ϕ of the dispersed phase results in a differential equation for the time evolution of the average droplet diameter:

$$\frac{dD(t)}{dt} = 0.525\phi\dot{\gamma}D(t)\exp\left[-(mD(t))^{5/2}\dot{\gamma}^{3/2}\right], \quad (5.11)$$

where m is defined as:

$$m = 0.358\left(\frac{p}{h_{cr}}\right)^{2/5}\left(\frac{\eta_m}{\alpha}\right)^{3/5}. \quad (5.12)$$

To obtain the change in drop diameter as function of the shearing time, Eq. 5.11 is integrated:

$$\int_{m\dot{\gamma}^{3/5}d_0}^{m\dot{\gamma}^{3/5}d_t} \frac{du(t)}{0.525u(t)\exp[-u(t)^{5/2}]} = \phi\dot{\gamma}t, \quad (5.13)$$

where

$$u(t) = m\dot{\gamma}^{3/5}D(t). \quad (5.14)$$

Eq. 5.13 is used to predict the time evolution of the radii, the only unknown is h_{cr} .

Coalescence results

The h_{cr} values used to calculate the predictions of the PM model, are chosen based on a sensitivity analysis, see Figure 5.10. In the range of the average experimental radii values (see next sections), the theoretical radius predicted with the PM model is not very sensitive to changes in the value of h_{cr} , except for the largest step-down in shear rate, see Figure 5.10. However, we will use again the h_{cr} values corresponding to $R = 50 \cdot 10^{-6} \text{ m}$ as a first approximation.

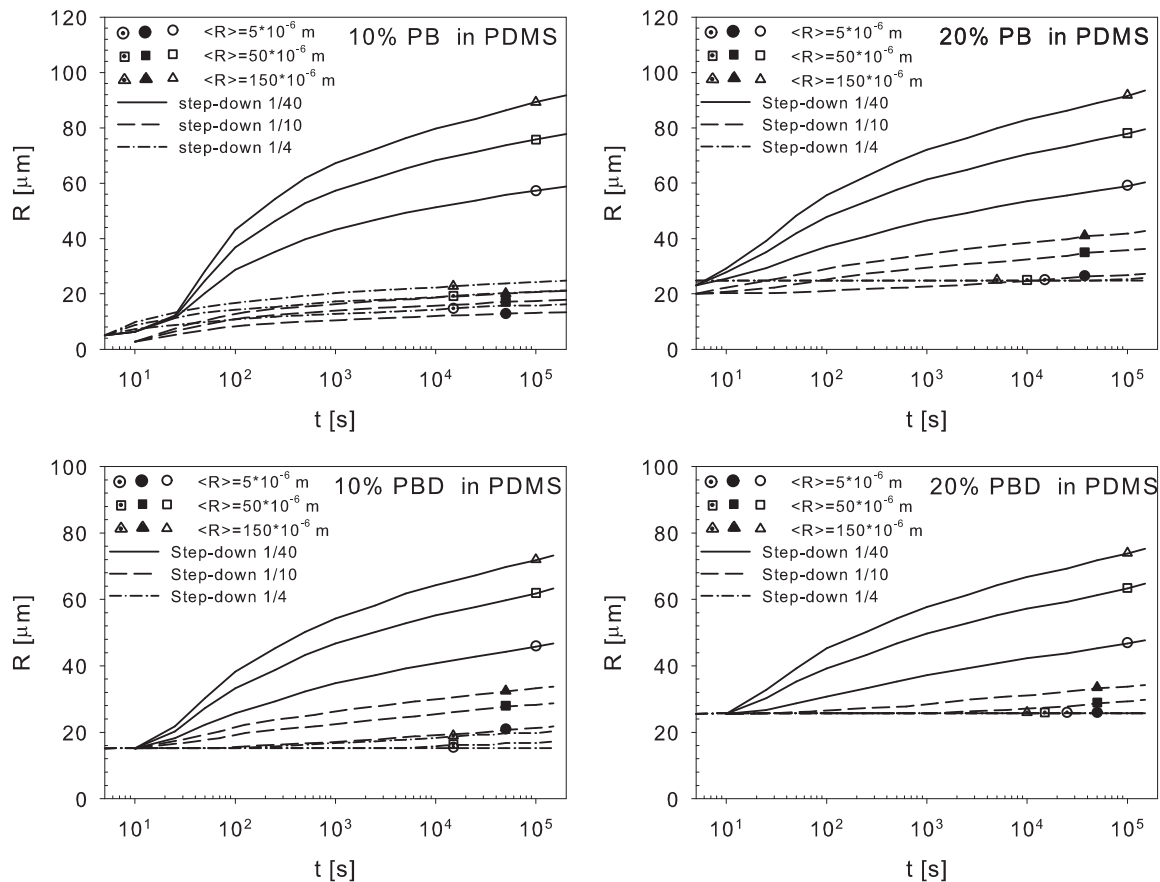


Figure 5.10: Influence of different radii, and the corresponding h_{cr} values (Eq. 5.5) on the transient average radii calculated with the PM model (Eq. 5.4) after step-down in shear rate of 1/40 (solid line), 1/10 (dashed line) and 1/4 (dash-dotted line) for the PB/PDMS system (top) and PBD/PDMS system (bottom) for concentrations of 10 wt% (left) and 20 wt% (right). Symbols indicate the radius used to calculate h_{cr} (Eq. 5.5), the corresponding values are reported in Table 5.2.

PB in PDMS

Figure 5.11 shows the results of the dynamic measurements for different strains, for a step down in the shear rate of 1/40. The slope of G' vs ω never reaches the terminal zone, i.e. becoming equal to 2 and, therefore, these results should be treated with caution. The resulting relaxation spectra are shown in Figure 5.11 (bottom) for a limited frequency range of 1 – 100 rad/s . A second peak occurs for different strain levels. The average radii calculated from the first peak are shown in Figure 5.12 (top), with the average radii corresponding to the second peaks and for all the step-downs, summarized in Table 5.4. The largest average radius is, as expected, found for the largest step-down in shear rate and for all the three experiments the data show a pronounced scattering. The lines shown in Figure 5.12 represent the average radius calculated with Eq. 5.13 and $h_{cr} = 2 \cdot 10^{-8}m$ for the three step-downs of 1/40, 1/10, and 1/4, respectively. The values of $\langle R \rangle$ corresponding to the second peak compare reasonably well with the size of the larger droplets obtained from OM measurements for the same blend, see Figure 5.4. These coalescence results also indicate the existence of a bimodal drop radius distribution. OM is carried out for the step down 1/4, showing a smoother trend of the average radii in time compared to the rheological results, see Figure 5.12 (top) and, at strain units above 5000, few larger drops with radii in the order of $\langle R_{2^{nd} peak} \rangle$ are found in the majority of smaller droplets.

Table 5.4: Average radius $\langle R \rangle$ calculated with relaxation times from the first and second peak in the relaxation spectra, for the 10% PB in PDMS system, at step-down of 1/40, 1.10, and 1.4.

step-down	$\langle R_{1^{st} peak} \rangle$ [μm]	$\langle R_{2^{nd} peak} \rangle$ [μm]
1/40	~ 20	100 - 200
1/10	~ 20	35 - 170
1/4	~ 20	30 - 45

Figure 5.13 shows the elastic modulus versus the frequency (left) and the weighted relaxation spectra (right) for the 20% PB/PDMS system. For this blend the terminal zone is reached, even at the lowest strain units.

In Figure 5.12 (bottom) the average radii for the three different step downs are compared with PM model predictions. In the first 1000s the average radii seem to grow almost independently of the step down size. At longer times, the radii obtained with the larger step-down in shear rate (1/40 and 1/10) increase sharply while for the step-down of 1/4, the growth of the average radius slows down with increasing shearing time. The steep increase in drop radius is consistent with the hysteresis results, i.e. the large average drop sizes compared to theoretical curves. The average radius seems to approach a constant value which is in good agreement with the average radius predicted at $\dot{\gamma} = 2s^{-1}$ by the coalescence models.

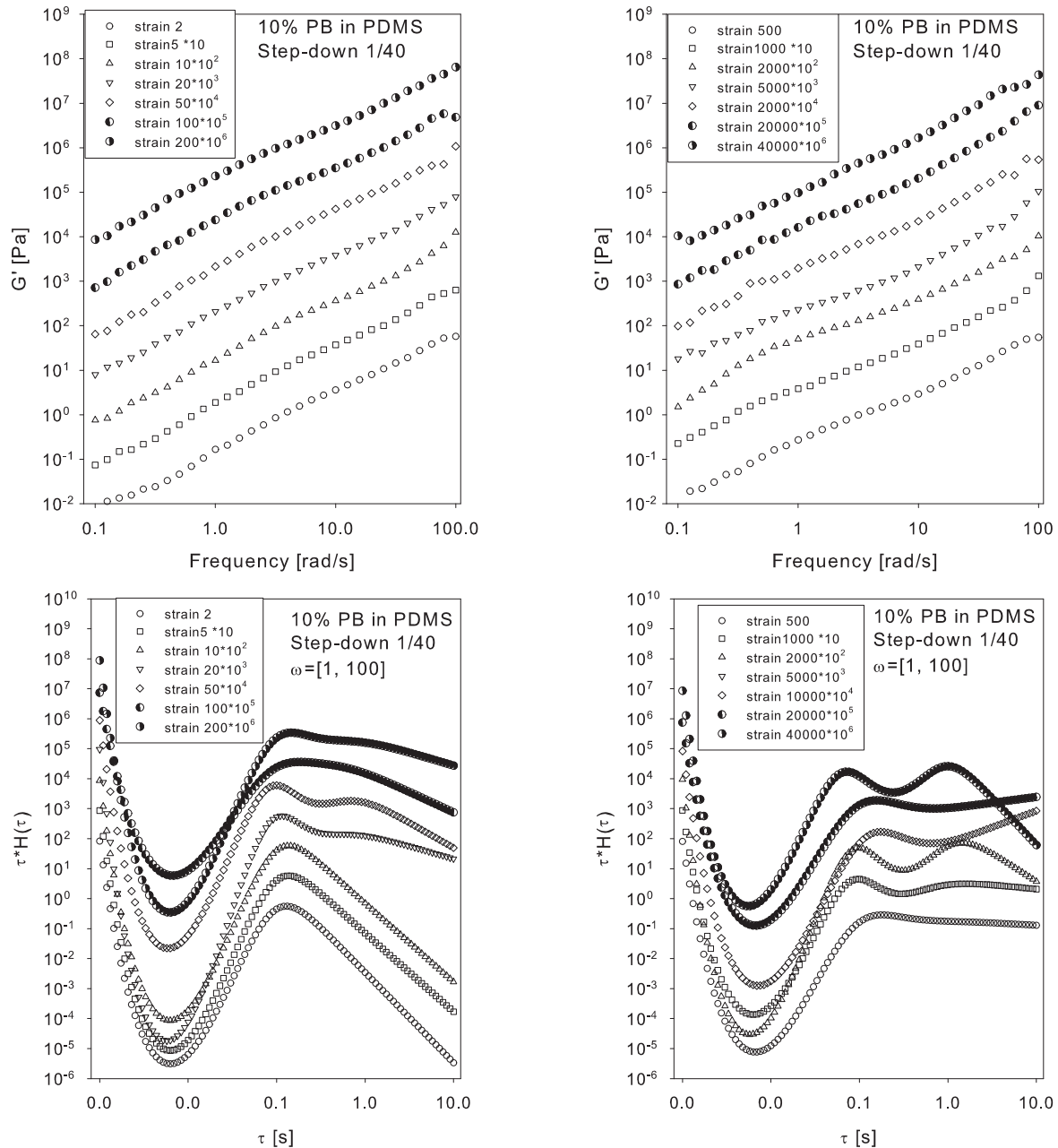


Figure 5.11: Storage modulus G' (top figures) and weighted relaxation spectra (bottom figures) after a step down of 1/40 at different strains. For convenience, the data have been split in two plots (strain 2 to 200 on the left, 500 to 40000 on the right) and in both cases the curves are shifted upwards with increasing the strain units.

PBD in PDMS

Also for the storage moduli measured after step downs of 1/40, 1/10 and 1/4 for the 10 wt % PBD in PDMS blend the terminal zone is never reached and a second peak

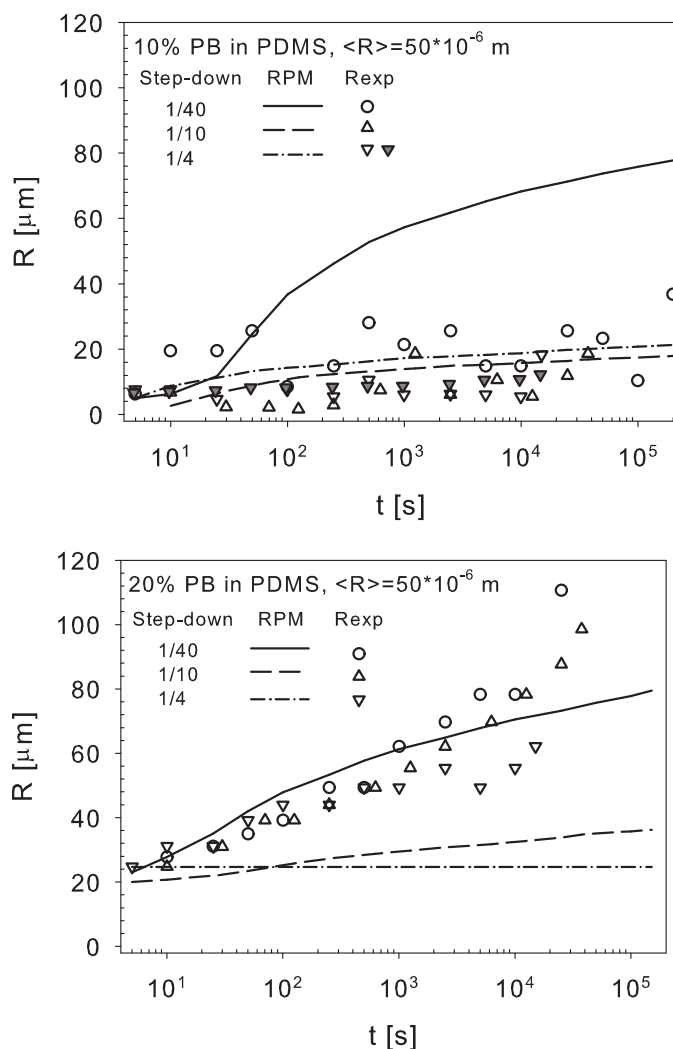


Figure 5.12: Average radii calculated for the 10% PB/PDMS system (top) and the 20% PB/PDMS system (bottom) with Eq. 5.1, relaxation times obtained from weighted relaxation spectra. Lines represent the average radii calculated with Eq. 5.13, step-down of 1/40 (solid line), 1/10 (long dashed line), 1/4 (short dashed line). The values of h_{cr} used are given in the legend. Average radii calculated with OM after a step down of 1/4 are also shown (gray filled circle).

occurs for all the strains (data not shown here). Different from the 10% PB/PDMS system, the second peak occurs at relatively long times, corresponding to large radii which are unrealistic when compared to the gap height of the cone-plate geometry. The average radii calculated from the first peak in relaxation spectrum are shown in Figure 5.14 (top). For the step-down of 1/10 the average radii at large strains increase quickly. The average radii obtained from OM when applying a step-down of 1/4 are

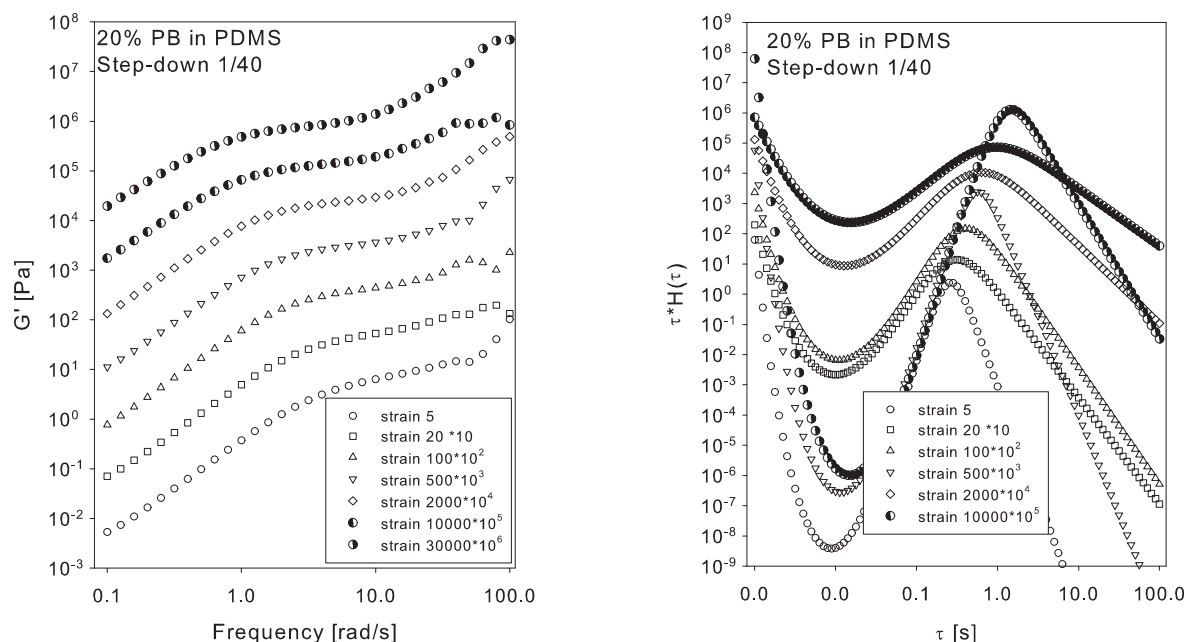


Figure 5.13: G' vs frequency (left) and weighted relaxation spectra (right) after a step down of $1/40$ to a shear rate of $0.2s^{-1}$.

also shown in Figure 5.14 (top, filled triangle), and are in reasonable agreement with the rheological results.

For the 20 wt% PBD in PDMS, the elastic modulus reaches the terminal zone for all the three steps-down. The relaxation spectra always show one peak only. Figure 5.14 (bottom) shows the calculated average radii. Radii grow in the first 1000s independently of the step-down procedure. At longer times, the average radii increase steeply for step downs of $1/40$ and $1/10$ while they approach a "plateau" value for a step down of $1/4$. As already shown when investigating the hysteresis zone, the average radii are larger than the coalescence theory predictions.

5.5 Conclusions

We investigated the morphology development in two blends of *partially-miscible* polymers at two different concentrations by using rheological dynamic measurements and optical microscopy. The difference between the two blends is the miscibility of the components. Experimental results are compared with predictions of relatively simple models for coalescence and break-up of droplets. The experimental results are rather scattered but still it can be concluded that, for most of the cases investigated, the trends observed do not match the theoretical results. A typical feature of immiscible blends, predicted by the models and often observed in literature, is the occurrence of a hysteresis zone where the average drop size of the

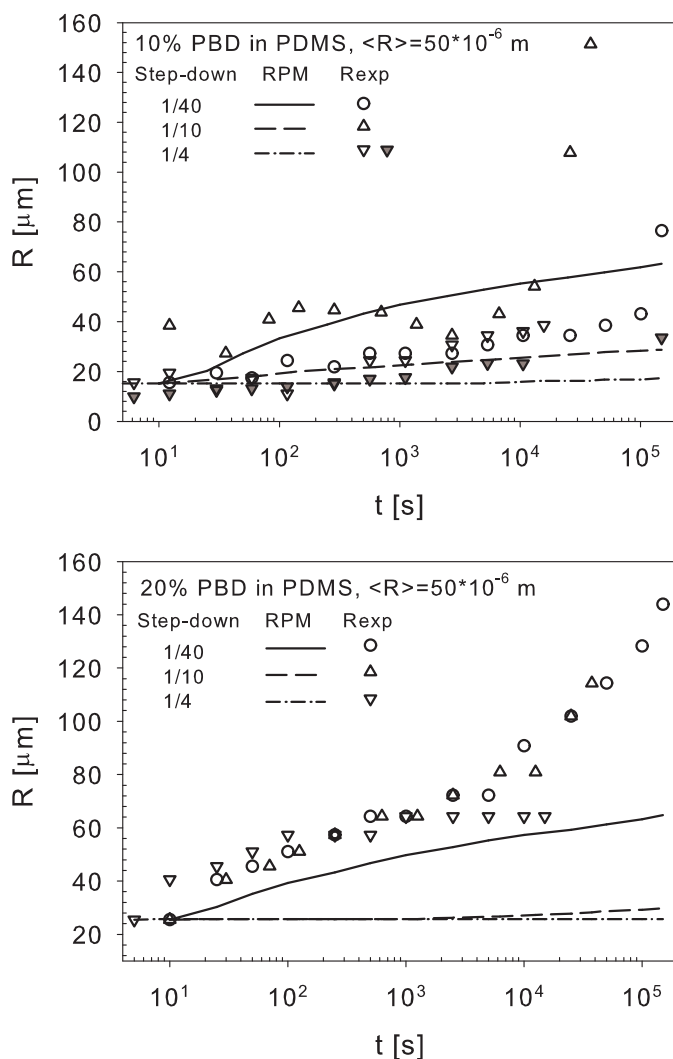


Figure 5.14: As Figure 5.12, now for the 10% PBD/PDMS system (top) and the 20% PBD/PDMS system (bottom).

dispersed phase does not change with varying shear rate. This hysteresis zone is bounded between the coalescence line and the break-up line in a plot of the average radius versus shear rate. In contrast with existing literature, where the critical film thickness, h_{cr} , is used as a fitting parameter, we calculate h_{cr} from theory to predict the coalescence lines for all concentrations in a given blend. Deviations from theory, and differences between blends, become more evident in this way. For both blends studied, the experimental hysteresis zone is always narrower than predicted by break-up and coalescence theories. This is in accordance with the results of Minale et al. [9] who measured the narrowing of the hysteresis zone with increasing concentration in *immiscible* polymer pairs. In our experiments the narrowing is pronounced in the (*less miscible*) PBD/PDMS system, while in the (*partially-miscible*) PB/PDMS system the situation is less clear since the experimental data points are also found

outside the hysteresis zone, especially going beyond the break-up lines. Deviations from theory can be due to the *partial miscibility* of the components or to confinement effects in the cone-plate configuration used. Confinement yields different structures like ordered droplets, strings, threads, etc. Their stability depends on the degree of confinement [37]. After stopping the flow, and before applying oscillatory shear to determine the average drop radius, retraction of extended structures or break-up of threads can occur. In all cases the resulting drop radii are larger than those present without confinement. Quantification clearly requires more study.

The problem of dealing with our polymer systems is that *partial miscibility* itself can enhance the confinement effects mentioned. To illustrate this, coalescence is followed in time. *Immiscible* systems follow the predictions of coalescence of partially mobile systems with average radii approaching a limiting value, see [2]. In our *partially-miscible* systems we observe at longer process times a rather steep and a - in the experimental time scale of 10^5 seconds - unbounded increase in average drop radius. The growth in structure far beyond its limiting value is enhanced by increasing the concentration (from 10 to 20%) and increasing the step-down in shear rate (from 1/4 to 1/40). However, maybe surprisingly, it is present in both systems investigated, PBD/PDMS and PB/PDMS. *Partial miscibility* results in enhanced dynamic coalescence, yielding larger drops that feel confinement earlier in time. Confinement effects could explain the quasi-unlimited growth in drop size measured after stopping the flow. Confinement effects, and the critical shear rate at which they occur, strongly depend on the viscosity of the components and the viscosity ratio. This could explain the unexpected differences found between the *less miscible* (PBD/PDMS) and the *partial miscible* (PB/PDMS) systems. Clearly, to interpret data on morphology development in *partially-miscible* polymers from dynamic rheological measurements, using a cone-plate geometry, should be used with caution. More quantitative studies, e.g. using combined rheological and optical experiments or applying e.g. advanced diffuse interface modeling that can deal with concentrated two-phase flows, should conclude whether the rheological experimental technique used could be a reliable one to approach this problem, or whether it should be abandoned.

References

- [1] Takahashi, Y., Kurashima, N., Noda, I. (1994). Experimental tests of the scaling relation for textured materials in mixtures of two immiscible fluids. *J. Rheol.*, **38**, 699–712.
- [2] Vinckier, I., Moldenaers, P., Mewis, J. (1996). Relationship between rheology and morphology of model blends in steady shear flow. *J. Rheol.*, **40**, 613–631.
- [3] Grace, H.P. (1982). Dispersion phenomena in high viscosity immiscible fluid systems and application of static mixers as dispersion devices in such systems. *Chem. Eng. Commun.*, **14**, 225–277.

- [4] Chesters, A.K. (1991). The modelling of coalescence processes in fluid-liquid dispersions. *Trans IChemE*, **69A**, 259–281.
- [5] Elmendorp, J.J. (1986). *A Study on Polymer Blending Microrheology*. PhD thesis, Technical Univ. of Delft, Delft, The Netherlands.
- [6] Grizzuti, N. and Bifulco, O. (1997). Effects of coalescence and breakup on the steady-state morphology of an immiscible polymer blend in shear flow. *Rheol. Acta*, **36**, 406–415.
- [7] Vinckier, I., Moldenaers, P., Terracciano, A.M., Grizzuti, N. (1998). Droplet size evolution during coalescence in semiconcentrated model blends. *AIChE J.*, **44**, 951–958.
- [8] Minale, M., Moldenaers, P., Mewis, J. (1997). Effect of shear history on the morphology of immiscible polymer blends. *Macromolecules*, **30**, 5470–5475.
- [9] Minale, M., Mewis, J., Moldenaers, P. (1998). Study of the morphological hysteresis in immiscible polymer blends. *AIChE J.*, **44**, 943–950.
- [10] Janssen, J.M.H. and Meijer, H.E.H. (1995). Dynamics of liquid-liquid mixing: A two zone model. *Polym. Eng. Sci.*, **35**, 1766–1780.
- [11] Elmendorp, J.J. and van der Vegt, A. (1986). A study on polymer blending microrheology: Part iv. the influence of coalescence on blend morphology origination. *Polym. Eng. Sci.*, **26**, 1332–1338.
- [12] Fortelny, I. and Kovar, J. (1988). Theory of coalescence in immiscible polymer blends. *Polym. Compos.*, **9**, 119–124.
- [13] Rusu, D. and Peuvrel-Disdier, E. (1999). In-situ characterization by small angle light scattering of the shear-induced coalescence mechanisms in immiscible polymer blends. *J. Rheol.*, **43**, 1391–1409.
- [14] Verdier, C. and Brizard, M. (2002). Understanding droplet coalescence and its use to estimate interfacial tension. *Rheol. Acta*, **43**, 514–523.
- [15] Gramespacher, H. and Meissner, J. (1992). Interfacial tension between polymer melts measured by shear oscillations of their blends. *J. Rheol.*, **36**, 1127–1141.
- [16] Graebing, D., Muller, R., Paliarne, J.F. (1993). Linear viscoelastic behaviour of some incompatible polymer blends in melt. interpretation of data with a model of emulsion of viscoelastic liquids. *Macromolecules*, **26**, 320–329.
- [17] Graebing, D., Benkira, A., Gallot, Y., Muller, R. (1994). Dynamic viscoelastic behaviour of polymer blends in the melt - experimental results for pdms-poe-do, ps/pmma and ps/pema blends. *Eur. Pol. J.*, **30**, 301–308.
- [18] Honerkamp, J. and Weese, J. (1993). A nonlinear regularization method for the calculation of relaxation spectra. *Rheol. Acta*, **32(1)**, 65–73.
- [19] Paliarne, J.F. (1990). Linear rheology of viscoelastic emulsions with interfacial tension. *Rheol. Acta*, **29**, 204–214.
- [20] De Bruijn, R.A (1989). *Deformation and break-up of drops in simple shear flows*. PhD thesis, Technical Univ. of Eindhoven, Eindhoven, The Netherlands.
- [21] Taylor, G.I. (1932). The viscosity of a fluid containing small drop of another fluid. *Proc. R. Soc. London, A*, **138**, 41–48.
- [22] Jackson, C.L.,N.E. and Tucker. (2003). A model for large deformation of an ellipsoidal droplet with interfacial tension. *J. Rheol.*, **47**, 659–682.

- [23] Yu, M. and Grmela M. and Palierne J.F. and Zhou C.X.,W. and Bousmina. (2002). Quantitative relationship between rheology and morphology in emulsions. *J. Rheol.*, **46**, 1381–1399.
- [24] Yu, C.X. and Bousmina M.,W. and Zhou. (2005). Theory of morphology evolution in mixtures of viscoelastic immiscible components. *J. Rheol.*, **49**, 215–236.
- [25] Anderson, D.M., McFadden, G.B., Wheeler, A.A. (1998). Diffuse-interface methods in fluid mechanics. *Annu. Rev. Fluid Mech.*, **30**, 139–165.
- [26] Cahn, J.E.,J.W. and Hilliard. (1958). Free energy of a nonuniform system. i. interfacial free energy. *J. Chem. Phys.*, **28**, 258.
- [27] Cahn, J.E.,J.W. and Hilliard. (1965). Phase separation by spinodal decomposition in isotropic systems. *J. Chem. Phys.*, **42**, 93.
- [28] Mackay, G.D.M. and Mason, S.G. (1963). The gravity approach and coalescence of fluid drops at liquid interfaces. *J. Chem. Eng.*, **41**, 203–212.
- [29] Tufano, C., Peters, G.W.M., Anderson, P.D., Meijer, H.E.H. (2008). Transient interfacial tension of partially-miscible polymers. *J. Coll. Int. Sci.*, **Submitted**.
- [30] Janssen, J.M.H. (1993). *Dynamics of liquid-liquid mixing*. PhD thesis, Technical Univ. of Eindhoven, Eindhoven, The Netherlands.
- [31] Tufano, C., Peters, G.W.M., Meijer, H.E.H. (2008). Confined flow of polymer blends. *Langmuir*, **Accepted**.
- [32] Zdravkov, A., Peters, G.W.M., Meijer, H.E.H. (2006). Film drainage and interfacial instabilities in polymeric systems with diffuse interfaces. *J. Coll. Int. Sci.*, **296**, 86–94.
- [33] Migler, K.B. (2001). String formation in sheared polymer blends: coalescence, breakup, and finite size effect. *Phys. Rev. Lett.*, **86**, 1023–1026.
- [34] Pathak, J.A., Davis, M.C., Hudson, S.D., Migler, K.B. (2002). Layered droplet microstructures in sheared emulsions: finite-size effects. *J. Coll. Int. Sci.*, **255**, 391–402.
- [35] Pathak, J.A. and Migler, K.B. (2003). Droplet-string deformation and stability during microconfined shear flow. *Langmuir*, **19**, 8667–8674.
- [36] Vananroye, A., Van Puyvelde, P., Moldenaers, P. (2006). Structure development in confined polymer blends: steady-state shear flow and relaxation. *Langmuir*, **22**, 2273–2280.
- [37] Son, J., Martys, N.S., Hagedorn, J.G., Migler, K.B. (2003). Suppression of capillary instability of a polymeric thread via parallel plate confinement. *Macromolecules*, **36**, 5825–5833.
- [38] Smoluchowski, von M. (1917). *Phys. Chem.*, **92**, 129.

Confined flow of polymer blends¹

The influence of confinement on the steady-state morphology of two different emulsions is investigated. The blends, made from polybutene (PB) in polydimethylsiloxane (PDMS), and polybutadiene (PBD) in PDMS, are sheared between two parallel plates, mostly with a standard gap spacing of $40\ \mu\text{m}$, in the range of shear rates at which the transition from "bulk" behavior towards "confined" behavior is observed. For both cases, the influence of the concentration was systematically investigated, as well as the shear rate effects on the final steady-state morphology.

By decreasing the shear rate, for each blend, the increasing droplets, i.e. increasing confinement for a fixed gap spacing, arrange themselves first into two layers and, when the degree of confinement reaches an even higher value, a single layer of droplets is formed. The ratio between the drop diameters and the gap spacing at which this transition occurs is always lower than 0.5. While decreasing the shear rate, the degree of confinement increases due to drop coalescence. Droplets arrange themselves in superstructures like ordered pearl necklaces and, at the lower shear rates, strings.

The aspect ratio and the width of the droplet obtained from optical micrographs are compared to predictions of the single droplet Maffettone-Minale model (MM model, [1]). It is found that the theory, meant for unconfined shear flow, is not able to predict the drop deformation when the degree of confinement is above a critical value that depends on the blends considered and the shear rate applied. A recently developed extension of the MM model is reported by Minale (M model [2]) where the effect of the confinement is included by using the Shapira-Haber correction [3]. Further extending this M model, by incorporating an effective viscosity as originally proposed by Choi and Showalter [4], we arrive at the modified Minale (mM) model that accurately describes the experiments of blends in confined flow.

¹Reproduced from: Tufano, C., Peters, G.W.M., Meijer, H.E.H., Confined flow of polymer blends. *Langmuir*, accepted.

6.1 Introduction

Blends in unconfined flow

The technological importance of physical blends of immiscible polymers is evident. When blending two "immiscible" polymers, they acquire a small-scale arrangement which is a function of the fluid properties and of the flow history applied during processing. This microstructure affects the rheological, optical and transport properties of the mixture and, therefore, the properties of the final product. Basic understanding of the dispersion mechanisms originates from the work of Taylor [5] and morphology development in emulsions has been subsequently extensively studied for different types of flow (for reviews see e.g. [6–9]). When flow is imposed on a mixture (restricting to Newtonian components), shear stresses tend to deform the droplets, while the interfacial tension tends to keep them in the spherical shape. The ratio of the viscous and interfacial stresses defines the capillary number, $Ca = (\eta_m \dot{\gamma} R) / \sigma$, where η_m is the viscosity of the matrix phase, $\dot{\gamma}$ is the shear rate, R the drop radius, and σ the interfacial tension. The critical capillary number is a function of the viscosity ratio, defined as $p = \eta_d / \eta_m$, where η_d is the viscosity of the dispersed phase, and reflects the situation when interfacial tension is not longer able to balance the deformation stress induced by the flow. Once $Ca(p)$ exceeds a critical value, Ca_{cr} , the droplets deform irreversibly and break up.

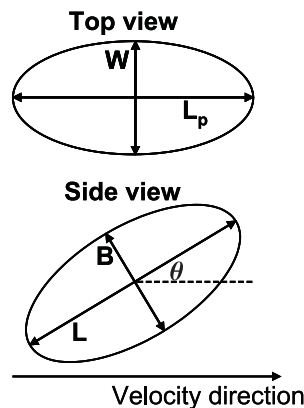


Figure 6.1: Schematic picture of a deformed droplet in simple shear flow. Top and side view, with the notation for the axes L , B and W and orientation angle θ .

When $Ca \ll 1$, the deformation of the droplet in flow is limited and the drop shape is close to spherical. In this case, Taylor approximated the drop shape by an ellipse. Given the major (L) and the minor (B) axis of the ellipse in the velocity-velocity gradient plane (see Figure 6.1), the deformation parameter, D , was defined:

$$D = \frac{L - B}{L + B}. \quad (6.1)$$

D is equal to zero in the case of a spherical drop, and it increases asymptotically to one, when the drop deforms. For values of D close to one slender-body theories apply [10–12], and assuming that during the deformation the cross-section of the deformed droplet remains circular ($B = W$ in Figure 6.1), a more appropriate deformation parameter, related to D , was defined:

$$r_p = \frac{L}{B} = \frac{1 + D}{1 - D}. \quad (6.2)$$

A relatively simple, phenomenological, 3D model for drop deformation in an arbitrary flow field was presented by Maffettone and Minale [1] and it describes the transient evolution of an elliptically deformed drop in terms of the three axes (L , B , W). Analytical solutions for the steady-state shape in simple shear and in elongational flow are reported, preserving drop volume at any deformation. These models, as well as most of the present experimental work, address polymer blends used in *macroscopic* devices and results are restricted to the "bulk regime", where the characteristic size of the blend components is much smaller than the typical size of the flow geometry.

Blends in confined flow

More recently, emulsions flowing in *microscopic* devices have received attention [13–15] and miniaturization leads to processes in which the characteristic sizes of device and morphology are comparable. When limiting to homogeneous shear flows, two types of studies in confined flow can be considered: studies focussed on the effects of confinement on a single droplet, experimental [16–18] and numerical [1–3, 19], and studies focussing on blends [20–24]. We will investigate to what extent the relatively simple single-droplet models apply to the blends investigated (see Sections 6.4.1 and 6.4.2). Only limited experimental work is available in literature and the physics behind the flow of emulsions in confined geometries is a new and growing field of investigation. Migler [20] reported a droplet-string transition for a blend of polydimethylsiloxane (PDMS) in polyisobutylene (PIB) at a mass ratio of 0.28 and viscosity ratio p equal to 1. The sample was loaded in a parallel-plate geometry, with a fixed gap, $H = 36 \mu\text{m}$. The shear rate was decreased gradually and the size of the inclusions increased due to coalescence. It enhanced the degree of confinement, inducing the transition droplets-strings. Strings, wide enough to interact with the walls, were found to be stable even upon cessation of flow. The stability of narrower strings during flow, and the occurrence of break-up

upon cessation of flow, was explained by the suppression of the Rayleigh-Tomotika mechanism by a shear field [25]. Pathak et al. [21] reported effects of the composition on the flow-induced morphology, again for blends of PDMS in PIB with p equal to unity. Apart from the transition droplets-strings, they observed that the droplets arrange into discrete layers during shear. The formation of two layers was observed at higher shear rates, while the transition to a single layer was found at lower shear rates. This transition was attributed to the increase in the average droplet size, i.e. an increase in the degree of confinement. The effects of mixture composition, shear rate applied and confinement, on the development of the morphology in the transition zone between bulk behavior and string transition were summarized in a morphology diagram. Some arguments were offered to explain the layering of droplets, based on the finite-size effects, migration of droplets from the walls towards the center and droplet collisions. However, the physics behind the phenomena occurring is still poorly understood. Pathak et al. [22] investigated the effect of the confinement for a blend containing 9.7 wt% of PDMS in PIB with p equal to unity. They reported three additional states to stable and unstable droplets present in the bulk: stable and unstable strings, and squashed droplets, and they concluded that confinement promotes deformation and allows for the existence of droplets with high aspect ratios, with dimensions above the critical values predicted by bulk theories. Finite-size effects were also reported in Mietus et al. [23] for a mixture of water droplets in oil in a Couette flow. They observed the formation of toroidal rings and water sheaths. Recently, Vananroye et al. [24] also investigated the effects of confinement on the morphology of PIB/PDMS mixtures with p equal to 0.46 and showed that, for this case, the mean droplet size during simple shear can be predicted by the same relations that apply in bulk situations. However, they also reported an organization of droplets in superstructures depending on shear rates and concentrations applied and a transition to a single layer was observed for confinement ratios lower than those reported in literature.

Our goal is to study flow-induced morphology development for two material combinations that differ in viscosity ratio, in a confined geometry using optical microscopy and check for what experimental conditions the geometrical confinement influences the blend morphology. We will compare our experimental results with those found in literature, we will check when the Maffettone-Minale model still applies. In addition, the results are compared to the predictions of a modified version of the Maffettone-Minale model, recently proposed by Minale [2], that takes into account the degree of confinement. We propose a further step by using the effective blend viscosity in this Minale model. The influence of shear rate and concentration applied on droplet deformation is systematically investigated. The two emulsions used are: polybutene (PB)/polydimethylsiloxane (PDMS) and polybutadiene (PBD)/PDMS with PDMS as the continuous phase in both cases. The viscosity ratios p are equal to 0.33 and 1.26, respectively. Concentrations of 10%, 20% and 30% are investigated. Confinement is generated by means of a parallel-plate geometry and the shear rate is gradually decreased to enter the transition zone between bulk-like behavior and the range in which finite-size effects

are present. Further, a comparison between the steady-state average drop size and the predictions of the partially mobile interface model is made.

6.2 Materials and methods

Materials

Polybutene (Indopol H-25, BP Chemicals, UK; $M_n = 635$ [g/mol]) and polybutadiene (Ricon 134, Sartomer; $M_n = 8000$ [g/mol]) are used as dispersed phases, polydimethylsiloxane (PDMS, UCT; $M_n = 62700$ [g/mol]) as the continuous phase. The materials are liquid and transparent at room temperature. With a digital density meter (DMA 5000, Anton Paar), the density of PB ($\rho_{PB} = 874$ kg/m³), PBD ($\rho_{PBD} = 891$ kg/m³) and PDMS ($\rho_{PDMS} = 972$ kg/m³) were measured at 23°C. Given the time scale of the experiments, the density difference for the PB/PDMS as well as for the PBD/PDMS emulsions is small enough to neglect buoyancy effects. Zero shear viscosities were measured at 23°C using a rotational rheometer (Rheometrics, ARES II rotational rheometer with a 10GM FRT transducer) equipped with a parallel-plate geometry and applying steady shear rates: $\eta_{PB} = 3.7$ Pa·s, $\eta_{PBD} = 13.6$ Pa·s, $\eta_{PDMS} = 10.9$ Pa·s. The viscosity ratios are $p_{PB/PDMS} = 0.34$ and $p_{PBD/PDMS} = 1.24$, respectively. For the whole range of shear rates applied, the viscosities of the pure components are independent of shear rate and the first normal stress differences are too small to be measured with our equipment. The pure components behave as Newtonian fluids in the conditions in which the optical experiments are carried out. The viscosity ratio p dependent critical capillary number $Ca_{cr}(p)$ can be found e.g. in Grace's original data [26], or by using de Bruijn's fit to these data [27], once p is known; we find $Ca_{cr} = 0.47$ for PB/PDMS and $Ca_{cr} = 0.5$ for PBD/PDMS. The equilibrium interfacial tension was measured at room temperature, $\sigma_{PB/PDMS} = 2.2 \cdot 10^{-3}$ N/m and $\sigma_{PBD/PDMS} = 4.2 \cdot 10^{-3}$ N/m. Three compositions, 10, 20, and 30% mass fraction of PB and PBD respectively, were investigated and the blends were prepared following the proven protocol of Vinckier et al. [28] and Takahashi et al. [29] (the correct amount of the two phases were weighted and mixed by hand with a spatula for around 15 minutes). White, cream like blends were obtained and, using a vacuum oven for one hour at room temperature, air-free samples were prepared.

Experimental methods

Flow experiments were performed on freshly-made mixtures using a CSS-450 Linkam shear cell from Linkam Scientific Instruments. The sample chamber consists of two parallel quartz plates. The gap, H , between these can be varied by means of a stepper motor. Steady shear flow, at the desired shear rates, can be applied. In most of the experiments the gap between the plates, H , was set to 40 μ m and calibration

of the shear cell was performed prior each experiment. To carefully set the gap, after checking the parallelism between the plates, two markers were applied, on the top and on the bottom window. The distance between the two windows was determined by measuring the translation of the microscope stage, when focussing on the markers in the presence of air. This procedure was already adopted by Pathak et al. [22]. Once the sample was loaded, the shear cell was placed on the stage of an Olympus optical microscope. Images were acquired, during and after flow, in the velocity-vorticity plane, using objectives with a magnification of 5X, 10X, 20X and 50X. Experiments with PB/PDMS blends were performed at shear rates ranging between 10s^{-1} and 0.8s^{-1} and an Olympus color view III camera was used. To detect the transition from bulk to confined behavior for the PBD/PDMS system, it was necessary to perform experiments at shear rates as high as 20s^{-1} . A high speed camera, able to acquire up to 200 fps was used for these experiments. In the first case, images were analyzed with software tailor made for the Olympus camera (analySIS), while in the second case, commercial image analysis software was used (Scion Image). The temperature was set at $23 \pm 1^\circ\text{C}$.

Samples were sheared at high shear rates for a sufficient long time. Once a fine morphology was created, the shear rate was decreased in steps of 20% or less, allowing at least two hours shearing at each shear rate, required to obtain a steady morphology, after which the flow was stopped and the droplets were allowed to relax. Next, the flow was restarted at a lower shear rate.

In the results presented in Sections 6.4.1 and 6.4.2, we will refer to a dimensionless shear rate, $\dot{\gamma}/\dot{\gamma}_d$, as proposed by [20], where $\dot{\gamma}_d = \sigma/H\eta_m$.

From the images taken during flow, the axes W and L_p can be measured (see Figure 6.1) and from images taken after cessation of flow the droplet radius R is measured. However, to investigate the influence of the degree of confinement, shear rate, and blend concentration on the morphology evolution, the aspect ratios of the droplets need to be known. When droplets are approximated with an ellipsoid, L and B are related to the projection of L in the velocity-vorticity plane, L_p :

$$L_p^2 = B^2 + L^2 \cos^2 \theta - B^2 \cos^2 \theta. \quad (6.3)$$

The orientation angle, θ , is not measured, since acquisition of images in the velocity-velocity gradient plane is not possible in our experimental set-up. We will use the two limiting cases for θ to determine r_p , i.e. the orientation angle for unconfined flow predicted by the Maffettone-Minale model (θ_{MM}) in combination with volume conservation (see Section 6.3) and the case of $\theta = 0$, corresponding to droplets fully aligned in the flow direction.

6.3 Modeling

Maffettone-Minale model

Maffettone et al. [1] proposed a phenomenological model (MM model in the rest of the text) to predict the deformation (L , B and W) and the orientation angle (θ_{MM}) for a single 3D droplet in an unconfined flow. The model is an extension of the well known Taylor model that is limited to small deformation [5]. The model, based on the assumptions that the drop is incompressible and its shape is ellipsoidal during flow, predicts the three main axes of an elliptical drop and its orientation in an arbitrary flow field. The applicability of the model was proven for viscosity ratios below and above one, up to Ca_{cr} , which is the case in all the experiments we show here.

For simple shear flow, analytical solutions for L , B , W and θ as function of Ca and p are available:

$$L = 2R \left[\frac{f_{1MM}^2 + Ca^2 + f_{2MM}Ca (f_{1MM}^2 + Ca^2)^{1/2}}{(f_{1MM}^2 + Ca^2)^{1/3}(f_{1MM}^2 + Ca^2 - f_{2MM}^2Ca^2)^{2/3}} \right]^{1/2}, \quad (6.4)$$

$$B = 2R \left[\frac{f_{1MM}^2 + Ca^2 - f_{2MM}Ca (f_{1MM}^2 + Ca^2)^{1/2}}{(f_{1MM}^2 + Ca^2)^{1/3}(f_{1MM}^2 + Ca^2 - f_{2MM}^2Ca^2)^{2/3}} \right]^{1/2}, \quad (6.5)$$

$$W = 2R \left[\frac{f_{1MM}^2 + Ca^2 - f_{2MM}^2Ca^2}{(f_{1MM}^2 + Ca^2)^{1/3}(f_{1MM}^2 + Ca^2 - f_{2MM}^2Ca^2)^{2/3}} \right]^{1/2}, \quad (6.6)$$

$$\theta_{MM} = \frac{1}{2} \arctan \left(\frac{f_{1MM}}{Ca} \right), \quad (6.7)$$

where f_{1MM} and f_{2MM} are dimensionless and non-negative functions of p and Ca given by

$$f_{1MM} = \frac{40(p+1)}{(2p+3)(19p+16)}, \quad (6.8)$$

$$f_{2MM} = \frac{5}{2p+3} + \frac{3Ca^2}{2+6Ca^2}. \quad (6.9)$$

The aspect ratio of a drop as function of the dimensionless numbers Ca and p , is obtained by substituting Eq. 6.4 and Eq. 6.5 in the definition of r_p (Eq. 6.2):

$$r_p = \frac{f_{2MM}Ca + (f_{1MM}^2 + Ca^2)^{1/2} - (f_{1MM}^2 + Ca^2 - f_{2MM}^2Ca^2)^{1/2}}{f_{2MM}Ca + (f_{1MM}^2 + Ca^2)^{1/2} + (f_{1MM}^2 + Ca^2 - f_{2MM}^2Ca^2)^{1/2}}. \quad (6.10)$$

Using conservation of volume, L , B , W and the radius of the relaxed droplets, R , can be related:

$$LBW = 8R^3. \quad (6.11)$$

With the measured values of L_p , W and R and using eqs. 6.3, 6.7 and 6.11, L and B , and therefore the droplet aspect ratio r_p , can be calculated, i.e. assuming the orientation angle from the MM model applies. The other limiting case is obtained by taking $\theta = 0$ instead of using Eq. 6.7.

In the case strings are present, they break-up upon cessation of flow. In that case, following Pathak et al. [22], the radius of the relaxed drop can be calculated by approximating the elongated drop with a cylinder and equating the volume of the string ($\pi LB^2/4$) to the volume of the equivalent sphere ($4\pi R^3/3$). This choice neglects the contribution of the two ends of each string.

The aspect ratio of the droplets, r_p , can be compared to the predictions of Eq. 6.10. Eq. 6.7 has been reported to properly predict the drop orientation, up to a degree of confinement $2R/H < 0.5$ [24]. However, we will show that, for the blends and in the conditions investigated here, deviations from the MM model predictions start to occur for a smaller degree of confinement.

The width of the droplets found experimentally are well-predicted by the MM model, up to a certain degree of confinement. This value of $2R/H$ is found to be a function of the blend components, the blend concentrations and the shear rates applied. Above a critical value of the degree of confinement, the width of the elongated droplets becomes independent of the radius.

Shapira and Haber [3] extended the Taylor model [5] to take into account the effect of confinement. However, this model is still limited to small droplet deformations. An extended version of the MM model, including the Shapira-Haber correction, is discussed in the next section. To detect the conditions to predict the formation of superstructures like strings or, more general, to identify situations when confinement plays a role, the dependence of L and B on the Ca number has also been studied.

Minale model

Recently Minale [2] modified the MM model to account for the effects of a geometrical confinement on the drop shape during flow. We will refer to this model as the M

model. While the MM model imposes that the drop recovers the analytical asymptotic limits of Taylor for small deformation, in the M model the drop is forced to recover the analytical limits of the Shapira and Haber model [3]. The following analytical expressions to calculate the aspect ratio r_p and the width W of the droplet in a confined shear flow were derived:

$$r_p = \left[\frac{(f_{1M}^2 + Ca^2)^{\frac{1}{2}} + Caf_{2M}}{(f_{1M}^2 + Ca^2)^{\frac{1}{2}} - Caf_{2M}} \right]^{\frac{1}{2}}, \quad (6.12)$$

$$W = 2R \frac{[f_{1M}^2 + Ca^2(1 - f_{2M}^2)]^{1/6}}{(f_{1M}^2 + Ca^2)^{1/6}}, \quad (6.13)$$

where the functions f_{1M} and f_{2M} are defined as follow:

$$f_{1M} = \frac{f_{1MM}}{1 + C_S \left(\frac{R}{H}\right)^3 f_{1c}}, \quad f_{2M} = f_{2MM} \left[1 + C_S \left(\frac{R}{H}\right)^3 f_{2c} \right]. \quad (6.14)$$

The functions f_{1MM} and f_{2MM} are given by eqs 6.8 and 6.9 respectively, the constant C_S is taken equal to 5.7, the value for a drop placed in the mid plane [3]. We will keep this value the same for all our calculations. The term R/H in the expressions of f_{1M} and f_{2M} accounts for the degree of confinement and the functions f_{1c} and f_{2c} are defined as follow:

$$f_{1c} = \frac{44 + 64p - 13p^2}{2(1+p)(12+p)}, \quad f_{2c} = -\frac{10 - 9p}{12+p}. \quad (6.15)$$

Minale model with effective viscosity

We extended the model proposed by Minale by incorporating an effective viscosity to make the model more suitable for realistic blend systems. The effective blend viscosity used is according to Choi and Showalter [4]:

$$\eta_{meff} = \eta_m \left[1 + \phi \frac{5p+2}{2(p+1)} \left(1 + \phi \frac{5(5p+2)}{4(p+10)} \right) \right], \quad (6.16)$$

where ϕ is the blend volume fraction. This changes the Ca number and the viscosity ratio p in the M model. We will refer to this model as the modified M model (mM)

model). Of course, we can expect this to be also a less approximation when the blend starts to become structured, i.e. layer formation occurs. In Sections 6.4.1 and 6.4.2 the experimental values of r_p and W are compared to the predictions of the MM model, M model, and mM model. In most cases the latter choice gives better agreement with the experimental data.

6.4 Results

6.4.1 PBD/PDMS system.

Figure 6.2 left reports the measured deformation (symbols) as a function of Ca of single droplets in the confined geometry, for a 10 wt% PBD in PDMS. Results based on the orientation angle predicted by the MM model (r_p , open symbols) and with the orientation angle set equal to zero (r_p , filled symbols), are shown. Determining the experimental r_p values with the M model or mM model gives only slightly lower values compared to the MM model and, therefore, we will not report these data. The lines are the predictions for the three different models. The agreement found is reasonable (although the scatter in experimental results is sometimes quite large) and no serious deviations occur. It can be observed that the agreement improves for $\theta = 0$ (filled symbols in Figure 6.2). This indicates that droplets, under the effect of confinement, orient more than predicted by the MM model. Minor deviations were reported also by Vananroye et al. [24], when $Ca < Ca_{cr}$, which is also the case for this blend.

The right-hand side of Figure 6.2 shows the drop width W as a function of drop radius R in the relaxed state after stopping the flow. At lower radii, W increases linearly with R and follows the MM theory. At a critical radius, that depends slightly on the shear rate applied, the width becomes constant and does not increase with R . This starts at a degree of confinement in the order of 0.3, which is less than reported by Vananroye et al. [24], who showed a constant width for a 5 wt% PIB in PDMS blend at a degree of confinement equal to 0.42.

The widths of droplets becoming constant, which was not reported by Pathak et al. [21], was attributed to the organization of droplets in pearl necklaces in Vananroye et al. [24], but in our case we find a constant width even before pearl necklace structures are formed, see the two top pictures on the right in Figure 6.2. In addition, the critical degree of confinement above which W is constant, increases with decreasing the dimensionless shear rate. The M model does predict the leveling off of the width, although the results are only qualitative. When the mM model is used, the agreement with the experimental data improves, but the constant width is still not fully captured for these cases.

To investigate the influence of the dispersed phase concentration, blends with mass fraction of 20% and 30% were analyzed, see Figures 6.3 and 6.4, respectively. The range of shear rates investigated is the same as in the case of the 10 wt% PBD blend.

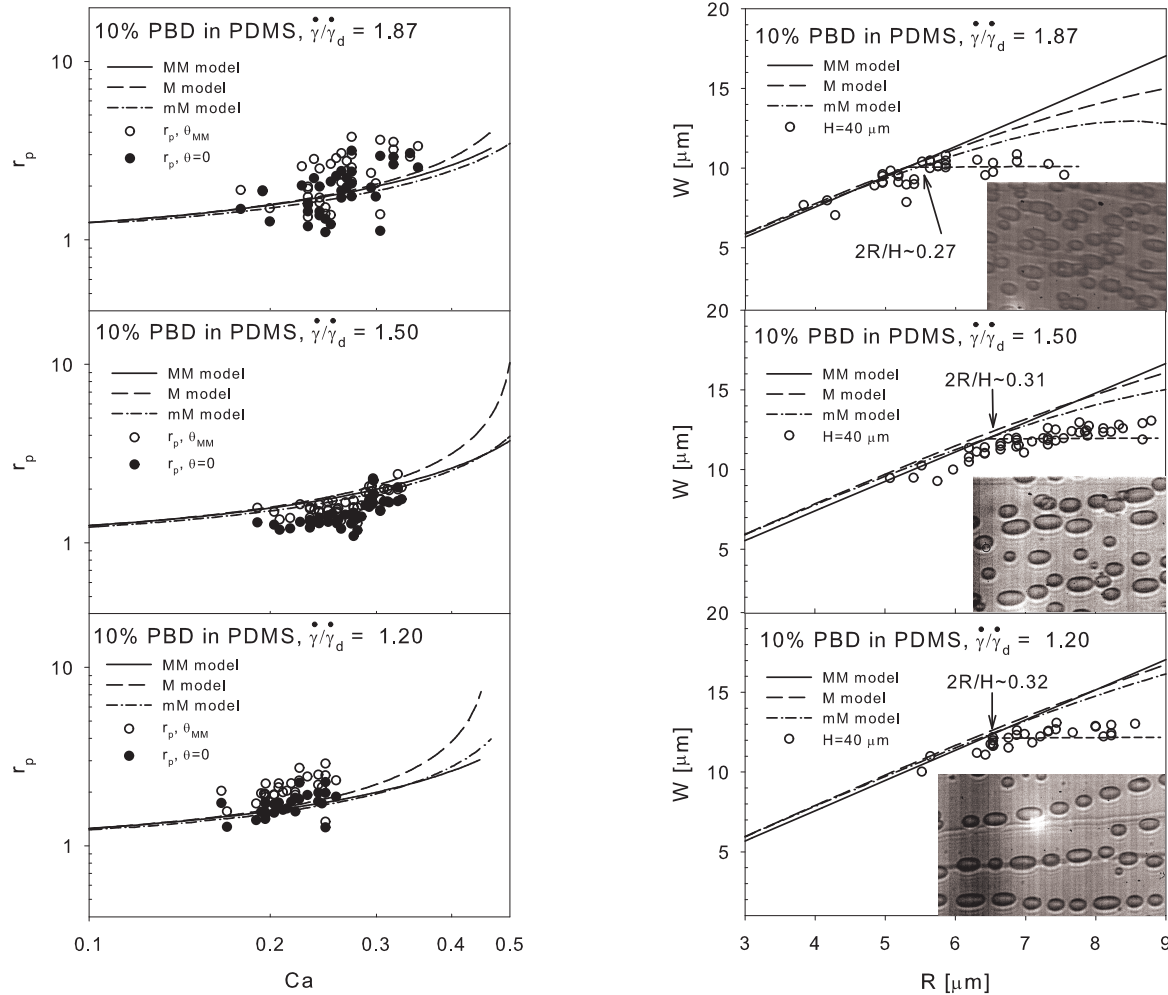


Figure 6.2: Left: droplet aspect ratio (r_p) vs capillary number. Experimental data calculated when assuming θ predicted by the MM model (θ_{MM} , open circles) and $\theta = 0$ (filled circles), r_p predicted by the MM model (Eq. 6.10, solid line), M model (Eq. 6.12, dashed line) and mM model (dash-dotted line). Right: steady-state droplet widths vs the radius in the relaxed shape, experimental data measured from microscopy images (circle), predictions of the MM model (Eq. 6.6, solid lines), the M model (Eq. 6.13, dashed line), and the mM model (dash-dotted line). The inserts show the steady morphologies. Shear rates are made dimensionless (see Section 6.2).

In the experimental range of Ca numbers the aspect ratio of the droplets is well captured by all three models and, for the width of the 20 wt% droplets, the agreement is quite good at least for the first two shear rates. At a dimensionless shear rate of 1.20 strings start to form; the analysis was limited only to the droplets. For the 30 wt% droplets, the discrepancy between the MM model and measured width already starts for a degree of confinement of 0.26 (see Figure 6.4, right). The mM model, again, gives good agreement with the experimental data.

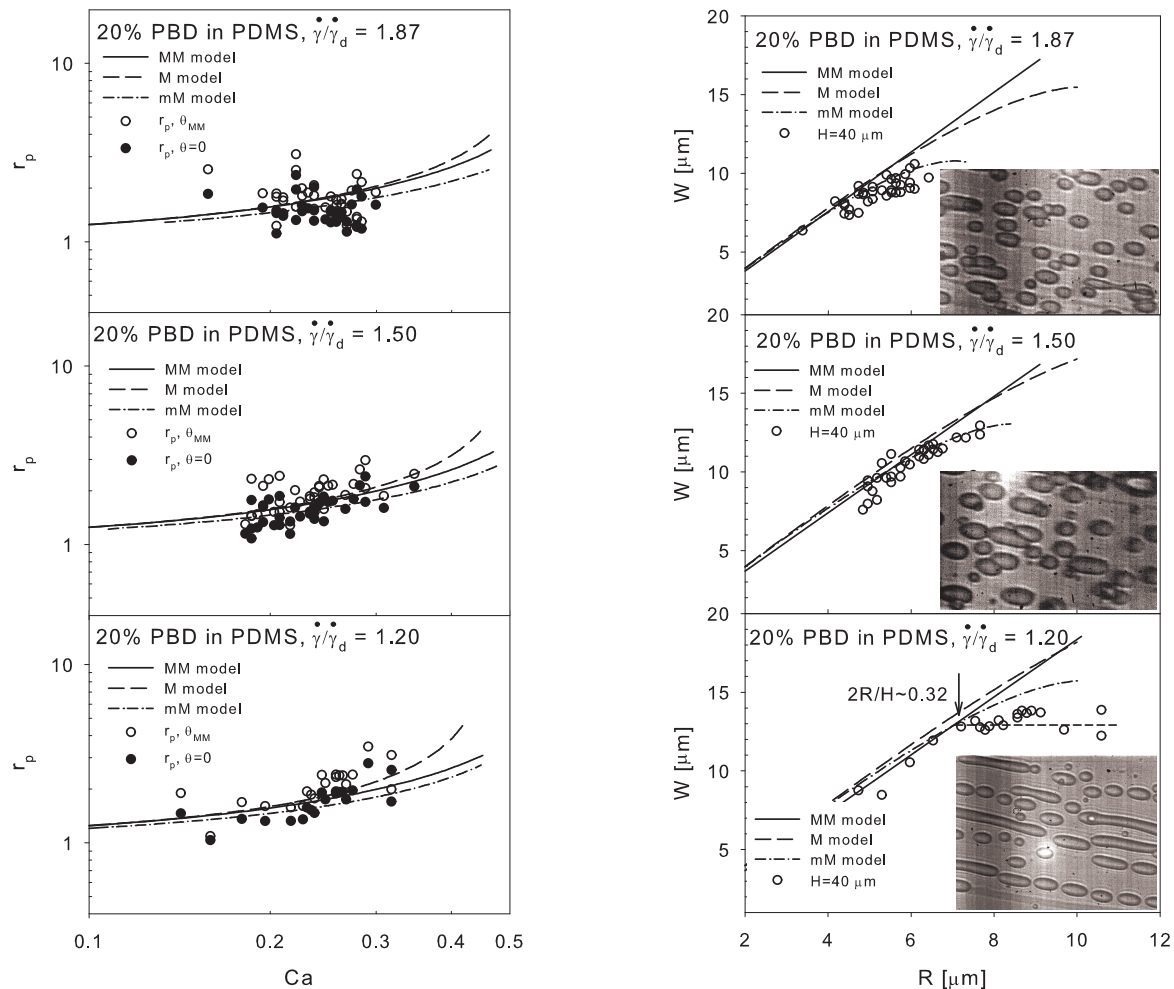


Figure 6.3: As Figure 6.2, now for a 20% concentration.

Summarizing: for the range of Ca considered, the measured droplet aspect ratios can be predicted well by all three models at all concentrations and apparently the most simple MM model can still be applied to express droplet deformation in confined geometries. In some cases the agreement was improved by reducing the orientation angle suggesting that in confinement drops orient more.

The predicted widths of the droplets show that the MM model is applicable only when the degree of confinement is limited, failing when $2R/H$ exceeds a critical value. The minimum degree of confinement, above which the MM model fails, is a function of the shear rate, and increases with decreasing shear rate. For these conditions the M model was developed. The best agreement of the experimental widths of the droplets with the predicted W is obtained with the mM model, i.e. when the viscosity of the matrix is substituted by the effective blend viscosity. The agreement improves for an increasing concentration.

For lower shear rates, long elongated droplets, with $L_p/W > 4$, and superstructure arrangements, like pearl necklaces and strings, start to form. In agreement with the

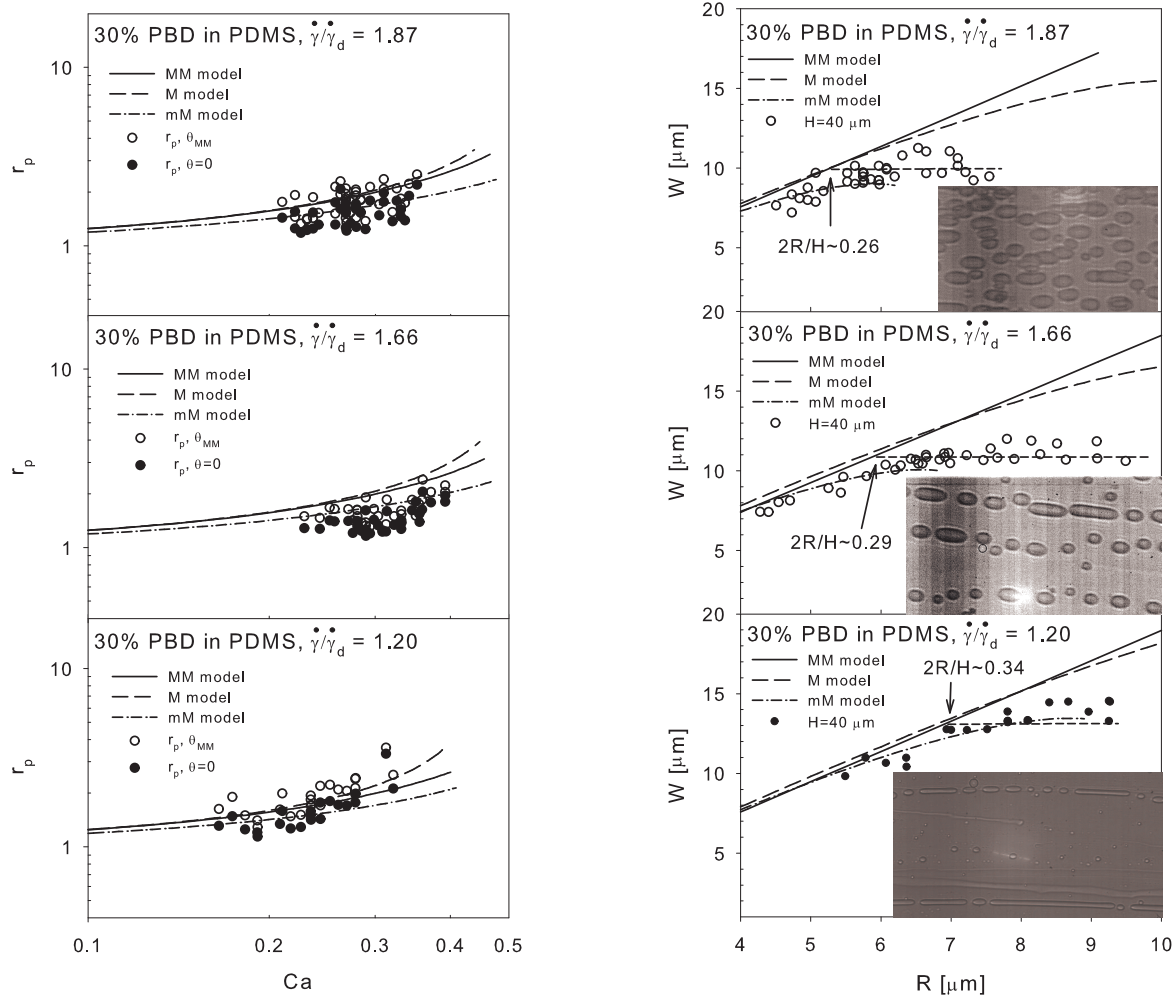


Figure 6.4: As Figure 6.2, now for a 30% concentration.

morphological diagram presented by Pathak et al. [21], changes in the concentration, from 10 to 30 wt%, seem not to significantly affect the dimensionless shear rate at which this transition occurs, .

6.4.2 PB/PDMS system

Next we investigated the PB/PDMS blends using the same three concentrations as for the PBD/PDMS blends. The gap between the parallel plates was kept $40 \mu\text{m}$, and the temperature was fixed at 23°C .

The transition towards confined behavior was found to occur at lower shear rates as compared to the PBD/PDMS blends. Therefore, experiments were carried out starting from a dimensionless shear rate of 1.98 downwards.

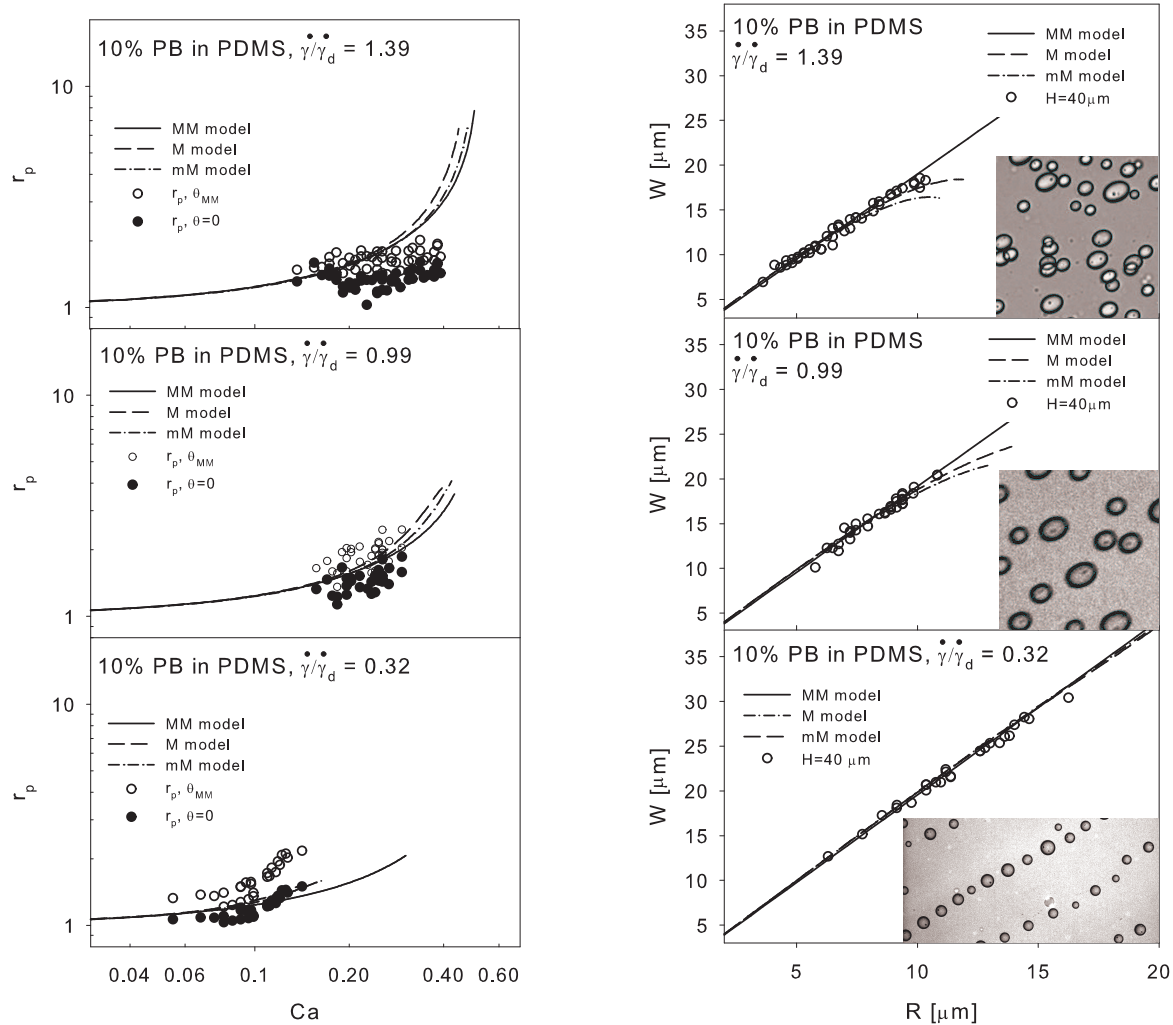


Figure 6.5: Left: droplet aspect ratio (r_p) vs capillary number. Experimental data calculated when assuming θ predicted by the MM model (θ_{MM} , open circles) and $\theta = 0$ (filled circles), r_p predicted by the MM model (Eq. 6.10, solid line), M model (Eq. 6.12, dashed line), mM model (dash-dotted line). Right: steady-state droplet widths vs the radius in the relaxed shape, experimental data measured from microscopy images (circle), predictions of the MM model (Eq. 6.6, solid lines), the M model (Eq. 6.13, dashed line), and the mM model (dash-dotted line). The inserts show the steady morphologies.

Figure 6.5 left, shows the experimental droplet ratio determined by, again, using the MM model-assumption for the orientation angle, θ_{MM} , or $\theta = 0$, at dimensionless shear rates of 1.39, 0.99 and 0.32 (top to bottom). Also for the PB/PDMS system, the r_p values determined by using the orientation angle θ from the M model or the mM model do not differ much from the values calculated by using the MM model and, therefore, we will not report these data in the figures here after.

For the highest shear rate, the experimental data for r_p agree with the predictions of the three models only in the low Ca zone, whereas deviations appear for $Ca \simeq 0.2$ and higher. The droplets deform less than predicted by the models and arrange into a two layer disordered structure, as can be seen in the optical micrographs shown in Figure 6.5 right top.

Similar results were found by Vananroye et al. [24] at a shear rate at which the morphology is comparable to the one presented here. However, in their paper, consistent deviations of the experimental r_p from the theoretical predictions were found for Ca values very close to, and even higher than Ca_{cr} , which is clearly not the case here, i.e. deviations occur at a lower Ca values. With the 10 wt% PB blend, droplets at Ca slightly larger than the Ca_{cr} were encountered only at a dimensionless shear rate of 1.98 and they were found to be stable under the flow, in accordance with the observations of Pathak et al. [22].

When the dimensionless shear rate is reduced to 0.99, droplets start to deform more than predicted by the MM model and slightly better agreement is found with the M model and the mM model. When r_p is calculated assuming the orientation angle equal to zero, the data shift below the r_p curves, suggesting that the droplets are not fully aligned (see Figure 6.5 middle).

While reducing the shear rate further, Figure 6.5 (bottom), the droplets accumulate into a one layer structure and align in the flow direction. The aspect ratio calculated with $\theta = 0$ gives very good agreement with all three models. At a dimensionless shear rate of 0.16, three strings were present, two of them, with width W of 25 μm and 27 μm , break-up into droplets when the flow is stopped, while the one with $W = 70 \mu m$, by definition a ribbon ($W > B$), remains stable. Migler [20] explained this by suggesting that the walls suppress the break-up due to the Rayleigh-Tomotika mechanism.

For the 10 wt% PB blend, the predictions of the width of the droplets are, for the two lowest shear rates, in good agreement with the measured values (see Figure 6.5 right). For these cases the model predictions do not differ much in the range of experimental results, in contrast with the PBD/PDMS blends (see Figures 6.2 - 6.4). The mM model is less predictive for the highest shear rate although the trend of leveling off is also seen in the experimental results.

The effect of gap spacing on the transition from bulk to confined behavior was investigated for the 10 wt% PB blend using $H = 65 \mu m$. The case shown (see Figure 6.6) is similar to $H = 40 \mu m$ where the aligned droplet structure occurs (Figure 6.5, bottom). Also the experimental results for r_p , W and the model predictions are very similar. The transition occurs at a somewhat larger dimensionless shear rate, 0.37 compared to 0.32 for $H = 40 \mu m$.

Figure 6.7 shows the results for the 20 wt% PB/PDMS system with the predicted and experimental values of r_p (left) and the droplet width W (right) for, from top to bottom, dimensionless shear rates of 0.99, 0.79 and 0.63.

Increasing the drop concentration to 20 wt% causes the droplet aspect ratio r_p to be higher than the MM model prediction and to agree better with the M model for

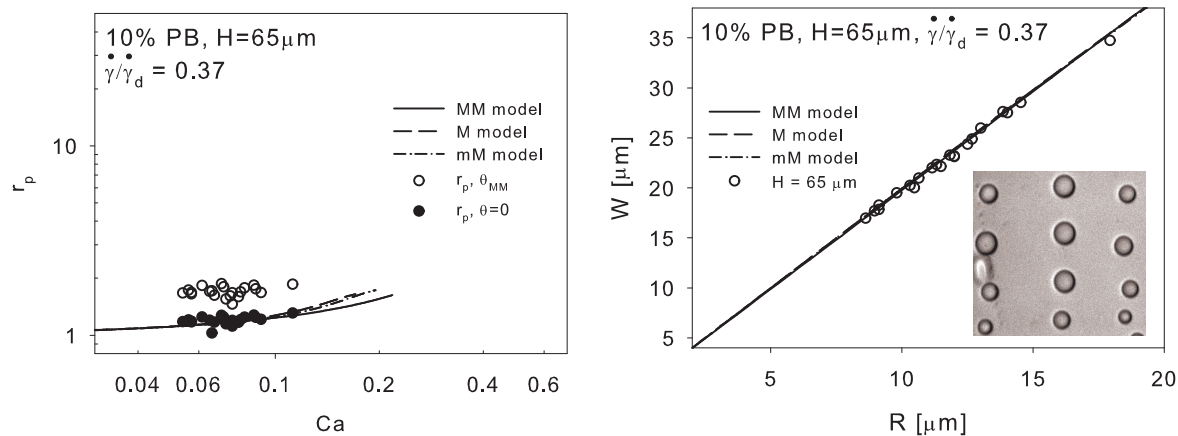


Figure 6.6: As Figure 6.5, now for $H = 65 \mu\text{m}$.

all the shear rates investigated. The discrepancy becomes more pronounced when decreasing the shear rate and for $Ca > 0.2$ for all the three models.

Different from the 10 wt% blend, a clear effect of the confinement on the width W of the droplets is observed, like in the PBD/PDMS system. Already at $\dot{\gamma}/\dot{\gamma}_d = 0.99$ droplets are in a single plane, although no ordered pearl necklaces are seen, and at $2R/H \simeq 0.4$, the width of the droplets starts to deviate from the MM prediction. This discrepancy reduces when the mM model is used. Decreasing the shear rate increases the value of $2R/H$ where confinement becomes noticeable, similar to the results reported in Section 6.4.1.

Also for this concentration, the gap was varied by increasing it to $H = 50 \mu\text{m}$ and $H = 100 \mu\text{m}$, see Figures 6.8 and 6.9 respectively. Increasing the gap, the shear rate at which confinement effects are detected must decrease, to result in a larger average droplet radius. This is confirmed, especially for the twice as large gap of $100 \mu\text{m}$. For $H = 50 \mu\text{m}$, for the case shown, similar behavior as for $H = 40 \mu\text{m}$ is found (see Figure 6.7, top) and the width W is well predicted by the mM model. For $H = 100 \mu\text{m}$, no confinement effect on W is observed anymore and this is also predicted by the models.

Results for the 30 wt% PB blend are summarized in Figure 6.10. The agreement between experimental and calculated values of r_p is good when the M model is considered and the degree of confinement at which the W becomes independent of the droplet radius increases from $2R/H \simeq 0.42$ till $\simeq 0.65$ for $\dot{\gamma}/\dot{\gamma}_d = 1.27$ and $\dot{\gamma}/\dot{\gamma}_d = 0.79$, respectively. The mM model gives good prediction of the width of the drops, confirming the statement that this modification of the M model gives better agreement with the measurements for the higher concentrated blends.

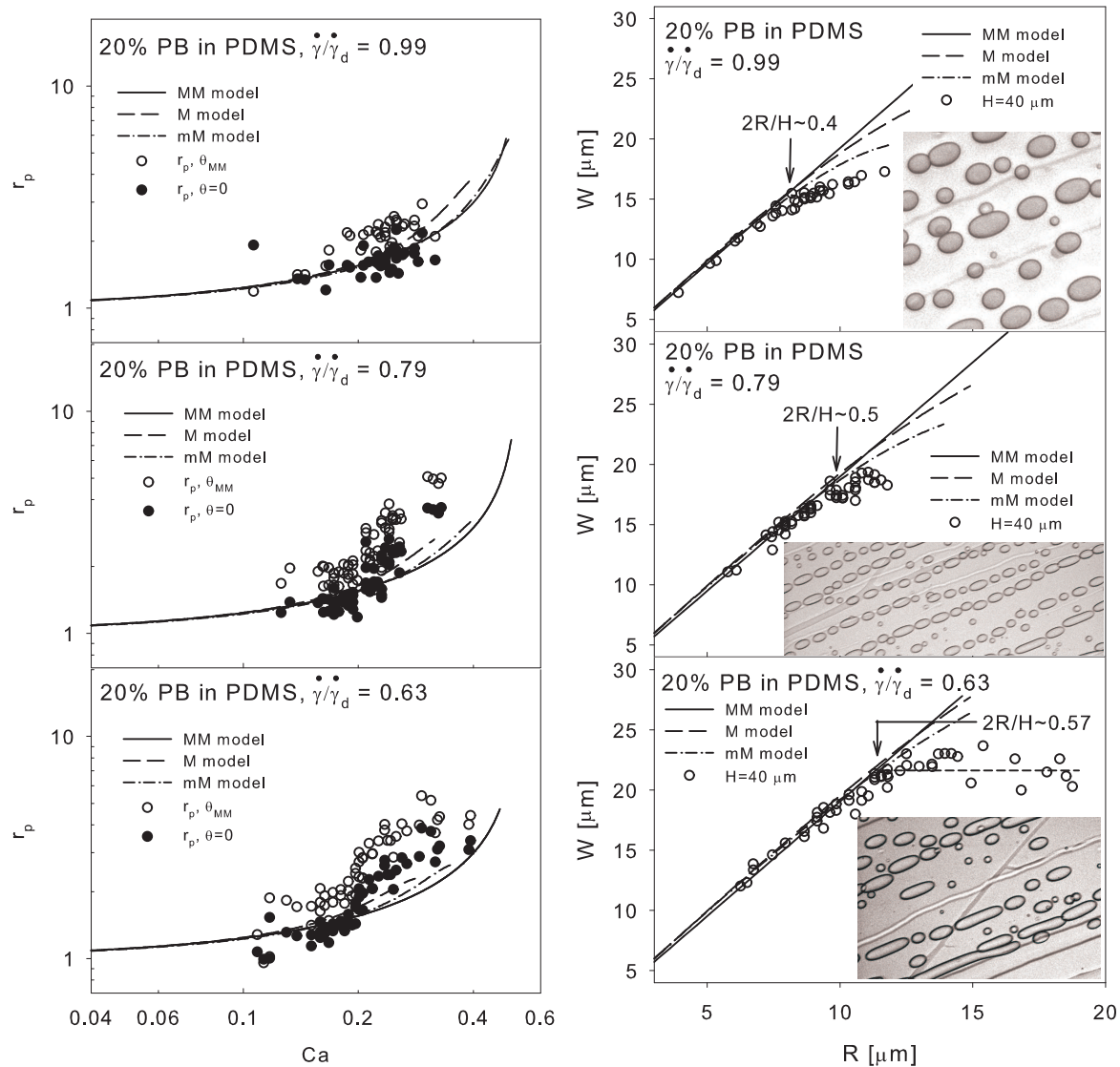


Figure 6.7: As Figure 6.5, now for a 20% concentration.

6.4.3 Conditions to identify strings

Pathak et al. [21] also investigated the dependence of L and B on Ca across the transition from droplets to strings. When only droplets were present, they reported L and B to scale proportionally to Ca , but when strings started to form, for a blend 9.7 wt% PDMS in PIB, at shear rate of $3s^{-1}$, L/H and B/H scaled with $(R/H)^{2.93}$ and $(R/H)^{0.03}$, respectively, and they calculated that L/B scales with $Ca^{2.93}$. This strong dependence, not found for droplet-like morphologies, was addressed as an unique condition for string formation in confined emulsions.

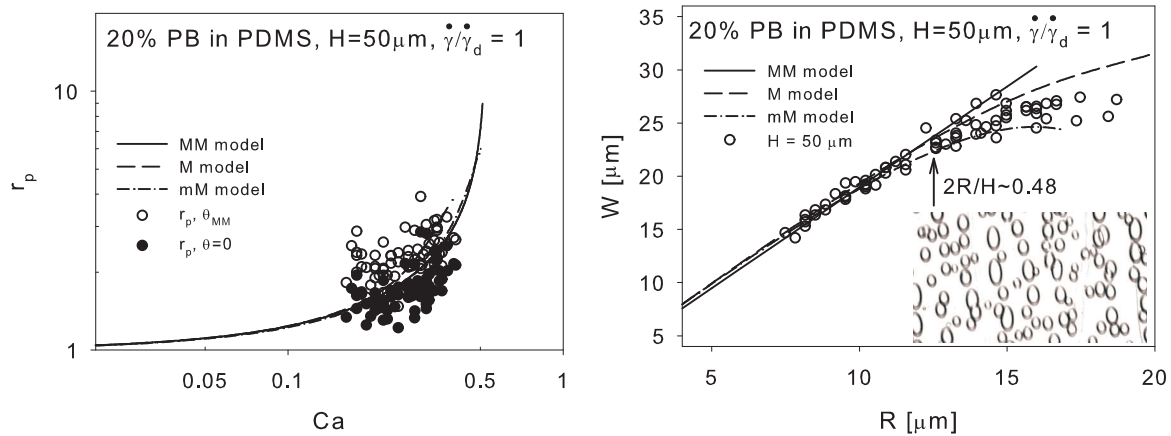


Figure 6.8: As Figure 6.5 now for a 20% concentration and $H = 50 \mu m$.

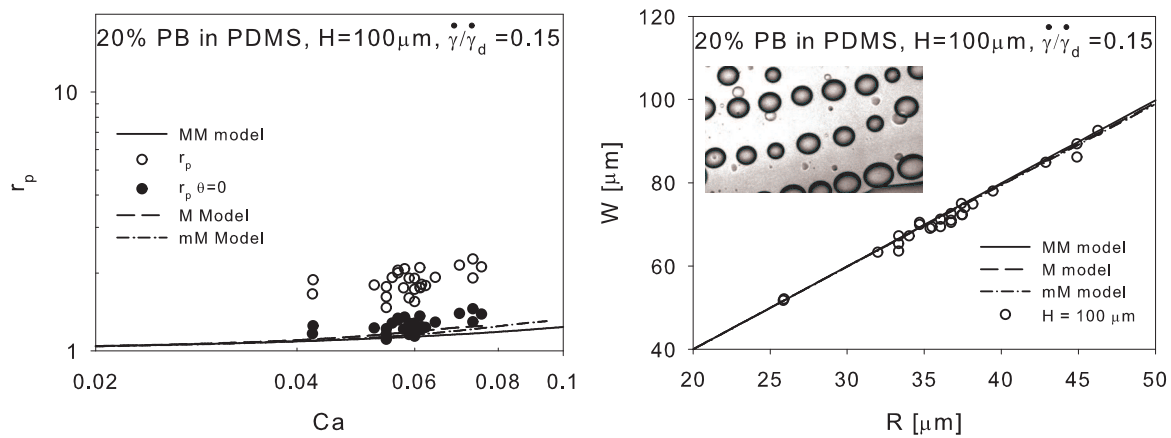


Figure 6.9: As Figure 6.5 now for a 20% concentration and $H = 100 \mu m$.

We fitted our experimental L and B values with straight lines, Eq. 6.17, to verify this dependence.

$$L \propto Ca^l, \quad B \propto Ca^b. \quad (6.17)$$

For the 20 wt% PBD/PDMS and PB/PDMS systems, the powers l and b are calculated for the two extreme cases of bulk-like morphology and strings.

Next, we show how l and b change with decreasing shear rate. Only the results obtained for the 10 wt% PB in PDMS are reported since the analysis in all the other cases yields the same conclusions.

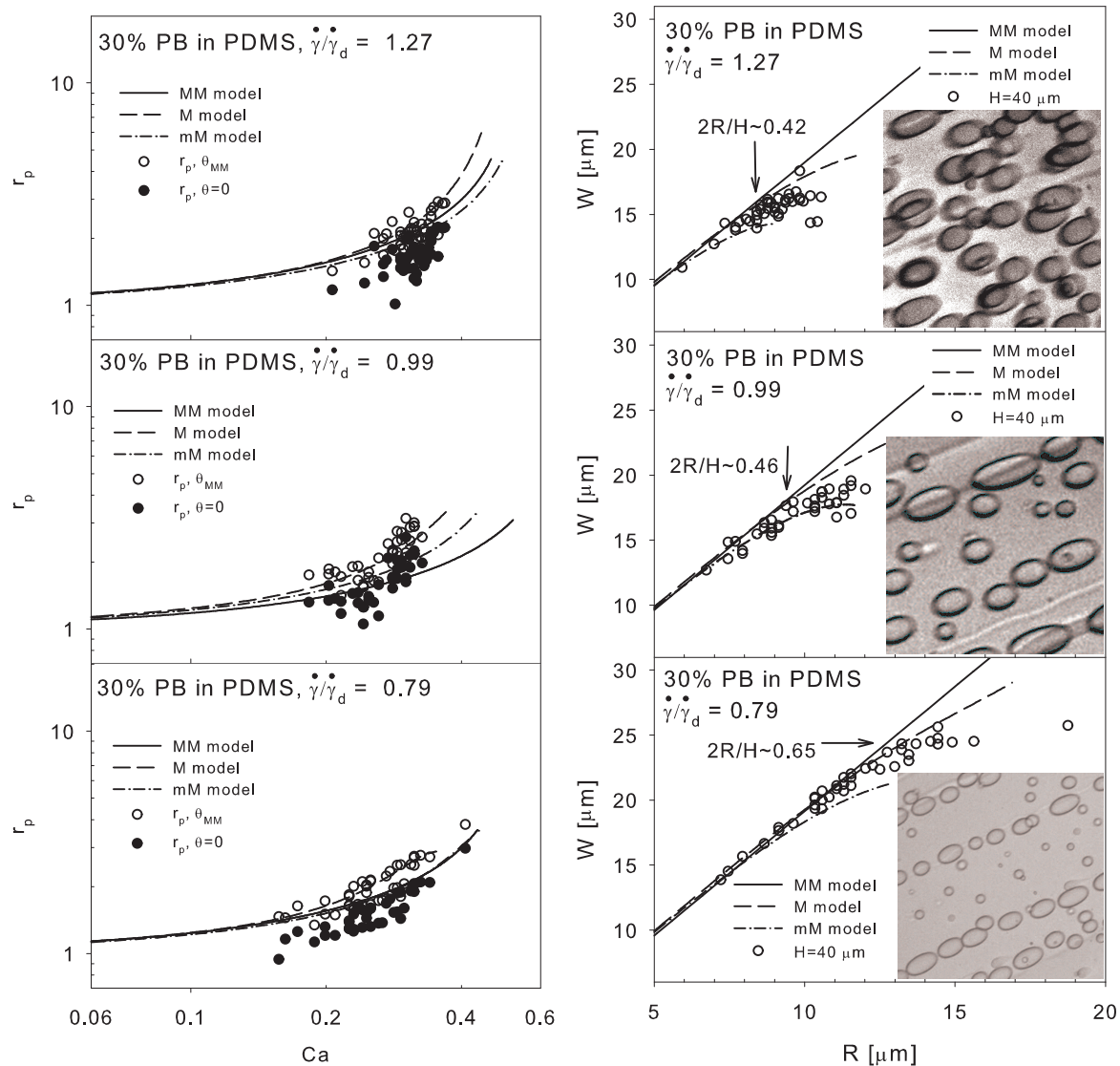


Figure 6.10: As Figure 6.5, now for a 30% concentration.

20 wt% PBD

The experimental results for the 20 wt% PBD blend are shown in Figure 6.11 giving L and B versus Ca , for $\dot{\gamma}/\dot{\gamma}_d = 1.87$ (left) and $\dot{\gamma}/\dot{\gamma}_d = 0.96$ (right).

The L and B values reported are calculated from the experimental L_p , W and R with the MM model. The L and B values obtained using the M model and mM model, do not differ much from these values and, therefore, are not reported here.

At the higher shear rate, elongated droplets are present while for the lower shear rate strings are found. For drops (Figure 6.11, left), L and B depend on the Ca , approximately with the same order, $l = 1$ and $b = 1.4$. For the strings (Figure 6.11, right) we find B to be a weak function of Ca , $b = 0.2$, while L indeed strongly depends on Ca ,

$l = 2.6$.

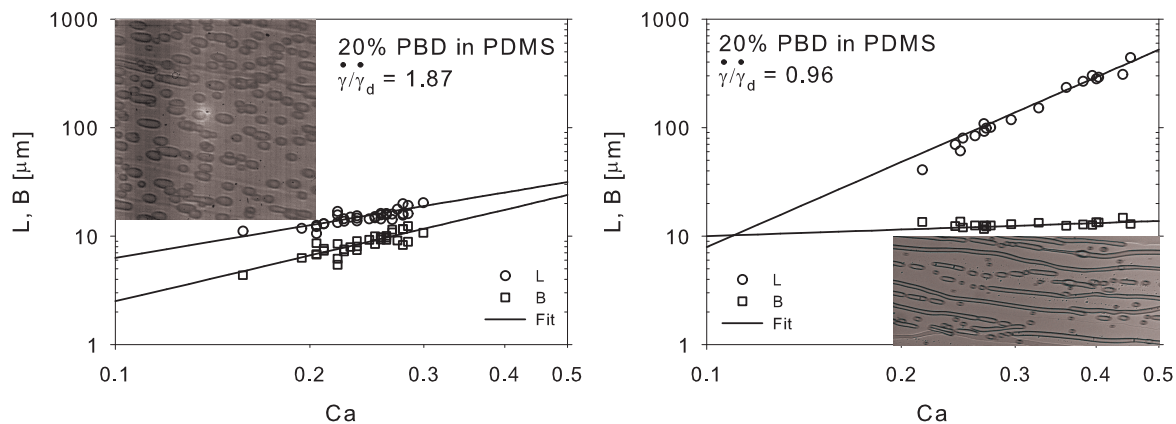


Figure 6.11: Dependence of the two sizes of droplets (left) and strings (right) on the capillary number. Experimental data for L (circles) and B (squares), and the results of fitting with Eq. 6.17 (solid lines). The inserts show the steady morphologies.

20 wt% PB

The dependence of L and B on Ca for $\dot{\gamma}/\dot{\gamma}_d = 0.99$ are shown in Figure 6.12, where a bulk-like morphology is present, and for $\dot{\gamma}/\dot{\gamma}_d = 0.5$, where also strings are present. Fitting with Eq. 6.17 yields $l = 1.21$ and $b = 1.06$ at dimensionless shear rate of 0.99, and $l = 3.06$ and $b = 0.01$ at dimensionless shear rate of 0.5.

Analogous to the case of the 20 wt% PBD blend, when strings form, L becomes a strong function of Ca , while B approximately becomes independent from Ca . The presence of strings apparently coincide with a strong dependence of aspect ratio on capillary number.

Dependence of L and B on the dimensionless shear rate

In this section we show how the dependence of L and B changes with reducing the dimensionless shear rate. Only results for the 10% PB in PDMS blend are presented, since the conclusions we draw for this system hold also for all the other blends.

The lengths L and the widths B of the drops, and the fitted lines obtained by using Eq. 6.17, are shown as a function of the capillary number in Figure 6.13 and the values for the parameters l and b obtained when fitting L and B respectively, are 1.1 and 0.89 at $\dot{\gamma}/\dot{\gamma}_d = 1.39$, 1.28 and 0.77 at $\dot{\gamma}/\dot{\gamma}_d = 0.99$, 1.48 and 0.63 at $\dot{\gamma}/\dot{\gamma}_d = 0.32$.

With decreasing the shear rate, L becomes a stronger function of Ca , while the B dependence becomes weaker. It should be noticed that, although the dependence

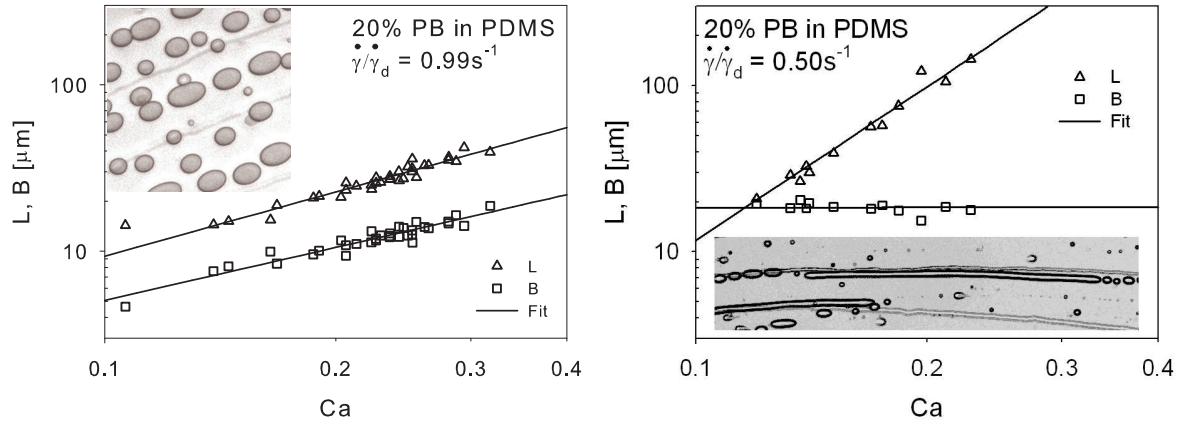


Figure 6.12: As Figure 6.11, now for 20% PB in PDMS.

of B on Ca is significantly lower than the dependence of L , it is still higher than the one calculated for the 20 wt% PBD at $\dot{\gamma}/\dot{\gamma}_d = 0.96$ (see Figure 6.11 right) and for the 20 wt% PB at $\dot{\gamma}/\dot{\gamma}_d = 0.50$ (see Figure 6.12 right). This difference can be explained considering the two morphologies. Indeed, while for the 20% PBD and the 20% PB blends strings are present, in the case of the 10% PB blend, still a droplet-matrix morphology exists, even at the lowest shear rate investigated.

It can be concluded that, according to the results of Pathak et al. [22], the strong dependence of the $r_p = L/B$ on Ca is characteristic only for strings and, in addition, increasing the degree of confinement, the dependence of r_p on Ca increases.

6.4.4 Steady-state morphology and layering effects

Average droplet size

Goal is to test whether bulk theories can be applied to describe blend morphology at rest, even when, due to the limited gap spacing, confinement effects are present.

Figure 6.14 shows the average droplet radii for the two systems investigated: PBD/PDMS (left) and for the PB/PDMS (right). The mean radii were determined from micrographs, once the shear flow was stopped and the droplets relaxed, excluding daughter droplets formed after breaking up of strings eventually present during the flow.

The break-up line is found by imposing $Ca = Ca_{cr}$ at all shear rates; the coalescence lines, yielding R_{PM} , are calculated based on bulk theory for immiscible blends [30] using partially mobile interfaces:

$$R_{PM} = \left(\frac{4}{\sqrt{3}} \frac{h_{cr}}{p} \right)^{2/5} \cdot \left(\frac{\sigma}{\eta_m \dot{\gamma}} \right)^{3/5}, \quad (6.18)$$

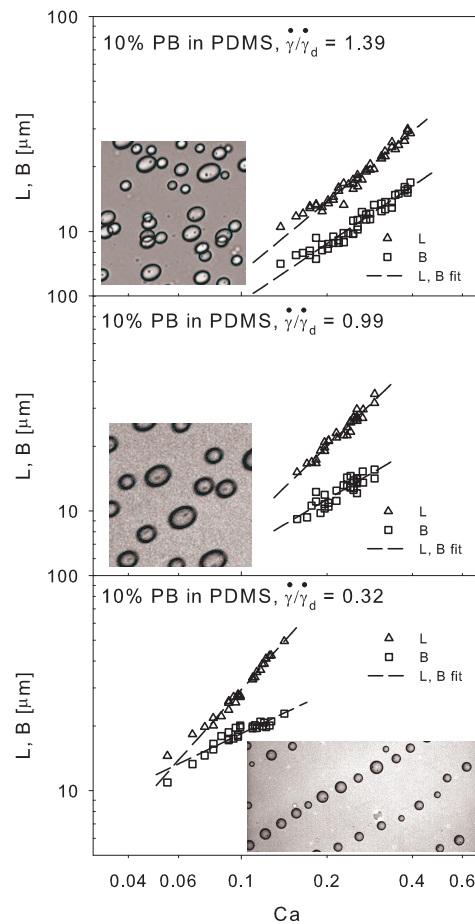


Figure 6.13: As Figure 6.11, now for 10% PB in PDMS.

where h_{cr} is the critical matrix film thickness between two colliding droplets that was used here as an adjustable parameter, resulting in $h_{cr} = 13.1 \mu\text{m}$ for PBD/PDMS and $h_{cr} = 38.2 \mu\text{m}$ for PB/PDMS.

The experimental radii are all in the vicinity of the coalescence curve, as expected since experiments were performed by reducing the shear rates.

Layering effect

Layering of drops into a single plane is expected to occur at confinements of 0.5, since above this value, there is not enough space anymore to place droplets into two different layers [21]. However, for the PBD/PDMS system, the transition to a single layer occurred already at degree of confinement in the order of $2R/H \sim 0.3$ while, for the PB/PDMS blend, we found $2R/H \sim 0.4$. These values increased slightly when higher concentrations were considered.

The low Reynolds number, $Re \sim O(10^{-7})$, shows that inertia can be neglected and

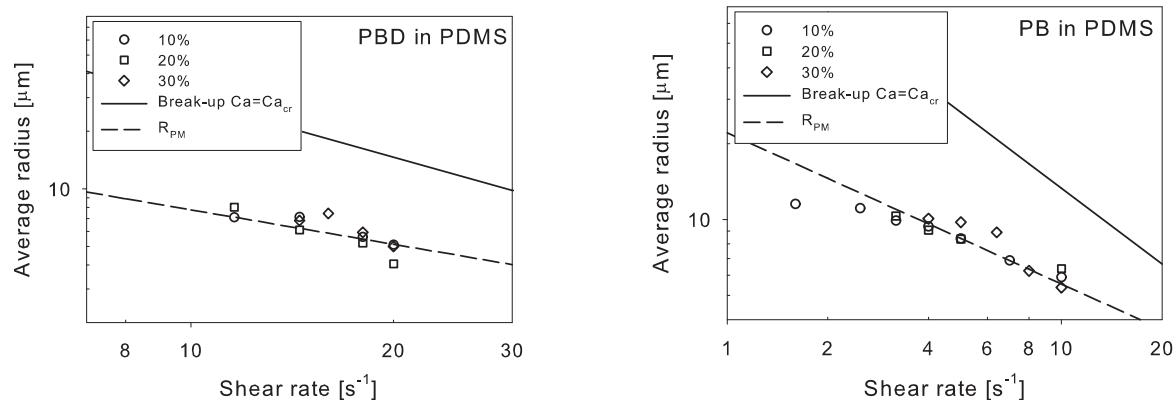


Figure 6.14: Steady-state droplet size as a function of the shear rate for the PBD/PDMS system (left) and PB/PDMS system (right). Model prediction for break up (solid line) and coalescence (dashed line) are shown.

Stokes flow prevails in all the experiments; the large Peclet number, $Pe \sim O(10^6)$, indicates that hydrodynamic interactions are much more important than Brownian motions, and the low Bond number, $Bo \sim O(10^{-4})$, illustrates that interfacial tension dominates buoyancy. The conditions used in our experiments are the same as those reported in Pathak et al. [21], who argued that the number of layers in which droplets in a confined emulsion can arrange, at a given shear rate, is controlled by three competing phenomena. The first is wall migration as reported by King et al. [31], due to an "asymmetric disturbance velocity", droplets are drifted away from the walls toward the centerline. The other two are finite size effects and droplet collision during shear. However, it has to be stressed that the physics behind the layering is still poorly understood.

6.5 Conclusions

Morphology evolution in confined geometries was investigated for two different binary emulsions using three different droplet concentrations. The gap space was $40 \mu\text{m}$ and the shear rates were reduced to allow for coalescence, thereby increasing the droplet radius to enter the confinement region. The transition between a bulk-like behavior and a confinement effects was found in all the cases. For the blends with lower viscosity ratio, this transition was found at lower shear rates compared to the high viscosity ratio blends. At the higher shear rates, droplets arrange in two or more layers. When the shear rate is decreased, a migration towards the centerline occurs. Due to coalescence, pearl necklaces and strings are formed at the lower shear rates. The transition from two to one layer occurs at $2R/H < 0.5$, suggesting that the finite size effects are probably not the only reason for such an arrangement. At each shear rate, the projections of the two axes of the elliptical deformed droplets are

measured from optical micrographs, the aspect ratio calculated and compared with the predictions of three different models: the MM model, M model and mM model. In most cases, the three models predict reasonably well the experimental aspect ratio, in some cases better agreement is found by assuming a zero orientation angle, thus a confined geometry orients more compared to the situation of equally sized droplets subjected to the same flow history, but in a non-confined environment. The droplet width W is measured from optical images and compared to the predictions of the three aforementioned models and, depending on the system and concentration, a critical degree of confinement, above which all the droplets have a constant width, was found that increases with shear rate. This deviation from unconstrained theory occurs even before the formation of ordered pearl necklaces structures. When the M model is used, meant for drops flowing in simple shear rate and in confined geometries, this discrepancy is reduced. By using the effective viscosity instead of the matrix viscosity in the M model, we obtain the mM model and better agreement between model predictions and experiments is found, improving with increasing the volume fraction of the dispersed phase. The dependence of L and B on the capillary number ($L \propto Ca^l$, $B \propto Ca^b$) shows that upon reducing the shear rate, l increases, while b decreases, while r_p depends stronger on Ca . When a drop-matrix morphology is present, l and b are almost equal and close to 1 while, when strings form, b is small while l becomes large, resulting in an aspect ratio proportional to $Ca^{2.6}$ for PBD/PDMS and $Ca^{3.1}$ for PB/PDMS. It was shown that this strong dependence of the drop aspect ratio on the capillary number arises only when confinement effects are present; thus this is a fingerprint of the presence of strings. The steady-state average radii calculated when stopping the flow were compared with the predictions of the partially mobile drainage model describing coalescence. The results show that the theory for non confined situations can describe the morphology evolution also in confined geometries.

References

- [1] Maffettone, P.L. and Minale, M. (1998). Equation of change for ellipsoidal drops in viscous flow. *J. Non-Newt. Fluid Mech.*, **78**, 227–241.
- [2] Minale, M. (2008). A phenomenological model for wall effects on the deformation of an ellipsoidal drop in viscous flow. *Rheol. Acta*, **In press**.
- [3] Shapira, M. and Haber, S. (1990). Low Reynolds number motion of a droplet in shear flow including wall effects. *Int. J. Multiph. Flow*, **16**, 305–321.
- [4] Choi, S.J. and Showalter, W.R. (1975). Rheological properties of nondilute suspensions of deformable particles. *Phys. Fluids*, **18**, 420–427.
- [5] Taylor, G.I. (1932). The viscosity of a fluid containing small drop of another fluid. *Proc. R. Soc. London, A*, **138**, 41–48.
- [6] Rallison, J.M. (1984). The deformation of small viscous drops and bubbles in shear flow. *Annu. Rev. Fluid Mech.*, **16**, 45–66.

- [7] Stone, H.A. (1994). Dynamics of drop deformation and breakup in viscous fluids. *Annu. Rev. Fluid Mech.*, **26**, 65–102.
- [8] Ottino, J.M. and, De Roussel, P., Hansen, S., Khakhar, D.V. (1999). Mixing and dispersion of viscous fluids and powdered solids. *Adv. Chem. Eng.*, **25**, 105–204.
- [9] Tucker, C.L. and Moldenaers, P. (2002). Microstructural evolution in polymer blends. *Annu. Rev. Fluid Mech.*, **34**, 177–210.
- [10] Hinch, E.J. and Acrivos, P. (1980). Long slender drops in simple shear flow. *J. Fluid Mech.*, **98**, 305–328.
- [11] Khakhar, D.V. and Ottino, J.M. (1986). Deformation and breakup of slender drops in linear flows. *J. Fluid Mech.*, **166**, 265–285.
- [12] Bentley, B.J. and Leal, L.G. (1986). An experimental investigation of drop deformation and breakup in steady, two-dimensional linear flows. *J. Fluid Mech.*, **166**, 265–285.
- [13] Stone, H.A., Stroock, A.D., Ajdari, A. (2004). Engineering flows in small devices: Microfluidics toward a lab-on-a-chip. *Annu. Rev. Fluid Mech.*, **36**, 381–411.
- [14] Link, D.R., Anna, S.L., Weitz, D.A., H.A., Stone (2004). Geometrically mediated breakup of drops in microfluidic devices. *Phys. Rev. Lett.*, **92**, 0545031–0545034.
- [15] Utada, A.S., Lorenceau, E., Link, D.R., Kaplan, P.D., Stone, H.A., Weitz, D.A. (2005). Monodisperse double emulsions generated from a microcapillary device. *Science*, **308**, 537–541.
- [16] Sibillo, V., Pasquariello, G., Simeone, M., Cristini, V., Guido, S. (2006). Drop deformation in microconfined shear flow. *Phys. Rev. Lett.*, **97**, 0545021–0545024.
- [17] Vananroye, A., Van Puyvelde, P., Moldenaers, P. (2006). Effect of confinement on droplet breakup in sheared emulsions. *Langmuir*, **22**, 3972–3974.
- [18] Vananroye, A., Van Puyvelde, P., Moldenaers, P. (2007). Effect of confinement on the steady-state behavior of single droplets during shear flow. *J. Rheol.*, **51**, 139–153.
- [19] Janssen, P.J.A. and Anderson, P.D. (2007). Boundary-integral method for drop deformation between parallel plates. *Phys. Fluids*, **19**, 0436021–04360211.
- [20] Migler, K.B. (2001). String formation in sheared polymer blends: coalescence, breakup, and finite size effect. *Phys. Rev. Lett.*, **86**, 1023–1026.
- [21] Pathak, J.A., Davis, M.C., Hudson, S.D., Migler, K.B. (2002). Layered droplet microstructures in sheared emulsions: finite-size effects. *J. Coll. Int. Sci.*, **255**, 391–402.
- [22] Pathak, J.A. and Migler, K.B. (2003). Droplet-string deformation and stability during microconfined shear flow. *Langmuir*, **19**, 8667–8674.
- [23] Mietus, W.G.P., Matar, O.K., Seevaratnam, G., Wong, A., Briscoe, B.J., Lawrence, C.J. (2001). Couette flow of two immiscible liquids between two concentric cylinders: The formation of toroidal drops and liquid sheaths. *Phys. Rev. Lett.*, **86**, 1211–1214.
- [24] Vananroye, A., Van Puyvelde, P., Moldenaers, P. (2006). Structure development in confined polymer blends: steady-state shear flow and relaxation. *Langmuir*, **22**, 2273–2280.

- [25] Frischknecht, A. (1998). Stability of cylindrical domains in phase-separating binary fluids in shear flow. *Phys. Rev. Lett.*, **E 58**, 3495–3514.
- [26] Grace, H.P. (1982). Dispersion phenomena in high viscosity immiscible fluid systems and application of static mixers as dispersion devices in such systems. *Chem. Eng. Commun.*, **14**, 225–277.
- [27] De Bruijn, R.A (1989). *Deformation and break-up of drops in simple shear flows*. PhD thesis, Technical Univ. of Eindhoven, Eindhoven, The Netherlands.
- [28] Vinckier, I., Moldenaers, P., Mewis, J. (1996). Relationship between rheology and morphology of model blends in steady shear flow. *J. Rheol.*, **40**, 613–631.
- [29] Takahashi, Y., Kurashima, N., Noda, I. (1994). Experimental tests of the scaling relation for textured materials in mixtures of two immiscible fluids. *J. Rheol.*, **38**, 699–712.
- [30] Janssen, J.M.H. and Meijer, H.E.H. (1995). Dynamics of liquid-liquid mixing: A two zone model. *Polym. Eng. Sci.*, **35**, 1766–1780.
- [31] King, M.R. and Leighton, D.T. (2001). Measurement of shear-induced dispersion in a dilute emulsion. *Polym. Eng. Sci.*, **13**, 397–406.

Conclusions and recommendations

7.1 Conclusions

This work focusses on the effects of partial miscibility on the morphology development of polymer blends. When dealing with low molecular weight (LMW) polymers or with a high polydispersity, polymers can not be considered immiscible, as often done as a first approximation. Instead, due to interdiffusion of low molecular weight components between the two phases, they behave as *partially-miscible*. After mixing the components, a diffuse interface is established that affects the interfacial tension. Since the interfacial tension is an important parameter in morphology development, partial miscibility of polymers can not be always neglected.

Interfacial tension

After the formation of a new interface, the transient interfacial tension follows a four-step scenario: 1) reduction, 2) pseudo steady-state, 3) increase (depending on the diffusion direction of the LMW species), 4) plateau value. This behavior is explained with an accumulation of LMW components in the interphase, yielding thickening of the interphase (1), migration of molecules into the receiving phase, during which the interphase thickness stays nearly constant (filling and depletion of the interface occur at the same rate) (2). Next, in case the matrix is the receiving phase, due to a limited amount of LMW components in the drop emptying of the interphase (thinning) occurs (3) and, when the diffusion process is exhausted, the polymers can be seen as immiscible (4). When reversing the blend, the drop is a finite receiving phase and depletion does not occur.

Increasing the molecular weight (MW) of the drop phase yields to the same transient behavior, but the time scale to complete the diffusion process increases. Comparison of the transient interfacial tension for a *highly-diffusive* drop material (low molecular

weight and high polydispersity) with a *slightly-diffusive* drop material (higher molecular weight and polydispersity close to one) in the same matrix, shows that some stages disappear or can not be measured given limitations in accessible experimental time-scales and that the four stages are peculiar for *partially miscible* systems, corroborating our interpretation. Also higher molecular weight components lead to higher steady interfacial tension.

Increasing the temperature does not change the interfacial tension behavior, but yields to 1) lower transient values of the interfacial tension, 2) larger changes in the transient behavior (both because a larger number of small molecules now takes part in the process) and 3) different (surprisingly longer) time scales (because larger amounts of molecules overrule the faster diffusion).

A thermodynamic model, based on the diffusion equation, is proposed and two cases are considered, addressed as the two-zone model and the three-zone model. The two-zone model, which predicts a steep drop in concentration after reaching the maximum thickness interphase, not observed experimentally, is excluded. The three-zone model qualitatively describes the experimentally found transient interfacial tension. For a constant-thickness interphase, the ratio of the diffusion coefficients of the source phase and interphase is found to affect the time scale of accumulation of molecules into the interphase, while the ratio of the diffusion coefficients of the interphase and receiving phase, controls the time scale of depletion. A fit of the experimental data with a discrete version of the three-zone model gives the characteristic time-scales of diffusion. A kinetic model, derived as a special case of our thermodynamic formulation, and applied to relate the characteristic diffusion times to the molecular parameters, shows that the chain lengths of the migrating molecules play a dominant role compared to the bulk viscosities of the polymers.

Droplet attraction

Partial miscibility leads to some special phenomena. When two drops of a *highly-diffusive* system are placed in the matrix, at a distance smaller than their equivalent radius but still much larger than the critical film thickness, attraction and coalescence occurs. The same rate of drop attraction is found in the last $\sim 100s$ before film rupture occurs. These phenomena are not observed for the *slightly-diffusive* system. The findings are explained in terms of thick diffusive layers present only with the highly-diffusive system which overlap when drops are close to each other, leading to gradients in interfacial concentration which, in turn, induce Marangoni flow in the same direction of the film drainage. Gradients in interfacial tension are proven to induce lateral migration of single droplets in quiescent conditions. Simulations with the diffuse-interface method support the experimental results.

Morphology: diluted systems

The morphology evolution of *diluted* systems is found to be determined by the competition of two phenomena: diffusion and coalescence. For the *highly-diffusive* system, in the time scale in which changes in interfacial tension occur, the morphology is fully dominated by the interfacial properties, while, once that the interfacial tension reaches the steady-state value, the morphology evolution is dominated by coalescence. For the slightly-diffusive systems, due to the short time scale of the transient interfacial tension when compared to the time scale of the flow experiments, coalescence is overruling. By reversing the phases of each system, due to fast saturation of the drop phase (diffusion from the matrix into the drop), no effects of a short-term transient interfacial tension on the morphology evolution is found. Average radii measured are compared to predictions of the drainage model for sharp interfaces, indicating that the interfaces are immobile here.

Morphology: concentrated systems

When increasing the concentration of the blends, a hysteresis zone bounded by the break-up and the coalescence lines, is present. This hysteresis zone, for which theoretical predictions agree quite well with experimental results when using *immiscible* systems, is found narrower than predicted by theories, with average radii even beyond the break-up line for the *highly-diffusive* system. Deviations from theories, found also when following the shear induced coalescence in time, are attributed to the partial miscible character of the systems, yielding to enhanced coalescence which, in turn, can induce confinement effects.

Confinement effects

Systematic investigation of these confinement effects for the two partial miscible systems investigated, show that the transition between a bulk-like behavior and a confined behavior occurs, once a critical ratio of droplet size to gap spacing is reached. This transition occurs at lower shear rates for the blend with a lower viscosity ratio. By decreasing the shear rate, i.e. increasing the degree of confinement, formation of new structures, like mono-layer arranged droplets, pearl-necklaces and strings occurs.

Comparison of the experimentally found drop aspect ratio with theoretical predictions, using three different models, the MM model, M model and mM model (see Chapter 6), show that good agreement is found with an extended version of a recently proposed single drop deformation model.

The agreement between experimental data and model predictions increases with the volume fraction of the blend.

7.2 Recommendations

Transient interfacial tension can play a decisive role in defining the morphology of the systems. This transient behavior depends on the fraction of short molecules that can cross any newly formed interface.

It was not possible, however, to quantify the amount of molecules that actually crossed the interface and to specify the relation with the transient interfacial tension. In future work, grades of monodisperse materials should be used, differing in molecular weight, allowing us to make drop phases with a known amount of migrating molecules. By measuring the interfacial tension of drops having different amounts of potentially migrating molecules, it becomes possible to relate the fraction of migrating molecules to the interfacial tension, and thus to calculate the diffusion coefficients for the blends. These diffusion coefficients, used in the thermodynamic model proposed, will then lead to a quantitative prediction of the transient interfacial tension.

For the confined flows, a further step is to investigate blends in a transparent Couette geometry, to get a 3D picture of the morphology and to measure directly the three characteristic dimensions of a deformed drop (L , B , and W) and the orientation angle (θ). In that case, comparison with theories can be carried out without the need of extra assumptions.

Samenvatting

Vergeleken met het ontwerpen en synthetiseren van nieuwe polymeren vertegenwoordigt het proces van het mengen van twee of meer bestaande polymeren een relatief snel, flexibel en goedkoop alternatief om nieuwe materialen met een gewenst pakket aan eigenschappen te bereiden. Eigenschappen van materialen op die manier via een fysisch mengproces gemaakt worden bepaald door het dynamisch evenwicht van de twee concurrerende processen die zich tijdens mengen simultaan afspelen: het opbreken en de coalescentie van druppels. De grensvlakspanning tussen de twee betrokken fasen speelt een belangrijke rol, aangezien beide processen erdoor worden beïnvloed. Het doel van dit werk is te onderzoeken wat de effecten zijn van een gedeeltelijke mengbaarheid van beide componenten op de grensvlakspanning en dus tevens de invloed daarvan op de ontwikkeling van de morfologie van suspensies.

Voor de disperse fase werden twee types polybuteen (PB) gebruikt, verschillend in moleculair gewicht, en één type polybutadieen (PBD), met een polydispersiteitsindex van ongeveer 1; voor de continue fase werd polydimethylsiloxaan (PDMS) gekozen met een moleculair gewicht veel hoger dan van de polymeren van de druppelfase.

Er zijn tijdsafhankelijke en stationaire grensvlakspanningsmetingen uitgevoerd. Voor het systeem PB/PDMS wordt een specifiek gedrag gevonden dat afwijkt van dat van het PBD/PDMS systeem. Na het tot stand brengen van het contact tussen de PB druppel en de matrixfase, begint de grensvlakspanning af te nemen. Dit wordt toegedicht aan de diffusie van laag moleculaire componenten vanuit de druppelfase naar de matrixfase, leidend tot een toename van de grensvlakdikte. Langzamerhand start de diffusie van moleculen geaccumuleerd op het grensvlak naar de matrixfase, leidend tot een toename in grensvlakspanning. Wanneer het diffusieproces stopt door uitputting van laag moleculair materiaal in de (eindige) druppelfase, bereikt de grensvlakspanning een plateauwaarde waarop hij blijft. Bepaling van de afname van het druppelvolumen tijdens dit proces bevestigt dit beeld. Het blijkt dat het systeem PB/PDMS bijzonder diffusief is, terwijl het systeem

PBD/PDMS als niet-diffusief kan worden aangemerkt. De tijdschaal voor diffusie neemt toe met toenemend moleculair gewicht van de PB druppelfase en terwijl een toenemende temperatuur het proces opmerkelijk genoeg het proces vertraagt, veroorzaakt door de mogelijkheid dat op hogere temperatuur meer materiaal (ook het iets hogere moleculair gewicht) mee kan doen aan het diffusieproces, blijktbaar het effect van hogere diffusieconstanten overrullend.

Er is een continu model ontwikkeld, gebaseerd op de diffusievergelijk, dat is gebruikt de gemeten trends kwalitatief te verklaren. Een discrete versie van het model laat toe de typische tijdschalen te berekenen. Het is in staat de experimenten te beschrijven.

Diffuse grensvlakken veroorzaken enkele speciale effecten. Zo wordt onderlinge aantrekking en uiteindelijk ook coalescentie gevonden tussen twee druppels van het laagst molaire PB in PDMS, geplaatst op een afstand van elkaar die veel kleiner is dan hun equivalente diameter maar veel groter dan de kritische filmdikte. Druppels in het PBD/PDMS systeem coalesceren niet, ook als ze tegen elkaar aan worden geplaatst. Er wordt Zelfs onderlinge afstoting gemeten. beide fenomenen worden verklaard in termen van gradiënten in grensvlakspanning langs het grensvlak, veroorzaakt door een inhomogene grenslaagdikte, die leiden tot Marangoni convectie, een stroming in het grensvlak.

Om aan te tonen dat gradiënten in grensvlakspanning inderdaad kunnen leiden tot druppelbewegingen worden individuele druppels in de nabijheid van wanden gemaakt van verschillend materiaal geplaatst. Voor PB druppels vinden we aantrekking en beweging naar zowel PTFE (Teflon) als wanden van glas (gebruikt om benattings-effecten uit te sluiten). PBD druppels ondergaan afstoting en verwijdering. Beide fenomenen vinden we terug in modelberekeningen gebaseerd op DIM, diffuse interface modelling.

Het effect van een tijdsafhankelijke grensvlakspanning is onderzocht in laan geconcentreerde systemen met behulp van twee in-situ technieken: SALS, small angle light scattering, kleine hoek lichtverstrooiing, en OM, optische microscopie. Zowel PB/PDMS als PBD/PDMS systemen als de inverse blends zijn bestudeerd en allen toonden een sterke invloed op de morfologieontwikkeling.

Voor (half) geconcentreerde systemen werd de morfologieontwikkeling bestudeerd met OM en reologische metingen gebruikmakend van de conus-plaat geometrie. Er worden, ten op zichte van theoretische verwachtingen, relatief grote druppels gevonden en hun grootte benadert die van de (variërende) spleet tussen conus en plaat waardoor interactie met de wanden plaatsvindt en effecten van de beperkte bewegingsvrijheid merkbaar worden. Door deze bewegingsbeperking van de druppels bepalen de wanden de morfologieontwikkeling. Meer geprononceerde

coalescentie in het onderzochte gedeeltelijk mengbare blendsysteem leidt tot een hogere mate van beperking in bewegingsvrijheid van druppels en dus invloed van de wanden hier.

Deze invloed is uiteindelijk meer systematisch onderzocht gebruikmakend van drie concentraties (10, 20 en 30%) van beide systemen, PB/PDMS en PBD/PDMS. De gevonden meetresultaten worden vergeleken met de voorspellingen op basis van het (i) Maffetone-Minale (MM) model dat is afgeleid voor bulkgedrag, (ii) het Minale (M) model dat de invloed van de bewegingsbeperking verdisconteert, en (iii) het gemodificeerde Minale (mM) model, waarin een effectieve viscositeit wordt gebruikt om te compenseren voor de aanwezigheid van de disperse fase. Voor alle onderzochte systemen wordt een transitie van bulk gedrag naar bewegings-beperkt gedrag gevonden, echter bij lagere graden van beperking dan verwacht. De kritische waarde van de graad van bewegingsbeperking, waarboven de experimenten de modelvoorspellingen niet meer volgen, nemen toe met afnemende afschuifsnelheid. Verschillende graden van bewegingsbeperking leiden tot verschillen in morfologie.

De conclusie is dat gedeeltelijke mengbaarheid in polymeersystemen leidt tot een sterke invloed op de morfologie van de uiteindelijke blend. Zodra de fenomenen voldoende goed begrepen zijn kunnen ze worden gebruikt om de uiteindelijke eigenschappen van blendsystemen te controleren.

Acknowledgements

My first thanks go to my promoter Han Meijer, for giving me the chance to join the Materials Technology group and perform the research shown in this thesis. Han, I want to thank you for your suggestions and constructive criticism which made it possible to successfully complete my work. I did really appreciate the faith you had in me, especially when you decided to invest your time for a one-to-one five-hours crash course in numerics.

My deep gratitude goes to my co-promotor Gerrit Peters, a volcano of ideas. Thanks for the freedom you gave to me to work on this project and for being always available and open to discussions.

I would like to especially acknowledge Prof. Patrick Anderson for his interest in my work and for being always willing to help. Part of my research would have been definitely not possible without your support and encouragement.

I sincerely thank Prof. Peter van Puyvelde for the possibility to perform experiments at KU in Leuven. I did learn a lot there. Thanks for the friendly behavior, which made my staying in Belgium really pleasant, and for the confidence you always had in my skills to complete my PhD project.

During these four years, many custom-made solutions were needed in order to perform my experiments. For that, the professional skills of Sjef and all people from the workshop(s) helped a lot. Thanks to all of you! Marc van Maris, 50X thanks ;)

The troubleshooting skills of Patrick and Leo helped a lot... thanks, I did appreciate the external HD for my images.

Life was much easier thanks to the three bosses of the MaTe group: Marleen, Yvon and Alice. I would like to thank you for your kindness and for helping with all the paper work typical of this procedure-ruled country.

I am thankful to my (ex)-colleagues and friends that helped to make life enjoyable, even during the long Fridays spent in Utrecht for RPK: Edwin Klompen, Varja Koutnezova, Katja Viatkina, Müge Erinç, Frederico Custodio, Izzet Özdemir, Pieter The Grouch, Matej Hrapko, Viny Khatavkar, JF Vega, Tom Engels, Lambert van Breemen, J.W. Housman, Rudi Steenbakkens, Frank Swartjes, Christina Hristova and Alex Zdravkov, Denka Hristova and Arjen Bogaerds, Rheinard and Andrea, and all

the others. My acknowledgments go to my colleagues at KU Leuven for helping me in the lab, for the nice lunches at Alma, and frozen-pizza based dinners.

Of course, my sincere gratitude goes to all people I did share my life with during these four years...

...just too many to be listed here :)

I am pleased to deeply thank the Italian football team for winning the World Cup the day of my birthday, it was by far the best birthday party I have ever had!

Last, but not least, I would like to thank my family for supporting me during all these years.

Curriculum Vitae

Carmela Tufano was born on July 9th 1977 in Naples, Italy. She attended primary and secondary school (Liceo Scientifico "E. Pascal") in Pompei, Italy. Subsequently, she studied Chemical Engineering at "Federico II", University in Naples, Italy. She obtained her masters degree with a thesis on the effects of the matrix viscoelasticity on the coalescence in flow of polymer blends under the supervision of Prof. Stefano Guido and Prof. Francesco Greco.

In January 2004 she joined the Materials Technology group within the Mechanical Engineering department at Eindhoven University of Technology, in Eindhoven, The Netherlands, to start her PhD study under the supervision of Prof. Gerrit Peters and Prof. Han Meijer. Part of the experimental work was performed in close collaboration with Prof. Peter Van Puyvelde at the Chemical Engineering department of the Katholieke Universiteit Leuven, in Leuven, Belgium. The results of this PhD study are presented in this thesis.

During her PhD, she also successfully completed all five modules of the course "Registered Polymer Technologist"(RPK, Register Polymeerkundige), organized by the "National Dutch Graduate School of Polymer Science and Technology"(PTN, Polymeertechnologie Nederland).